

The Flow History of Siple Dome and
Ice Streams C and D, West Antarctica:
Inferences from Geophysical Measurements
and Ice Flow Models

by

Nadine A. Nereson

A dissertation submitted in partial fulfillment of
the requirements for the degree of

Doctor of Philosophy

University of Washington

1998

Approved by _____

(Chairperson of Supervisory Committee)

Program Authorized
to Offer Degree _____

Date _____

In presenting this dissertation in partial fulfillment of the requirements for the Doctoral degree at the University of Washington, I agree that the Library shall make its copies freely available for inspection. I further agree that extensive copying of this dissertation is allowable only for scholarly purposes, consistent with "fair use" as prescribed in the U.S. Copyright Law. Requests for copying or reproduction of this dissertation may be referred to University Microfilms, 1490 Eisenhower Place, P.O. Box 975, Ann Arbor, MI 48106, to whom the author has granted "the right to reproduce and sell (a) copies of the manuscript in microform and/or (b) printed copies of the manuscript made from microform."

Signature_____

Date_____

University of Washington

Abstract

The Flow History of Siple Dome and
Ice Streams C and D, West Antarctica:
Inferences from Geophysical Measurements
and Ice Flow Models

by Nadine A. Nereson

Chairperson of Supervisory Committee

Professor Charles F. Raymond

Geophysics Program

Siple Dome (81.65° S, 148.81° W) is an ice ridge between Ice Streams C and D on the Siple Coast of West Antarctica. Its location near the coast and between two ice streams makes it a favorable place for the study of paleo-climate and paleo-ice-stream activity. The analyses presented in this dissertation are based on geophysical measurements made at Siple Dome in 1994 and 1996 as part of a collaborative project among the University of Washington, St. Olaf College, and the University of Colorado. The measurements were made to characterize the the geometry of the dome, investigate its stability, infer possible changes in the ice stream configuration, and support an ice core paleo-climate project at the Siple Dome summit.

In this dissertation, geophysical measurements are used with quasi-time-dependent ice flow models and inverse methods to infer the history of ice flow at Siple Dome and

place limits on the past activity of adjacent ice streams C and D. Information about past ice flow is inferred primarily from the shapes of internal layers detected across Siple Dome from radio-echo sounding measurements. The continuity of the internal layers and the shape of a warp feature in the layer pattern at the divide suggest that Siple dome has not been over-run by ice streams over the past 10^4 years and that the divide position has been slowly migrating northward toward Ice Stream D for the past few thousand years. Gradual thinning of the boundary between Siple Dome and a relict piece of Ice Stream C prior to its stagnation may be responsible for the divide migration. The pattern of ice thickness change across the south flank of Siple Dome, calculated from measurements of ice flow and an inferred accumulation pattern, is interpreted as a response to recent (< 500 a) stagnation of a piece of Ice Stream C adjacent to Siple Dome. The topography of surface lineations on the Ice Stream D-side of Siple Dome indicates recent (< 500 a) stagnation of another relict ice stream. These recent stagnation events may represent a major reorganization of the ice stream system around Siple Dome after a relatively stable period which lasted several thousand years.

TABLE OF CONTENTS

| | |
|--|-----------|
| List of Figures | vi |
| List of Tables | xi |
| Chapter 1: Introduction | 1 |
| 1.1 Background | 1 |
| 1.2 Motivation and Goals | 3 |
| 1.3 Measurements and Analysis Methods | 4 |
| 1.4 Synopsis | 7 |
| Chapter 2: Predicted Age-Depth Scales for Siple Dome and Inland WAIS Ice Cores in West Antarctica | 9 |
| 2.1 Summary | 9 |
| 2.2 Introduction | 10 |
| 2.3 Age Field Calculation Method | 10 |
| 2.4 Ice Flow Calculation for Siple Dome | 12 |
| 2.5 Age Calculation for Siple Dome | 14 |
| 2.6 Age Calculation for Inland WAIS | 17 |
| 2.7 Conclusions | 19 |
| Chapter 3: Ice Velocity and Mass Balance of Siple Dome | 21 |
| 3.1 Summary | 21 |

| | | |
|---|--|-----------|
| 3.2 | Introduction | 22 |
| 3.3 | GPS Data Collection | 22 |
| 3.4 | GPS Data Processing | 28 |
| 3.5 | Siple Dome Velocity Patterns | 30 |
| 3.5.1 | Velocity and Mass Balance of the Summit Area | 30 |
| 3.5.2 | North Flank and Siple Ice Stream | 33 |
| 3.5.3 | South Flank and Duck's Foot | 36 |
| 3.5.4 | The Cross-Dome Velocity Profile | 39 |
| 3.6 | Mass Balance Across Siple Dome | 39 |
| 3.6.1 | Calculation of Flux Divergence | 39 |
| 3.6.2 | Spatial Pattern of Mass Balance | 47 |
| 3.7 | Conclusions | 50 |
| Chapter 4: Migration of the Siple Dome Ice Divide, West Antarctica | | 52 |
| 4.1 | Summary | 52 |
| 4.2 | Introduction | 53 |
| 4.3 | Measurements | 56 |
| 4.4 | Flow Models | 60 |
| 4.4.1 | Steady-State Reference Model | 61 |
| 4.4.2 | Kinematic Representation of Flow Field | 62 |
| 4.4.3 | Case 1: Non-Linear Divide Deformation | 66 |
| 4.4.4 | Case 2: Accumulation Minimum at Divide | 68 |
| 4.5 | Choosing the Best Model | 69 |
| 4.5.1 | The Expected Error | 71 |
| 4.5.2 | The Weighting Function | 72 |

| | | |
|---|--|------------|
| 4.6 | Results | 73 |
| 4.7 | Discussion | 78 |
| Chapter 5: Sensitivity of the Divide Position at Siple Dome, West Antarctica to Boundary Forcing | | 83 |
| 5.1 | Summary | 83 |
| 5.2 | Introduction | 85 |
| 5.3 | The Linearized Ice Sheet Equation | 87 |
| 5.4 | Calculation of Normal Modes | 89 |
| 5.5 | Estimating Divide Motion | 91 |
| 5.6 | Normal Modes of Siple Dome | 92 |
| 5.7 | Response to Boundary Elevation Perturbation | 97 |
| 5.8 | Response to Accumulation Rate Perturbation | 101 |
| 5.9 | Conclusions | 105 |
| Chapter 6: Regional-Scale Accumulation Pattern at Siple Dome | | 108 |
| 6.1 | Summary | 108 |
| 6.2 | Introduction | 109 |
| 6.3 | Measurements | 110 |
| 6.4 | Data Analysis | 112 |
| 6.5 | Ice Flow Model | 114 |
| 6.6 | Residual Calculation | 117 |
| 6.7 | Results | 120 |
| 6.7.1 | The Predicted Steady-State Accumulation Pattern | 120 |
| 6.7.2 | Comparison with other Measurements | 123 |
| 6.7.3 | Temporal Changes in the Spatial Accumulation Pattern | 125 |

| | | |
|---|--|------------|
| 6.8 | Sensitivity to Temporal Changes in Accumulation Distribution | 128 |
| 6.9 | Sensitivity to Changes in Ice Thickness | 136 |
| 6.10 | Conclusions | 139 |
| Chapter 7: The Evolution of Ice Domes and Relict Ice Streams | | 143 |
| 7.1 | Summary | 143 |
| 7.2 | Introduction | 143 |
| 7.3 | Finite Difference Continuity Model | 146 |
| 7.4 | Analytic Evolution Model | 154 |
| 7.5 | Numeric vs. Analytic Comparison | 158 |
| 7.6 | Tracking the Scar Features | 164 |
| 7.7 | Application to Siple Dome | 166 |
| 7.8 | Discussion | 169 |
| 7.9 | Conclusions | 171 |
| Chapter 8: Synthesis | | 173 |
| 8.1 | The Modern Geometry of Siple Dome | 173 |
| 8.2 | Using RES Internal Layers to Infer Ice-Flow History | 174 |
| 8.3 | The History of Siple Dome | 176 |
| 8.3.1 | The Distant Past (> 5000 a) | 176 |
| 8.3.2 | The Intermediate Past (1000–5000 a) | 177 |
| 8.3.3 | Present and Recent Past (< 1000 a) | 178 |
| 8.3.4 | Complimentary Studies | 178 |
| 8.4 | Implications for Past Activity of Ice Streams C and D | 179 |
| Bibliography | | 182 |

| | |
|---|------------|
| Appendix A: The Horizontal Strain Tensor | 193 |
| A.1 Finding Tensor Components using Least-Squares | 193 |
| A.2 Principal Values and Vectors | 195 |
| Appendix B: Vertical Motion of the Firm | 197 |

LIST OF FIGURES

| | | |
|-----|---|----|
| 1.1 | Map of WAIS showing the Siple Dome and the Siple Coast Ice Streams. | 2 |
| 1.2 | AVHRR image of Siple Dome. | 4 |
| 1.3 | Radio-echo sounding profile across the width of Siple Dome. | 5 |
| 2.1 | Map of Ross drainage showing the general location of Siple Dome and inland WAIS ice core sites. | 11 |
| 2.2 | Grid representation of the flow-line used for finite element model calculations and selected calculated ice particle paths. | 13 |
| 2.3 | Accumulation rate histories used for depth-age calculations. | 15 |
| 2.4 | Age and annual layer thickness versus depth relationships derived from FEM calculations for Siple Dome. | 16 |
| 2.5 | Age and annual layer thickness versus depth relationships for the inland WAIS site. | 19 |
| 3.1 | AVHRR image of Siple Dome and Ice Streams C and D. | 23 |
| 3.2 | Map of survey poles. | 24 |
| 3.3 | Detailed map of the summit area showing survey poles, radar profile lines, snow pit and ice core sites, and camp locations. | 25 |
| 3.4 | GPS baselines near the summit. | 27 |
| 3.5 | Velocity vectors and surface elevation contours for the summit area. | 31 |
| 3.6 | Strain ellipses and strain rate contours for the summit area. | 32 |

| | | |
|------|---|----|
| 3.7 | Velocity vectors for the northern flank of Siple Dome. | 34 |
| 3.8 | Velocity vectors and surface elevation for the northern scar area. . . . | 35 |
| 3.9 | Velocity vectors for the south flank of Siple Dome. | 37 |
| 3.10 | Velocity vectors and surface elevation for the south flank of Siple Dome in the vicinity of the topographic features known as the “Duck’s Foot”. | 38 |
| 3.11 | The component of surface velocity along the survey pole line. | 40 |
| 3.12 | Distance variation between flowlines. | 42 |
| 3.13 | Siple Dome flux divergence calculated from the pattern of horizontal velocity. | 43 |
| 3.14 | Adjusted horizontal flux divergence. | 45 |
| 3.15 | Flux divergence and inferred accumulation pattern. | 48 |
| 3.16 | Surface profiles from a finite difference model of Siple Dome. | 49 |
| 4.1 | AVHRR image of Siple Dome and Ice Streams C and D. | 55 |
| 4.2 | Radar profiles of lengths 10 km and 4 km of Siple Dome taken perpen- dicular to the divide at the summit. | 58 |
| 4.3 | 3-D representation of a $10 \times 10 \times 1$ km cube centered at the Siple Dome summit showing surface elevation contours, bed topography, and the shape of one prominent internal layer identified from RES measurements. | 59 |
| 4.4 | Comparison between isochrone shapes predicted by a steady-state ice flow model with a non-linear flow law and the shapes of internal layers observed using RES. | 63 |
| 4.5 | Horizontal velocity shape functions. | 67 |
| 4.6 | Best-fit case assuming the internal layer warping is caused primarily by non-linear ice flow. | 74 |

| | | |
|-----|---|-----|
| 4.7 | Mismatch index J as a function of each model parameter for Case 1: non-linear ice flow law. | 75 |
| 4.8 | Best-fit case assuming the internal layer warping is caused by a local low in accumulation over the divide. | 77 |
| 4.9 | Mismatch index J as a function of each model parameter for Case 2: local accumulation low. | 78 |
| 5.1 | Map of West Antarctic Siple Coast ice streams showing Siple Dome and Ice Streams C and D. | 86 |
| 5.2 | Ice sheet geometries used to calculate normal modes. | 93 |
| 5.3 | Slowest normal modes for the Siple Dome ice sheet and a Vialov-Nye ice sheet | 95 |
| 5.4 | Evolution of ice sheet thickness for an instantaneous 100-meter increase in elevation of the margin of Siple Dome near Ice Stream D. | 97 |
| 5.5 | Evolution of divide elevation and position for an instantaneous 100 m increase of the ice sheet boundary. | 99 |
| 5.6 | Steady-state divide migration rates for various rates of boundary ele- vation. | 100 |
| 5.7 | Evolution of SDM thickness for an instantaneous change in the accu- mulation pattern. | 102 |
| 5.8 | Evolution of divide position for an instantaneous accumulation pertur- bation. | 104 |
| 5.9 | Steady state divide migration rates for various rates of increase in ac- cumulation gradient. | 106 |

| | | |
|------|--|-----|
| 6.1 | AVHRR image of Siple Dome showing the summit grid and main traverses where RES and GPS measurements were made. | 111 |
| 6.2 | Radio-echo sounding profile across the width of Siple Dome. | 113 |
| 6.3 | Smoothed internal layers detected by radio-echo sounding. | 114 |
| 6.4 | Steady-state accumulation pattern which produces the best fit to the observed layer shapes. | 121 |
| 6.5 | Calculated layer shapes a spatially constant accumulation pattern and the spatially variable accumulation pattern. | 122 |
| 6.6 | Comparison between the inferred accumulation pattern and the flux divergence derived from GPS measurements. | 124 |
| 6.7 | Depth distribution of residuals for layers south and north of the divide. | 126 |
| 6.8 | Possible time-change in accumulation pattern allowed by the data. | 127 |
| 6.9 | Schematic of sensitivity test. | 130 |
| 6.10 | Hypothetical accumulation history at Site B. | 131 |
| 6.11 | Contours of maximum $\Delta z/H$ values in the ice column versus the duration w and mean age t_0 of an anomalous accumulation pattern. | 133 |
| 6.12 | The predicted depth to a given isochrone assuming various spatial accumulation histories. | 134 |
| 6.13 | The effect of symmetric ice sheet thickness change on internal layer shapes for a 500-meter thinning which begins 3000 years before present. | 139 |
| 6.14 | The effect of asymmetric ice sheet thickness change on internal layer shapes for thinning which begins 3000 years before present. | 140 |
| 7.1 | AVHRR image of Siple Dome and Ice Streams C and D. | 144 |

| | | |
|------|---|-----|
| 7.2 | Schematic of the initial and final states of simplified ice dome/relict ice stream system. | 147 |
| 7.3 | Ice surface profiles plotted every 200 years for an evolving ice dome similar in size to Siple Dome. | 150 |
| 7.4 | Ice surface profiles plotted every 200 years for a small ice dome. | 151 |
| 7.5 | Propagation and diffusion of thickening wave. | 152 |
| 7.6 | Evolution of an ice dome where the relict margin is allowed to thicken at the accumulation rate. | 153 |
| 7.7 | Contours of growth time τ_{fii}/τ_0 | 156 |
| 7.8 | A comparison between the initial and final surface profiles from an FD model calculation and from a perfectly plastic approximation. | 158 |
| 7.9 | Comparison of ice dome evolution predicted by the finite-difference model and by an analytic approximation based on a perfectly-plastic ice sheet. | 161 |
| 7.10 | Volume evolution $V_1(t)$ for 10 dome/stream evolution cases. | 162 |
| 7.11 | Surface profiles from the FD evolution model for Siple dome at 0, 200, 400, and 600 years since synchronous stagnation of the Duck's Foot and Siple Ice Stream. | 167 |
| 7.12 | Predicted and GPS-inferred thickening along the south flank. | 169 |

LIST OF TABLES

| | | |
|-----|--|-----|
| 4.1 | Notation | 54 |
| 4.2 | Summary of RES measurements. | 56 |
| 5.1 | Notation | 84 |
| 5.2 | Response time constants for slowest ice sheet modes. | 96 |
| 7.1 | Volume evolution time-scales. | 163 |

ACKNOWLEDGMENTS

This dissertation and the work represented by it would not have been possible without the help and support of several people. I would like to particularly thank my adviser, Charlie Raymond, for his support, encouragement, guidance and inspiration over the past five years. He has spent countless hours helping me to focus my research, clarify my thoughts, and better understand many aspects of glaciology. I am fortunate to have had the opportunity to work with him at the University of Washington and in the field at Siple Dome. Ed Waddington introduced me to ice flow modeling during my first year as a graduate student and continued to be a central part of my education throughout my graduate career. I am thankful for many enlightening discussions with him. In 1997, I had the fortunate opportunity to collaborate with Richard Hindmarsh at the British Antarctic Survey under an EISMINT exchange grant. I learned a tremendous amount from him during our one-month collaboration and am grateful for the many hours he devoted to my research interests. I am deeply indebted to the creators of the UW radar system (Bruce Weertman, John Chinn, Anthony Gades, David Morse), the people who made field measurements in 1994 and 1996 as part of the Siple Dome Geophysics project (Robert Jacobel, Ted Scambos, Anthony Gades and Howard Conway), and to my fellow students and colleagues who made these graduate school years particularly enjoyable.

On a personal note, I would like to thank Tony Gades who has seen me through all of my higher education since we were freshmen at St. Olaf College, and who has been an especially important part of my life for the last few years. I also cannot express enough gratitude to my parents and family for their unfailing love and support.

This work was financially supported by a National Science Foundation grant to C. F. Raymond (NSF-OPP 9316807, *Collaborative Research: Siple Dome Glaciology and Ice Stream History*). Financial support for collaboration with Richard Hindmarsh was provided by a grant from the European Science Foundation, European Ice Sheet Modeling Initiative (No. 9614). Logistical support for the field work was provided by Antarctic Support Associates under a contract from NSF.

Chapter 1

INTRODUCTION

1.1 Background

The West Antarctic Ice Sheet (WAIS) may be unstable because it is grounded below sea level. It has been hypothesized that relatively small changes in sea-level could decouple the ice from its bed, leading to rapid ice drainage and eventual disintegration of the ice sheet (*Hughes, 1973*). Collapse of WAIS would correspond to a 6-meter increase in sea-level (*Alley and Whillans, 1991*). The present flow of ice from WAIS to the ocean is dominated by several coastal “streams” of very fast ice ($10^2 - 10^3 \text{ m a}^{-1}$) flowing through slow ice ($1-10 \text{ m a}^{-1}$; Fig. 1.1; *Bentley, 1987*). Since ice streams carry about 60% of all the ice flowing from West Antarctica, the stability of WAIS may hinge on the stability of the ice stream system (*Hughes, 1977; Van der Veen, 1987*). Not much is known about the stability of WAIS ice streams, their past behavior, or the mechanisms which control their motion. Understanding the history of these ice streams would lead to better understanding of their present and future stability.

The WAIS ice stream system has experienced significant changes in recent history. Radio-echo sounding (RES) of buried crevasses has shown that the lower part of Ice Stream C essentially stopped flowing as recently as 130 years ago (*Retzlaff and Bentley, 1993*). RES has also been used to determine recent migration of the margin of Ice Stream B (*Clarke and Bentley, 1995*). Satellite images show that the lower

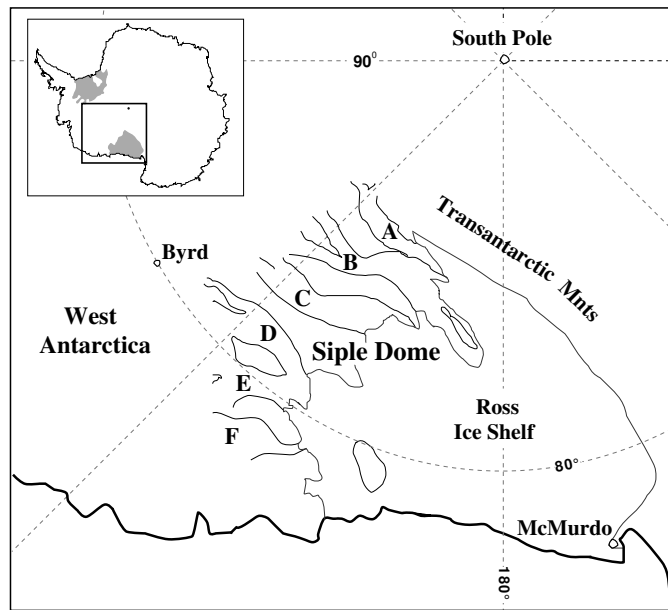


Figure 1.1: Map of WAIS showing the Siple Dome and the Siple Coast Ice Streams.

part of Ice Stream B has widened by 4 km and slowed by 50% over the past 35 years (*Bindschadler and Vornberger, 1998*), while the upper part of Ice Stream B is thinning (*Alley and Whillans, 1991*). Other satellite images of the ice stream region show linear topographic features located outside present ice streams, some of which may be flow features or former ice stream margins. This has been verified in one case by RES studies (*Jacobel et al., 1996*). These and similar studies of the near-surface give information about the recent history of specific ice streams. Evidence for older changes ($> 10^3$ a BP) must be sought in the structure of the internal stratigraphy at depth.

1.2 Motivation and Goals

Siple Dome is a ridge of ice flowing slowly ($\sim 10^{-1} - 10^1$ m a $^{-1}$) into Ice Streams C and D (Fig. 1.2). Because of its location between two ice streams, Siple Dome ice flow may have been affected in the past by changes in the activity of these ice streams. In fact, a long history of ice stream activity may be recorded in Siple Dome because the residence time of ice is long ($\sim 10^4$ a) due to slow flow. Siple Dome is therefore an appropriate place to look for evidence of past changes in the configuration and activity of these ice streams.

Siple Dome may also contain a high-resolution record of southern hemisphere climate. A deep ice core was started near the summit in 1996. Once complete, it will be examined for its climate record. Detection of past changes in the configuration and flow of Siple Dome will aid interpretation of physical and chemical stratigraphic variations in the ice core. Our field work and preliminary analysis have been used to aid in selection of the core site.

Information about the dynamic history of Siple Dome is recorded in the present geometry of both the surface and stratigraphic layers in the ice (Fig 1.3). The ice sheet surface shape responds gradually to changes in climate and to changes at its boundaries. The present surface geometry thus contains some “memory” of past events that cause the ice sheet to change shape. As this surface is buried in the ice, it becomes a marker of constant age (isochrone) that is gradually deformed by ice flow. Internal stratigraphic layers that represent isochrones therefore also contain a record of past ice flow regimes.

The goal of this dissertation is to (1) extract information of past ice flow at Siple Dome from measurements of the present flow and geometry of the ice surface and from the geometry of internal layers in the ice, and (2) to infer from this flow history information about the past activity of the bounding ice streams.

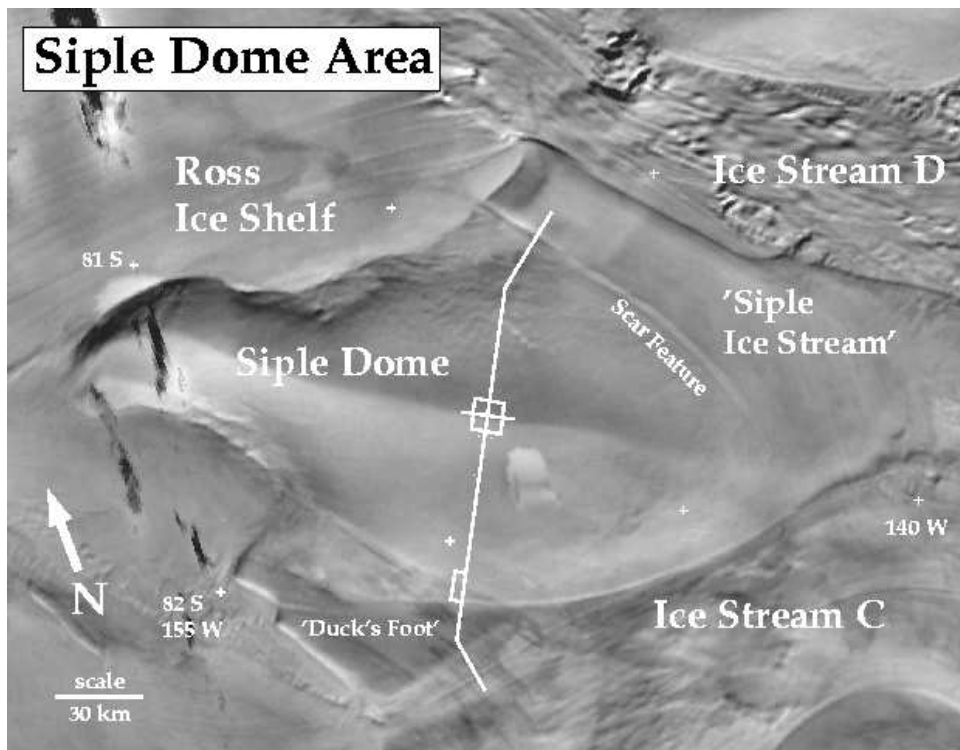


Figure 1.2: Advanced Very High Resolution Radiometer (AVHRR) image showing Siple Dome, Ice Streams C and D, and relict flow features named Siple Ice Stream and Duck's Foot on the north and south flanks of Siple Dome. Field measurements were collected in 1994 and 1996 along the white lines. Image courtesy of Ted Scambos, National Snow and Ice Data center, University of Colorado.

1.3 Measurements and Analysis Methods

Field measurements were made in 1994 and 1996 as part of a collaborative project among the University of Washington, St. Olaf College, and the University of Colorado. The internal layers were mapped using radio-echo sounding (RES) of reflecting horizons in the ice (Fig. 1.3). These reflecting horizons are assumed to represent isochrones: former ice-sheet surfaces that have been buried and deformed by ice flow (Hammer, 1980; Paren and Robin, 1975). All of the radar data presented in this dis-

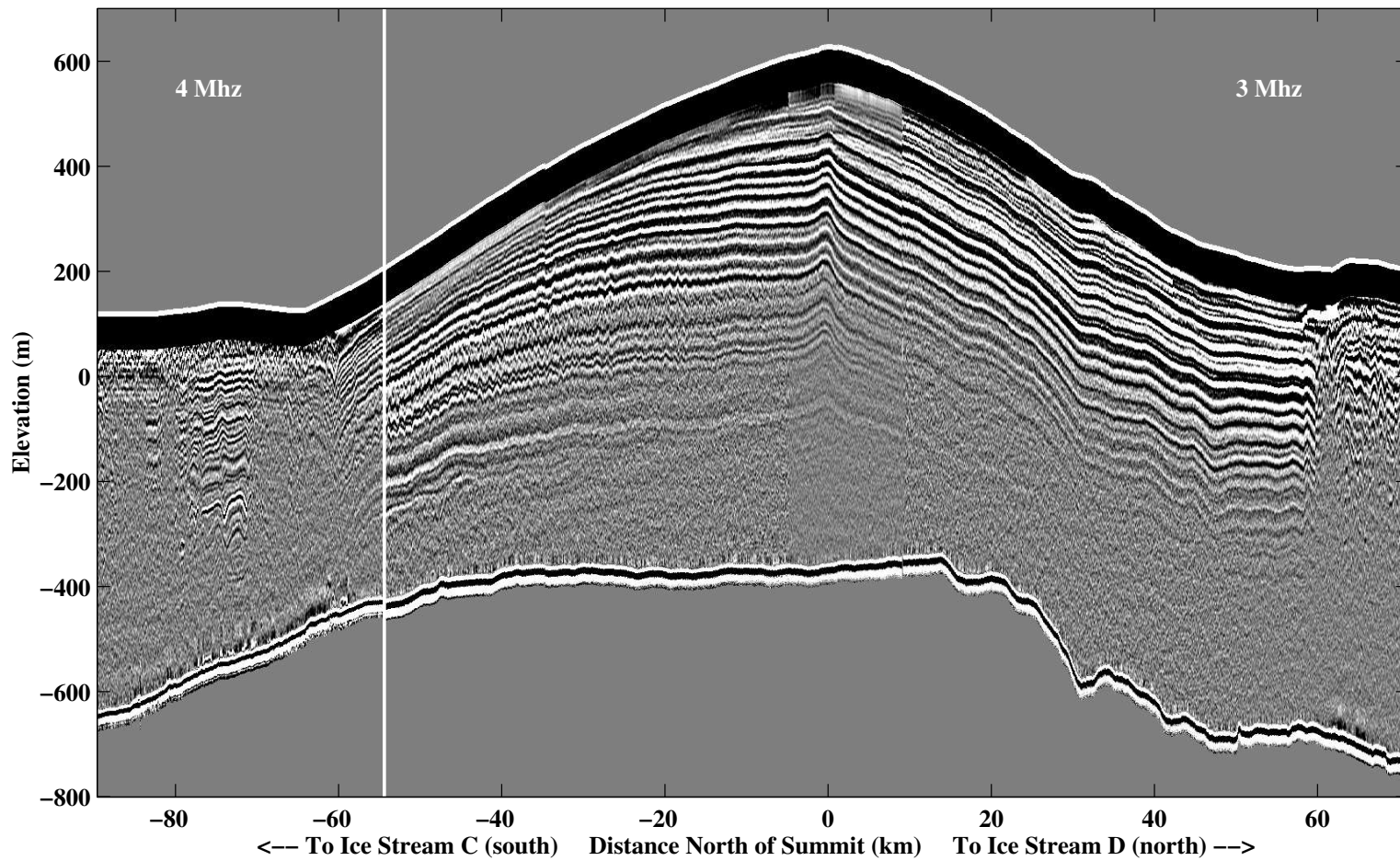


Figure 1.3: Radio-echo sounding profile across the width of Siple Dome. The profile corresponds to the long white line in figure 1.2 beginning at Ice Stream C and ending at the Siple Ice Stream.

sertation were collected by Anthony Gades (University of Washington) and Robert Jacobel (St. Olaf College). Many of the software packages I have used to analyze the radar data were written by Anthony Gades. Charlie Raymond and Howard Conway (both University of Washington) set out survey poles, made optical survey measurements, measured density profiles in snow pits, collected wind and temperature data, and helped collect radar data. Ted Scambos (University of Colorado) and I measured the position of survey poles in 1994 and 1996 with Global Positioning System (GPS) receivers. Bjorn Johns (UNAVCO) and Xin Chinn (NASA) and Chris Shuman (NASA) made GPS measurements of survey poles along the south flank of Siple Dome in 1997. All AVHRR images presented in this dissertation were compiled by Ted Scambos. Researchers at University of New Hampshire obtained a 160-meter core near the Siple Dome summit in 1994, made measurements on the core, and provided us with the data.

These measurements show that Siple Dome is a ridge about 100 km wide and 200 km long overlying a bedrock plateau. Ice thickness at the summit as determined from radar measurements is 1009 ± 7 m (*Raymond et al.*, 1995). The accumulation rate at the summit (1000-year average) is about 0.11 m a^{-1} ice equivalent (*Mayewski et al.*, 1995). Flow in the vicinity of the summit is primarily two-dimensional in a vertical plane perpendicular to the ridge. Figure 1.3 shows the pattern of internal stratigraphy. Internal layers are continuous across the full width of the dome and are detected to about 70% depth. The layers are disrupted where the profile crosses the linear topographic features apparent in the satellite image (Fig. 1.2; *Jacobel et al.*, 1996). The layers are asymmetric about the divide with layers on the Ice Stream D-side (north) of the divide appearing deeper than the same layers on the Ice Stream C-side (south). At the divide, there is a distinct convex-up warp feature in the internal layer shapes.

Inferring past ice flow from the shapes of these internal layers using ice flow models and inverse methods is a central part of my dissertation. I develop quasi-time-dependent ice flow models to simulate the deformation of isochrones in the vicinity of the Siple Dome ice divide and on the flank. The simulated isochrone shapes are compared to the measurements of internal layers to determine the history of ice flow required to explain the data. I also develop inverse methods to quantitatively distinguish among different models. I model the effects of changing conditions at the boundaries of Siple Dome with a time-dependent continuity model and perturbation methods. These continuity and perturbation models simulate the evolution of the dome surface and are used to determine the evolving boundary conditions required by the inverse analysis, the present surface geometry, and the modern flow field. Because the internal layers detected by RES are a discrete set, sampling only certain depths and certain time periods, there are inherent limitations to using RES layer shapes to determine the flow history of an ice sheet. I develop simple sensitivity tests to quantify the general limitations for using RES data to detect ice flow changes in the context of Siple Dome data.

1.4 Synopsis

Each chapter has been written as a stand-alone manuscript. Chapters 2, 4, and 5 have been published (or are in press) in their present form in various journals. Chapters 6 and 7 are manuscripts in preparation for publication. Some figures and descriptions of the measurements are therefore repeated in different chapters. Descriptions of the measurement techniques and data analysis methods are presented in each chapter as needed; there is not a separate chapter describing the measurements.

Chapter 2 (*Nereson et al.*, 1996) describes a finite-element model calculation of the age versus depth profile for Siple Dome based on 1994 field measurements. This

age-depth relationship is used in subsequent chapters to place approximate ages on internal layers. Chapter 3 describes GPS data collection and analysis and describes the present velocity field at Siple Dome. These measurements are compared to the spatial accumulation pattern inferred from RES measurements in Chapter 6 to determine the present distribution of thickening and thinning across Siple Dome. In Chapter 4 (*Nereson et al.*, 1998b), I use the shape of the internal layers near the divide to determine that the Siple Dome divide has been migrating toward Ice Stream D for the past several thousand years. Chapter 5 (*Nereson et al.*, 1998a) was developed in collaboration with Richard Hindmarsh of the British Antarctic Survey. Perturbation methods are used to determine whether changes in accumulation distribution over the dome or changes in elevation at its boundaries could cause the divide to migrate at the rate determined in Chapter 4. In Chapter 6 (*Nereson et al.*, 1997), I analyze the shapes of the internal layers across the full width of the dome to infer the long-term accumulation pattern at Siple Dome and determine whether there is evidence for past changes in the pattern, such as those required to move the ice divide. In Chapter 7, I present a model of the evolution of a dome which is flanked by stagnated ice streams. The model shows that the present elevation of the flow features marking the Siple Ice Stream and the Duck's Foot (Fig. 1.2) is consistent with a shut-down age of less than 500 years ago. This recent shut-down age eliminates the hypothesis that thickening associated with the shut down of the Siple Ice Stream is responsible for the Siple Dome divide migration. Chapter 8 ties together the conclusions presented in each previous chapter to show that Siple Dome and the configuration of its bounding ice streams have likely been stable for the 5 – 10 ka prior to recent (< 500 a BP) stagnation of both relict ice streams flanking Siple Dome.

Chapter 2

PREDICTED AGE-DEPTH SCALES FOR SIPLE DOME AND INLAND WAIS ICE CORES IN WEST ANTARCTICA

This chapter was published under the same title in *Geophysical Research Letters* 23(22): 3163–3166, 1996, with co-authors E. D. Waddington, C. F. Raymond, and H. P. Jacobson, all at Geophysics Program, University of Washington. Helpful review comments were provided by J. Bolzan and R. Hindmarsh.

2.1 Summary

Geophysical data are used with ice flow models and generalized accumulation histories to estimate age and annual layer thickness versus depth for two anticipated ice core sites in West Antarctica: Siple Dome (81.65° S, 148.81° W) and an inland site on the West Antarctic Ice Sheet (WAIS). This modeling experiment predicts that 10^4 year-old ice is at $\sim 50\%$ depth and 10^5 year-old ice is at $\sim 90\%$ depth at both sites. Both of these cores could contain climate information through the last glacial cycle with annual resolution through the Holocene. The predicted similarity in resolution and record length between the two cores suggests that they could be compared in detail to obtain both spatial and temporal information about the paleo-climate and history of the West Antarctic ice sheet.

2.2 Introduction

Ice cores located on the interior of the West Antarctic Ice Sheet (WAIS) and on the inter-ice stream ridges near its edges contain records of southern hemisphere paleoclimate and information about the past behavior and stability of the ice sheet. We estimate age and thickness of annual layers versus depth for two anticipated ice core sites that have been selected for their potential to provide such information: the summit vicinity of Siple Dome (81.65° S, 148.81° W) between Ice Streams C and D, and a site near the WAIS divide which has yet to be determined (*Bindschadler, 1995*) (Fig. 2.1). Our results show the potential extent of annual resolution of stratigraphic variations and total record length for each core site. Prior to drilling, these estimates can help determine appropriate ice-sampling strategies for physical and chemical analyses and the potential for inter-ice core comparisons. After drilling, our estimates can be used as a reference against which measurements of age and layer thicknesses can be compared to help detect past changes in ice sheet configuration and to improve paleo-accumulation rate estimates.

The calculations are based on available geophysical data, reasonable generalized accumulation histories, and ice flow models. For Siple Dome calculations, we use a 2-d finite element ice flow model because the necessary data for model input parameters are available. Since a specific core site on inland WAIS has not been determined, we use a 1-d ice flow model appropriate to general conditions in the targeted inland WAIS region.

2.3 Age Field Calculation Method

The age $A(x, z, t_0)$ of ice at a given position (x, z) at a given time t_0 is found by integrating the vertical velocity w from its origin elevation H at time $t = (t_0 - A)$ to

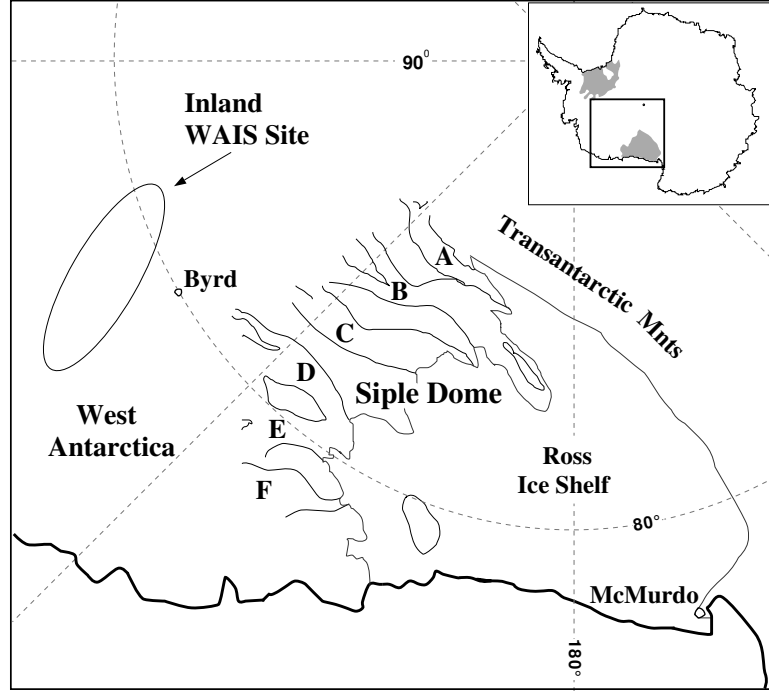


Figure 2.1: Map of Ross drainage showing the general location of Siple Dome and inland WAIS ice core sites.

its elevation z at time t_0 along its flow path $(x'(t'), z'(t'))$:

$$A(x, z, t_0) = \int_H^z \frac{1}{w(x'(t'), z'(t'), t')} dz'. \quad (2.1)$$

Vertical velocity w is a function of position and time. Following *Schøtt et al.* (1992), we assume that the ice sheet and flow geometry are time-independent, and temporal changes in accumulation rate $\dot{b}(t)$ scale the flow rates instantaneously, so that

$$w(x, z, t) = \tilde{w}(x, z) \frac{\dot{b}(t)}{\dot{b}_0} \quad (2.2)$$

where \dot{b}_0 is a reference value taken to be $\dot{b}(t_0)$.

2.4 Ice Flow Calculation for Siple Dome

To calculate $\tilde{w}(x, z)$, we use a two-dimensional, time-independent, finite element model (FEM) of ice flow developed by *Raymond* (1983). The FEM calculations are based on the following assumptions:

1. The ice sheet geometry is steady-state.
2. The ice deforms in plane strain, consistent with the present approximate 2-dimensional ridge geometry of both the surface and bed of Siple Dome (*Chapter. 3; Scambos and Nereson, 1995; Fisher et al., 1995*)).
3. The bottom of the ice sheet is frozen to its bed.
4. The ice surface is stress-free.
5. Velocities corresponding to laminar flow are prescribed at the edges of the flow domain such that the total ice volume in the domain is constant.
6. Ice deforms according to Glen's flow law, $\dot{\epsilon} = \left(\frac{\tau}{2B}\right)^3$, which relates the effective shear strain rate, $\dot{\epsilon}$, to the effective shear stress, τ .
7. The parameter B in the flow law is a function of temperature T :

$$B(T) = B_0 \exp\left(\frac{T^*}{T} - \frac{C}{(T_r - T)^k}\right) \quad (2.3)$$

where $T^* = 3155$ K, $T_r = 273.39$ K, $C = 0.16612$ K^k, $k = 1.17$ (*Hooke, 1981*). B_0 is an adjustable reference value. We do not account for the effects of ice fabric, impurities, or other factors on the flow law.

8. The accumulation rate is 10 cm a⁻¹ ice-equivalent (*Mayewski et al., 1995*). A possible small spatial variation (*I. Whillans, pers. comm.*) is ignored.
9. The temperature profile is steady state as determined from the current measured surface temperature (-26^0 C), accumulation rate, an assumed geothermal heat flux of 65.5 mW m⁻² (*Alley and Bentley, 1988*), and a simple, 1-dimensional heat

flow model.

10. Ice sheet thickness (1009 ± 7 m at the summit (*Raymond et al.*, 1995), is reduced by 17.3 m to ice-equivalent thickness based on snow and firn density measurements (*M. Twickler, pers. comm.*).

The 2-d (66×20) finite element grid, extends 80 km along a line perpendicular to the ridge and centered at the summit. The bedrock topography is determined from surface-based radio-echo sounding (RES) and GPS measurements for the northern 55 km of this line (*Raymond et al.*, 1995; *Scambos and Nereson*, 1995) and extended to the south using one measurement of ice thickness from airborne RES near the margin of Ice Stream C (*D. Blankenship, pers. comm.*). With this grid geometry, errors from the side boundary conditions will not be significant within 20 km of the summit (*Raymond*, 1983; *Waddington et al.*, 1986).

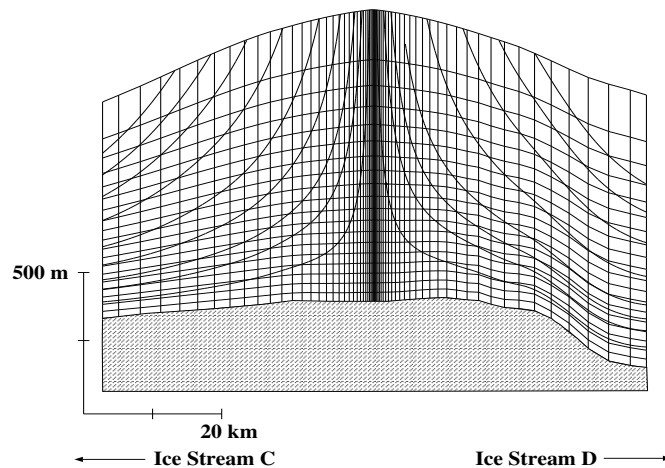


Figure 2.2: Grid representation of the flow-line used for finite element model calculations and selected calculated ice particle paths. Bed topography is derived from RES measurements.

The initial FEM calculation shows that the measured surface geometry is not consistent with the prescribed accumulation rate, which contradicts assumption (1). Therefore, the ice sheet surface and corresponding velocity field are allowed to evolve until they reach a steady-state configuration. We “tune” the model so that the calculated steady-state geometry best matches the measured geometry by adjusting the viscosity parameter B_0 (Eq. 2.3). We then put a vertical velocity profile from 3 km away from the divide into a simple 1-dimensional heat flow model following *Firestone et al.* (1990) to determine a new temperature profile. This new temperature profile is scaled to the ice thickness at each position x , and a new velocity field is predicted using the FEM. This iterative process is repeated until these velocity and temperature profiles are self-consistent.

The resulting value for B_0 (1.35×10^{-5} bar $\text{a}^{1/3}$) is largely consistent with experimental results, since it is about 40% larger (stiffer) than Hooke’s recommended value (*Hooke*, 1981), and only about 5% stiffer than Paterson’s recommended value (*Paterson*, 1994, page 97). The modeled surface differs from the measured surface by a maximum of 8 m ($< 1\%$ of ice thickness) within 20 km of the divide, and by less than 4 m within 10 km of the divide. The final basal temperatures range from -8° to -2° C.

2.5 Age Calculation for Siple Dome

To calculate the age field $A(x, z, t_0)$ from Equation 2.1, we construct $w(x, z, t)$ from Equation 2.2 using two alternative accumulation rate scenarios (Fig. 2.3) which assume $\dot{b}(t)$ was substantially lower during glacial times than interglacial times (*Robin*, 1977; *Lorius et al.*, 1984). Vertical velocity $w(x, z, t)$ is dependent on position x because of special flow conditions spanning a few ice thicknesses near a flow divide (*Raymond*, 1983; *Hvidberg*, 1996). To avoid this complication in the integration of

Equation 2.1, we limit calculations to positions at the divide ($x = 0$) where the ice trajectory is vertical, and to positions greater than 3 ice thicknesses from the divide ($|x| > 3H$).

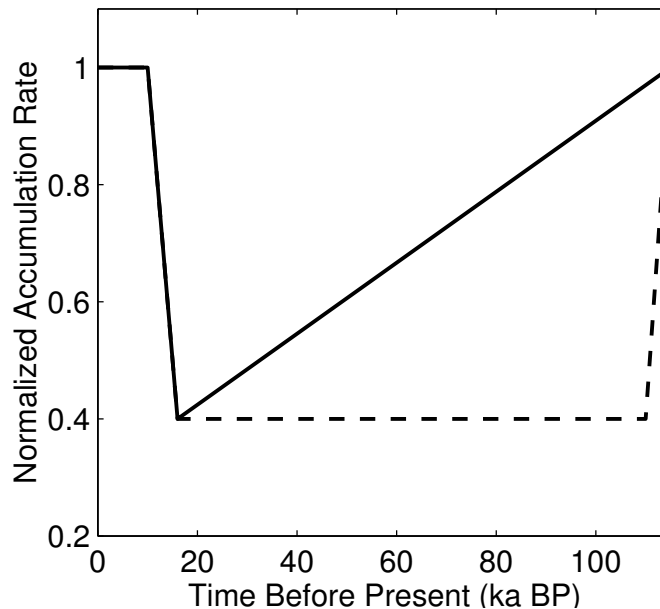


Figure 2.3: Accumulation rate histories used for depth-age calculations in Figures 2.4 and 2.5. The vertical axis is presented in units of $\dot{b}(t)/\dot{b}_0$ where \dot{b}_0 is the present accumulation rate.

Figure 2.4a shows the predicted depth-age relationship assuming accumulation rate histories shown in Figure 2.3 for both flank and divide positions. Our calculations predict ice from 10^4 a BP is located at about 550-650 m (55-65%) depth, and ice from 10^5 a BP is located at about 850-950 m (85-95%) depth. Figure 2.4b shows the annual layer thicknesses predicted for each case. Annual layers reach sub-centimeter thicknesses at about 60-70% depth. If annual stratigraphic or chemical signals exist and have been preserved in the ice, they may be resolved throughout the Holocene (*Alley et al.*, 1997).

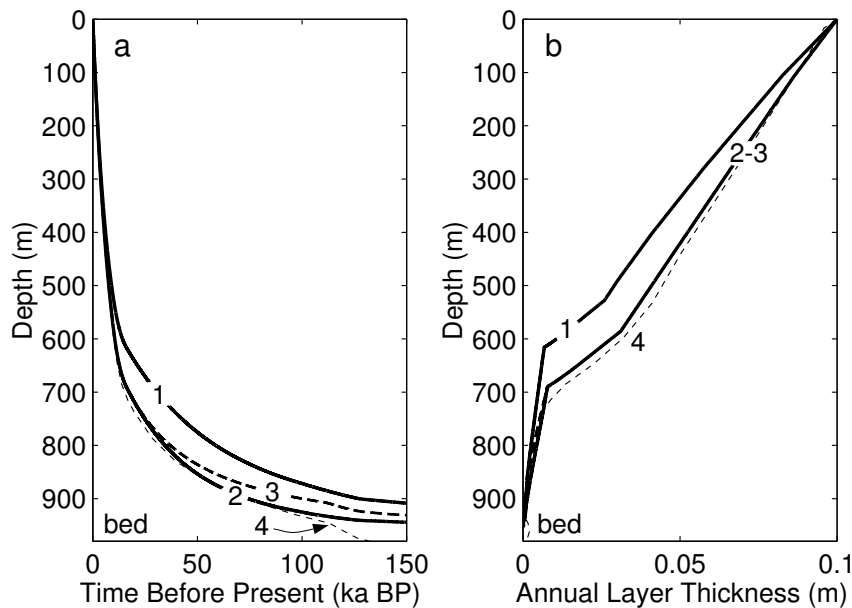


Figure 2.4: (a) Age-depth relationships derived from FEM calculations for Siple Dome. (1) Divide, $\dot{b}(t)$ given by solid line in Figure 2.3. (2) Flank, $\dot{b}(t)$ same as (1). (3) Flank, $\dot{b}(t)$ given by dashed line in Figure 2.3. (4) Flank, $\dot{b}(t)$ same as (1) with basal melt rate of 2 mm a^{-1} . (b) Annual layer thicknesses for cases shown in (a). Cases 2 and 3 are indistinguishable at the plotting scale.

We must consider the effects of our assumptions on our results. We do not expect that Siple Dome is in steady-state given the dynamic nature of WAIS ice streams (assumption 1). A comparison between our estimates and ice core measurements could be used to test this assumption and detect evidence for past changes in the configuration of Siple Dome.

Analysis of the internal layer pattern from RES measurements suggests that the flow divide has moved a few kilometers in the last 10^4 years (*Chapter 4*; *Nereson et al.*, 1998b). Therefore, ice within a few ice thicknesses of the summit may have experienced flow regimes associated with both flank and divide positions. In that

case, the predicted depth-age scale would lie between the curves for flank and divide locations shown in Figure 2.4a.

It is possible that the bed of Siple Dome is currently near melting and/or has experienced melting conditions in the past, since the bed of nearby Ice Stream B is not frozen (*Engelhardt et al.*, 1990).¹ A simple model developed by *Firestone et al.* (1990) was used to test the sensitivity of the depth-age scale to basal melting. Melting removes the oldest ice and shortens the age record. However, the predicted age-depth relationship through most of the last glacial cycle is virtually unchanged with a basal melt rate of 2 mm a^{-1} (Fig. 2.4a).

Surface temperature variations over time (e.g., from glacial-interglacial transitions) change the internal ice temperature and thereby affect the ice viscosity and the corresponding predicted flow field. To test the sensitivity of our results to temperature, we ran the FEM with a different steady-state temperature profile having temperatures about 5° C colder at the bed. The predicted ages for a given depth differ from those shown in Figure 2.4a by less than 10% for the deepest ice and less than 5% for the upper half of the ice sheet.

2.6 Age Calculation for Inland WAIS

To estimate an age-depth scale for a generic site in the targeted WAIS ice core region (Fig. 2.1), we use a 1-d flow model developed by *Dansgaard and Johnsen* (1969). The model assumes that vertical velocity \tilde{w} is independent of x and is determined from a vertical strain rate which is constant above some depth ($H - h$) then decreases linearly to zero at the bed, so that

¹A frozen bed beneath Siple Dome has been independently inferred from RES reflectivity analysis of the bed (*Gades*, 1998) and from borehole temperature measurements (*H. Engelhardt, pers. comm.*).

$$\begin{aligned}\tilde{w}(x, z) &= \frac{\dot{b}_0(z - h/2)}{(H - h/2)} \quad , \quad H \geq z \geq h, \\ \tilde{w}(x, z) &= \frac{\dot{b}_0 z^2}{2h(H - h/2)} \quad , \quad h \geq z \geq 0.\end{aligned}\tag{2.4}$$

We use the 2-D FEM calculation for Siple Dome to help determine the parameter h appropriate for a WAIS site. The 1-d model matches the age vs. depth prediction given by the 2-d FEM model for a Siple Dome flank site to within 10^3 years at 90% depth when $h = 21.7\%$ of the total thickness. A comparison between this value for h for a Siple Dome flank site and the values for h used to date two Greenland ice cores, Camp Century (*Dansgaard and Johnsen, 1969*) and Summit (GISP2/GRIP) (*Dahl-Jensen et al., 1993; Dahl-Jensen, pers. com. to EDW*), shows a linear relationship between h and ice thickness H such that

$$h = 0.49H - 268 \text{ m}.\tag{2.5}$$

We assume Equation 2.5 is valid for H much greater than 268 m.

Equations 2.1, 2.4, and 2.5 provide an estimate of a flank depth-age scale for a steady-state ice sheet of a given thickness and accumulation rate. WAIS ice thickness is about 2500 m (*Drewery, 1983*) and the present accumulation rate is $\dot{b}_0 \approx 20 \text{ cm a}^{-1}$ ice-equivalent (*Giovinetto and Bull, 1987*). With the accumulation history shown by the solid line in Figure 2.3, Equation 2.4 predicts that ice from 10^4 a BP is at about 1300 meters ($\sim 50\%$) depth and ice from 10^5 a BP is at about 2250 meters ($\sim 90\%$) depth (Fig. 2.5a). The corresponding layer thickness profile predicts annual layers greater than 2 cm thick to 1800 meters depth, or through the Holocene and part of the last glacial period (Fig. 2.5b). Figure 2.5 also shows the depth-age and layer thickness predictions for a plausible range of values for h .

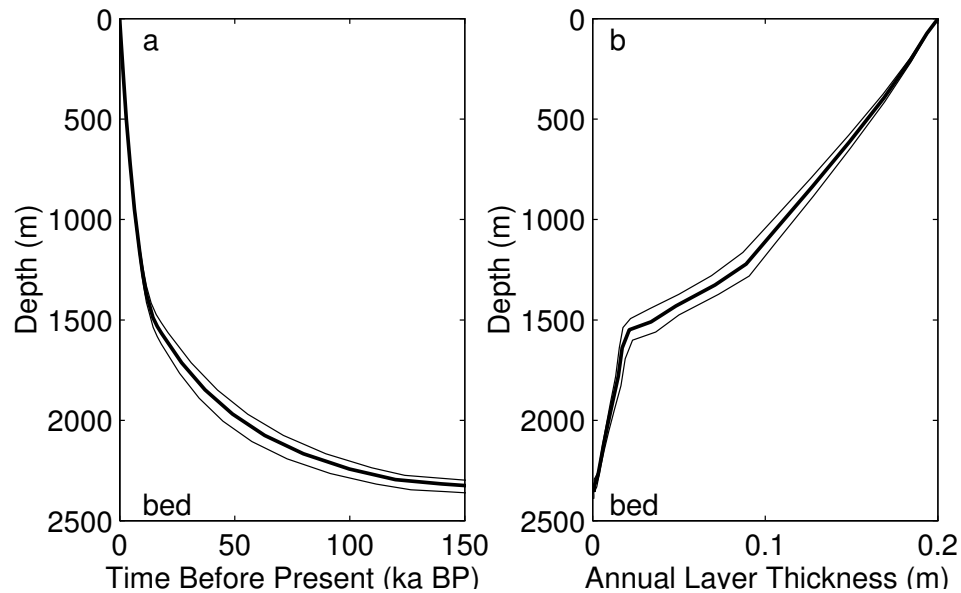


Figure 2.5: (a) Age-Depth relationships calculated from the Dansgaard-Johnsen model for a flank WAIS site. For all cases, $\dot{b}(t)$ is given by the solid line in Figure 2.3. The middle curve corresponds to $h/H = 0.38$ (Eq. 2.5). The upper and lower curves correspond to $h/H = 0.48$ and $h/H = 0.28$, respectively. (b) Annual layer thicknesses for cases shown in (a).

2.7 Conclusions

Figures 2.4 and 2.5 show that both Siple Dome and WAIS cores may give climate records of similar total duration. This result is not surprising since the characteristic timescales for these ice sheets are comparable ($\propto H/\dot{b} \approx 10^4 \text{a}$). The predicted depth-age scales for both ice core sites place the transition to the Holocene ($\sim 10^4$ years BP) at about 50% depth and the previous interglacial period ($\sim 10^5$ years BP) at about 90% depth given a reasonable assumption about the accumulation rate history. Modest basal melting leads to a shorter geochemical record, but the depth-age scale through most of the last glacial period is similar to predictions with no basal melting.

In addition, the layer thickness predictions show that both cores could provide annual resolution of detectable stratigraphic variations at least through the Holocene. These similarities suggest that detailed comparisons between ice core records from these sites could be valuable in determining spatial and temporal relationships between past coastal and inland climate changes.

Chapter 3

ICE VELOCITY AND MASS BALANCE OF SIPLE DOME

3.1 Summary

Global Positioning System (GPS) measurements of survey poles at Siple Dome in 1994, 1996, and 1997 are used to determine the present ice flow near the summit and along the flanks perpendicular to the ridge. The measurements show that ice flow is mostly parallel to a line of survey poles crossing Siple Dome perpendicular to the ridge and is 2-dimensional in the vicinity of the summit. The measured strain rate and corresponding horizontal flux divergence near the summit are slightly larger than the accumulation rate, possibly indicating thinning of 0.02 m a^{-1} . However, the uncertainty in the measurements also allows the possibility that the summit region of Siple Dome is in steady state. The relict ice streams at either margin of Siple Dome are moving less than 0.30 m a^{-1} . Flow from the north flank of Siple Dome is channeled along a trough which defines the Siple Ice Stream margin. The velocity gradient across the margin yields a shear rate of 0.002 a^{-1} . The velocity pattern north of the summit is generally consistent with the long-term accumulation pattern inferred from the shape of internal layers, suggesting that the north flank is in a steady configuration. However, there is evidence for significant thickening of the south flank. The predicted thickening is especially pronounced in a zone 40 to 70 km south of the divide near the Duck's Foot where the calculated horizontal flux divergence is negative.

3.2 Introduction

The magnitude and spatial pattern of modern thickening and thinning across Siple Dome can be determined from measurements of the present flow field and an inferred accumulation pattern (*Chapter 6*). The flow field is determined from the displacement of survey poles over a 1- or 2-year period as measured by Global Positioning System (GPS) survey techniques. The goals of this chapter are three-fold: (1) to outline the GPS data collection and data analysis techniques used for this study, (2) to use these measurements to describe the modern flow field across Siple Dome and over the relict flow features on its flanks, and (3) to infer from this flow field (with measurements of dome geometry and an inferred accumulation pattern) the spatial pattern of mass balance across Siple Dome.

3.3 GPS Data Collection

Ninety steel survey poles were placed in the firn at Siple Dome in 1994 to a depth of about 1.5 meters in a 10 km square grid surrounding the summit, along a line traversing the north flank of the summit, and in a smaller grid configuration over the relict flow feature. The position of each pole was measured using Global Positioning System (GPS) and optical survey techniques. In November and December 1996, their positions were re-measured and 35 additional poles were placed in the firn along the south flank of Siple Dome, across several scar features near Ice Stream C, and near the original summit grid. The line of poles extending along the south flank of Siple Dome were re-surveyed in December 1997 by Bjorn Johns (UNAVCO) and Xin Chen (NASA).

Figure 3.1 shows the GPS pole lines relative to the Siple Dome ridge and topographic “scar” features at the boundaries of Siple Dome. Figures 3.2 and 3.3 show

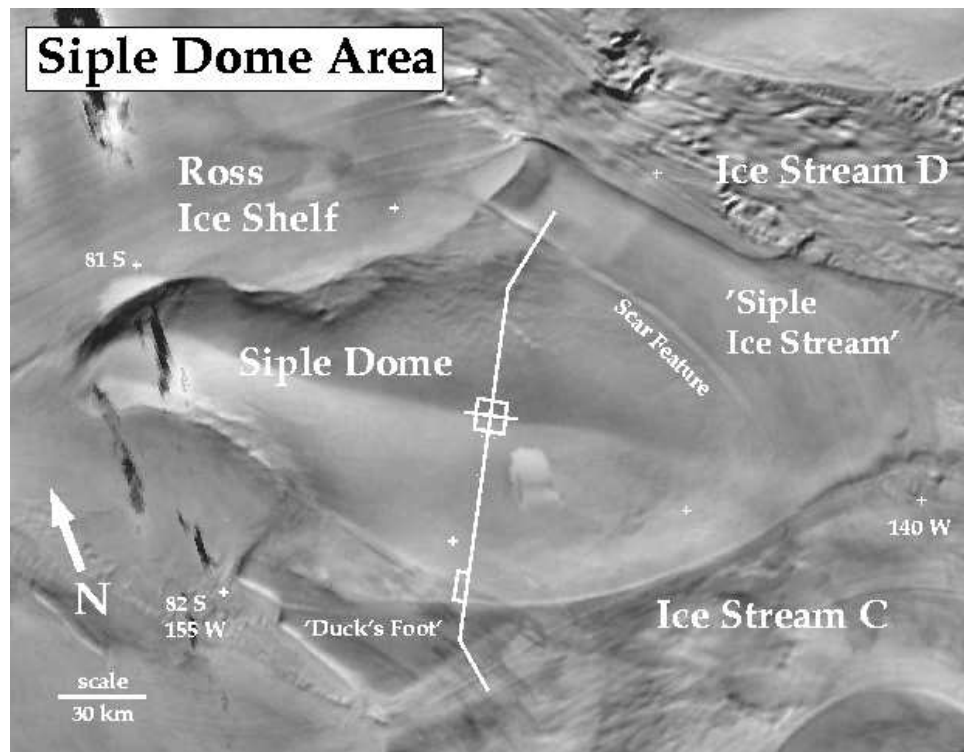


Figure 3.1: AVHRR image of Siple Dome and Ice Streams C and D. The relict Siple Ice Stream and Duck's Foot are evident as linear topographic features on the north and south flank of Siple Dome.

the configuration of the survey poles, the pole labeling convention, and the local coordinate system adopted for this study. We choose the local x coordinate to run approximately west-east along the divide ridge with the origin at the summit. The local y coordinate is perpendicular to the ridge, originating at the summit, and bearing 16.4 degrees east from true geographic north. We refer to the “north” flank of Siple Dome as the side of the ridge with positive y values and closest to Ice Stream D. Similarly, the “south” flank is the side of the ridge with negative y values and closest to Ice Stream C.

GPS data were collected with TRIMBLE 4000 SSE dual frequency receivers and

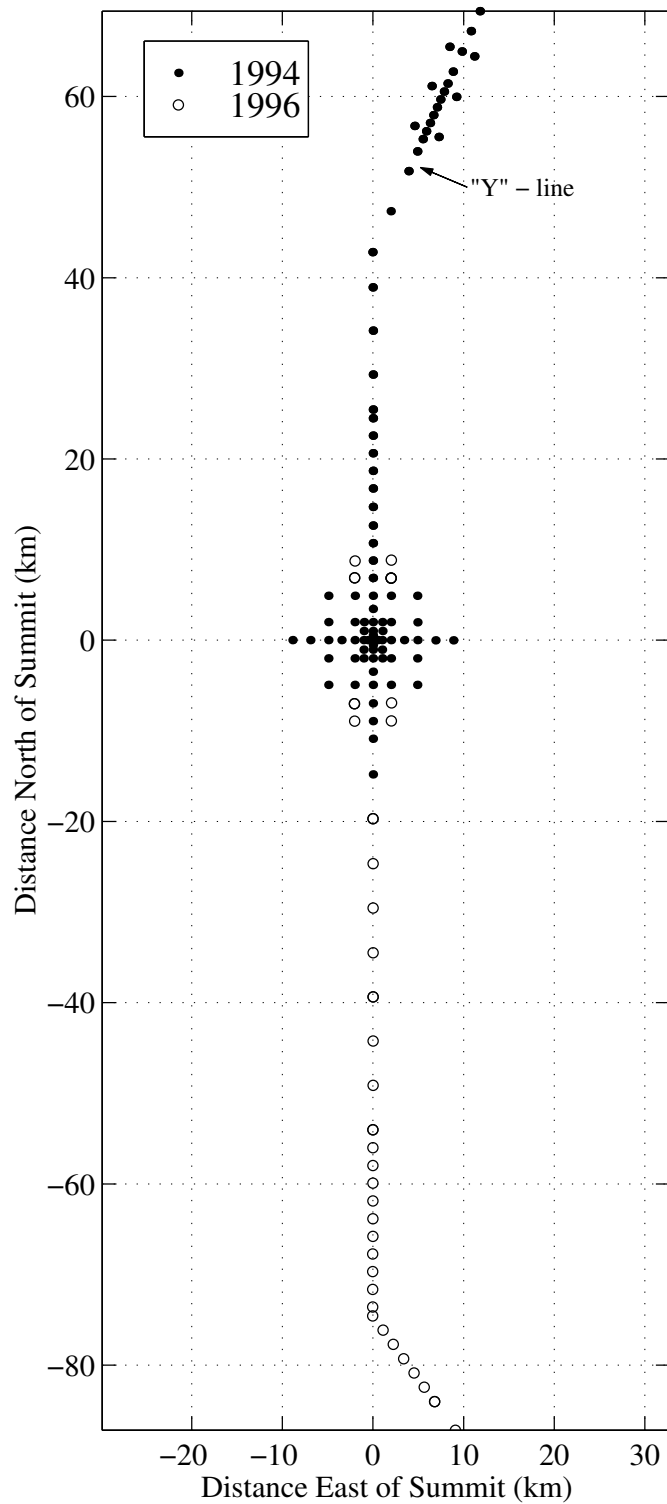


Figure 3.2: Map of survey poles planted in 1994 (solid circles) and 1996 (open circles). Poles established in 1994 were re-surveyed in 1996. Poles south of -15 km were re-surveyed in 1997. The “Y” line over the northern scar begins at 44 km north of the summit and continues 30 km across the Siple Ice Stream margin.

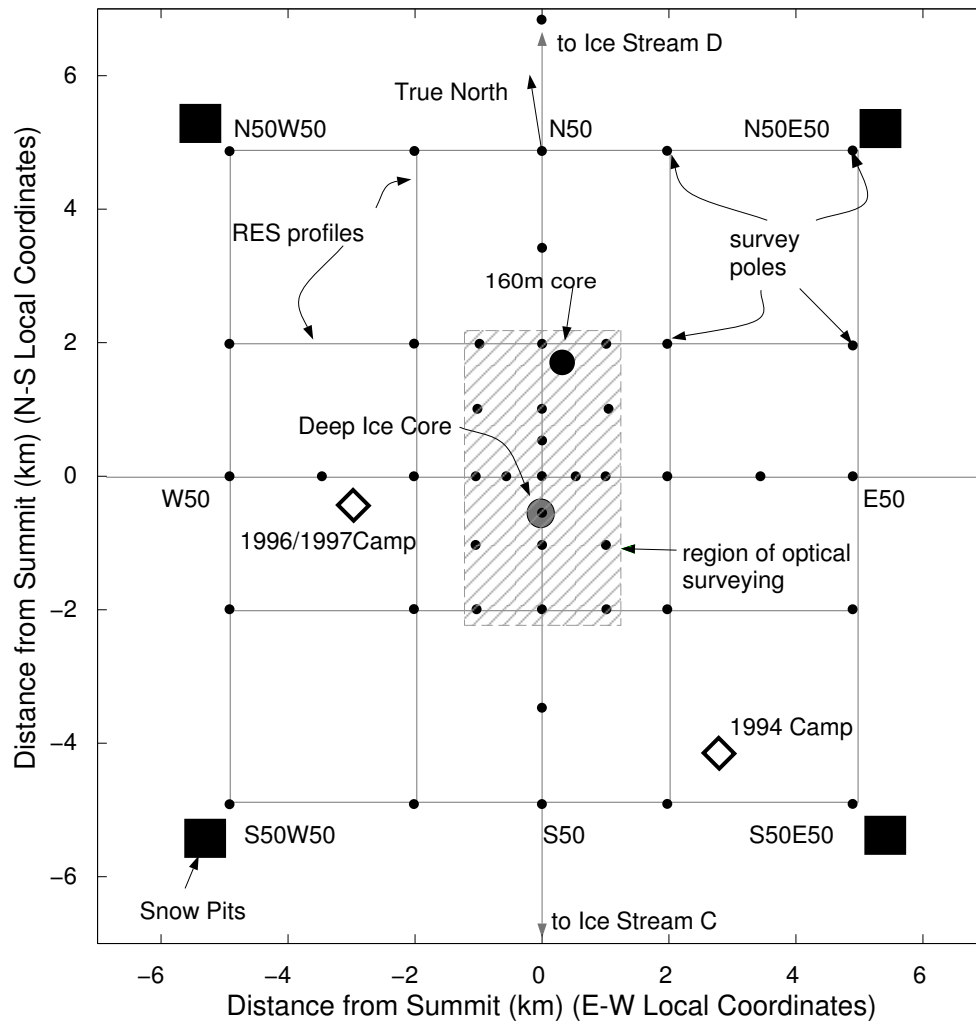


Figure 3.3: Detailed map of the summit area showing survey poles, radar profile lines, snow pit and ice core sites, and camp locations.

L1/L2 Geodetic Antennas using a combination of kinematic and fast static techniques (e.g., *Dixon*, 1991; *Hulbe and Whillans*, 1993, 1994). Kinematic techniques were used where the pole spacing was small, or in places where detailed topography was desired. Fast static techniques were used in sparse sections of the grid where survey time was limited by pole-to-pole transit time and where correcting for possible "loss of lock" to the satellites would have been excessively time consuming.

The kinematic technique was used to survey the grid within 2 km of the summit. Two base station receivers were positioned at poles S35 and E35. Two roving receivers mounted on snow machines were used to occupy all points in the 2 km grid. This process was repeated for base stations at W20 and N20. Each point in the 2 km grid was measured at least once from each of the 4 base station locations. All poles within 2 km of the summit were measured relative to 4 different base stations at least once.

Fast static techniques were used to survey the outer part of the summit grid. Each quadrant (a 5 km square area with a corner at the summit) was surveyed separately with base stations at 2 of the base points (e.g., N20 and E20 for the NE quadrant). The two roving receivers were used to survey the perimeter of the quadrant in a leap-frog fashion. We timed our roving sessions to overlap over certain segments so that we could obtain the rover-rover measurement as well as the two rover-base station measurements. With this technique, each pole on the outer grid is associated with three or four independent measurements. A similar technique was used to survey the poles positioned at 7 and 9 km east and west of the divide along the ridge. Figure 3.4 shows the configuration of baselines obtained in the vicinity of the summit.

The lines of survey poles extending south and north from the summit were surveyed using a combination of continuous (15 second) kinematic and fast static techniques. Two roving receivers were operated in a leap-frog fashion along the line and each pole was occupied long enough to be processed as fast-static occupation relative

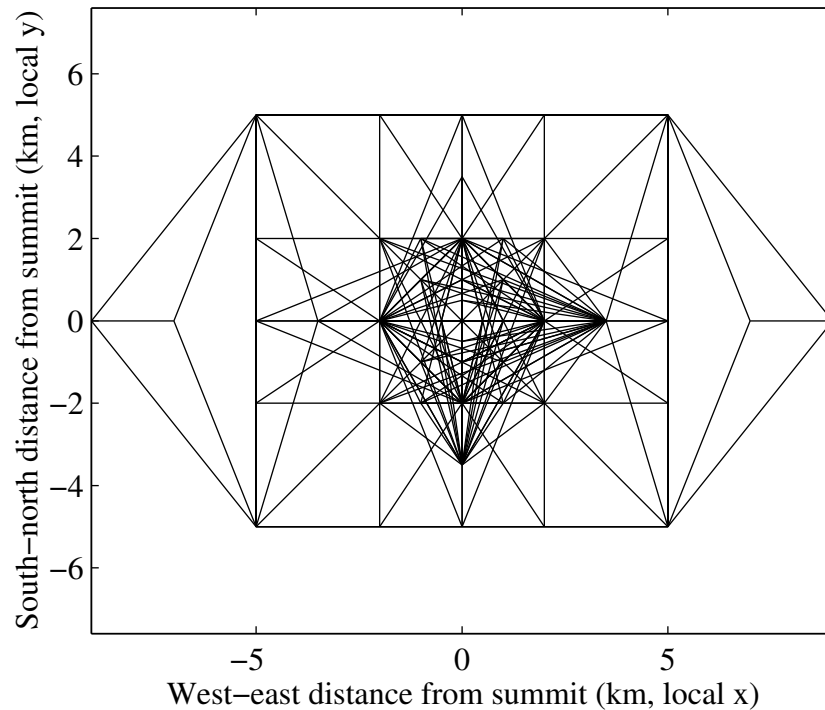


Figure 3.4: Configuration of GPS baselines collected near the Siple Dome summit in 1994 and 1996.

to the other roving receiver. These measurements were used to initialize the continuous kinematic segments. This technique enabled the continuous kinematic profile to consist of short base-lines between the survey poles. This technique was continued over the scar features about 50–70 km from the summit.

The grid on the margin of the Siple Ice Stream was also surveyed using a combination of kinematic and fast static techniques. Two base stations were located 1.5 km off the main “Y” line. One roving receiver occupied each pole along the main line for about 10 minutes in continuous kinematic mode. After half of the grid was complete, base stations were moved to two other locations and the remaining line was measured with the roving receiver. During these measurements, a fourth receiver was collecting

data at the summit. This enabled the Siple Ice Stream grid to be linked to the main survey grid at the summit.

In 1996, two additional sub-grids were established near the summit in anticipation of a vertical strain experiment. These sub-grids are 4 km square grids centered at N70 and S70. These grids were surveyed using the kinematic technique with base stations at N70W20 and N70E20 and with overlapping roving occupations. The line extending along the south flank of Siple Dome was measured in the same fast static/continuous kinematic fashion as described for the north flank. In 1996 and 1997, only the fast static technique was used along the long northern and southern lines.

3.4 GPS Data Processing

GPS data were processed using the TRIMBLE GPSurvey 2.20 software package. Satellite position information was obtained from the broadcast ephemeris data file. All baselines were processed with an elevation mask of 10 degrees, and an ionosphere correction was applied to all baselines longer than 5 km. The software allows a wide range of solution types depending on the quality and type of data collected. The optimum solution type (iono-free-fixed) was obtained for all Siple Dome baselines. This means that all baseline solutions contain no ionospheric biases, with a calculated error typically less than 1 mm. The actual measurement uncertainty is greater (5-10 mm) because the error reported by GPSurvey is a measure of the scatter of the calculated solution, and does not reflect systematic errors arising from imprecise ephemeris data or imprecise coordinates of the reference station. Two baselines were measured with both GPS and optical survey techniques. Over a 1.5 km distance, the unadjusted baseline GPS and EDM distances agree to within 0.02 m. After separate adjustment of GPS and optical data, the agreement improves to within 0.01 cm.

The network of over 300 baselines is used to calculate the optimal position of

each survey pole relative to other poles in the survey. Closure discrepancies are calculated for sets of geometric figures in the grid. The positions of the poles in the network are then adjusted to minimize the closure discrepancies. This process is called “network adjustment.” The GPSurvey Network Adjustment Module was used to adjust the Siple Dome network. All Siple Dome survey grids were adjusted according to a “minimally constrained adjustment” where one fixed point is specified, and the network is adjusted around this fixed point using inner constraints. An 8-hour occupation of the summit in 1994 established a baseline between Siple Dome Summit and McMurdo Station, giving a summit position (to the top of the survey pole) of 81.65434° S, 148.8081° W and an elevation of 622.114 m relative to the WGS84 ellipsoid, with horizontal and vertical errors of 0.05 m and 0.1 m respectively. The summit is held fixed at these coordinates for the network adjustment of 1994 data.

For 1996 data, we assume Siple Dome is in steady state and use the same horizontal coordinates and fix the summit pole height at 623.23 meters to account for the addition of a 1.53-meter pole extender and estimated vertical motion of the pole over the 2-year period. The vertical motion was estimated assuming firn density at the base of the pole of 400 kg m^{-3} and an accumulation rate of 0.10 m a^{-1} (*Appendix B*). However, the actual firn density at the base of the pole is closer to 340 kg m^{-3} and the modern accumulation rate is 0.13 m a^{-1} (*Mayewski et al., 1995*). This difference means that the fixed pole height is probably an over estimate by 0.10 meters. The effect of this possible error on the network adjustment results is negligible. For 1997 data, the same horizontal coordinates for the summit were used and the summit pole height was fixed at 622.45 m. Because of the steady-state assumption and forced match at the summit from year-to-year, information about the absolute vertical motions cannot be obtained from the GPS data. Only measurements of vertical motion relative to the divide are possible.

The adjustment results give relative pole positions within the summit grid with residuals less than 0.01 m. Residuals for poles along the north flank and in the Siple Ice Stream grid were larger (0.1 to 0.2 m) since this grid did not have "strength of figure" and did not contain redundant measurements. Residuals along the south flank of Siple Dome were about 0.02 m in 1996 and 0.03 m in 1997. Vertical positions are generally less well-determined where few baselines were measured. Vertical residuals are about 0.01 m for the summit grid (1994 and 1996); 0.05 m for the north flank and Siple Ice Stream grid (1994 and 1996); and 0.02 m (1996) and 0.10 m (1997) for the south flank and Duck's Foot.

For display purposes, the adjusted WGS84 coordinates are projected to a Lambert Conformal map with the intersecting lines of latitude at 81 and 82 degrees south. The projected coordinates are then rotated so that the 1994 position of pole N20 is locally "north" of the summit pole.

3.5 Siple Dome Velocity Patterns

3.5.1 Velocity and Mass Balance of the Summit Area

Figure 3.5 shows the calculated annual velocity of each pole in the summit region. The velocity pattern is generally 2-dimensional and perpendicular to the surface contour lines. The horizontal strain rate and divergence of horizontal surface velocity is shown in figure 3.6. The values were calculated from a least-squares strain-rate fit to polygons in the grid (*Appendix A*).

These measurements can be used to determine whether the summit is thinning or thickening. Let (u, v, w) denote the (x, y, z) components of surface velocity. Continuity of ice mass requires

$$\partial_t h = -(\partial_x q_x + \partial_y q_y) + b \quad (3.1)$$

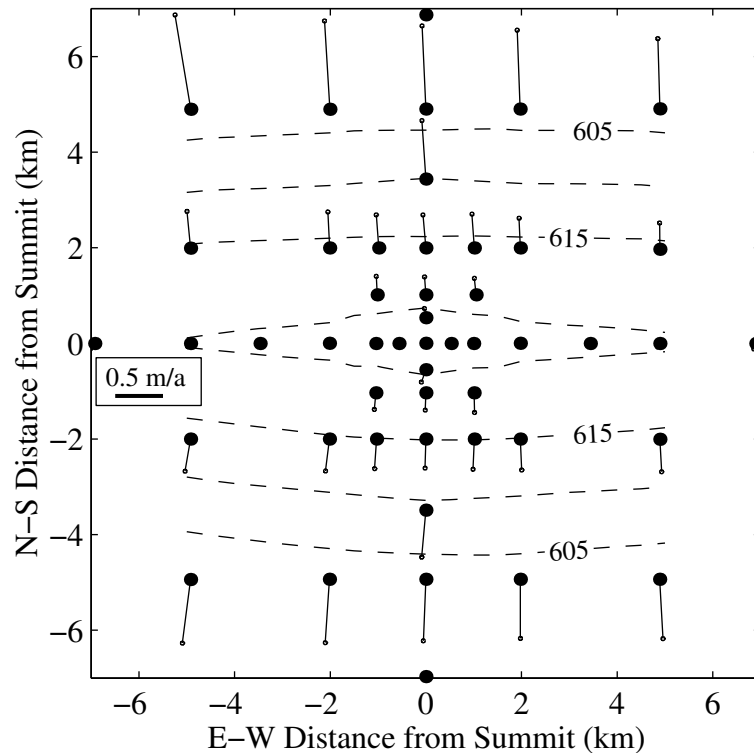


Figure 3.5: Velocity vectors and surface elevation contours for the summit area.

where h is the ice thickness, b is the accumulation rate, and (q_x, q_y) are components of horizontal ice flux. Assuming ice thickness h does not vary significantly within 2 km of the summit, the horizontal flux divergence can be expressed in terms of the horizontal velocity divergence:

$$\partial_x q_x + \partial_y q_y = \gamma h (\partial_x u_s + \partial_y v_s) \quad (3.2)$$

where $\gamma = \bar{\mathbf{u}}/\mathbf{u}_s$ is the ratio of the average horizontal velocity of the ice column $\bar{\mathbf{u}}$ to the surface velocity \mathbf{u}_s .

Based on chemical analysis of snow pits and shallow cores by colleagues at the

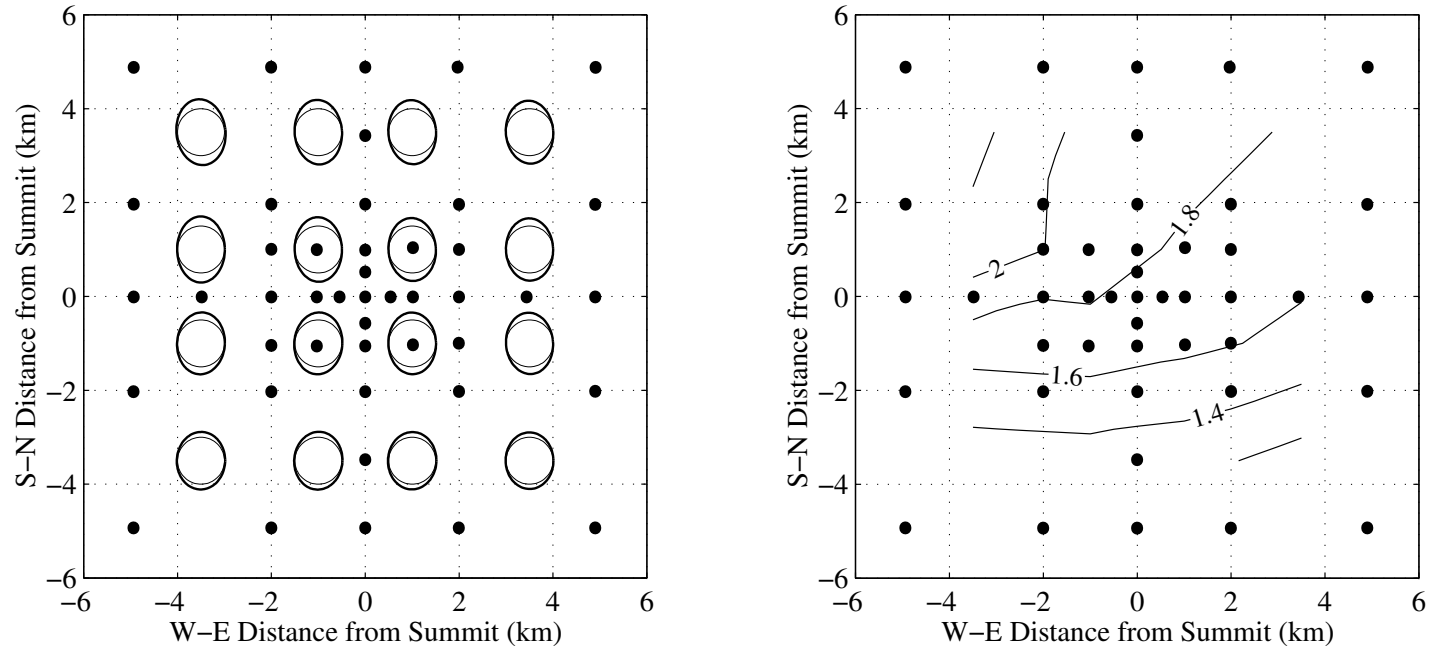


Figure 3.6: Left panel shows 1000-year strain ellipses based on the relative motion of the surrounding poles over 2 years. Ellipse centers are plotted in the center of the square from which they were calculated. Right panel shows contours of the horizontal strain rate in units of 10^{-4} a^{-1} . The general SE to NW pattern of strain rate is consistent with a south-north accumulation gradient over the summit.

University of New Hampshire, the average accumulation rate over the past 1000 years at 1.5 km north of the summit has been about 0.11 m a^{-1} ice equivalent, with slightly higher rates over the most recent 30 years of about 0.13 m a^{-1} (Mayewski *et al.*, 1995). We assume that this accumulation rate is spatially constant in the immediate vicinity of the summit. Ice thickness h measured 400 meters south of the summit is 1004 ± 4 meters (H. Englehardt, *pers. comm.*). This value is reduced by 17.3 meters to account for the density variation in the firn column (Mayewski *et al.*, 1995) so that $h = 987 \pm 4$ m in ice equivalent units. The right-hand side of Equation (3.1) can be calculated from these measurements:

$$\gamma h(\partial_x u_s + \partial_y v_s) = \gamma(987 \pm 4)((1.75 \pm 0.10) \times 10^{-4}) = 0.14 \pm .05 \text{ m a}^{-1},$$

$$b = 0.11 \text{ to } 0.13 \text{ m a}^{-1}.$$

The factor γ is assumed to range from 0.80 (isothermal, laminar flow, with flow-law power $n = 3$) to 0.85 (determined from a finite element model of ice flow (Chapter 2; Nereson *et al.*, 1996)). The uncertainty in the horizontal velocity divergence is determined from the range of results obtained when various pole configurations are used to calculate the velocity divergence at the summit. Although the flux divergence is slightly higher than the long-term accumulation rate, suggesting slight thinning at the summit, the measurement error allows the possibility that the Siple Dome summit is in steady state.

3.5.2 North Flank and Siple Ice Stream

Figure 3.7 shows the velocity field along the north line and across the topographic scar feature. Flow is parallel to the survey pole line until about 20 km from the summit, where ice begins to flow westward toward the Ross Ice Shelf. Velocities are largest (12 m a^{-1}) at 44 km north of the divide. Flow is channeled along the length of the

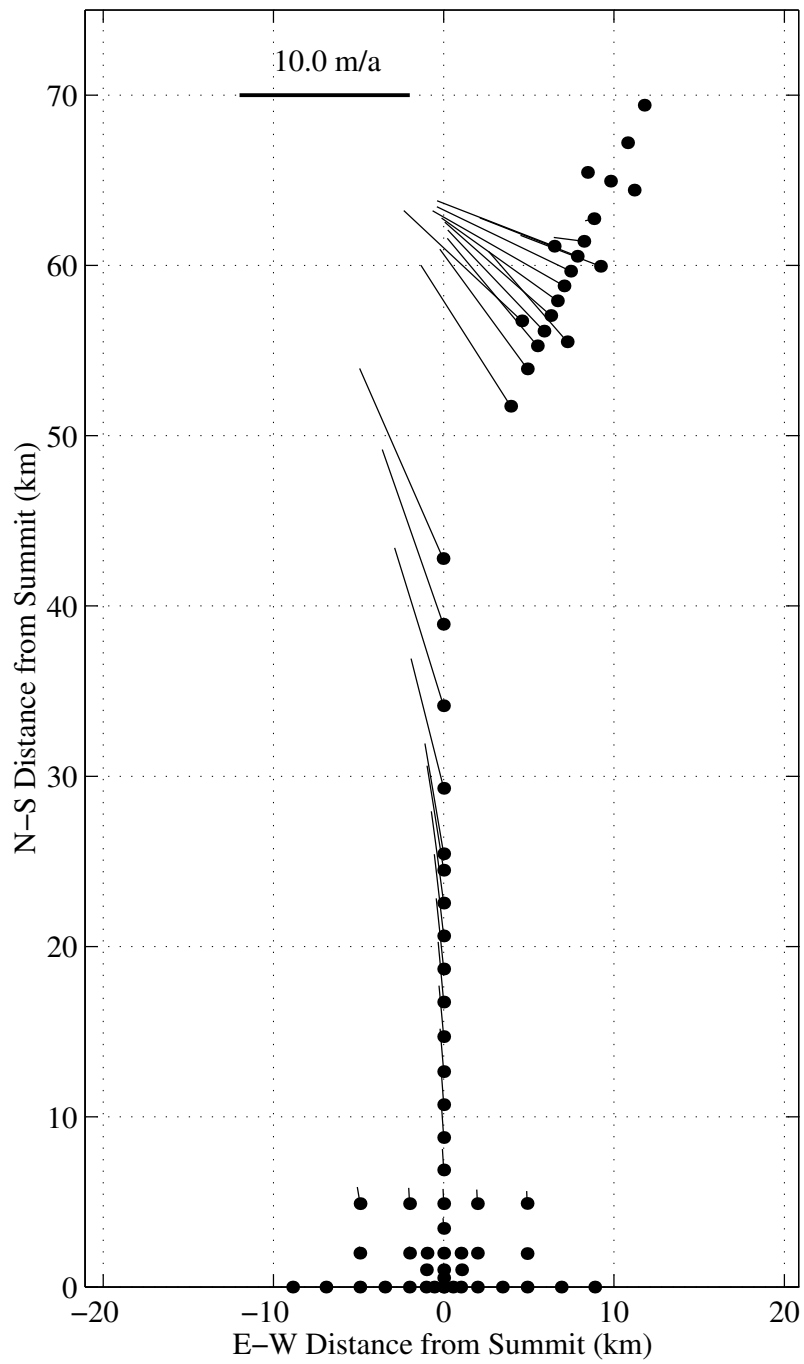


Figure 3.7: Velocity vectors for the northern flank of Siple Dome. Flow is primarily along the pole line until about 20 km north of the summit.

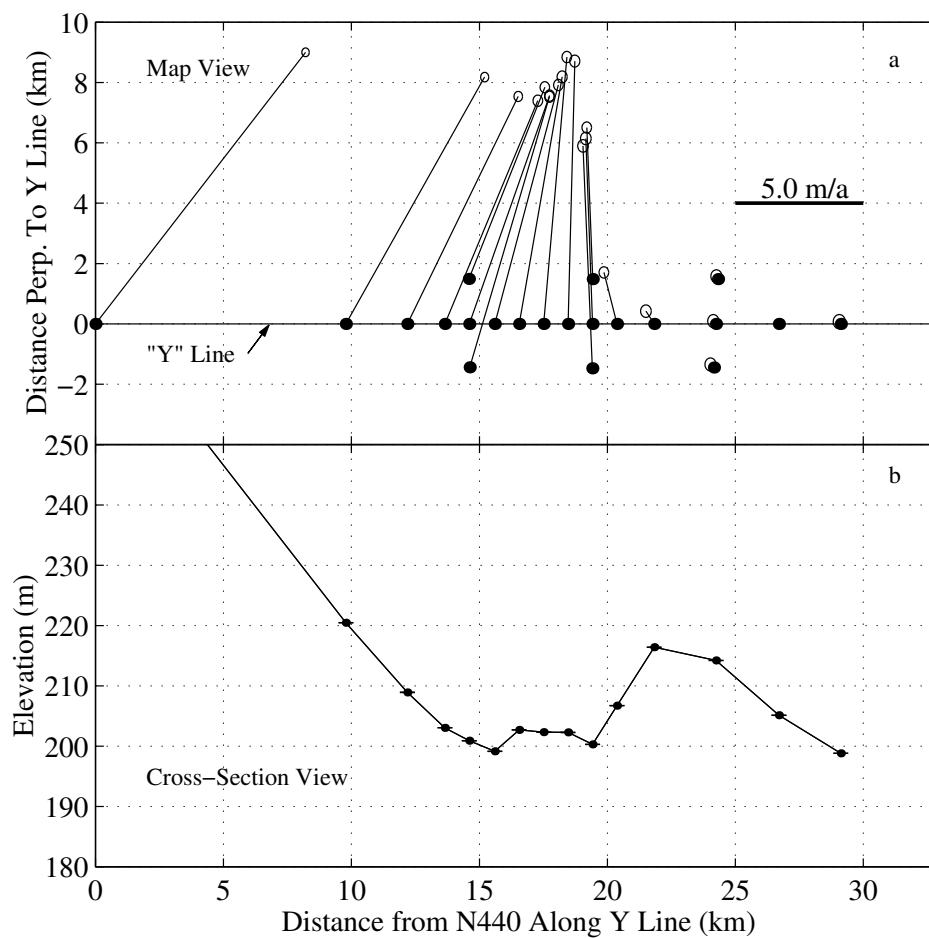


Figure 3.8: (a) Velocity vectors for the northern scar area. Circles at the end of the velocity vectors denote errors. (b) Topography of the scar feature relative to the WGS84 ellipsoid. Fastest velocities occur in the trough of the scar feature. Siple Ice Stream on the right (> 20 km) is nearly stagnant.

trough of the topographic feature defining the Siple Ice Stream margin. Velocities in the trough are large. There is little detectable motion ($< 0.10 \text{ m a}^{-1}$) on the relict ice stream itself (Fig. 3.8) showing complete stagnation with no remnant flow at reduced velocities as observed for the upper part of Ice Stream C (*Whillans and van der Veen, 1993; Anandakrishnan and Alley, 1997*). The present shear is in the opposite sense to what one would expect for an active ice stream margin. The present shear rate across the margin is about 0.002 a^{-1} . Strain rates in the trough show that the trough area is extending along its length. The extensional strain rate along the trough is $(8.6 \pm 0.6) \times 10^{-4} \text{ a}^{-1}$, while the compressional strain rate perpendicular to the trough is $(7.1 \pm 0.2) \times 10^{-4} \text{ a}^{-1}$. The net horizontal velocity divergence may contribute to the persistence of the trough topography through time.

3.5.3 *South Flank and Duck's Foot*

Figure 3.9 shows the velocity vectors along the south flank of Siple Dome and across topographic features near Ice Stream C, called the “Duck’s Foot”. Figure 3.10 shows the velocity vectors and surface profile for the Duck’s Foot area. In general, flow along the south flank is slower than to the north; a maximum velocity of 2 m a^{-1} is reached about 45 km south of the summit. The velocity vectors on the south flank are parallel to the pole-line for its entire length, indicating that the radar profiles collected along this line coincide with an ice-flow line. Ice flow slows to about 0.30 m a^{-1} as the Duck’s Foot area is approached. The present flow direction and magnitude is not correlated with the small-scale topography of the Duck’s Foot. The flow direction and magnitude in this area is very uniform, angling slightly to the west toward the Ross Ice Shelf.

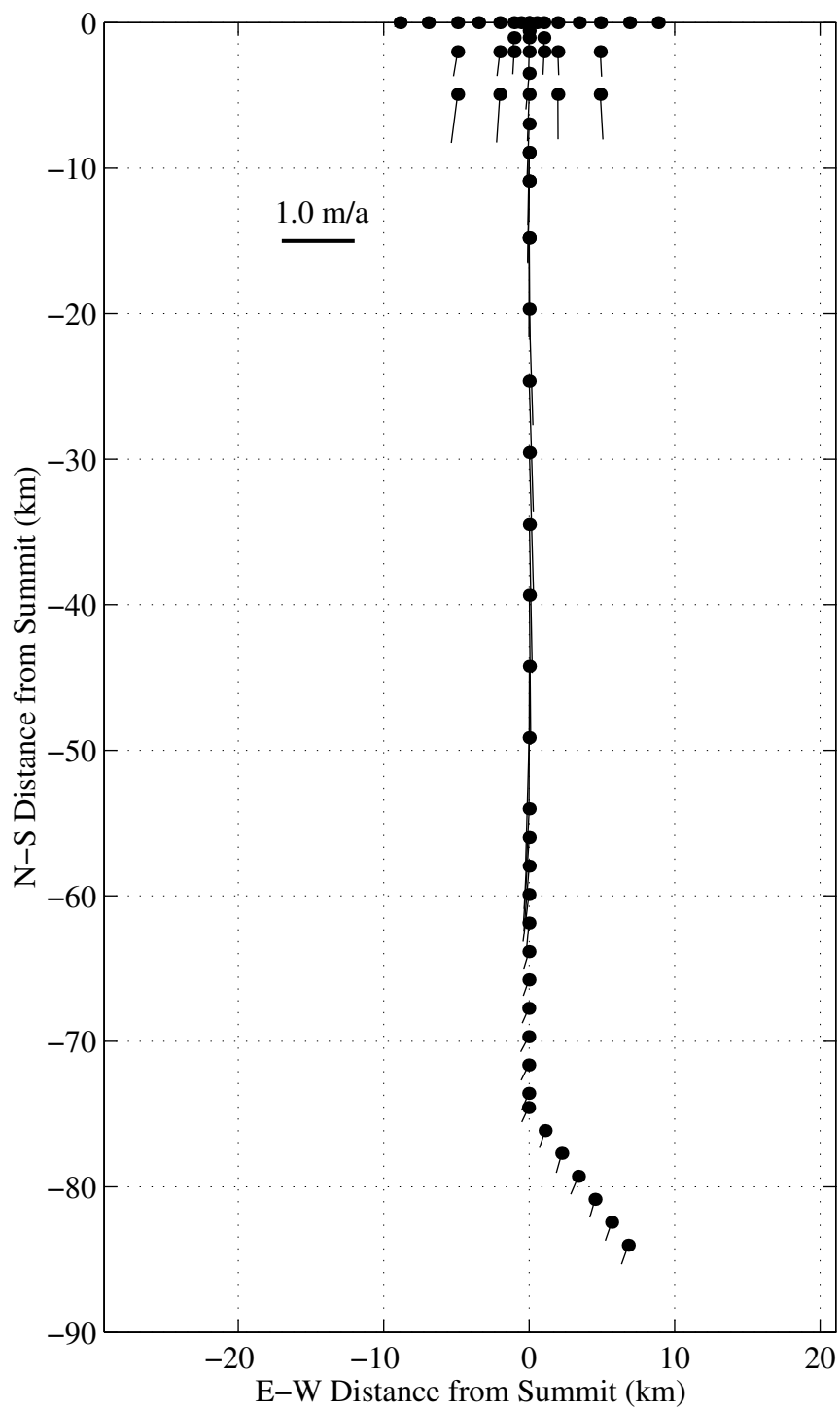


Figure 3.9: Velocity vectors for the south flank of Siple Dome.

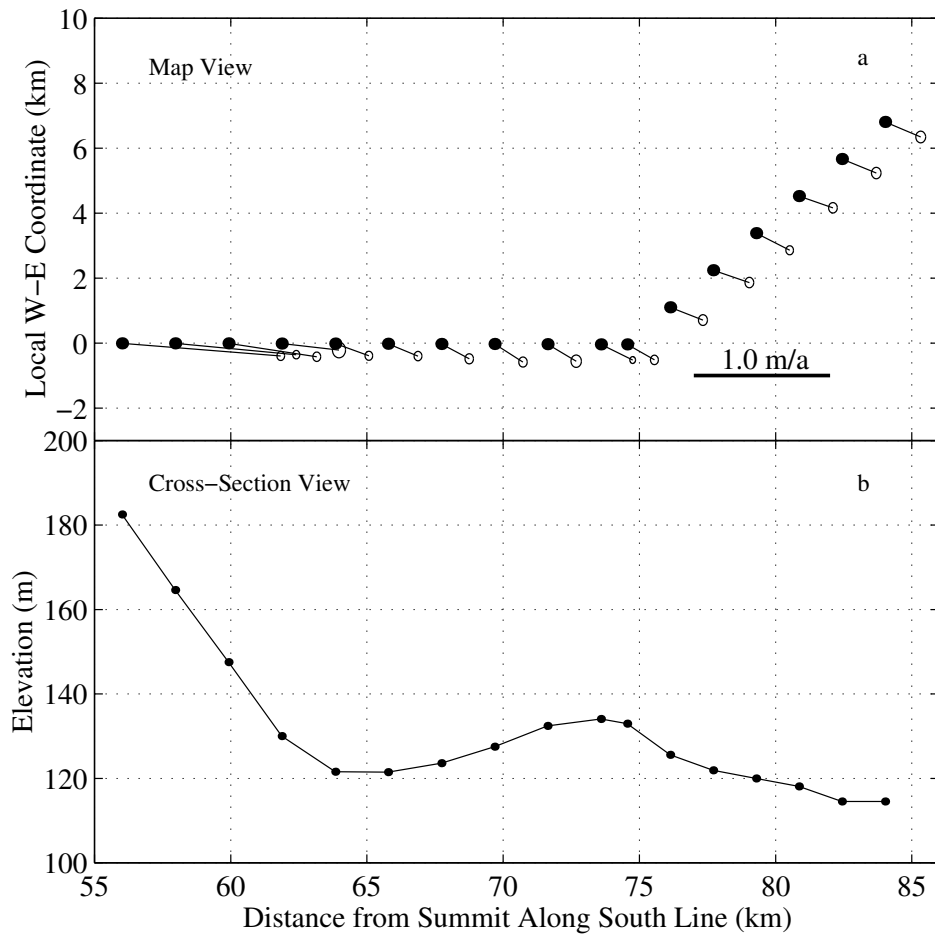


Figure 3.10: (a) Velocity vectors for the south flank of Siple Dome in the vicinity of the topographic features known as the “Duck’s Foot”. Circles at the end of the velocity vectors denote the measurement error. (b) Surface elevation profile.

3.5.4 The Cross-Dome Velocity Profile

For 2-dimensional, isothermal, laminar flow, the pattern of horizontal velocity v_s assuming Glen's ice flow law with $n = 3$ is given by

$$v_s(x) = \frac{2\bar{A}}{n+2}(\rho g)^n \partial_y S^n h^{n+1}, \quad (3.3)$$

where $S(y)$ is the surface elevation profile determined from GPS measurements, ice density $\rho = 917 \text{ kg m}^{-3}$, gravity $g = 9.8 \text{ m s}^{-2}$, and \bar{A} is an effective depth-averaged flow parameter (*Paterson, 1994*). Given RES measurements of ice thickness from across Siple Dome, this equation can be used to predict velocity versus distance from the divide. Figure 3.11 shows the component of measured velocity along the GPS pole line and the calculated velocity from equation (3.3). The calculated and measured velocities show good agreement when we choose $\bar{A} = 2.5 \times 10^{-17} \text{ Pa}^{-3} \text{ a}^{-1}$ (corresponding to a weighted average ice temperature of about -8 C ; *Paterson, 1994*), except where the flow deviates from the pole line at 20 km north and 60 km south of the summit. The measured flow in this -60 km to 20 km region is generally consistent with 2-d laminar flow.

3.6 Mass Balance Across Siple Dome

3.6.1 Calculation of Flux Divergence

Continuity of ice mass averaged over the ice column requires

$$\partial_t h = -\nabla_2 q + b. \quad (3.4)$$

where the horizontal flux divergence $\nabla_2 q = (\partial_x q_x + \partial_y q_y)$. The horizontal flux divergence $\nabla_2 q$ can be calculated from measurements of either vertical velocity pattern (emergence velocity) or the horizontal velocity pattern. Traditionally, $\nabla_2 q$ is calculated from measurements of horizontal velocity because measurements of vertical

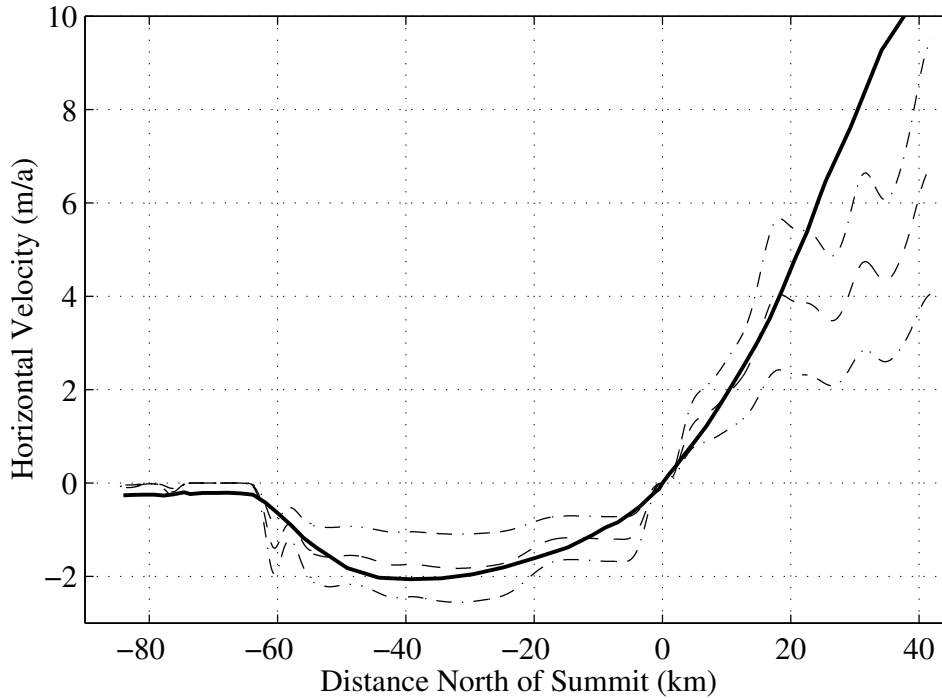


Figure 3.11: The northward component of surface velocity along the pole line (solid curve). The velocity component calculated from equation (3.3) is also shown assuming flow parameter values $\bar{A} = 2.5 \times 10^{-17} \text{ Pa}^{-3} \text{ a}^{-1}$ (dashed) and $\bar{A} = 1.5 \times 10^{-17} \text{ Pa}^{-3} \text{ a}^{-1}$ (dot-dash, lower velocities), and $\bar{A} = 3.5 \times 10^{-17} \text{ Pa}^{-3} \text{ a}^{-1}$ (dot-dash, higher velocities).

motion on a glacier are not sufficiently reliable. However, high precision GPS survey techniques may enable vertical motion to be measured with sufficient resolution to directly calculate ice flux. Here, we compare $\nabla_2 q$ calculated from GPS measurements of horizontal velocity and from independent GPS measurements of vertical motion at Siple Dome.

Calculated From Horizontal Velocity Measurements

We assume that the flow line is parallel to the local y coordinate at $x = 0$, ice velocity perpendicular to y is zero ($\bar{u} = 0$), the variation of ice thickness along x is zero

($\partial_x h = 0$), and $\bar{\mathbf{u}} = \gamma \mathbf{u}_s$. With these assumptions, the 2-d horizontal flux divergence written in terms of horizontal velocity pattern is

$$\nabla_2 q = \gamma[\partial_y(v_s h) + h \partial_x u_s], \quad (3.5)$$

where u_s and v_s are determined from GPS measurements of surface velocity in the x and y directions and h is given by RES measurements of ice thickness. We assume $\gamma = 0.85$ as predicted by a finite element model of Siple Dome flow (*Chapter 2; Nereson et al., 1996*) and the variation of u_s along x is related to the spacing between adjacent flow lines $W(y)$ (*Paterson, 1994*),

$$\partial_x u_s = \frac{v_s}{W} \partial_y W. \quad (3.6)$$

The Siple Dome ridge is nearly two dimensional near the summit and the radius of curvature of surface elevation contours here is near infinity. Far from the divide ($x \gg L$, where L is some transitional length scale), we expect flow to be more divergent according to the radius of curvature, R , of the surface elevation contours there. We choose a parabolic function to represent $W(y)$ so that near the divide, $W(y)$ is constant and away from the divide, $W(y)$ diverges:

$$\frac{W(y)}{W(0)} = \left(\frac{y}{L}\right)^2 + 1. \quad (3.7)$$

When $y = L$, adjacent flow lines are twice as far apart as at $y = 0$. The length scale L is chosen to be the radius of curvature at the boundary of Siple Dome R minus the half-width of the dome Y : $L = R - Y \approx 50$ km. We use $L = 35$ km to account for errors in L .

The satellite images of Siple Dome (Fig. 3.1) suggest that the surface elevation contours may be slightly concave-outward north of the divide, indicating that $W(y)$ may decrease with distance from the divide. Therefore, we also consider a $W(y)$

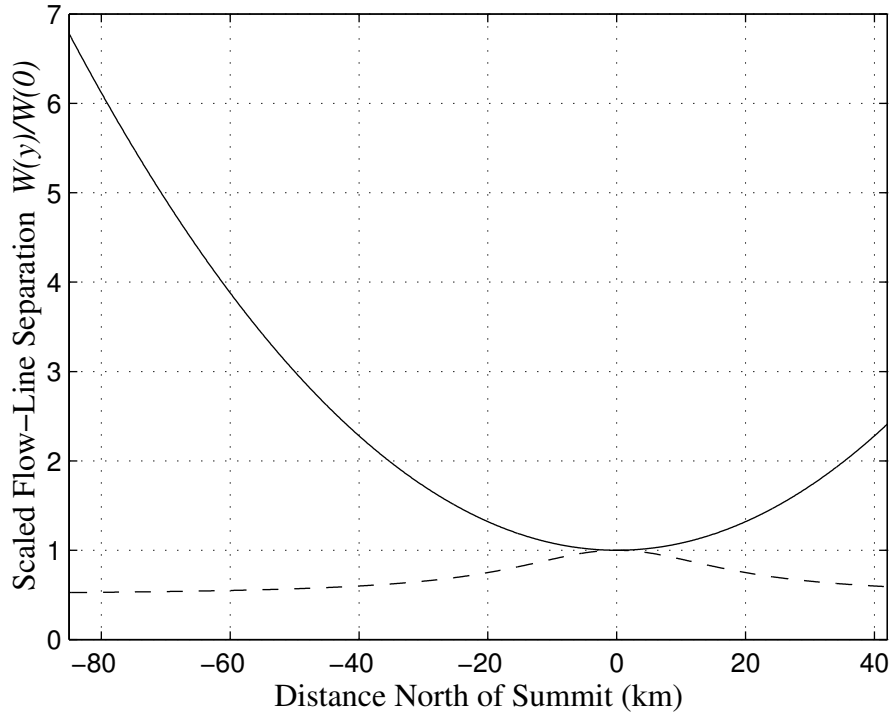


Figure 3.12: A scaled functions of distance variation between adjacent flowlines $W(y)/W(0)$ used to calculate the horizontal flux divergence (Fig. 3.13). The range between these two curves includes flow-line divergence (solid curve, Eq. 3.7) and slight flow-line convergence (dashed curve, Eq. 3.8).

function that allows for a zone of slightly converging flow near the divide and no convergence or divergence away from the divide ($y \gg D$):

$$\frac{W(y)}{W(0)} = \frac{A}{1 + (y/D)^2} + B. \quad (3.8)$$

The length scale $D = 20$ km defines the zone of convergence and is arbitrarily chosen to be about $Y/2$. The constants $A = 0.5$ and $B = 0.5$ define the magnitude of the convergence and are chosen such that $A + B = 1$. Figure 3.12 shows two $W(y)$ functions which bracket the expected range of flow-line separation functions.

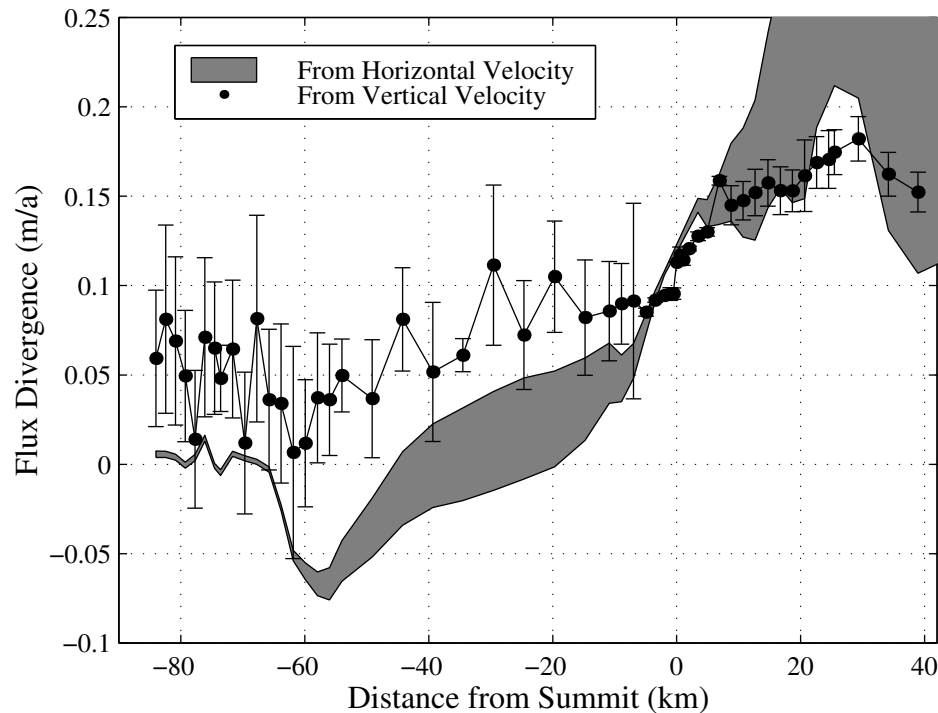


Figure 3.13: Siple Dome flux divergence calculated from the pattern of horizontal velocity (Eq. 3.5, gray) and from the pattern of vertical velocity (Eq. 3.10, dots).

Calculated From Vertical Velocity Measurements

The horizontal flux divergence calculated from measurements of vertical motion w_s is called the emergence velocity (submergence velocity in an accumulation area). For 2-d flow assuming the ice is frozen to its bed (*Nereson et al.*, 1996; *Gades*, 1998), the horizontal flux gradient is (*Paterson*, 1994)

$$\nabla_2 q = \partial_y \int_B^S v \, dz \quad (3.9)$$

$$= v_s \partial_y S + \int_B^S \partial_y v \, dz, \quad (3.10)$$

where B is the bed elevation, S is the surface elevation (from continuous GPS mea-

surements), and v_s is the velocity along y at the ice surface. Assuming the transverse strain rate is zero, then $\partial_y v = -\partial_z w$ and

$$\nabla_2 q = v_s \partial_y S - w_s. \quad (3.11)$$

The surface slope $\partial_y S$ is negative, and the GPS-measured vertical velocity w_s is negative and in ice-equivalent units. Assuming the density profile in the firn is not changing in time, the vertical motion of the surface firn can be corrected to reflect vertical motion of the ice by the relation (*Appendix B*)

$$w_{ice} = w_{firn} \frac{\rho_f}{\rho_i}. \quad (3.12)$$

Based on measurements from snow pits, we choose $\rho_f = 340 \text{ kg m}^{-3}$. Although variation among snow pits and cores from Siple Dome shows that this value can range from 300 to 400 kg m^{-3} (*H. Conway, pers. comm.*), our results are not sensitive to this range.

Comparison of Flux Divergence Calculations

The horizontal flux divergence calculated from either the horizontal velocity pattern (Eq. 3.5) or the vertical velocity pattern (Eq. 3.10) should be equivalent. Figure (3.13) shows the flux divergence calculated from both methods. Emergence velocity errors are larger south of the divide primarily because measurements there were made over a 1-year period while measurements to the north span a 2-year period. Both methods agree for values north of the divide (1994 and 1996 data). South of the divide (1996 and 1997 data), the shape of the pattern is the same, but there appears to be a systematic disagreement between the two flux divergence calculations. Because the horizontal positions of the survey poles are well-determined and because the horizontal motions are large compared to the measurement error, the flux divergence calculated

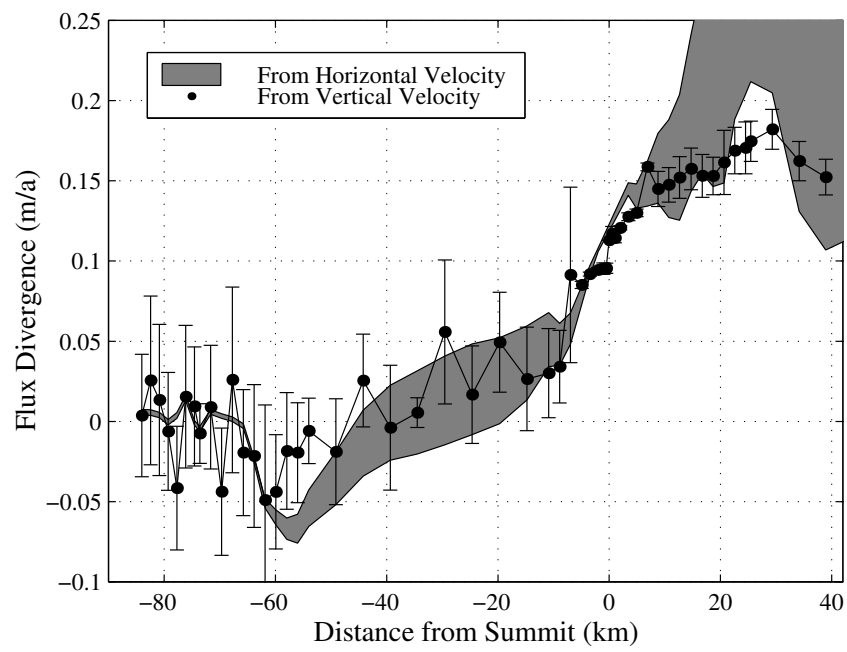


Figure 3.14: Horizontal flux divergence calculated from measurements of horizontal velocity and from vertical velocity. 1997 vertical position measurements have been shifted upward 0.15 m relative to the summit.

from these measurements (Eq. 3.5) is more reliable than the calculation from vertical motion.

The 1996-1997 submergence velocity appears to be too high relative to the calculated horizontal flux divergence. The discrepancy could be caused by systematic errors associated with reduction of GPS measurements, from anomalous upward motion of the summit pole between 1996 and 1997, or from anomalous downward motion of all poles established in 1996 along the south flank. However, the results are not sensitive to the parameters used in the network adjustment process (Sec. 3.4). If the summit pole was anomalously high (or the rest of the poles anomalously low), the poles along the flank would be interpreted as having anomalously high vertical motion relative to the summit pole. The observed discrepancy would require a downward shift of poles along the south flank by about 0.15 m. Figure 3.14 shows the improved agreement that results after this correction.

Anomalous motion of the summit survey pole could occur if the base of the pole did not always move vertically with the firn. In this case, some of the approximately 0.3 meters of expected annual vertical motion from ice flow (assuming $b = 0.10 \text{ m a}^{-1}$ and $\rho_f = 350 \text{ kg m}^{-3}$) would not occur and the summit pole would appear artificially high. Differential settlement of the survey poles could also contribute to erroneous inferred vertical motion. In 1996, the base of the summit pole was about 2 meters below the surface while the newly established south flank poles reached a depth of about 1 meter. Differential settlement of 0.15 m over one meter could occur if the density at the base of the summit pole is 15% greater than the density at the base of poles along the south flank. This difference is plausible given available density-depth measurements and qualitative evidence of low density firn along the south flank (*C. Raymond, pers. comm.*)

3.6.2 Spatial Pattern of Mass Balance

Assuming the flux divergence pattern calculated from measurements of horizontal velocity, the pattern of thickening or thinning across the dome can be calculated from the continuity equation,

$$\partial_t h = -\gamma[\partial_y(v_s h) + h\partial_x u_s] + b. \quad (3.13)$$

The accumulation pattern $b(y)$ is taken to be the steady-state pattern inferred from the RES layer shapes (*Chapter 6*). The horizontal velocity components v_s and u_s are from GPS measurements, and ice thickness h is determined from RES measurements across the dome (*Chapter 6*). Figure 3.15a (upper panel) shows the calculated flux divergence from equation (3.5) for the range of width functions $W(y)$ shown in Figure 3.12 and the range of accumulation patterns inferred from RES measurements at the 2σ confidence level (*Chapter 6*). Their difference, the inferred rate of thickening, is shown in the lower panel. No thickening or thinning is predicted at the summit. Although the accumulation rate at the summit is fixed at the 1000-year average from ice core measurements (*Mayewski et al., 1995*), the regional flux divergence is a completely independent measurement. The agreement is consistent with the detailed measurements of the 2-d flux divergence in the summit grid. Along the north flank, the flux divergence and accumulation rate are of similar magnitude, suggesting little thickening or thinning is occurring there. The flux divergence increases sharply at 20 km north of the summit where there is a step in bedrock topography and an increase in ice thickness gradient. This small-scale feature is not allowed by the function used to describe the accumulation pattern (*Chapter 6*). Estimates of ice thickness change beyond 20 km north of the summit are not shown because ice flow there deviates significantly from the pole line. South of the divide, the flux divergence is much less than the accumulation rate and becomes negative at about 40 km

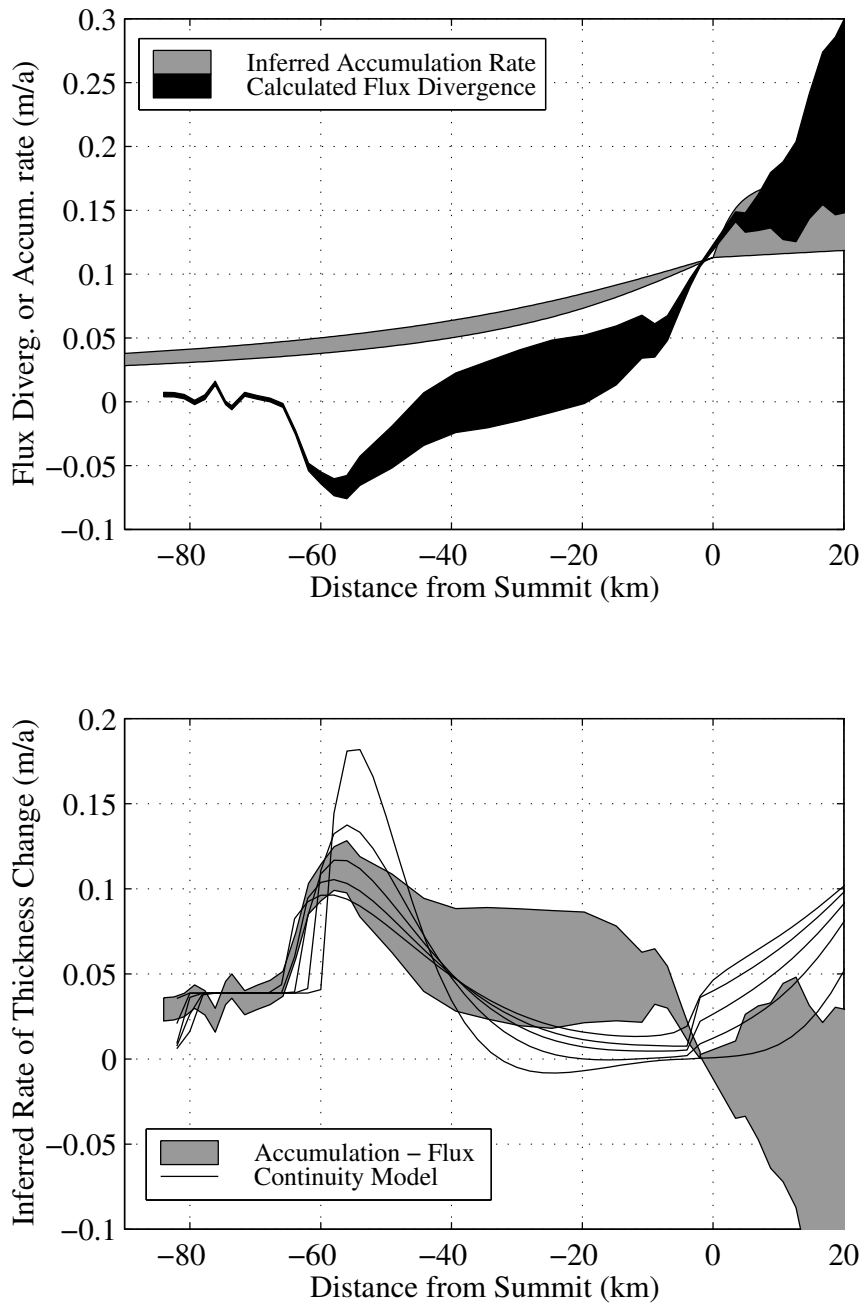


Figure 3.15: (a) Flux divergence inferred from measurements of ice velocity and ice thickness for the south flank of Siple Dome (black) and the inferred accumulation pattern from analysis of RES internal layer shapes (gray). (b) The inferred pattern of thickening and thinning rates across the dome (gray), and the thickening rates calculated from a model of Siple Dome evolution for 100, 200, 300, 400 and 500 years since stagnation of the Duck's Foot and Siple Ice Stream (dashed). Positive ordinate denotes positions north of the divide.

from the summit. This difference suggests that the south flank is thickening with a maximum rate of $0.10\text{--}0.13\text{ m a}^{-1}$ at about 57 km south of the summit. This region of maximum predicted thickening is just north of the innermost topographic “scar” feature of the Duck’s Foot.

The pattern of thickening and thinning is somewhat sensitive to a reasonable choice of $W(y)$. Increasing (decreasing) $\partial_y W$ increases (decreases) the flux divergence and predicts slightly less (more) thickening to the south and more (less) thinning to the north, but the general pattern is unchanged. At 40 km south of the divide, the flux divergence becomes negative. Errors in the inferred accumulation pattern would not change the sign of the predicted thickening here. Even if the accumulation rate approached zero at the Duck’s Foot, thickening of about 0.07 m a^{-1} would still be predicted at about -57 km.

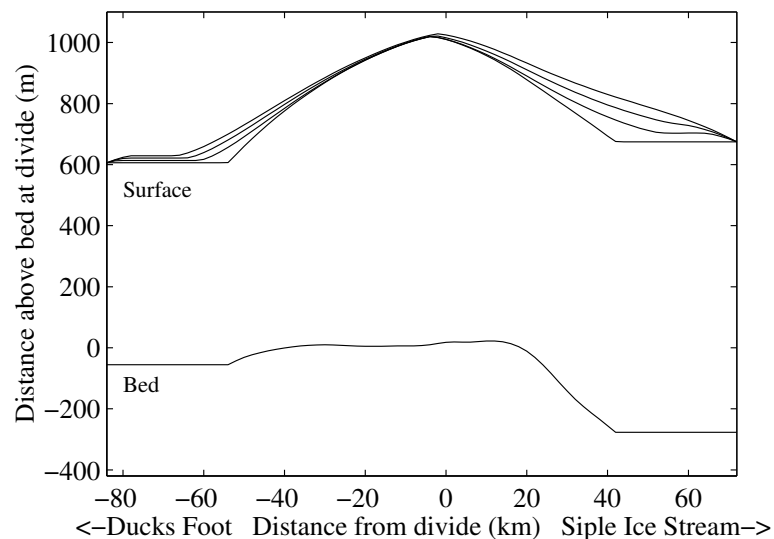


Figure 3.16: Surface profiles from a finite difference model of Siple Dome evolution described in Chapter 7. Profiles shown are at 0, 200, 400, and 600 years since synchronous stagnation of the ice streams on both flanks.

If the Duck's Foot represents a former region of fast flow which has recently stagnated, its evolution may be described by the continuity evolution model discussed in Chapter 7. The model uses the smoothed Siple Dome bed topography determined from RES measurements (*Chapter 6*), the accumulation pattern shown in Figure (3.15a), and a parabolic increase in distance between adjacent flow lines according to equation 3.7 with $L = 50$ km. The model is first used to calculate a steady state dome profile that is consistent with the accumulation pattern assuming laminar ice flow according to Glen's flow law. For the second model run, flat ice stream sections are added to the boundaries of the dome and the dome is allowed to evolve while the far margins of the ice streams are held at their initial elevations. Figure 3.16 shows the initial dome/stream profile before evolution begins and subsequent profile evolution. Figure 3.15b (lower panel) shows the thickening predicted by the model for 100, 200, 300, 400, and 500 years since synchronous stagnation of the Duck's Foot and the Siple Ice Stream. The character of the predicted thickening is similar to the thickening inferred from the velocity measurements with the maximum thickening occurring at the former junction of the dome and ice stream. The agreement is best when the time since stagnation in the model is about 300-400 years.

3.7 Conclusions

The positions of 125 survey poles relative to the divide were determined from GPS measurements to within 0.01 m in the summit region and to within 0.10 m in the vicinity of the northern and southern scar features. Measurements over 1- and 2-year periods give the velocity field relative to the divide. Ice flow is primarily two-dimensional near the summit. Ice flow is parallel to the pole line across the dome between 60 km south and about 20 km north of the divide. Outside of this region, flow turns westward to the Ross Ice Shelf. Velocities along the pole line increase away

from the divide and reach a maximum value of about 12 m a^{-1} at 44 km north. At the Siple Ice Stream margin, ice flow channels into the topographic trough and flows toward the Ross Ice shelf. On the relict Siple Ice Stream, the velocities are less than 0.10 m a^{-1} . South of the divide velocities increase to about 2 m a^{-1} at 40 km south and then decrease to less than 0.30 m a^{-1} across the Duck's Foot.

These measurements are used to determine the flux divergence in the summit area and across the dome. When compared to the accumulation rate, the rate of thickening and thinning at the Siple Dome summit and along its flanks can be inferred. At the summit, the flux divergence is slightly higher than the accumulation rate, suggesting slight thinning of about 0.02 m a^{-1} . However, measurement errors allow the possibility that Siple Dome is in steady state.

The horizontal flux divergence calculated from measurements of horizontal velocity or from measurements of the vertical velocity can be compared to the accumulation pattern to determine whether there are areas of thickening or thinning across the dome, relative to the divide. The horizontal flux divergence and emergence velocity calculated from GPS measurements do not agree. We suspect errors in vertical motion measurements are responsible for the discrepancy. Calculations of flux divergence from the horizontal velocity measurements suggest that the north flank is generally in balance (or perhaps thinning) while the south flank is likely thickening. Thickening is especially pronounced at about 57 km south of the summit, approximately coincident with the northern-most topographic feature defining the Duck's Foot. The character of the predicted thickening south of the divide is consistent with the model of dome evolution described in Chapter 7. The magnitude of the thickening is consistent with the dome evolution model assuming the Duck's Foot is a former streaming region which stagnated 300-500 years ago.

Chapter 4

MIGRATION OF THE SIPLE DOME ICE DIVIDE, WEST ANTARCTICA

This chapter is in press under the same title for the *Journal of Glaciology* with co-authors C. F. Raymond (University of Washington), E. D. Waddington (University of Washington) and R. W. Jacobel (St. Olaf College). D. Dahl-Jensen and R. Hindmarsh provided helpful review comments which led to significant improvements to the paper.

4.1 *Summary*

The non-linearity of the ice flow law or a local accumulation low over an ice divide can cause isochrones (internal layers) to be shallower under the divide relative to the flanks, forming a “divide bump” in the internal layer pattern. This divide signature is analyzed using ice flow models and inverse techniques to detect and quantify motion of the Siple Dome ice divide in West Antarctica. The principal feature indicating that migration has occurred is a distinct tilt of the axis of the peaks of the warped internal layers beneath the divide. The calculated migration rate is $0.05 - 0.50 \text{ m a}^{-1}$ toward Ice Stream D and depends slightly on whether the divide bump is caused by the non-linearity of ice flow or by a local accumulation low. Our calculations also suggest a strong south-north accumulation gradient of $(5-10) \times 10^{-6} \text{ a}^{-1}$ in a narrow zone north of the divide. A consequence of divide migration is that pre-Holocene ice is thickest about 0.5 km south of the present divide position. Divide motion indicates that non-steady processes, possibly associated with activity of the bounding ice streams, are affecting the geometry of Siple Dome. The migration rate is sufficiently slow that the divide bump is maintained in the internal layer pattern at all observable depths.

This suggests that major asynchronous changes in the elevation or position of the bounding ice streams are unlikely over at least the past 10^3 to 10^4 years.

4.2 Introduction

The stability of the West Antarctic Ice Sheet (WAIS) has been in question since the early 1970s when *Weertman* (1974) made the argument that ice sheets grounded below sea level are unstable and could collapse catastrophically in response to a modest increase in sea level. Characterizing the present and future stability of the WAIS is complicated by the presence of several ice streams. Their capacity to transport mass rapidly from the interior to the sea possibly increases the potential for rapid collapse of the WAIS. Understanding the past behavior of these ice streams should provide important clues to their role in WAIS stability.

Inter-ice stream ridges are good places to look for evidence of past ice stream activity because a record of changes in ice flow at the edges of these ridges may be recorded in their geometry and internal stratigraphy. Siple Dome is the ridge between Ice Streams C and D in West Antarctica (Fig 4.1). There is evidence for recent change at its boundaries. *Retzlaff and Bentley* (1993) used ice penetrating radar to detect buried crevasses of the former shear margin and date the shut-down of Ice Stream C at about 130 years ago. *Jacobel et al.* (1996) showed that internal layers are truncated beneath a linear feature on the NE flank of Siple Dome and suggested that this feature is a formerly active margin. It is possible that these or other past events have altered the ice flow at Siple Dome and have left a signal in the pattern of internal layers.

In this paper, we present evidence for migration of the Siple Dome divide over the past several thousand years at a rate of $0.05 - 0.50 \text{ m a}^{-1}$ northward toward Ice Stream D. Our results are based on analysis of the shape of internal layers obtained from radar measurements in the vicinity of the divide. Ice flow models and inverse

Table 4.1: Notation

| Variable | Meaning |
|------------------------------|---|
| $b(x)$ | accumulation rate |
| l_1, l_2 | length scales for partitioning function $\phi(x)$ |
| m | divide migration rate |
| p | one less than number of free parameters |
| $u(x, z)$ | horizontal velocity |
| $w(x, z)$ | vertical velocity |
| x | distance along flow from divide |
| \tilde{x} | scaled distance x/H |
| z | height above bed |
| $A(x)$ | scaled amplitude of cosine curve |
| $B(x)$ | integral over distance x of accumulation rate b |
| G_s, G_n | scaled accumulation gradient south and north of divide |
| H | ice thickness |
| J | mismatch parameter |
| L | number of observed layers |
| M | scaled divide migration rate $m/b(0)$ |
| N | number of points along a layer |
| $S(x, \bar{z})$ | shape of a layer with average height \bar{z} |
| T | total number of sample points |
| ϵ | expected combined error in layer shapes |
| λ | wavelength of cosine curve |
| $\phi(x)$ | divide/flank flow partitioning function |
| ω | residual weighting function |
| $\xi(x, z)$ | horizontal velocity shape function |
| $\zeta_{div}(z), \zeta_f(z)$ | divide and flank shape functions |
| $\Xi(x)$ | integral over ice thickness H of shape function ξ |
| Sup/Subscript | Meaning |
| * | in moving-divide reference frame |
| m | model value |
| d | observed value |

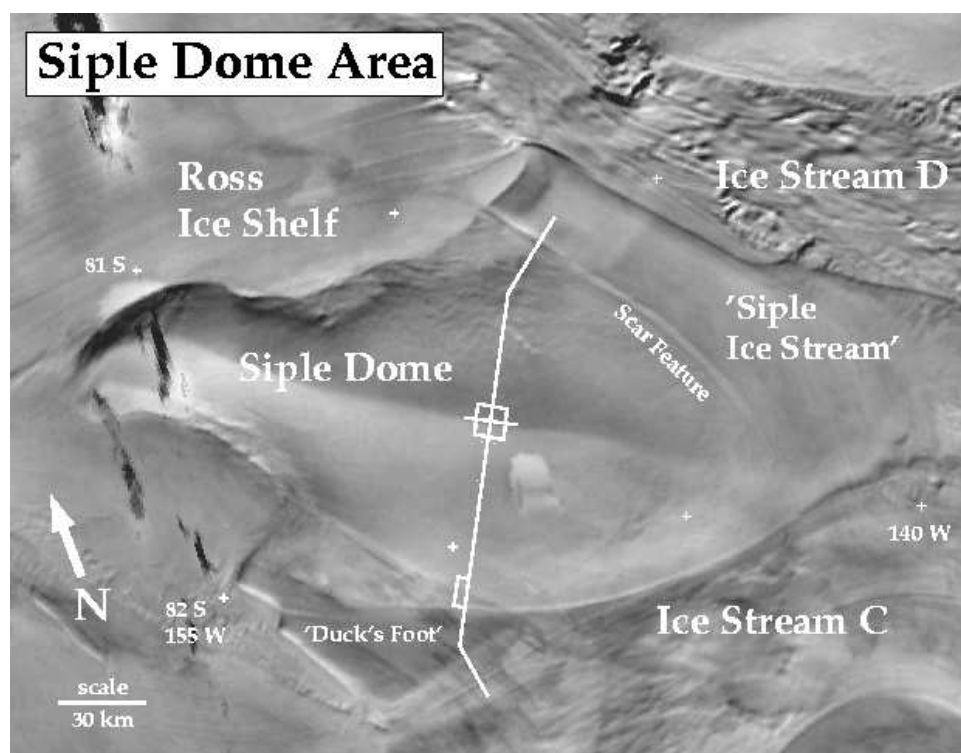


Figure 4.1: AVHRR image of Siple Dome and Ice Streams C and D. Radio-echo sounding profiles measured in 1994 and 1996 are shown by the white lines. Courtesy of T. Scambos, National Snow and Ice Data Center, University of Colorado.

Table 4.2: Summary of RES measurements.

| Center Frequency (Mhz) | Wavelength in Ice (m) | Horizontal Spacing (m) |
|------------------------|-----------------------|------------------------|
| 2 | 80 | 20 |
| 2 | 80 | 100 |
| 5 | 35 | 20 |
| 7 | 25 | 20 |

techniques are used to estimate the rate of divide motion and its sensitivity to the pattern of accumulation near the divide. We do not attempt to identify the specific cause of divide migration in this analysis. *Nereson et al. (1998a) (Chapter 5)* found that this divide migration could be caused by either an increase (decrease) in elevation of the Ice Stream D (Ice Stream C) - side boundary of Siple Dome by less than 100 meters, or by a modest change in the accumulation pattern over the past several thousand years.

4.3 Measurements

Measurements of the surface, bed, and internal layer geometry in the vicinity of the Siple Dome summit were obtained using Global Positioning System (GPS) surveys and radio-echo sounding (RES) measurements in 1994 and 1996 as part of a collaborative project among the University of Washington, St. Olaf College, and the University of Colorado. Detailed RES measurements were made every 20 – 100 m along a 4 km profile across the summit at several frequencies (wavelength 25 – 80 m in ice, Table 4.2). Low frequencies were chosen to reveal deep internal layers while higher frequencies were chosen to reveal shallower layers. Each RES measurement is a voltage time series that is filtered with a zero-phase, 4th-order Butterworth filter at 1 – 10 Mhz to reduce high frequency noise and low frequency coupling within the radar system. The signal voltage is mapped to color. Sequential, equally-spaced measurements of

a profile are plotted together to reveal the shape of the bedrock and internal layer pattern. The internal layers are caused by variations of electrical properties in the ice (*Harrison, 1973; Moore et al., 1992*). They are assumed to be isochrones, that is, former ice sheet surfaces which have been buried and deformed over time by ice flow (*Hammer, 1980*).

The measurements show that Siple Dome is a two-dimensional ridge overlying flat bedrock with ice thickness 1009 ± 7 m at the summit (*Raymond et al., 1995; Scambos and Nereson, 1995; Jacobel et al., in press*). Figure 4.2a shows a 10 km cross section of Siple Dome obtained from RES measurements with a wavelength of ~ 80 m in ice. A detailed 4 km profile measured using a shorter wavelength (≈ 35 m) is shown in Figure 4.2b. The internal layers are digitized for shape analysis by selecting the signal travel-time associated with the maximum or minimum reflection amplitude in a hand-prescribed time window. Each digitized internal layer is then smoothed horizontally with either a 100-meter box-car filter (for profiles with 20 m measurement spacing) or a zero-phase low-pass filter routine with cutoff frequency at $5 \times 10^{-4} \text{ m}^{-1}$ (for long profiles with 100 m measurement spacing). Travel-time is converted to depth using a ray-tracing program that includes a correction for the variation of density with depth (*Weertman, 1993*). Firn density is based on measurements of a 160 meter core taken near the divide in 1994 (*Mayewski et al., 1995*).

Figure 4.2 shows that the internal layers have a shape that varies with depth, with no relation to surface or bed topography. The layers are warped convex-up in a ≈ 2 km-wide zone beneath the divide with a maximum upward displacement of about 50 meters (*Nereson and Raymond, in press*). The pattern is asymmetric. The depth to a given layer on the north flank of Siple Dome is greater than its depth to the south. Figure 4.3 shows that variation in shape is small along the divide ridge, so that the layer shapes are largely 2-dimensional in a vertical plane perpendicular to

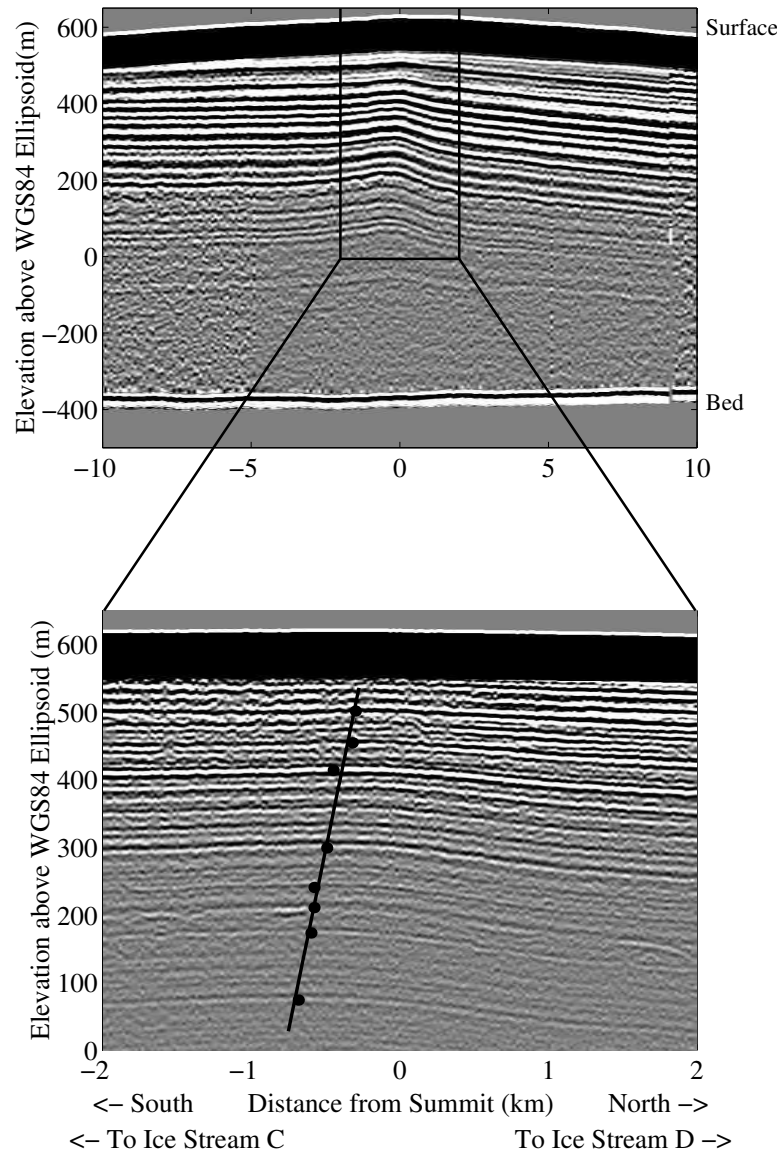


Figure 4.2: (a) A 10 km radar profile of Siple Dome measured perpendicular to the divide at the summit. Measurements were made every 100 meters with a center frequency of 2 Mhz. (b) Shallow part of a detailed radar profile where measurements were made every 20 meters with a center frequency of 5 Mhz. The data in both panels have been corrected for GPS-determined topography and bandpass filtered at 1 – 10 Mhz. The black band over the top 80 – 100 meters of the profiles denotes the portion of the returned RES signal obscured by the direct airwave. The apex of selected internal layers are marked with black dots in the lower panel. The solid line shows the trend of the apex axis.

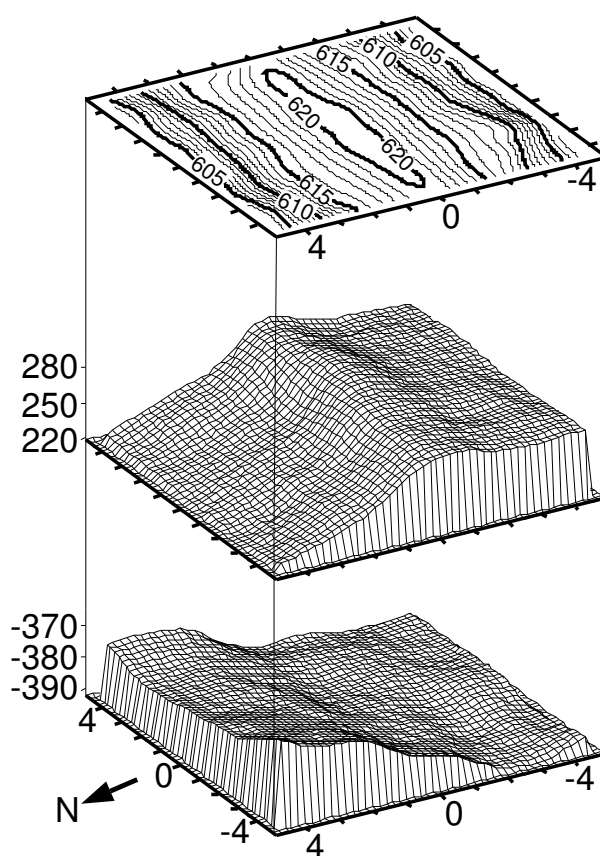


Figure 4.3: 3-D representation of a $10 \times 10 \times 1$ km cube centered at the Siple Dome summit showing surface elevation contours, bed topography, and the shape of one prominent internal layer identified from RES measurements. Horizontal coordinates are in kilometers and denote distance “north” and “east” of the summit relative to the east-west trending divide ridge. True geographic north is 16.4 degrees west of local “north”. Vertical coordinates are in meters above the WGS84 ellipsoid.

the ridge (*Jacobel et al., in press*). The positions of the apex of each curved layer are not vertically aligned; the axis is tilted toward the north side of Siple Dome by about 60° from vertical (Fig. 4.2b; *Nereson and Raymond, in press*).

Regardless of the cause of the local warping of the internal layers, the warping is likely a feature associated with the presence of the divide. Therefore we interpret the tilt of the apex axis as direct evidence for divide migration. However, inferring the rate of migration is not direct. An ice flow model predicts that a layer at 60% depth is about 10^4 a old (*Chapter 2; Nereson et al., 1996*). The horizontal displacement of its apex from the present divide position is about 700 meters, which might suggest a migration rate of 0.07 m a^{-1} . However, this simple analysis fails to include the integrated effect of ice flow on the shapes of isochrones over time.

4.4 Flow Models

Our goal is to determine the rate of divide migration and its sensitivity to unknown parameters. This goal requires a forward model that predicts the shape of an isochrone layer resulting from its deformation since deposition and includes a near-divide deformation process which produces up-warped isochrone layers.

Raymond (1983) showed that the non-linear creep of polar ice leads to an anomalous flow pattern spanning a few ice thicknesses beneath an ice divide. Deep ice is relatively 'stiff' due to low deviatoric stress, so that downward-moving isochrones are predicted to drape over this stiff zone and become warped convex-up. A two-dimensional, steady-state, finite element model (FEM) of this description of ice flow is used as a reference model against which the observed layer shapes are initially compared. We do not attempt to account for effects such as the linear behavior of ice under low shear stress (*Mellor and Testa, 1969; Doake and Wolff, 1985; Alley, 1992; Waddington et al., 1996*) or the development of crystal fabrics on the deformation

of isochrones. Rather, we consider the special divide flow regime predicted by an isotropic, non-linear flow law as one possible cause of warped isochrones.

Up-warped isochrones can also be caused by slow burial and low vertical velocities associated with a local minimum in the spatial accumulation pattern over the divide (as found by *Fisher et al.* (1983) at Agassiz Ice Cap). This is a second possible process leading to up-warped isochrones.

The actual deformation of isochrones near ice divides may be caused by some combination of anomalous flow from non-linear ice deformation and from the spatial accumulation pattern. We estimate divide migration rate at Siple Dome separately for each deformation process. The range of the results is assumed to be indicative of the uncertainty which arises from our lack of knowledge about the exact nature of deformation near the Siple Dome ice divide.

The FEM model provides the basis for constructing a kinematic flow model which is used to model the evolution of isochrone shapes for each case. The flow field in the kinematic model is shifted to simulate divide migration and adjusted to account for spatial variations in accumulation rate. The evolution of isochrone shapes is found by tracking particles in the resulting time-dependent flow field. The divide migration rate is then determined by the shift of the modeled flow field required to match the shape of internal layers observed at Siple Dome.

4.4.1 Steady-State Reference Model

The reference finite element model (FEM) incorporates the following assumptions (*Chapter 2; Nereson et al., 1996*):

1. The ice sheet geometry is two-dimensional and steady-state.
2. The bottom of the ice sheet is frozen to its bed.

3. Ice deforms according to Glen's non-linear flow law, $\dot{\epsilon} = \tau/(2B)^n$, which relates the effective shear strain rate, $\dot{\epsilon}$, to the effective shear stress τ with the degree of non-linearity described by $n = 3$.
4. The parameter B in the flow law is a function of temperature T following *Hooke* (1981).
5. The temperature field is steady state as determined from the current measured surface temperature (-26 °C), accumulation rate, an assumed geothermal heat flux of 65.5 mW m^{-2} (*Alley and Bentley*, 1988), and a simple, 1-D heat flow model (*Firestone et al.*, 1990, eq. 4). This model predicts basal temperatures ranging from -2 to -8 °C.
6. The accumulation rate is assumed to be 0.10 m a^{-1} ice-equivalent (*Mayewski et al.*, 1995).

Figure 4.4a shows the isochrone shapes predicted for this steady state case and the shape of observed internal layers from the radar measurements. The modeled and observed layers for each pair shown have the same average depth. Figure 4.4b shows the difference between the model and the data; dark colors show areas of large discrepancy. This standard, steady-state description of ice flow predicts significantly more warping (maximum amplitude ≈ 100 m) than we observe (≈ 50 m).

4.4.2 Kinematic Representation of Flow Field

The FEM is computationally intensive and does not allow for time-dependent effects such as migration of the divide flow field. A kinematic model is constructed to match the spatial variation of the flow field from the finite element model calculation. This kinematic flow model is computationally efficient and allows simulation of divide migration. It is time-dependent in the sense that it calculates the effect of a migrating divide on isochrone deformation. The model does not allow for varying rates of divide

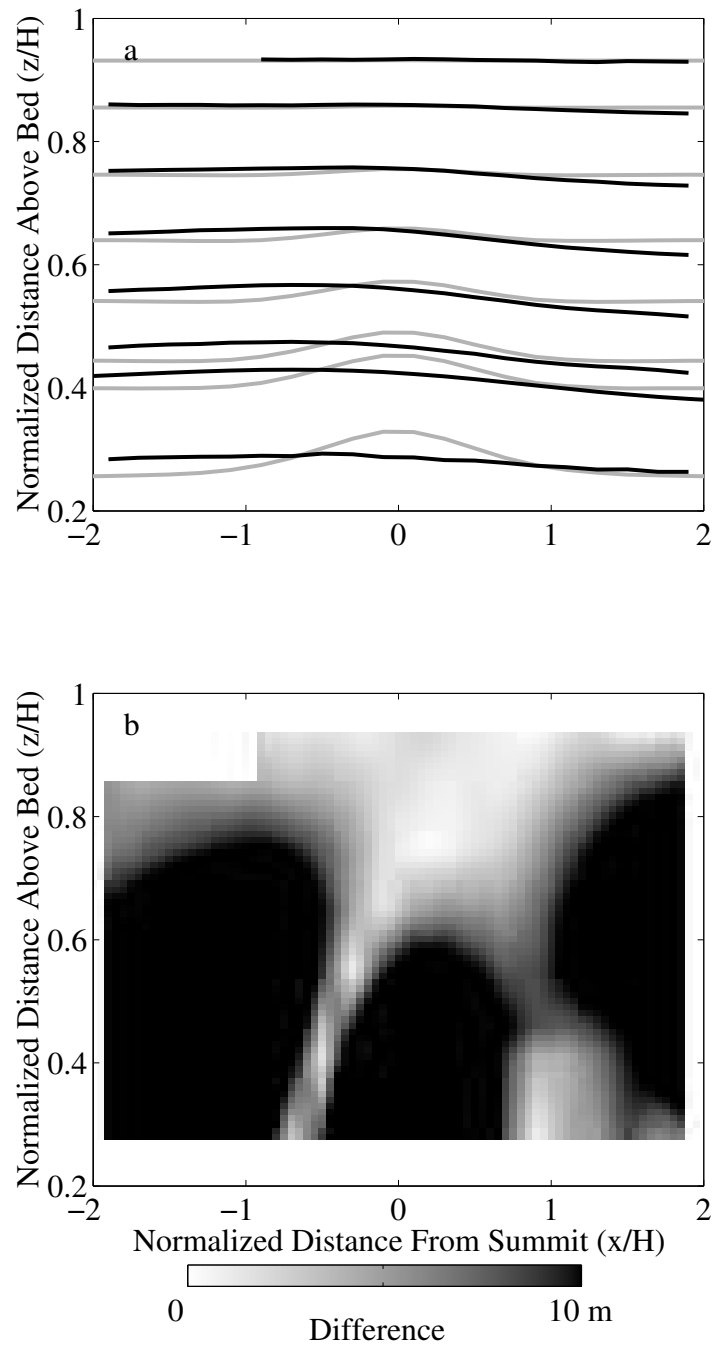


Figure 4.4: Comparison between isochrone shapes predicted by a steady-state ice flow model with a non-linear flow law and the shapes of internal layers observed using RES. (a) Modeled layers in gray and observed layers in black. (b) Model and data discrepancy plotted according to the grayscale to show the spatial pattern of the mismatch.

migration. The migration rate and accumulation pattern are assumed constant for all time. Therefore, the initial divide position is outside the model domain.

We assume that the ice thickness H is constant in the ± 4 km region around the divide since radar measurements show that the ice thickness there varies by less than 2%. We also assume that H has not changed over time. The depth-averaged horizontal velocity $\bar{u}(x)$, the mass balance $b(x)$, and the distance along flow from the divide x are related by

$$\bar{u}(x)H = \int_0^x b(x)dx. \quad (4.1)$$

The depth variation of horizontal velocity can be written in terms of a shape function ξ that varies with position x and height above the bed z in the vicinity of the summit,

$$u(x, z) = u_s(x)\xi(x, z), \quad (4.2)$$

where u_s is the horizontal velocity at the ice surface $z = H$, $\xi(x, 0) = 0$, and $\xi(x, H) = 1$. We construct $\xi(x, z)$ as a linear combination of a shape function typical of near-divide flow $\zeta_{div}(z)$ and a shape function typical of flank flow $\zeta_f(z)$,

$$\xi(x, z) = \phi(x)\zeta_{div}(z) + [1 - \phi(x)]\zeta_f(z), \quad (4.3)$$

where $0 \leq \phi(x) \leq 1$ describes the partitioning between flank and divide flow regimes.

Combining equations (4.2) and (4.3) and integrating over depth gives

$$\begin{aligned} \bar{u}(x) &= \frac{u_s(x)}{H} \int_0^H \xi(x, z)dz, \\ &= \frac{u_s(x)}{H} \left\{ \phi(x) \int_0^H \zeta_{div}(z)dz + (1 - \phi(x)) \int_0^H \zeta_f(z)dz \right\}. \end{aligned} \quad (4.4)$$

Equations (4.1) and (4.2) then require

$$u(x, z) = \frac{\xi(x, z)}{\Xi(x)} B(x), \quad (4.5)$$

where $\Xi(x) = \int_0^H \xi(x, z) dz$ and $B(x) = \int_0^x b(x) dx$. The vertical velocity field $w(x, z)$ is found from incompressibility,

$$\partial_x u = -\partial_z w, \quad (4.6)$$

which gives

$$w(x, z) = -\frac{b(x)}{\Xi} \int_0^z \xi(x, z) dz - \frac{B}{\Xi} \int_0^z \partial_x \xi dz + \frac{B}{\Xi^2} \partial_x \Xi \int_0^z \xi(x, z) dz. \quad (4.7)$$

Equations (4.5) and (4.7) describe a continuous 2-D flow field which includes a special near-divide flow regime. Tracking the motion of ice particles in this flow field through time predicts the shape of isochrone horizons. In the simplest case, $\xi(x, z) = 1$, $b(x) = b_0$, and equations (4.5) and (4.7) reduce to familiar expressions used to derive the ‘‘Nye’’ time-scale (e.g., *Paterson*, 1994, p. 277): $u(x, z) = (b_0/H) x$ and $w(x, z) = -(b_0/H) z$.

To simulate divide migration, the flow field is moved in the same reference frame as the divide, so that the horizontal velocity in the divide reference frame $u^*(x^*, z^*)$ is

$$u^*(x^*, z^*) = u(x^*, z^*) - Mb(0), \quad (4.8)$$

where $M = m/b(0)$ is a constant divide migration rate m scaled to a reference accumulation rate $b(0)$ which is taken to be $0.10 - 0.15 \text{ m a}^{-1}$ ice equivalent representing a range about the modern rate of 0.13 m a^{-1} (*K. Kreutz, pers. comm.*), $x^* = x - x_{div}$, and $z^* = z$. With this construction, $x^* = 0$ is always the divide position. The expression for vertical velocity $w(x, z)$ is unchanged so that $w^*(x^*, z^*) = w(x^*, z^*)$. We drop

the asterisks from now on, assuming we are always in the moving divide reference frame and $x = 0$ is the divide position.

4.4.3 Case 1: Non-Linear Divide Deformation

This model parameterization assumes that internal layer warping under the divide is caused only by the anomalous flow regime predicted near ice divides under a non-linear ice flow law. The shape functions ζ_f and ζ_{div} in equation (4.3) are described by an 8th-order Chebyshev Polynomial fit to the FEM flow field at $x = 10$ km and $x = 0$ km, respectively. The partitioning function $\phi(x)$ is chosen so that the horizontal velocity $u(x, z)$ given by equation (4.5) matches $u(x, z)$ predicted by the FEM. We find that $\phi(x)$ is well-approximated by the continuously differentiable, even function:

$$\phi(x) = 0.6 \exp \left[- \left(\frac{x}{\ell_1} \right)^2 \right] + 0.4 \exp \left[- \left(\frac{x}{\ell_2} \right)^2 \right], \quad (4.9)$$

where $\ell_1 = 775$ m and $\ell_2 = 3740$ m represent scale lengths which define the width of the divide zone. This partitioning function illustrates that the characteristic width of this zone associated with divide-flow is about 2 ice thicknesses (~ 2 km) (*Raymond, 1983; Hvidberg, 1996*). Figure 4.5 shows the horizontal velocity shape functions from the FEM and from equations (4.3) and (4.9). Despite the simplifications involved in defining $\xi(x, z)$, the kinematic model reproduces the layer shapes predicted by the finite element reference model with an rms error of 5 meters.

A simple spatial variation in accumulation $b(x)$ is allowed because the asymmetry of the observed layers implies some accumulation gradient across the divide independent of the layer warping. We describe a hinge-like accumulation pattern with two gradient parameters G_s and G_n which describe the accumulation gradient on the south ($x < 0$) and north ($x > 0$) sides of the divide, respectively:

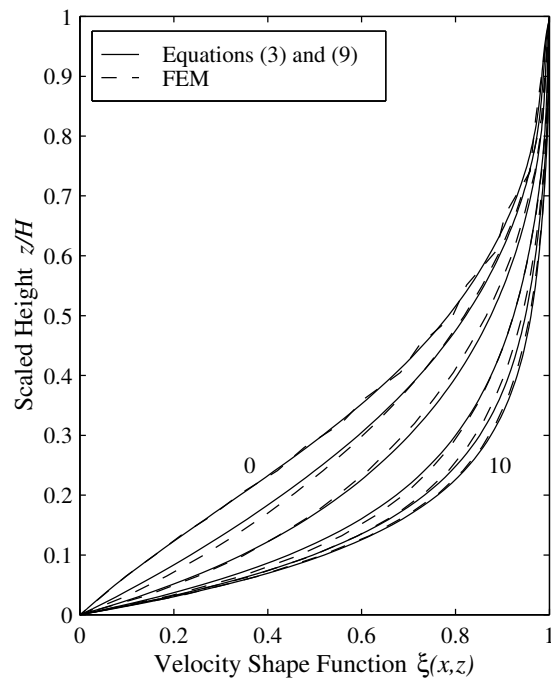


Figure 4.5: Horizontal velocity shape functions $\phi(x, z)$ from the finite element model calculation (dashed line) and from equations (4.3) and (4.9) (solid line) for $x = 0, 0.5, 1.0, 3.0, 5.0,$ and 10.0 km.

$$\frac{b(\tilde{x})}{b(0)} = G_s \tilde{x} + 1 \quad \tilde{x} \leq 0,$$

$$\frac{b(\tilde{x})}{b(0)} = G_n \tilde{x} + 1 \quad \tilde{x} > 0,$$
(4.10)

where $b(0)$ is a reference accumulation rate and $\tilde{x} = x/H$. Since we assume that the ice thickness H is constant, we scale the velocity pattern to the accumulation rate so that equation (4.1) holds. Velocity equations (4.5) and (4.7), with shape functions given by equations (4.3) and (4.9), and parameters given by equations (4.8) and (4.10) define the kinematic model for isochrone deformation due to a non-linear flow law. There are three non-dimensional free parameters, M , G_s , and G_n which we vary and find the combination which best fits the observed layer shapes.

4.4.4 Case 2: Accumulation Minimum at Divide

The second parameterization assumes that internal layer warping is caused solely by a local accumulation minimum over the divide. We construct a uniform flow field with no inherent special divide flow zone by setting $\phi(x) = 0$ in equation (4.3) thereby removing the spatial variation in the velocity shape function $\xi(x, z)$ so that

$$\xi(x, z) = \zeta_f(z). \tag{4.11}$$

We further define a new accumulation pattern that allows a local minimum over the divide. This pattern could be caused by wind-scouring at the divide and re-deposition elsewhere (*Fisher et al.*, 1983), or by a deposition pattern which causes less snow to be deposited over the divide relative to the flanks. The snowfall at Siple Dome may be associated with meso-scale cyclones which track from the north or north-east side of Siple Dome (*Carrasco et al.*, 1997; *Bromwich*, 1988). Numerical models suggest that winter surface winds are likely from the north to north-east (*Bromwich et al.*,

1994). Wind perpendicular to the east-west trending divide could cause scouring and re-deposition on the lee side. Orographic effects may cause more deposition on the north flank of Siple Dome, and a precipitation “shadow” on the south flank. We simulate these effects by superimposing one period of a cosine curve on the best-fitting hinge-like accumulation pattern from Case 1:

$$\frac{b(\tilde{x})}{b(0)} = \begin{cases} 1 + G_s^* \tilde{x}, & \tilde{x} \leq -\lambda/4, \\ 1 + G_s^* \tilde{x} - A \cos\left(\frac{2\pi\tilde{x}}{\lambda}\right), & -\lambda/4 < \tilde{x} \leq 0, \\ 1 + G_n^* \tilde{x} - A \cos\left(\frac{2\pi\tilde{x}}{\lambda}\right), & 0 < \tilde{x} \leq 3\lambda/4, \\ 1 + G_n^* \tilde{x}, & \tilde{x} > 3\lambda/4, \end{cases} \quad (4.12)$$

where G_s^* , and G_n^* emerge from Case 1 since the far-field layer shapes suggest an accumulation gradient independent of the divide zone.

Using this second parameterization, the model flow field $u(x, z)$ and $w(x, z)$ is defined by equations (4.5), (4.7), and (4.8) with the shape function given by equation (4.11) and accumulation pattern given by equation (4.12). We vary three non-dimensional parameters to find the best fit to the observations: the scaled amplitude A and wavelength λ of the superimposed cosine accumulation curve and the scaled divide migration rate M .

4.5 Choosing the Best Model

Because we do not know *a priori* the accumulation history of Siple Dome or the age of any layer, our goal is to match layer *shapes* rather than any particular isochrone. We must therefore decide which modeled layer we compare to a given observed layer in a way that makes a unique 1-to-1 assignment of observed to modeled layers. Options include comparing layers with the same height (1) at the present divide $x = 0$, (2) at their shallowest point, (3) at either edge of the domain, or (4) when averaged over the

domain. We want to emphasize the shape of layers near the divide to determine the divide migration rate. Options (1) and (2) are therefore poor choices because they emphasize the mismatch between the model and the data at edges of the domain where we expect the effects of a migrating divide to be smallest. Option (3) presents problems when the layers are asymmetric. We choose option (4) and compare modeled and observed layers with the same average height \bar{z} . The shape S of each layer is defined as its height variation relative to its average height:

$$S(x, \bar{z}) \equiv z(x, \bar{z}) - \bar{z}. \quad (4.13)$$

For a discrete set of digitized layers, each layer is denoted by the index j and identified by its average depth \bar{z}_j . Points along the horizontal coordinate are denoted by i . The shape of each layer is quantified by measuring the elevation S_{ij} at each position i along layer j so that

$$S_{ij} = S(x_i, \bar{z}_j) = z(x_i, \bar{z}_j) - \bar{z}_j. \quad (4.14)$$

To compare modeled (S_{ij}^m) and observed (S_{ij}^d) layer shapes (data), we define a mismatch index J ,

$$J = \frac{T}{T-p} \sum_{j=1}^L \sum_{i=1}^{N_j} \omega_{ij} \frac{(S_{ij}^m - S_{ij}^d)^2}{\epsilon_j^2}. \quad (4.15)$$

The term ϵ_j is the expected combined error from the model and the data for a particular layer j . A weighting function ω_{ij} for point i on layer j is chosen to give increased weight to the residual in the divide area. The number N_j is the total number of points i along a layer j , and $L = 30$ is the total number of layers, $T = \sum_j N_j$ is the total number of points sampled in the domain, and p is one less than the number of free parameters in the model. In this application, each layer is sampled every 200 m, and N_j depends on the length of the RES profile (3 to 7 km).

4.5.1 The Expected Error

The combined error term ϵ_j represents errors in layer shape $S(x_i, \bar{z}_j, z)$ and arises from errors in determining the elevation z of a point at x_i on a given modeled or observed layer and in determining the average height of the layer \bar{z}_j . For each layer j with average height \bar{z}_j we define

$$\epsilon_j = \left[\left(\frac{\partial S_d}{\partial \bar{z}_d} \right)^2 \Delta \bar{z}_d^2 + \Delta z_d^2 + \left(\frac{\partial S_m}{\partial \bar{z}_m} \right)^2 \Delta \bar{z}_m^2 + \Delta z_m^2 \right]^{1/2}, \quad (4.16)$$

where all values on the right-hand side correspond to layer j and subscripts m and d denote modeled and observed values, respectively.

Both the model and the data contribute to the total error. We do not include errors due to using possibly wrong assumptions in the flow model (flow law, temperature distribution, etc.) because we instead consider two distinct descriptions of internal layer deformation. However, there is an error in z_m associated with simplifications used to define the kinematic model. Based on a comparison to the FEM, these model simplifications correspond to $\Delta z_m = 1 - 5$ meters, depending on the height of the layer. We assume no error in average depth so that $\Delta \bar{z}_m = 0$.

Main sources of errors in the data include (1) picking errors: accurately defining an internal layer from the radar data, (2) processing errors: filtering and smoothing the internal layers, and (3) physics errors: converting the signal travel-time to depth. Part of the error Δz_d is due to random noise associated with picking a layer from the raw radar data which contributes to (1). This error is significantly reduced during the smoothing process and amounts to less than 1 meter. Another contribution to Δz_d is uncertainty associated with horizontal space between radar measurements, and how well this spacing is known: Δx_d . We somewhat arbitrarily set Δx_d to be half of the measurement spacing: 10 – 50 meters. The contribution to Δz_d is small (< 2 m)

because the layer shapes vary only slightly with position. The error in average depth of a layer $\Delta\bar{z}_d$ is systematic for a given layer and arises from identifying a specific return time associated with an internal layer from a rather broad reflection signal and from converting the signal travel time to depth. Both of these depend on signal frequency and with an error of about 1/10 of the wavelength of the transmitted pulse: about 2-10 meters. Based on these estimates, the total combined error ϵ_j from equation (4.16) ranges from 3 to 6 meters, depending on the average layer height and signal frequency.

4.5.2 *The Weighting Function*

The simplest weighting scheme is to prescribe equal weight to all of the residuals by setting $\omega_{ij} = 1$. However, we are primarily interested in determining the rate of divide migration, and information about divide position is contained in the shape of the “divide bump”. We therefore want to give greater weight to the residuals associated with this feature so that residuals occurring where the divide signature is most pronounced are given more weight than those where the signature is weak.

We define a weighting function ω_{ij} which is proportional to the component of the modeled layer shape that is caused by deformation processes associated with the presence of the divide. This divide shape component β_{ij} is obtained by subtracting the layer shape predicted under no special divide flow or divide accumulation pattern from the modeled layer shape S_{ij}^m . This removes the shape associated with bed topography and large-scale accumulation patterns. The resulting shape contains only the signature from the divide flow field. For Siple Dome layers, this adjustment amounts to removing any linear trend present in the modeled layer shape. The divide signature shape β_{ij} is generally positive because the divide deformation processes considered here produce up-warped isochrones. We do not consider models where the divide

deformation produces down-warped isochrones and negative β_{ij} values. The divide signature shape is normalized so that

$$\omega_{ij} = \frac{\beta_{ij}}{\sum_{j=1}^L \sum_{i=1}^{N_j} \beta_{ij}} \quad (4.17)$$

and

$$\sum_{j=1}^L \sum_{i=1}^{N_j} \omega_{ij} = 1. \quad (4.18)$$

With this definition of the weighting function, residuals far from the predicted divide signature receive little weighting, and layers with a more pronounced divide signature are weighted more heavily than layers with no signature such as those found near the surface and bed. Because the weighting function is normalized, models which produce a mismatch index $J < 1$ match the observations to within the weighted errors (a 68% confidence level), and models corresponding to $J < 2$ fit the data to within twice the weighted errors (a 95% confidence level). Over- or under-estimation of the errors would change the value of the minimum J (e.g., from 1 to 2), but not its dependence on the model parameters. Since we have only three free parameters for each case, we can explore the entire parameter space and find the shape of the 3-d parameter volume that defines the best fit (minimum J).

Our results are not sensitive to a reasonable choice of weighting functions. Prescribing equal weight to all points along a given layer by choosing $\omega_{ij} = 1$ does not change the value of the 3 best-fitting parameters for either case; though the overall value of the mismatch J increases slightly for Case 1.

4.6 Results

Figure 4.6 shows a comparison between the shape of the observed layers and the layers predicted by the kinematic model with the combination of parameters that produces

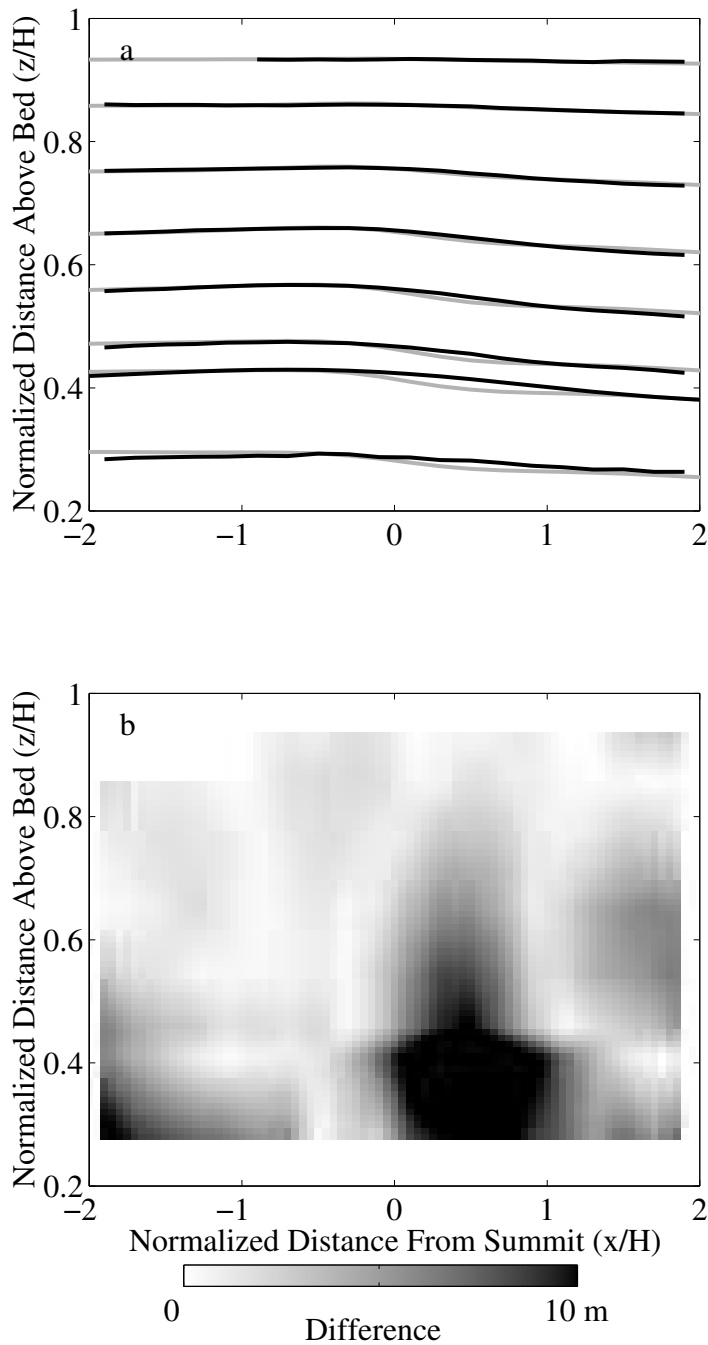


Figure 4.6: Best-fit case assuming the internal layer warping is caused primarily by non-linear ice flow. $M = 3$, $G_n = 0.06$, $G_s = -0.01$. (a) Modeled layers in gray and observed layers in black. (b) Model and data discrepancy plotted according to the grayscale to show the spatial pattern of the mismatch.

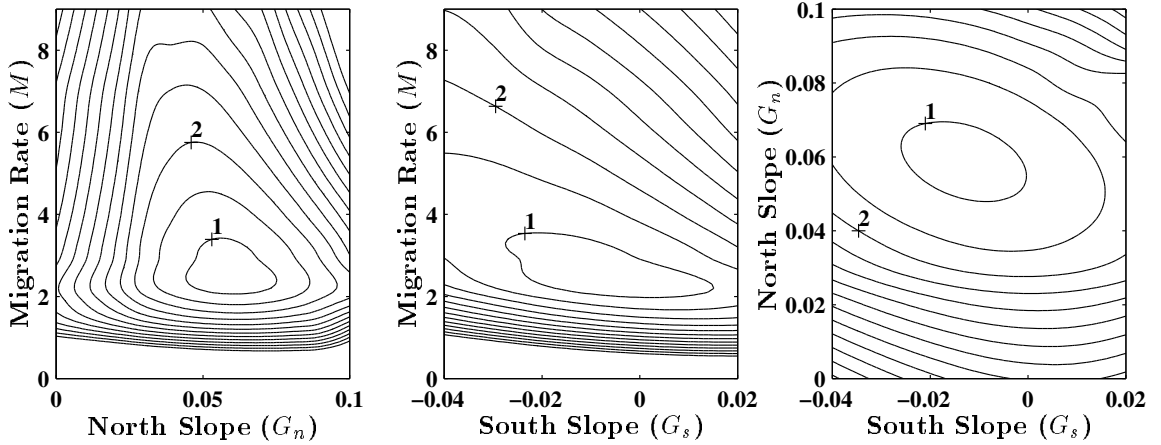


Figure 4.7: Mismatch index J as a function of each model parameter for Case 1: non-linear ice flow law. Each panel is a cross-section of J taken through the minimum at model parameter values $G_s = -0.01$, $G_n = 0.06$, and $M = 3$, respectively. Contour lines for J are shown in intervals of 0.5.

the smallest J for Case 1 where the divide bump is caused by a non-linear ice flow law. The small area of larger residuals likely indicates that the simple hinge-like spatial pattern of accumulation allowed in the Case 1 model is not sufficiently flexible to allow an exact match between model and observations. The real accumulation pattern is probably more complex.

Figure 4.7 shows how the mismatch parameter J depends on the three model parameters G_s , G_n and M . The models with parameters within the $J < 1$ contour fit the data to within the expected errors. Given this threshold, the inferred scaled migration rate $M = 2.0 - 3.5$ corresponds to a divide migration rate $m = 0.2 - 0.5 \text{ m a}^{-1}$ northward toward Ice Stream D when we take $b(0) = 0.10 - 0.15 \text{ m a}^{-1}$. This is 3 to 7 times faster than the migration rate inferred from the angle of the apex axis and a hypothetical depth-age scale. The inferred migration rate is relatively insensitive to the accumulation gradient south of the divide G_s (Fig. 4.7). Northward divide migration (toward Ice Stream D) smears out layer shapes to the south, leaving a “wake” of relatively flat

layers and obscuring information about accumulation patterns there (*Waddington et al., in prep.*). Therefore, G_s is not well-constrained and ranges from about -0.03 to 0.02 . The minimization indicates a relatively strong positive accumulation gradient north of the divide with $G_n = 0.05 - 0.07$.

For Case 2 where the divide bump is caused by a local accumulation low, we choose $G_n^* = 0.06$ and $G_s^* = 0$ in equation (4.12) as derived in Case 1. We also choose $p = 4$ in equation (4.15) to reflect 2 additional degrees of freedom because we allow a more complicated accumulation pattern and use results from Case 1 in equation (4.12). Figure 4.8 shows a comparison between the observed layers and the predicted layers for the combination of A , λ , and M which give the minimum J . Figure 4.9 shows the shape of J . Overall, the accumulation low model produces a slightly better fit ($J \ll 1$) to the observations than the non-linear flow law model, probably because of the curvature allowed in the prescribed accumulation pattern. However, this slightly improved fit is beneath the level of expected errors and does not imply that Case 2 is more plausible than Case 1. The predicted migration rate is slower than Case 1, with M ranging from $0.5 - 2.0$ at the $J < 1$ level. The predicted migration rate M is largely independent of the amplitude A or the wavelength λ of the accumulation pattern. The predicted amplitude A of the accumulation low ranges from 2 to 6 percent of $b(0)$. The predicted wavelength λ of the accumulation feature varies between 2.5 and 6.5 ice thicknesses ($2.5 - 6.5$ km), increasing with amplitude A . This range of λ is expected since the warped feature observed in the layer shapes spans about 2 – 4 ice thicknesses, suggesting $\lambda \approx 4 - 8$. The accumulation patterns predicted by this model are reasonable possibilities near the divide.

The lower predicted migration rates for Case 2 (accumulation low) arise from the fact that a combination of A and λ alone can be found to produce a sufficient match to the general shape of the observed layers with no divide migration. Only a slight

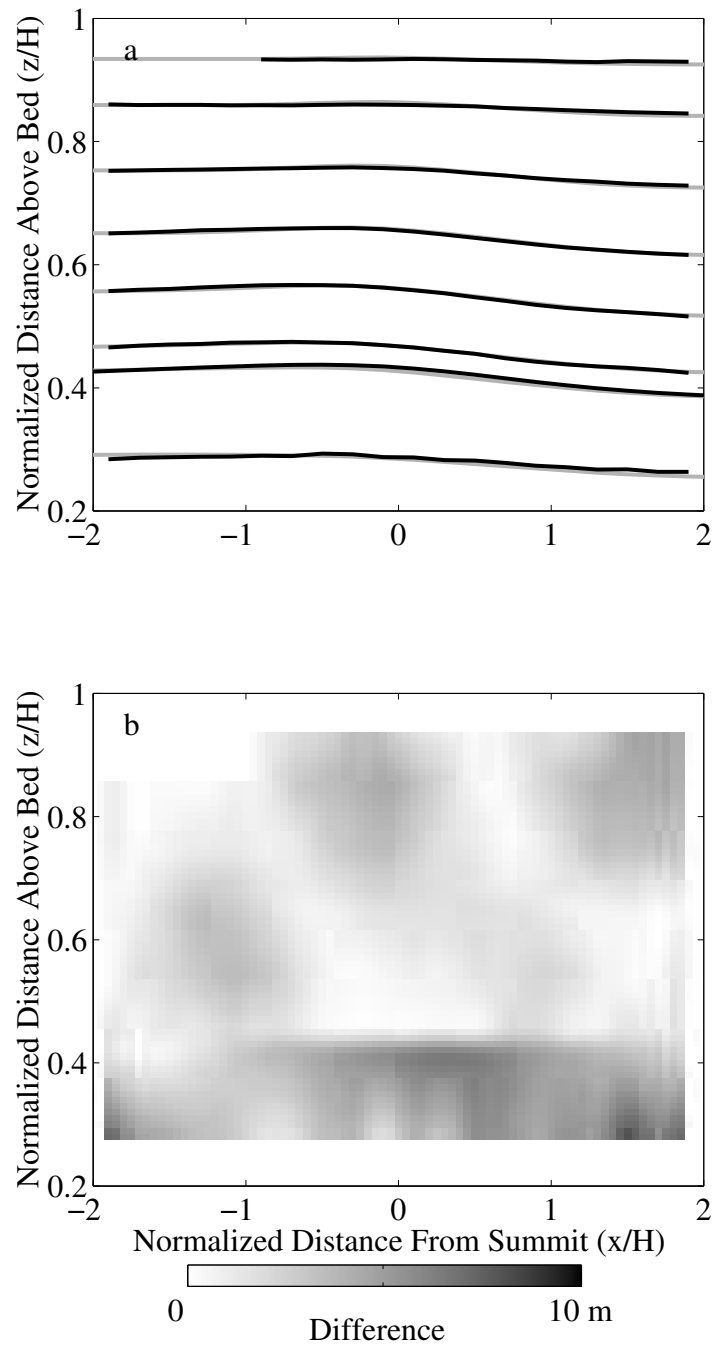


Figure 4.8: Best-fit case assuming the internal layer warping is caused by a local low in accumulation over the divide. $M = 1$, $A = 0.04$, $\lambda = 3$. (a) Modeled layers in gray and observed layers in black. (b) Model and data discrepancy plotted according to the grayscale to show the spatial pattern of the mismatch.

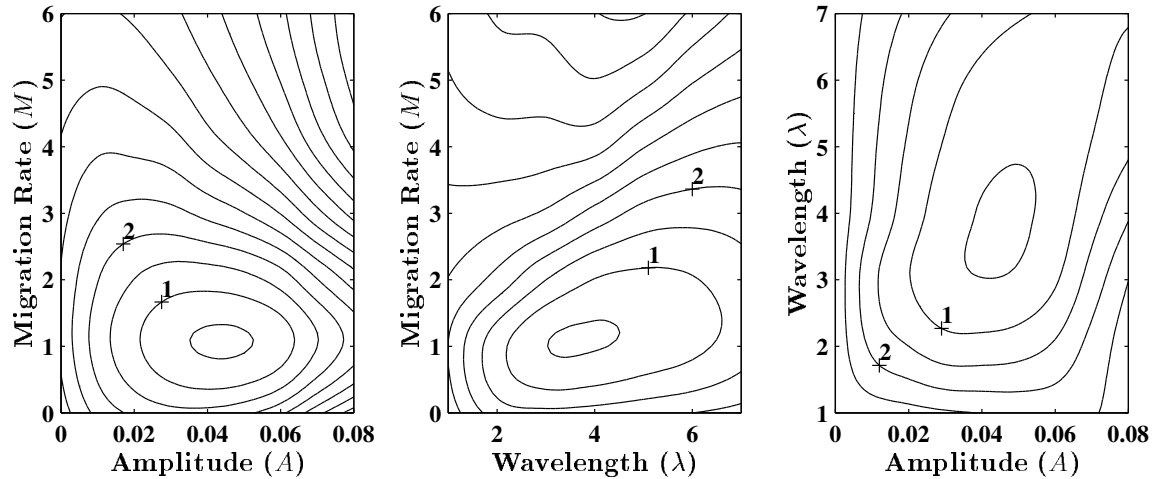


Figure 4.9: Mismatch index J as a function of each model parameter for Case 2: local accumulation low. Each panel shows a cross-section of J taken through the minimum at parameter values $\lambda = 3$, $A = 0.04$, and $M = 1$, respectively. Contour lines for J are shown at intervals of 0.5.

shift of the flow field (small migration rate) is required to bring the modeled layers into agreement with observations. For Case 1 (non-linear flow), the deformation field which produces the divide bumps is largely fixed by our assumptions about ice dynamics, and a more significant migration of the flow field is required to produce agreement between the model and the data.

4.7 Discussion

It is possible that the real situation at the divide is best described by a combination of a special flow regime associated with non-linear flow and a complex accumulation pattern. Assuming that Case 1 and Case 2 are equally likely, and using the $J < 1$ mismatch level as a reasonable threshold, we estimate that the Siple Dome divide is migrating northward toward Ice Stream D at about $0.05 - 0.50 \text{ m a}^{-1}$, corresponding to $M = 0.5 - 3.5$ and $b(0) = 0.10 - 0.15 \text{ m a}^{-1}$. If we have over- (under-) estimated

the errors, then the predicted range would be smaller (larger). The simple estimation of the migration rate from the angle of the layer apex axis and a presumed depth-age scale produces a value in the low end of this range at about 0.07 m a^{-1} . The predicted rate is only slightly sensitive to the presumed mechanism which produces the internal layer warping beneath the divide. The non-linear divide flow mechanism predicts higher migration rates than the accumulation minimum mechanism. However, this analysis does not distinguish which mechanism is operating at Siple Dome or reveal any information about the ice flow law. Resolution of these questions will require information from ice cores and measurements of the depth variation of strain.

A large south-north accumulation gradient of $(5-10) \times 10^{-6} \text{ a}^{-1}$ is a robust feature of our analysis in the 2-4 km zone north of the divide. This result is independent of the migration rate and is consistent with both mechanisms of bump formation considered here. The predicted accumulation gradient would be artificially high if the divide zone calculated using the FEM is too wide (giving low vertical velocities over a large zone). However, the accumulation pattern predicted for Case 2 (no divide zone from non-linear flow law) does not require a smaller gradient. Therefore, the large predicted accumulation gradient near the divide is a requirement of the data, not an artifact of the calculation. Measurements from shallow cores and snow pits in the vicinity of the Siple Dome summit indicate a regional-scale south-north accumulation gradient over the divide which is 10 – 30% of our prediction (*K. Kreutz, pers. comm., K. Taylor, pers. comm.*). We expect that the strong accumulation gradient predicted here is a divide-local effect and must decrease with distance from the divide. The available field sampling is too sparse to detect the localized pattern suggested by this analysis.

We do not allow for time variation of the migration rate. If past changes in migration rate or accumulation pattern have occurred, then the discrepancy between

the model and the data would be depth-dependent. A model which fits the shallower (younger) layers would not fit deeper (older) layers. Such a pattern is not clearly evident in Figures 4.6 and 4.8, suggesting that either the migration rate and accumulation pattern have been relatively constant in time, or that isochrone shapes are not sensitive to past changes that have occurred.

The insensitivity of isochrone shapes to past flow changes arises because isochrone deformation is an integrated effect. Their shapes lose evidence of old flow regimes over time. It is therefore difficult to determine how long the divide has been migrating. We assume that it has been migrating for $t \gg H/b$ (10^4 a). However, the actual onset of migration may be relatively recent and the layer shapes no longer contain onset information. It is not correct to use the age of the oldest (deepest) detectable isochrone with a displaced apex as the age of divide migration onset because the moving flow field affects the deformation history of all isochrones, regardless of their age. However, a deep layer can be used to place an upper bound on the date of migration onset. If the divide had been in one location for a long time and then started to migrate, we would expect to see remnant warping at the old divide position in the deeper layers where the warping is expected to be most pronounced. It would take $\sim 10^4$ a for the changing flow field associated with divide migration to smear out well-developed warped layers (*Waddington et al., in prep.*). Suppose the divide was once at the present apex of the deepest detected layer, about 700 meters south of the divide. Then the divide has been migrating toward Ice Stream D for at least $700/M$ years, or about 1.5 to 15 ka.

Migration of the ice divide suggests that non-steady processes are affecting the geometry of Siple Dome. Candidates include changes in the elevation or position of the bounding ice streams, or a change in the spatial accumulation pattern. *Nereson et al.* (1998a) (*Chapter 5*) have explored these possibilities and concluded that relatively

small changes in either candidate could produce the rate of observed divide motion. A further consequence of the Siple Dome divide migration and the associated effects on isochrone shapes is that pre-Holocene ice is thickest about 0.5 km south of the present ice divide. This information has been used to select the exact site for a deep ice core to be obtained for paleo-climate analysis.

The migration rate is sufficiently slow that the near-divide warping is maintained in the internal layer pattern. This indicates that the divide has been within a few ice thicknesses of its present position for the past $10^3 - 10^4$ years, and suggests that there have been no major asynchronous changes in the configuration of the bounding ice streams or in the geometry of Siple Dome in that time. Significant asymmetric forcing at the boundaries of Siple Dome would cause rapid motion of the divide (*Hindmarsh, 1996a*) and prevent the development of a near-divide isochrone bump.

Since the development of a divide bump takes time, its presence at Siple Dome raises the question about the age of Siple Dome itself. There are two distinct hypotheses. The first is that Siple Dome has existed in about its present state for the past 10^4 or more years. This suggests that Siple Dome has been a flow center for most of the Holocene and supports the theory that ice streams were present during the early stages of retreat of the Ross Ice Shelf (*Denton et al., 1989*). The second hypothesis is that Siple Dome formed more recently as a result of ice stream initiation and thinning of the WAIS.

The analysis presented here assumes the first hypothesis, constant ice thickness. Given this assumption and a time-averaged accumulation rate of 0.10 m a^{-1} ice equivalent, the time-scale to create a well-developed warp in the internal layers by either an accumulation low or by ice dynamic processes is related to the thickness/accumulation rate time-scale (inverse of the characteristic vertical strain rate), about 10^4 years. Without considering the smearing effects of divide migration, it would take at least

5 ka to deform isochrones to the extent we observe at Siple Dome. The first hypothesis is thus consistent with the data.

We cannot eliminate the second hypothesis, however. Possible rapid thinning of WAIS and the formation of Siple Dome would be associated with large vertical strain rates which increase the speed of ice deformation and reduce the time required to create internal layer warping under the divide. If Siple Dome formed by rapid synchronous thinning at its boundaries as a result of ice stream initiation, then it is possible to form isochrone bumps under the divide at all depths in as little as 10^3 years. For example, suppose Siple Dome was once twice as thick as present and thinned to its present thickness in about 10^3 years. Assuming no change in accumulation rate, the vertical strain rate during thinning would be roughly 10^{-3} a^{-1} which is about one order of magnitude larger than the vertical strain rate for the steady state case. The time to form a divide bump, which is related to the vertical strain rate, would correspondingly be reduced by about a factor of 10. Measurements of age versus depth and total gas content from the deep ice core will help resolve this question. If Siple Dome has thinned rapidly in the recent past, then the thickness of layers deposited during and prior to thinning would be smaller (due to larger vertical strain rates). Thus, these layers would appear in the present ice sheet at shallower depths than if no thinning occurred. Accumulation rate estimates from layer thickness profiles which assume no dome thinning would be artificially low.

Chapter 5

SENSITIVITY OF THE DIVIDE POSITION AT SIPLE DOME, WEST ANTARCTICA TO BOUNDARY FORCING

This chapter was developed in collaboration with R. Hindmarsh at the British Antarctic Survey, Cambridge, UK under an EISMINT exchange grant in May 1997. It was published in the *Annals of Glaciology*, volume 27 with co-authors R. C. A. Hindmarsh (British Antarctic Survey) and C. F. Raymond (University of Washington). Helpful review comments were given by D. Dahl-Jensen and R. Alley.

5.1 Summary

A linearized perturbation about a 2-D Vialov-Nye ice sheet profile is used to investigate the sensitivity of the divide position at Siple Dome, West Antarctica to small changes in the accumulation pattern and in the elevation of its lateral boundaries at the margins of Ice Streams C and D. Relaxation time-scales for the ice sheet surface and divide position are derived from the perturbation theory. For Siple Dome, these time-scales are short: 450-800 years for surface adjustment and 200-350 years for divide position adjustment. These short time-scales indicate that Siple Dome responds quickly to forcing at its boundaries. Therefore, the recent migration of the Siple Dome divide (*Chapter 4*; *Nereson et al.*, 1998b) is probably a response to an on-going, sustained forcing rather than a response to a long-past climate event such as the transition from the Last Glacial Maximum (LGM) to the Holocene.

Based on our analysis, the inferred rate of migration of the Siple Dome divide could be attained by: (1) a steady increase in the south-north spatial accumulation gradient of $(0.1 - 1.5) \times 10^{-9} \text{ a}^{-2}$, or (2) a steady increase (decrease) in elevation of

Table 5.1: Notation

| Variable | Meaning |
|--------------------|--|
| $a(x, t)$ | accumulation rate |
| $b(x)$ | bed topography |
| g | gravitational acceleration |
| $h(x, t)$ | ice thickness |
| k | boundary elevation rate |
| n | power in Glen's flow law |
| $q(x, t)$ | ice flux |
| $s(x, t)$ | ice surface elevation |
| t | time |
| $u(x, z)$ | horizontal ice velocity |
| x | distance along flow |
| z | distance above bed |
| \bar{A} | depth-averaged flow parameter |
| \mathbf{E} | matrix of eigenfunctions |
| \mathbf{G} | Green's function matrix for accumulation perturbations |
| $H(x)$ | eigenfunction/spatial component of h_1 |
| \mathbf{M} | discretized version of Θ |
| $Q(x)$ | spatial component of q_1 |
| \mathcal{R} | divide migration rate |
| $T(t)$ | temporal component of h_1, a_1, q_1 |
| X_d | divide position |
| $\alpha(x)$ | spatial component of a_1 |
| β | scaled accumulation gradient |
| γ | $(a_R/a_L)^{(1/(n+1))}$ |
| λ | eigenvalue |
| ρ | ice density |
| $\sigma(x, z)$ | shear stress |
| τ | time constant |
| ϕ | rate of change in scaled accumulation gradient β |
| Θ | linear perturbation operator |
| $\mathbf{\Lambda}$ | diagonal matrix of eigenvalues |
| Sup/Subscript | Meaning |
| * | initial condition |
| \sim | reference value |
| 0 | zeroth order (steady-state) |
| 1 | perturbation |
| d | divide position |
| v | volumetric |
| H | Hindmarsh |
| L | left |
| R | right |
| W | Weertman |

the Siple Dome lateral boundary adjacent to a relict margin of Ice Stream D (adjacent to Ice Stream C) of $0.005 - 0.040 \text{ m a}^{-1}$ over the past several thousand years. The required forcing is quite small, and suggests that major changes in the configuration of Ice Streams C and D associated with major changes in the elevation at boundaries of Siple Dome have not occurred over the past several thousand years.

5.2 Introduction

The motion of ice divides can be caused by changing conditions at ice sheet boundaries. A record of ice divide position may be a delayed and smoothed representation of boundary forcing. If the relationship between divide motion and boundary forcing can be established, then one could infer boundary forcing from a record of divide position, or predict divide position for a given boundary forcing. Ice divides are also theoretically associated with a narrow zone of anomalous ice flow which causes isochrones to be warped convex-up beneath steady divides (*Raymond, 1983; Hvidberg, 1996*). Small variations in divide position compared with the ice sheet span may cause perturbations to the flow field and complicate the interpretation of ice cores obtained at ice divides. The sensitivity of divide position to boundary forcing is therefore relevant to possible identification of forcing mechanisms occurring at ice sheet boundaries and to interpretation of ice cores obtained at ice divides.

Weertman (1973) investigated the effect of simple changes in ice sheet span and accumulation rate on divide position with the finding that steady-state divide position is most sensitive to changes in ice sheet span and less sensitive to the spatial pattern of accumulation. *Hindmarsh (1996a)* characterized the sensitivity of divide position to stochastic asymmetric accumulation forcing and found that the relaxation time-scale of divide position to such forcing is about $1/16$ times the fundamental thickness/accumulation rate (h/a) time-scale. *Anandakrishnan et al. (1994)* used in-

verse techniques to estimate that the Greenland ice divide may have shifted by about 40 km and thinned by 50 m over the last glacial cycle from changes in margin position and accumulation rate. *Cuffey and Clow (1997)* estimated the effect of margin expansion and retreat on the divide elevation in central Greenland over a glacial cycle, with a diffusive relaxation time of about 1900 years, about 1/5 of the fundamental h/a time-scale.

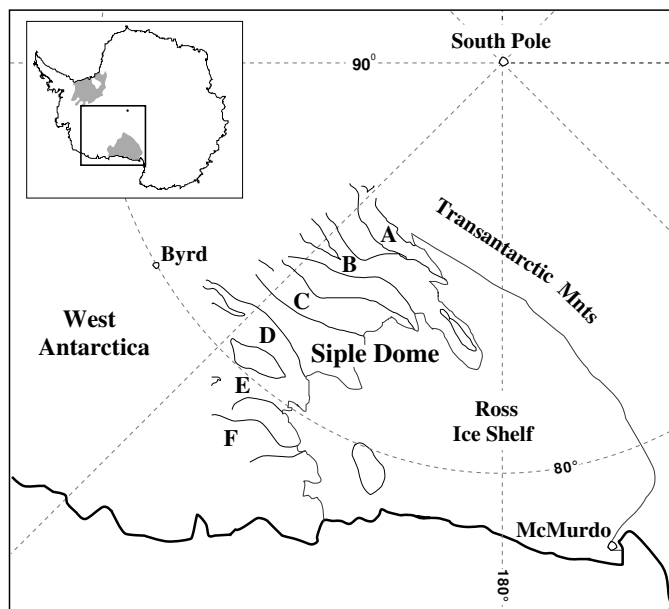


Figure 5.1: Map of West Antarctic Siple Coast ice streams showing Siple Dome and Ice Streams C and D.

In this paper, we determine the sensitivity of divide position of Siple Dome, the ice ridge between Ice Streams C and D in West Antarctica, to more subtle forcing at its boundaries (Figure 1). A deep ice core is being obtained near the present summit for paleo-climate analysis. Recent migration of the Siple Dome divide northward toward Ice Stream D at a rate of $0.05 - 0.50 \text{ m a}^{-1}$ over the past several thousand years has been inferred from analysis of the pattern of internal layers near the divide which

have been detected with an ice-penetrating radar (*Chapter 4; Nereson and Raymond, 1997; Nereson et al., 1998b*). We identify probable causes of this subtle divide motion by quantifying the effects of small changes in accumulation pattern and small changes in the elevation of the lateral boundaries of Siple Dome (an indicator of ice stream activity around Siple Dome) on the divide position.

5.3 The Linearized Ice Sheet Equation

We consider a linearized perturbation about a 2-D Vialov-Nye ice sheet solution. Standard ice flow models do not generally contain the scale of resolution required to simulate small changes in divide position ($< O(h)$). A linearized perturbation allows simulation of small-scale divide motion as it permits explicit tracking of divide position.

Mathematical development of the linearized ice sheet evolution equation is given in *Nye (1959a)* and *Hutter (1983)*. The main points are summarized here. The time-dependent evolution equation for a 2-D ice sheet is

$$\partial_t h = -\partial_x q + a, \quad (5.1)$$

where $h(x, t)$ is the ice sheet thickness, $q(x, t)$ is the ice flux, $a(x, t)$ is the mass balance, x is the distance along flow. For an ice sheet deforming in laminar flow with shear stress

$$\sigma_{xz} = -\rho g(s - z)\partial_x s, \quad (5.2)$$

and flow relation

$$\frac{1}{2}\partial_z u = A\sigma_{xz}^n, \quad (5.3)$$

we obtain an expression for the ice flux q ,

$$q = \frac{2(\rho g)^n}{m} \bar{A} h^m |\partial_x s|^{n-1} \partial_x s, \quad (5.4)$$

where $s(x, t)$ is the surface profile, obtained by the sum of the ice thickness $h(x, t)$ and bed elevation $b(x)$, z is the distance above the bed, ice density $\rho = 917 \text{ kg m}^{-3}$, gravitational acceleration $g = 9.8 \text{ m s}^{-2}$, depth-averaged flow law parameter \bar{A} is prescribed, $n = 3$, and $m = n + 2$. Substituting

$$C = \frac{2(\rho g)^n}{m} \bar{A} \quad (5.5)$$

yields the ‘Vialov-Nye’ or ‘VN’ ice sheet evolution equation,

$$\partial_t h = \partial_x (C h^m |\partial_x s|^{n-1} \partial_x s) + a. \quad (5.6)$$

The standard steady-state Vialov profile is obtained when $\partial_t h = 0$ and $a = a_0$ is a constant (*Vialov, 1958*).

We are interested in the effect of small perturbations in thickness h and accumulation a on the ice sheet geometry. We expand h and a such that

$$\begin{aligned} h(x, t) &= h_0(x, t) + h_1(x, t), \\ a(x, t) &= a_0(x, t) + a_1(x, t), \end{aligned} \quad (5.7)$$

where $h_1/h_0 \ll 1$. Substitution into equation (5.4) yields a corresponding flux expansion,

$$q(x, t) = q_0(x, t) + q_1(x, t). \quad (5.8)$$

The zeroth order state is defined to be steady state such that

$$\begin{aligned} \partial_t h_0 &= 0, \\ \partial_x q_0 &= a_0. \end{aligned} \quad (5.9)$$

Substituting equations (5.7), (5.8), and (5.9) into (5.6) and keeping only first order terms yields the linearized perturbation equation which we solve to determine the ice sheet response to small perturbations:

$$\partial_t h_1 = -\partial_x q_1 + a_1, \quad (5.10)$$

$$q_1 = q_0 \left(m \frac{h_1}{h_0} + n \frac{\partial_x h_1}{\partial_x s_0} \right), \quad (5.11)$$

where $s_0 = h_0 + b$. When $m = 0$ and $n = 1$ the standard linear diffusion equation is obtained (e.g., *Boyce and DiPrima*, 1986) and we expect diffusive type behavior when $m = 5$ and $n = 3$ (*Nye*, 1959a). It is convenient for developments in later sections to write equations (5.10) and (5.11) in operator form as

$$\partial_t h_1 = \Theta(h_1) + a_1 \quad (5.12)$$

where

$$\Theta(\bullet) \equiv -\partial_x \left\{ q_0 \left(m \frac{\bullet}{h_0} + n \frac{\partial_x \bullet}{\partial_x s_0} \right) \right\}. \quad (5.13)$$

5.4 Calculation of Normal Modes

Since equation (5.10) (or (5.12)) is a linear differential equation, its general solution can be expressed as a superposition of solutions to the homogeneous equation,

$$\partial_t h_1 = \Theta(h_1), \quad (5.14)$$

where $h_1 = 0$ at the lateral boundaries of the domain (*Boyce and DiPrima*, 1986). Following (*Hindmarsh*, 1996a,b, 1997a,b) we assume a separable solution,

$$h_1(x, t) = H(x)T(t). \quad (5.15)$$

Because the problem is linear, we may also write:

$$a_1(x, t) = \alpha(x)T(t) \quad (5.16)$$

$$q_1(x, t) = Q(x)T(t). \quad (5.17)$$

Substituting equations (5.15) and (5.17) into the homogeneous equation (5.14) allows us to separate the time-dependent and the space-dependent equations by use of a separation constant, or eigenvalue λ :

$$\lambda = \frac{\dot{T}}{T} = \frac{-\partial_x Q}{H}, \quad (5.18)$$

where

$$Q(x) = q_0 \left(m \frac{H}{h_0} + n \frac{\partial_x H}{\partial_x s_0} \right). \quad (5.19)$$

The solution for the time-dependent component of equation (5.18) is $T = T^* \exp(\lambda t)$, where T^* is an initial condition. The eigenvalue λ represents an inverse relaxation time-constant for the spatial solution $H(x)$, provided $\lambda < 0$.

The solution $H(x)$ is a spatial response function, or eigenfunction, associated with the time-constant given by λ . These spatial solutions are the *normal modes* of the ice sheet and are found by solving the spatial component (right hand side) of equation (5.18),

$$-\partial_x \left\{ q_0 \left(m \frac{H}{h_0} + n \frac{\partial_x H}{\partial_x s_0} \right) \right\} - \lambda H = 0. \quad (5.20)$$

Following Hindmarsh (1996b, in press) we discretize equation (5.20) according to the method of finite differences and solve the resulting algebraic eigenvalue problem written in matrix form as:

$$\mathbf{M}\mathbf{H} - \mathbf{\Lambda}\mathbf{H} = \mathbf{0}, \quad (5.21)$$

where $\mathbf{\Lambda}$ is a diagonal matrix of eigenvalues λ_i , \mathbf{M} is the discretized version of the operator Θ and \mathbf{H} is a vector of perturbations sampled at N discrete points in x . Specifically, \mathbf{M} is a tridiagonal matrix whose values are found by evaluating the discretized version of the operator Θ at $N - 2$ points in x . The solution is found by finding the eigenfunctions and eigenvalues of \mathbf{M} . We construct a matrix \mathbf{E} whose i -th column is the eigenfunction $H_i(x)$ corresponding to λ_i , and a vector $\mathbf{T} = \mathbf{T}^* \exp(\mathbf{\Lambda}t)$, where \mathbf{T}^* is an initial condition. The general solution to the perturbation equation (5.12) can be written in matrix form as a linear combination of the temporal and spatial solutions to the homogeneous equation (5.14):

$$\mathbf{h}_1(x, t) = \sum_i^N H_i(x) T_i(t) = \mathbf{E}\mathbf{T}. \quad (5.22)$$

5.5 Estimating Divide Motion

We are particularly interested in how the position of the ice divide is affected by perturbations. Following Hindmarsh (1996a), the evolution of divide position, where $\partial_x s(x = X_d) = 0$ can be written as

$$D_t \partial_x s(X_d) = \partial_t \partial_x s + \mathcal{R} \partial_x \partial_x s = 0, \quad (5.23)$$

where \mathcal{R} is the divide migration rate. In an increment of time, δt , the divide motion is then

$$X_d = \delta t \mathcal{R} = -\frac{\partial_x s}{\partial_x^2 s} \simeq -\frac{\partial_x s_1}{\partial_x^2 s_0}. \quad (5.24)$$

This relation implies that divides with high curvature are less sensitive to a given perturbation s_1 .

Equation (5.24) is technically invalid because it ignores the fact that the divide curvature $\partial_x^2 s_0$ is singular for VN ice sheet profiles. In general, accurate calculation of flow near the divide requires special mathematical treatment because the standard (VN) ice flow model is invalid there. While the separate solutions to symmetric and antisymmetric perturbations have been calculated while fully accounting for the divide singularity for the VN ice sheet solution (e.g., Hindmarsh 1997), the general problem has not been solved. We ignore the effect of the divide singularity and estimate divide curvature from a Taylor expansion of a discretized ice sheet. This approximation results in a small error in the estimation of divide position.

We quantify this error by comparing our solution to an analytic solution for a special case. Weertman (1974) considered the effect of a step change in accumulation rate on both right and left sides of an initially symmetric VN ice sheet profile, and determined that the total divide motion is

$$X_d^W = \frac{1}{2} \frac{\gamma - 1}{\gamma + 1}, \quad (5.25)$$

where $\gamma = (a_R/a_L)^{1/(n+1)}$ and a_R and a_L are spatially constant accumulation rates for the right and left sides of the ice sheet, respectively. Hindmarsh (1997) showed that the linearized solution for divide movement caused by imposing a step increase in a_R is

$$X_d^H = \frac{1}{n+1} \frac{\gamma}{(\gamma+1)^2} \frac{\Delta a_R}{a_R}. \quad (5.26)$$

A comparison between the analytic solutions X_d^W , X_d^H and the solution X_d given by equation (5.24) for a given Δa_R and for a range of discretization intervals dx shows that all results agree to within 10%. This error is smaller than errors due to uncertain accumulation rate and flow properties (leading to errors in q_0), and is acceptable since the flow divide and topographic divide do not exactly correspond for real ice sheets (Raymond, 1983). The exact solution of the problem that respects the divide singularity would probably not increase the accuracy of the physical solution.

5.6 Normal Modes of Siple Dome

Field measurements made in 1994 and 1996 show that Siple Dome is essentially a 2-dimensional ridge about 1000 m thick and 100 km wide overlying relatively flat bedrock (Raymond *et al.*, 1995). We are therefore justified, to first order, in applying this 2-d linearized perturbation model to Siple Dome. Figure 2 shows the zeroth order geometry (h_0 and b) for two similar ice sheet profiles for which we calculate normal modes: a theoretical flat-bed VN ice sheet, and the actual Siple Dome (SDM) ice sheet from field measurements of surface and bed topography (Raymond *et al.*, 1995). These two geometries are used to illustrate the sensitivity of our results to variations in ice sheet shape. We choose $\bar{A} = 10^{-24} \text{ s}^{-1} \text{ Pa}^{-3}$ and $a_0 = 0.10 \text{ m a}^{-1}$ to calculate the VN ice sheet geometry from equation (5.6). The domain is truncated at ± 47 km from the summit with $x = 0$ at the divide, approximately corresponding to the full span of Siple Dome.

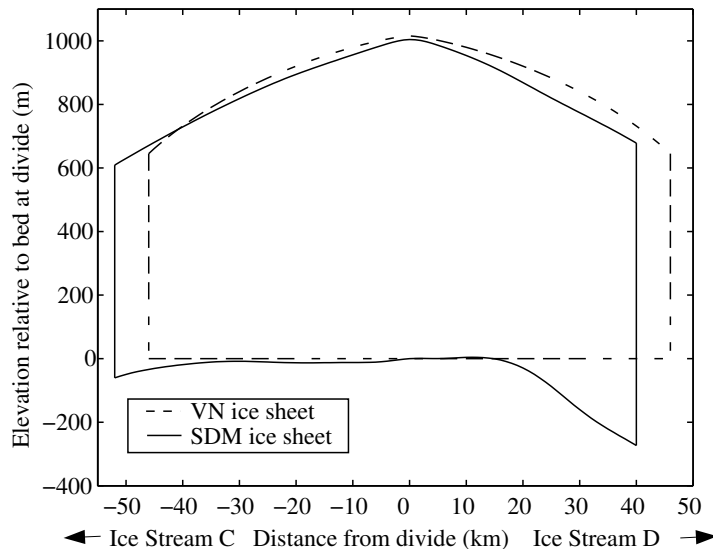


Figure 5.2: Ice sheet geometries used to calculate h_0 and s_0 in equation (5.11). The dashed profile corresponds to a symmetric Vialov-Nye profile with $\bar{A} = 10^{-24} \text{ s}^{-1} \text{ Pa}^{-3}$, $a_0 = 0.10 \text{ m a}^{-1}$ ice equivalent, and a half-width of 47 km. The solid profile corresponds to the Siple Dome profile determined from radar and GPS measurements (*Raymond et al.*, 1995)

We obtain the zeroth order flux q_0 directly by integrating the accumulation rate. This approach does not require explicit knowledge of the flow parameter \bar{A} , although \bar{A} can be deduced from the zeroth order accumulation rate and geometry. Measurements from snow pits and shallow cores show that the accumulation rate at the summit of Siple Dome is about $0.11\text{--}0.13 \text{ m a}^{-1}$ (ice equivalent) (*Mayewski et al.*, 1995), with a south-north accumulation gradient giving higher accumulation to the north (*K. Kreutz, pers. comm.; Chapter 6*). For convenience, a reference accumulation rate \tilde{a} is defined to be that at the divide: $\tilde{a} = a_0(0)$.

Figure 3 shows the slowest two ice sheet modes found by solving equation (5.21),

assuming constant accumulation rate for each ice sheet profile shown in Figure 2. The eigenfunction associated with the largest non-zero eigenvalue (labeled ‘Mode 1’ in Figure 3) is the first dynamic ice sheet mode and represents the slowest volumetric response of the ice sheet. Its time-scale (τ_v) is associated with the time it takes for the ice sheet to relax to a steady state after a perturbation. The second mode is the slowest mode representing divide position by virtue of its non-zero slope at the divide. Additional modes representing the ice sheet response at higher wave-numbers have faster response times ($< 10^2$ a) and are not shown in Figure 3. There are two “solutions” to equation (5.14) which correspond to the case where $Q = \text{constant}$ and have $\lambda = 0$ (see equation (5.20)). These “solutions” violate the boundary condition that $h_1 = 0$ at the lateral boundaries of the domain, and are therefore discarded as solutions which define the ice sheet modes. However, these functions will be valid solutions when we consider perturbations with non-zero values at the boundaries.

The relaxation time-scales associated with the slowest modes are shown in Table 2. The volumetric response time-scale τ_v is 450 – 800 years and the divide position response time-scale τ_d is twice as fast at 200 – 350 years. Both are much less than the fundamental h_0/a_0 time-scale ($\sim 10^4$ years). Increasing the accumulation rate shortens the fundamental time-scale and leads to a corresponding decrease in the mode relaxation time-scale. Because our domain is truncated with non-zero thickness at its boundaries, the volumetric relaxation time-scales are almost twice as fast as those found in Hindmarsh (1997). In our case, the divide-to-margin ice thickness is about half that for a full non-truncated ice sheet so that the time-scales are correspondingly scaled by about a factor of 2. The values in Table 2 are comparable to those calculated by *Cuffey and Clow* (1997). Using values appropriate for Siple Dome, they estimate τ_v at about 750 years. The fact that the VN ice sheet and the Siple Dome ice sheet have similar eigenvalues and eigenfunctions shows that the ice sheet response is relatively

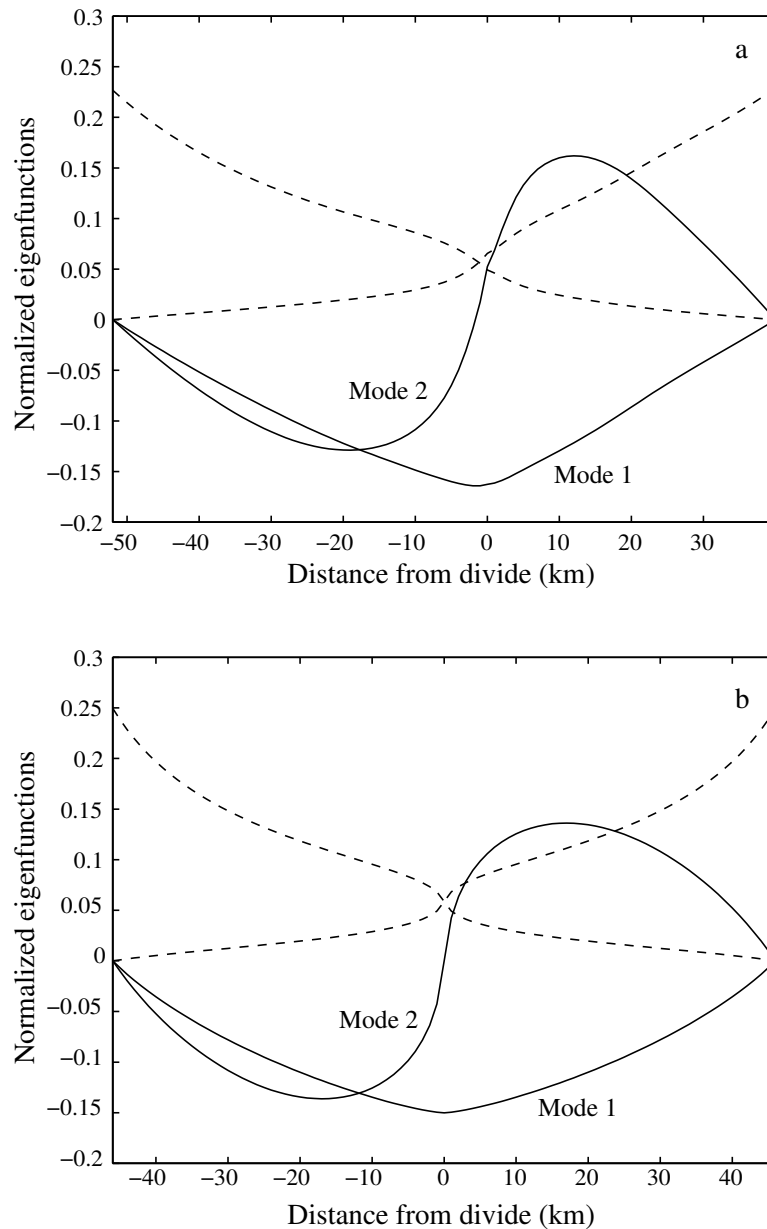


Figure 5.3: Slowest ice sheet normal modes from solution to equation (5.14) for (a) the Siple Dome (SDM) ice sheet geometry and (b) the Vialov-Nye (VN) ice sheet geometry shown in Figure 2. Accumulation rate, $a_0 = 0.10 \text{ m a}^{-1}$ ice equivalent is assumed constant in both cases. The volumetric response mode and divide position response modes are labeled “Mode 1” and “Mode 2,” respectively. Solutions with zero eigenvalue (no intrinsic dynamics), which permit external forcing of boundary elevation, are denoted by dashed curves. The similarity between the two ice sheets shows that the response modes are relatively insensitive to small variations in surface and bed topography.

insensitive to small variations in the zeroth order ice sheet shape or the presence of moderate bed topography.

These short time-scales indicate that Siple Dome responds quickly to boundary forcing. Information about changes in ice stream activity or in the spatial pattern of accumulation prior to a few thousand years ago is no longer contained in the geometry of Siple Dome. The time-scale associated with divide position is much shorter, indicating that the Siple Dome divide motion is not a response to a distant past event, such as the transition from the Last Glacial Maximum to the Holocene, nor a response to an abrupt event in the past few thousand years. The divide motion is more likely associated with an on-going, sustained forcing.

Table 5.2: Response time constants in years for slowest modes (volumetric response $\tau_v = -1/\lambda_1$ and divide position response $\tau_d = -1/\lambda_2$) for VN and SDM ice sheet profiles with various grid spacings and accumulation patterns $a_0(x)$ in m a^{-1} ice equivalent. For the last column, the spatial accumulation pattern is given by $\tilde{a}f(x)$ where $f(x) = 1.0 + 0.6 \arctan(x/40 \text{ km})$ and $\tilde{a} = a_0(0)$. Asterisks denote a range of time-constants corresponding to VN profiles calculated using $\bar{A} = 1.5 \times 10^{-24} \rightarrow 1.5 \times 10^{-25} \text{ s}^{-1} \text{ Pa}^{-3}$ and reflecting a range of average ice temperatures of -5 to -20 $^{\circ}\text{C}$ (Paterson, 1994).

| | grid size meters | VN | | SDM | | SDM, $a_0 = \tilde{a}f(x)$ | |
|----------|---------------------|--------------|--------------|--------------|--------------|----------------------------|--------------------|
| | | $a_0 = 0.10$ | $a_0 = 0.15$ | $a_0 = 0.10$ | $a_0 = 0.15$ | $\tilde{a} = 0.10$ | $\tilde{a} = 0.15$ |
| τ_v | 2000 | 731 | 513 | 706 | 471 | 782 | 522 |
| | 1000 | 732 | 513 | 706 | 471 | 783 | 522 |
| | 500 | 732 | 513 | 706 | 471 | 783 | 522 |
| | 1000 | 696-927* | 488-650* | | | | |
| τ_d | 2000 | 340 | 238 | 324 | 216 | 327 | 218 |
| | 1000 | 353 | 247 | 326 | 217 | 328 | 219 |
| | 500 | 362 | 254 | 326 | 217 | 328 | 219 |
| | 1000 | 334-446* | 235-313* | | | | |

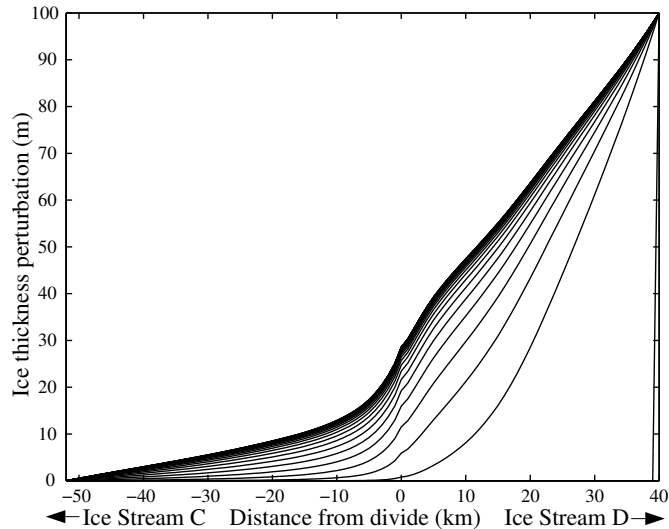


Figure 5.4: Evolution of thickness perturbation $h_1(x, t)$ for an instantaneous 100-meter increase in elevation of the margin of Siple Dome near Ice Stream D, plotted every 200 years.

5.7 Response to Boundary Elevation Perturbation

There is evidence that the ice streams bounding Siple Dome have recently changed their activity. The lower part of Ice Stream C essentially stopped stream flow about 130 years ago and is currently thickening at the accumulation rate (*Retzlaff and Bentley, 1993*). A linear feature on the north flank of Siple Dome near Ice Stream D is likely a former ice stream margin that ceased flow about 10^3 years ago (*Jacobel et al., 1996*). We expect that once stream flow ceases/begins, the ice streams may thicken/thin and change the elevation at the boundaries of Siple Dome. We consider 2 cases: (1) an increase in elevation at the ice sheet margin sufficiently fast that it can be represented as an instantaneous change, and (2) a steady increase in margin elevation at a constant rate.

The effect of perturbing the elevation of the ice sheet boundary is found by solving equation (5.12) as an initial value problem. For the first case, we specify as the initial condition a spike in elevation at the boundary ($h_1(x, 0) = h^*(x) = 0$ for all x except at the boundary). We hold the boundaries fixed at these initial values for $t > 0$. Since $\mathbf{h}_1 = \mathbf{E}\mathbf{T}$ by equation (5.22) the initial condition is

$$\mathbf{T}^* = \mathbf{E}^{-1}\mathbf{h}^*, \quad (5.27)$$

and the solution is

$$\mathbf{h}_1 = \mathbf{E}\mathbf{T} = \mathbf{E} \exp(\mathbf{\Lambda}t) \mathbf{E}^{-1}\mathbf{h}^*. \quad (5.28)$$

Figure 4 shows the ice sheet response for an instantaneous arbitrary increase in elevation of the Ice Stream D-side boundary by about 10% of the total ice thickness (100 m). The shape of the steady state ice sheet response corresponds to one of the eigenfunctions with zero eigenvalue (Fig. 3). This is expected since these eigenfunctions are the only ones which will not exponentially decay over time (all other $\lambda < 0$).

Figures 5a and 5b show the divide elevation and divide position response for a range of initial conditions. There is a divide response delay of 100–200 years when the effect of boundary perturbation is propagating up the ice sheet and has not yet affected the divide (*Alley and Whillans, 1984*). The characteristic time to reach steady-state for each case is similar to the volumetric and divide position relaxation time-scales shown in Table 2. The zeroth order, reference accumulation rate $\tilde{a} = a_0(0)$ affects only the response time-scales and thus the transient divide response. The final divide position and elevation are determined by the mode shapes which are independent of \tilde{a} and depend only on how h_0 and a_0 vary with x (e.g., compare curves A and B). Increasing the elevation of the Ice Stream D-side boundary by 10% of the scale thickness causes a 2-3% increase in divide ice thickness and migration of the divide

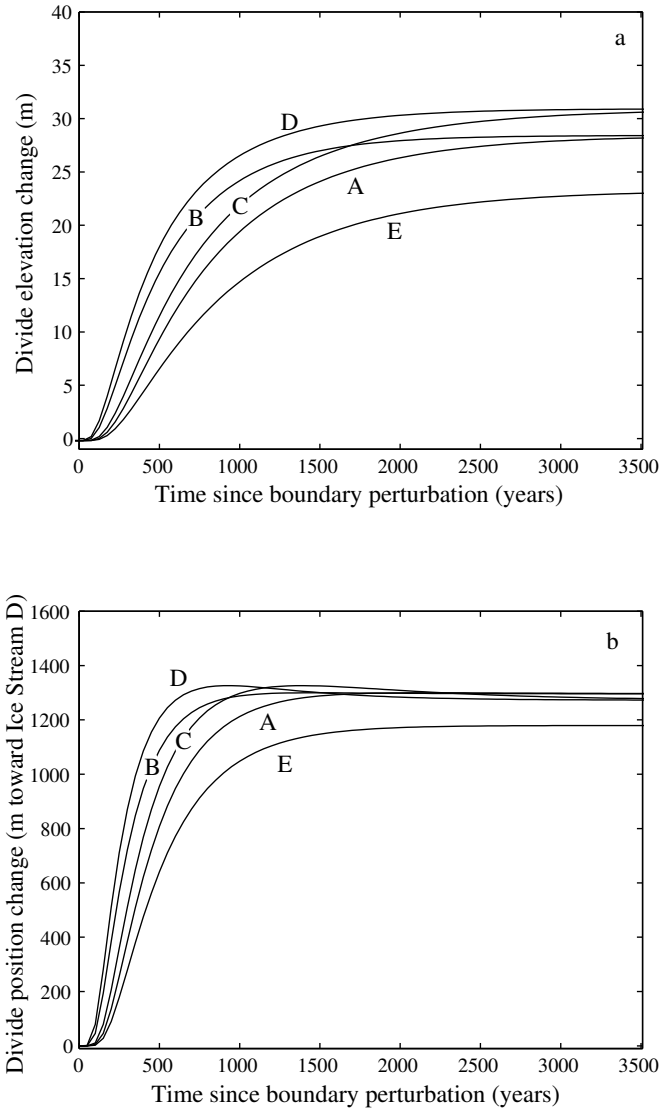


Figure 5.5: (a) Evolution of divide elevation for an instantaneous 100 m increase in elevation of the ice sheet boundary nearest Ice Stream D. The characteristic $(1 - 1/e)$ relaxation time for all cases is about 500-800 years. (b) Evolution of divide position with a relaxation time of about 200 to 350 years. (A) SDM geometry, $a_0(x) = 0.10 \text{ m a}^{-1}$; (B) SDM geometry, $a_0(x) = 0.15 \text{ m a}^{-1}$; (C) SDM geometry, $a_0(x) = 0.10(1 + \arctan(x/40 \text{ km})) \text{ m a}^{-1}$ (D) SDM geometry, $a_0(x) = 0.15(1 + \arctan(x/40 \text{ km})) \text{ m a}^{-1}$; (E) VN geometry, $a_0(x) = 0.10 \text{ m a}^{-1}$. There is a response delay of 100-200 years until the boundary perturbation affects the divide.

toward Ice Stream D by about 1% of the total span. Since the problem is linear, a 20% elevation change would predict a 4-6% change in ice thickness and a 2% divide shift. Because the ice sheet is largely symmetric, a similar *decrease* in elevation of the Ice Stream C boundary would also produce the divide shift shown in Figure 5b.

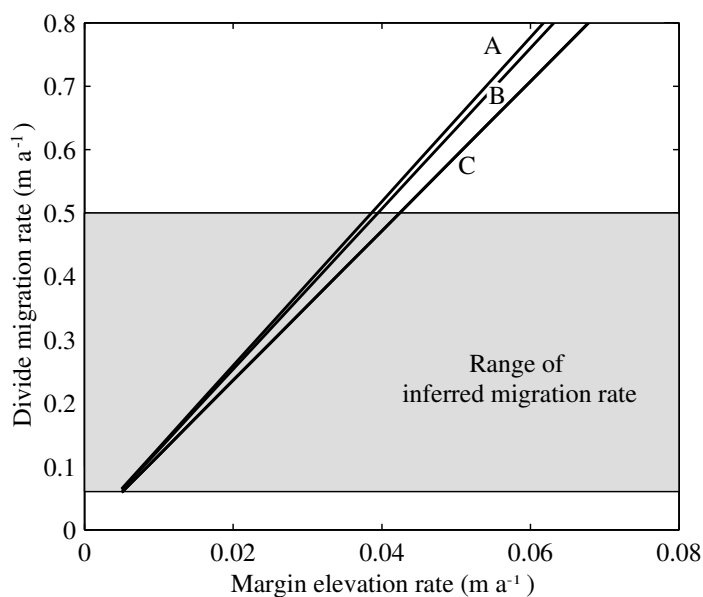


Figure 5.6: Steady-state divide migration rates for various rates of boundary elevation. The rate of Siple Dome divide migration inferred from the pattern of internal layering ($0.05 - 0.50 \text{ m a}^{-1}$) is bounded by solid horizontal lines. (A) SDM geometry, $a_0(x) = \tilde{a}$; (B) SDM geometry, $a_0(x) = \tilde{a}(1 + \arctan(x/40 \text{ km}))$; (C) VN geometry, $a_0(x) = \tilde{a}$. The divide migration rate depends only on how a_0 and h_0 vary with x , and is independent of the reference accumulation rate $\tilde{a} = a_0(0)$.

This analysis of an instantaneous change in boundary elevation helps determine divide response characteristics, but may not be physically reasonable. In reality, the boundaries of Siple Dome probably change their elevation over long time-scales. Moreover, we are particularly interested in what gradual boundary changes could

produce the constant rate of divide migration inferred for Siple Dome. Since the divide response delay time is 100-200 years, it is likely that the Siple Dome divide is just now beginning to experience the effects of any thickening associated with the shut down of Ice Stream C. Possible thickening associated with a shut down of the relict Ice Stream D margin would move the divide in the direction of the observed motion. Therefore, we wish to find the elevation rate k of the Ice Stream D-side boundary which produces the inferred Siple Dome divide migration rate. The solution is found by superposing solutions given by (5.28) which we write in matrix form as

$$\mathbf{h}_1 = \mathbf{E} \exp(\mathbf{\Lambda}t) \mathbf{E}^{-1} \mathbf{k}t. \quad (5.29)$$

Figure 6 shows the migration rate deduced by solving equation (5.29) for various elevation rates k and for various initial conditions. An elevation rate of 0.005 to 0.040 m a⁻¹ (ice equivalent) produces the inferred migration rate and corresponds to elevating the right boundary 10 to 80 m in the past 2000 years. This result is not unique, however. Boundary changes producing a similar *relative* difference in elevation of the two sides would also match the inferred divide motion. For example, it is possible that the boundary adjacent to Ice Stream C has decreased in elevation sometime in the past few thousand years, as a result of a past change in Ice Stream C flow.

5.8 Response to Accumulation Rate Perturbation

Divide migration can also be caused by a change in the accumulation pattern. The ice sheet response to such a perturbation is found by solving equation (5.12) which we write in matrix form as,

$$\partial_t \mathbf{h}_1 = \mathbf{M} \mathbf{h}_1 + \mathbf{a}_1. \quad (5.30)$$

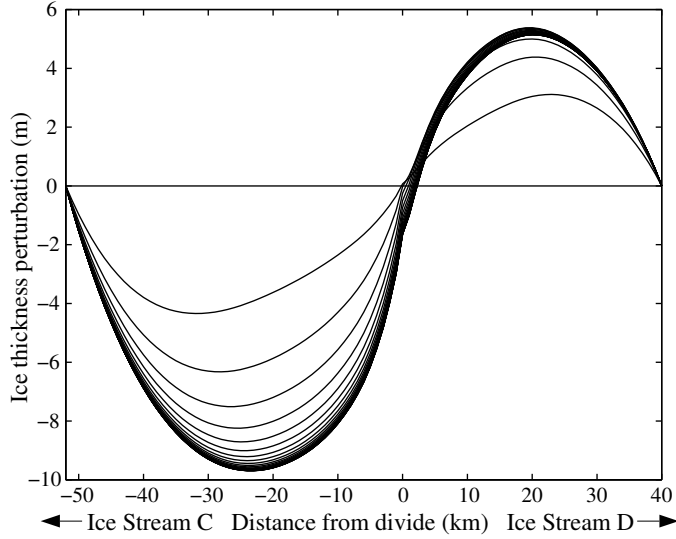


Figure 5.7: Evolution of SDM thickness perturbation $h_1(x, t)$ for an instantaneous change in the accumulation pattern $a_1(x) = 10^{-6}x$ plotted every 200 years.

After using equations (5.22) and (5.21) this becomes

$$\mathbf{E}\dot{\mathbf{T}} = \mathbf{E}\mathbf{\Lambda}\mathbf{T} + \mathbf{a}_1, \quad (5.31)$$

and reduces to

$$\dot{\mathbf{T}} = \mathbf{\Lambda}\mathbf{T} + \mathbf{E}^{-1}\mathbf{a}_1. \quad (5.32)$$

Since $\mathbf{T} = \mathbf{T}^* \exp \mathbf{\Lambda}t$ by equation (5.18), we solve for \mathbf{T}^* given \mathbf{a}_1 .

Again, we consider 2 cases: (1) the response of the ice sheet to an instantaneous accumulation rate perturbation, $a_1/\tilde{a} = \beta x$, and (2) the response to a constant increase in the spatial accumulation gradient, $a_1/\tilde{a} = \phi x t$, where

$$\phi = \frac{\partial_t(\partial_x a_1)}{\tilde{a}} = \partial_t \beta \quad (5.33)$$

is a prescribed constant. We fix the boundary elevations at their present values for both cases. The solution \mathbf{T} for each case is found using standard analytical techniques

for solving first-order ordinary differential equations. Upon using (5.22) the ice sheet response is:

$$\mathbf{h}_{1(\text{case1})} = \mathbf{E}(\exp(\mathbf{\Lambda}t) - \mathbf{I})\mathbf{\Lambda}^{-1}\mathbf{E}^{-1}\mathbf{x}\beta\tilde{a}, \quad (5.34)$$

$$\mathbf{h}_{1(\text{case2})} = \mathbf{E}(\exp(\mathbf{\Lambda}t) - \mathbf{I})\mathbf{\Lambda}^{-2}\mathbf{E}^{-1}\mathbf{x}\phi\tilde{a} - \mathbf{E}\mathbf{\Lambda}^{-1}\mathbf{E}^{-1}\mathbf{x}\phi\tilde{a}t, \quad (5.35)$$

for cases 1 and 2, respectively. The exponential terms in equations (5.34) and (5.35) represent the transient ice sheet response. At steady state ($t \rightarrow \infty$) these equations become

$$\mathbf{h}_{1(\text{case1})} = -\mathbf{E}\mathbf{\Lambda}^{-1}\mathbf{E}^{-1}\mathbf{x}\beta\tilde{a}, \quad (5.36)$$

$$\mathbf{h}_{1(\text{case2})} = -\mathbf{E}\mathbf{\Lambda}^{-2}\mathbf{E}^{-1}\mathbf{x}\phi\tilde{a} - \mathbf{E}\mathbf{\Lambda}^{-1}\mathbf{E}^{-1}\mathbf{x}\phi\tilde{a}t. \quad (5.37)$$

The quantity $\mathbf{G} = -\mathbf{E}\mathbf{\Lambda}^{-1}\mathbf{E}^{-1}$ is the Green's function for accumulation perturbations (*Hindmarsh, 1997a*).

Figure 7 shows the ice sheet response to an instantaneous change in accumulation, $a_1(x)/\tilde{a} = \beta x$, where $\beta = 10^{-5} \text{ m}^{-1}$. Figure 8 shows the divide position response for various initial conditions for the same fractional accumulation perturbation β . There is no divide response delay time in this case, and divide evolution begins immediately with relaxation time-scales consistent with those in Table 2. Unlike margin perturbations, accumulation perturbations excite in general all ice sheet modes which depend strongly on the characteristics of the zeroth order ice sheet configuration. The steady-state divide position is therefore more sensitive to the initial ice sheet geometry and the spatial pattern of accumulation, producing a 20% variation in Figure 8. However, like the case for margin elevation perturbations, the transient divide response is sensitive to \tilde{a} for a given β , but the steady state response is independent of \tilde{a} .

We are interested in what gradual changes in accumulation pattern would cause the rate of divide motion inferred for Siple Dome. Specifically, we consider a gradual

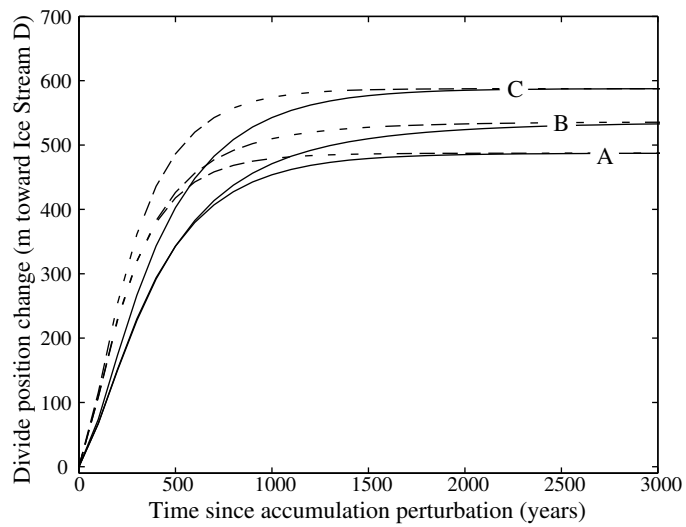


Figure 5.8: Evolution of divide position for an instantaneous accumulation perturbation $a_1(x) = \tilde{a} 10^{-5} x$. (A) SDM geometry, $a_0(x) = \tilde{a}$; (B) SDM geometry, $a_0(x) = \tilde{a}(1 + \arctan(x/40 \text{ km}))$; (C) VN geometry, $a_0(x) = \tilde{a}$. Solid and dashed curves correspond to $\tilde{a} = 0.10 \text{ m a}^{-1}$ and $\tilde{a} = 0.15 \text{ m a}^{-1}$ respectively. Relaxation time-scales are about 200 to 350 years. For a given geometry and spatial accumulation pattern, the steady state divide position is independent of \tilde{a} .

increase in the accumulation gradient over time producing lower accumulation rates toward Ice Stream C and higher rates toward Ice Stream D. Such a change could perhaps be linked to an evolution of WAIS which causes Siple Dome to emerge as a prominent topographic feature and so influence its climate, or a general change in circulation affecting Siple Dome climate over time. We use equation (5.35), find the divide response for various values of ϕ and for various initial conditions, and show the predicted steady-state migration rate in Figure 9. Values for the rate of change in accumulation gradient ($\phi \tilde{a}$) ranging from 0.1×10^{-9} to $1.5 \times 10^{-9} \text{ a}^{-2}$ would produce the inferred divide migration rate (0.05 to 0.50 m a^{-1}). At 10 km from the divide, these values correspond to a total increase/decrease in accumulation of .001 to .015 m a^{-1} (ice equivalent) in 1000 years. Accumulation changes in this range are may be reasonable.

5.9 Conclusions

Our results suggest that divide position at Siple Dome is quite sensitive to changes at its lateral boundaries and to changes in accumulation pattern. The divide motion inferred from the shapes of internal layers could be caused by either a change in elevation at its boundaries of less than 100 meters, or by a modest on-going change in the accumulation gradient over the past several thousand years. Since the perturbations required to move the divide are small, and since the Siple Dome divide has moved only slightly in the past several thousand years, it is unlikely that Ice Streams C or D have changed their relative thickness dramatically in that time.

The divide position at Siple Dome would respond to abrupt forcing in a few hundred years ($\tau_d = 200 - 350 \text{ a}$), with complete adjustment of the surface in a few thousand years ($\tau_v = 450 - 800 \text{ a}$). Therefore, only information about sustained forcing would persist in the geometry of Siple Dome for more than a few thousand

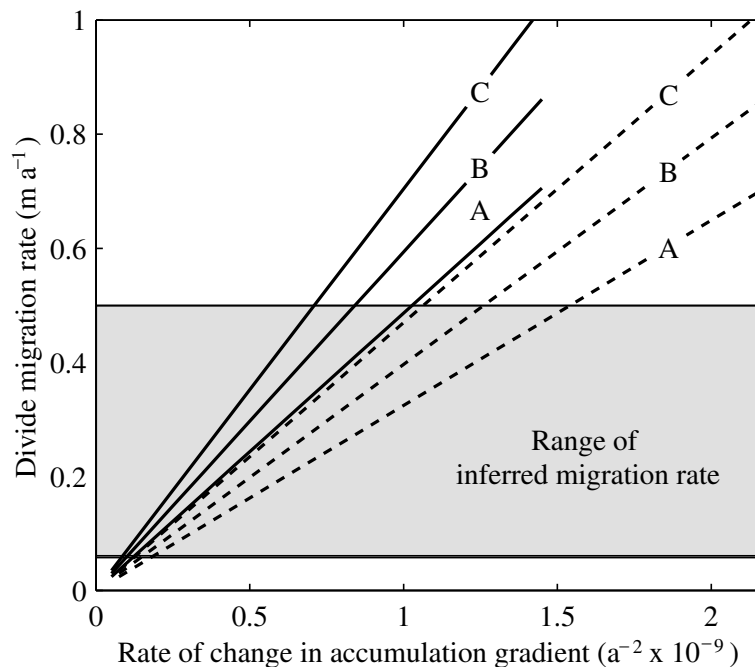


Figure 5.9: Steady state divide migration rates for various rates of increase in accumulation gradient. The rate of Siple Dome divide migration ($0.05 - -0.50 \text{ m a}^{-1}$) is bounded by solid horizontal lines. (A) SDM geometry, $a_0(x) = \tilde{a}$; (B) SDM geometry, $a_0(x) = \tilde{a}(1 + \arctan(x/40 \text{ km}))$; (C) VN geometry, $a_0(x) = \tilde{a}$. Solid and dashed curves correspond to $\tilde{a} = 0.10 \text{ m a}^{-1}$ and $\tilde{a} = 0.15 \text{ m a}^{-1}$ respectively. The range bounded by the inferred Siple Dome divide migration rate corresponds to a change in accumulation rate at 10 km from the divide of $0.001 - 0.015 \text{ m a}^{-1}$ in 1000 years.

years. The recent inferred migration of the Siple Dome divide is likely a response to on-going changes in the bounding ice streams or the local climate rather than a response to an event in the distant past ($> 3000 \text{ a BP}$).

Because of the delayed response to perturbations in margin elevation of $100 - 200$

years, the Siple Dome divide has not yet been affected by elevation changes associated with the shut down of Ice Stream C. However, a possible 20 – 80 m thickening associated with the shut down of the relict Ice Stream D margin would be consistent with the inferred divide motion. Such an elevation change has not been measured. Photoclinometric analysis of satellite images indicate that the relict ice stream surface is about 50 m above the present level of Ice Stream D (*Scambos et al.*, 1998), which is suggestive of recent thickening. This scenario is not unique. Small changes in the precipitation pattern over time are equally likely. Analysis of the pattern of internal layering at Siple Dome may help clarify which scenario has caused the inferred divide motion.

Chapter 6

REGIONAL-SCALE ACCUMULATION PATTERN AT SIPLE DOME

This chapter was presented as a poster at the American Geophysical Union 1997 Fall Meeting with co-authors C. F. Raymond (University of Washington), R. W. Jacobel (St. Olaf College) and E. D. Waddington (University of Washington).

6.1 Summary

The spatial distribution of accumulation across Siple Dome is determined from analysis of the shapes of internal layers detected by radio-echo sounding (RES) measurements. A range of assumed accumulation patterns is used in an ice flow model to calculate an internal layer pattern. Inverse techniques are used to determine which assumed accumulation pattern produces a calculated internal layer pattern that best matches the shape of internal layers from RES measurements. All of the RES internal layer shapes at Siple Dome can be matched using a spatially asymmetric accumulation pattern which has been steady over time. Relative to the divide, the best-fitting accumulation pattern predicts up to 60% less accumulation on the south flank and 40% more accumulation on the north flank. The data also allow the possibility for a small time-variation of the pattern north of the divide. The mismatch between the calculated and the observed layer shapes is slightly reduced when the accumulation gradient north of the divide is higher in the past (> 5000 a BP) than present. Sensitivity tests show that the predicted change in accumulation gradient required to cause the inferred divide migration would be detectable in the internal layer pattern

if it persisted for more than 2 ka. Analysis of the pattern of the mismatch shows no evidence that such a change has occurred, and the possible accumulation change allowed by the data is in the opposite sense. Therefore, it is unlikely that the divide motion has been caused by a temporal change in the spatial pattern of accumulation, and suggests the alternative of forcing from the boundaries with Ice Streams C and D.

6.2 Introduction

The evolution of ice domes in cold polar regions is driven by the accumulation rate history, its spatial pattern, and conditions at the ice sheet boundaries. The history of the spatial pattern of accumulation is an indicator of past climate conditions (e.g., *Morse*, 1997) and a predictor of ice sheet evolution (e.g., *Hindmarsh*, 1996a). Annual layer thickness measurements from ice cores have been used to determine the accumulation rate history for a particular point on an ice sheet (*Paterson and Waddington*, 1986; *Alley et al.*, 1993; *Bolzan et al.*, 1995; *Cutler et al.*, 1995; *Cuffey and Clow*, 1997). However, ice core measurements do not give information about the spatial distribution of accumulation or its changes with time.

The shapes of internal layers detected in ice sheets with radio-echo sounding (RES) can complement ice core measurements. Internal layers arise from variations in electrical properties in the ice (*Moore et al.*, 1992). These variations are likely associated with the original deposited snow. We therefore assume that the internal layers are isochrones – former ice sheet surfaces that have been buried and deformed by ice flow. Information about the spatial distribution of accumulation can be obtained from the horizontal variation in thickness between RES-detected internal layers. Since the shapes of un-dated internal layers do not contain information about the absolute accumulation rate, the age-depth relationship from ice core measurements is necessary

determine the accumulation rate and its variation with time. *Weertman* (1993) used RES measurements of internal layer shapes and annual layer thickness measurements from an ice core to determine the recent accumulation pattern on Dyer Plateau, Antarctica. *Morse* (1997) used RES and ice core measurements to determine past changes in the pattern of accumulation at Taylor Dome, Antarctica.

The spatial distribution of accumulation and any past changes in this distribution over Siple Dome are relevant to inferring the history of climate and ice dynamics in this region. The shapes of RES-detected internal layers near the Siple Dome divide suggest that the ice divide has been slowly migrating for the past several thousand years (*Chapter 4; Nereson et al., 1998b*). This motion could be caused by a gradual change in the accumulation pattern, or by small changes at the boundaries of Siple Dome (*Chapter 5; Nereson et al., 1998a*). In this chapter, the shapes of internal layers detected using RES techniques are analyzed to determine the spatial pattern of accumulation and any detectable changes in the pattern over time. Since annual layer thicknesses are not yet available from a deep ice core, this analysis is relevant only to the spatial pattern of accumulation. A steady-state pattern of accumulation over the past 10^4 years is found to provide a satisfactory fit to the layer shapes. A slight improvement to the fit is found if the accumulation gradient north of the divide was higher before about 5 to 10 ka BP.

6.3 Measurements

The geometry of the surface, bedrock, and internal layers of Siple Dome were determined from Global Positioning System (GPS) surveys and radio-echo sounding (RES) measurements made in 1994 and 1996 as part of a collaborative project among the University of Washington, St. Olaf College, and the University of Colorado. These measurements show that Siple Dome is a nearly 2-dimensional ridge overlying a flat

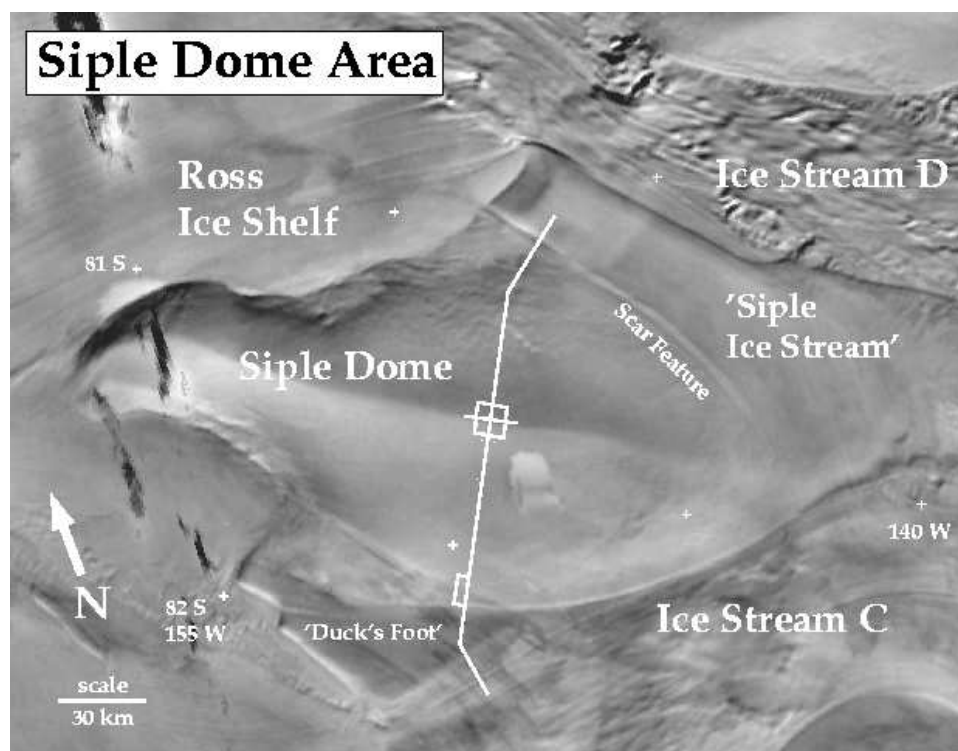


Figure 6.1: AVHRR image of Siple Dome showing the summit grid and main traverses where RES and GPS measurements were made. Image courtesy of Ted Scambos, National Snow and Ice Data Center, University of Colorado.

bedrock plateau. Velocity measurements over the 2 year study period support a 2-d description of the dome with flow generally normal to the ridge for several tens of kilometers from the summit. The RES data used in this study were collected along a line normal to the ridge. This line is assumed to be parallel to ice flow.

The composite RES profile shown in Figure 6.2 corresponds to the white line which begins at Ice Stream C in Figure 6.1, crosses several relict flow features, the dome, and a relict flow feature near Ice Stream D. Most measurements along the profile were made every 100 meters using a center frequency of about 2 MHz (wavelength in ice ≈ 80 m), with the exception of a 30 km section on the extreme south flank, which

was measured with a center frequency of 4 MHz. Internal layers are apparent and continuous over the entire width of the dome. At the dome boundaries near the relict flow features, the internal layers are disrupted from past or current dynamic activity (*Gades, 1998; Jacobel et al., 1996*).

It is immediately apparent that the shapes of internal layers in figure 6.2 are asymmetric. The depth to a given layer north (right) of the divide is greater than its depth south (left) of the divide. This asymmetry suggests that more accumulation occurs to the north than to the south. Such an asymmetry could also arise from an asymmetric strain history associated with the activity of the bounding ice streams.

We restrict our analysis to the region 50 km south to 40 km north of the summit where the internal layers are continuous and where RES measurements were along the assumed flow line perpendicular to the ridge. The velocity field derived from GPS measurements (*Chapter 3*) shows that the RES profile over most of the chosen region corresponds to an ice flow line. From 30 km to 40 km north of the divide, the flow turns westward toward the Ross Ice Shelf. At 40 km north, the RES profile and the flow line differ in azimuth by about 26° . Since about 90% of the velocity component at 40 km north is still along the RES profile, we ignore the deviation from the flow line for this analysis.

6.4 Data Analysis

Each RES measurement is a time-series of reflection amplitudes. To eliminate environmental and instrumental noise, each time-series measurement is filtered with a zero-phase, forward/reverse, 4th order Butterworth band pass filter from 1 to 10 MHz. Specific internal layers are selected from the filtered data using an automated routine that finds the time of maximum amplitude from each RES measurement in a hand-prescribed time-window (*Gades, 1998*). The resulting internal layers are then

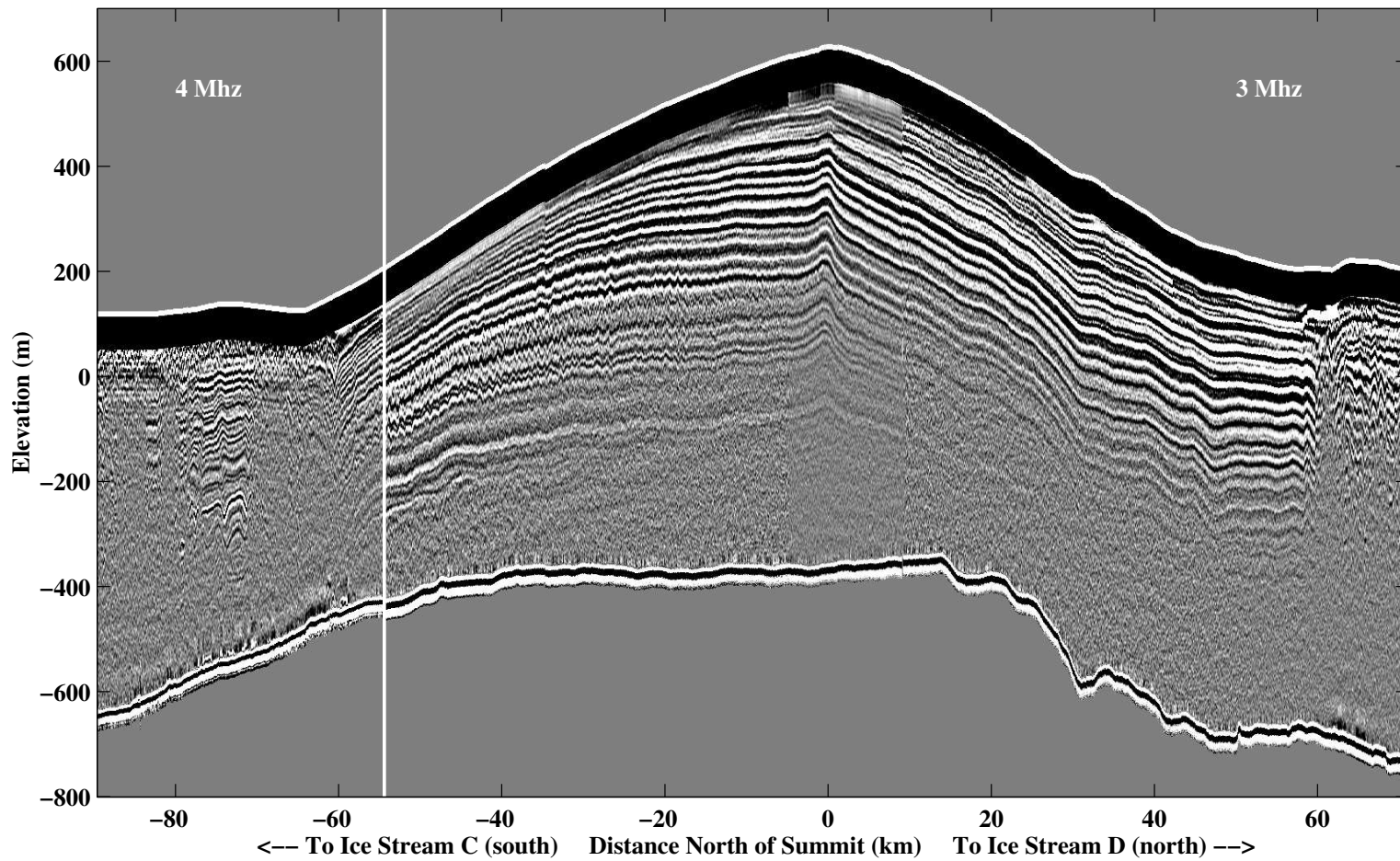


Figure 6.2: Radio-echo sounding profile across the width of Siple Dome. The profile corresponds to the long white line in figure 6.1 beginning at Ice Stream C and ending at the Siple Ice Stream.

smoothed horizontally using a low-pass filter with the cut-off frequency at 0.2 km^{-1} . Figure 6.3 shows selected smoothed internal layers.

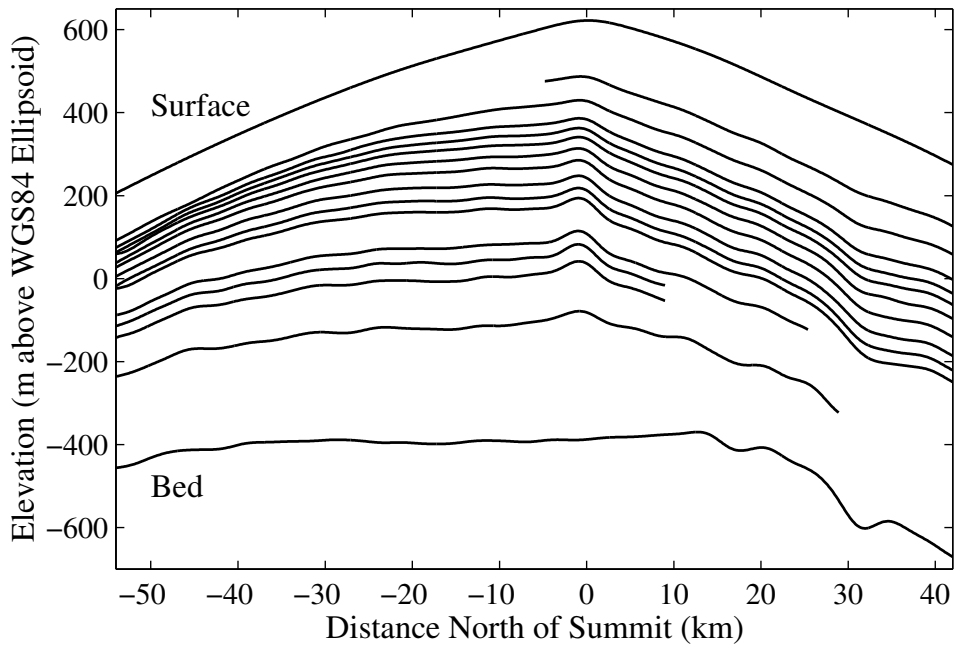


Figure 6.3: Smoothed internal layers detected by radio-echo sounding.

6.5 Ice Flow Model

A two-dimensional, plane-strain, steady-state ice flow model following *Reeh* (1988) is used to track ice particle paths and predict an internal layer geometry under various assumed patterns of accumulation over Siple Dome. Each set of predicted layer shapes is compared to the RES-measured layer shapes. The accumulation pattern giving the minimum mismatch between the modeled and RES layer shapes determines the steady-state accumulation pattern that produces the best fit to the data.

The ice flow model accounts for the effect of bed topography on ice flow and

allows the depth variation of horizontal velocity to be prescribed. The model does not allow ice thickness $H(x)$ or accumulation pattern $b(x)$ to change with time. The accumulation rate $b(x)$, the depth-averaged horizontal velocity $\bar{u}(x)$, ice thickness $H(x)$, and distance along flow from the divide x are related by¹

$$\int_0^x b(x)dx = \bar{u}(x)H(x). \quad (6.1)$$

It is convenient to define a normalized vertical coordinate \tilde{z} :

$$\tilde{z} = \frac{z - R(x)}{H(x)}, \quad (6.2)$$

where $R(x)$ is the bedrock elevation and z is measured upward from a horizontal datum below the bedrock. We construct $u(x, z)$ as

$$u(x, z) = u_s(x)\xi(\tilde{z}), \quad (6.3)$$

where u_s is the horizontal velocity at the ice surface and the shape function $\xi(\tilde{z})$ describes the depth variation of $u(x, z)$ such that $\xi(0) = 0$ and $\xi(1) = 1$. Equation (6.3) assumes that the shape function does not vary with position x . This assumption is valid where the ice thickness varies slowly with position (as is the case for Siple Dome) and remote from the anomalous flow regime predicted within a few ice thicknesses of an ice divide (*Reeh*, 1988; *Raymond*, 1983). Combining equations 6.1 and 6.3 yields

$$u(x, z) = \frac{B(x)}{\Xi H(x)}\xi(\tilde{z}), \quad (6.4)$$

where $B(x) = \int_0^x b(x)dx$ and $\Xi = \int_0^1 \xi(\tilde{z})d\tilde{z}$.

The vertical velocity field $w(x, z)$ is found from continuity:

¹Distance along flow from the divide is denoted x in this chapter. This differs from the notation used in Chapter 3 where the distance along the flow-line is denoted y to coincide with the local coordinate system.

$$\partial_x u = -\partial_z w. \quad (6.5)$$

Differentiation of equation (6.4) with respect to x yields

$$\partial_x u = \frac{b\xi + B\partial_x \xi}{\Xi H} - \frac{B(x)\partial_x H}{\Xi H^2} \xi. \quad (6.6)$$

The chain rule and equation (6.2) are used to calculate $\partial_x \xi(\tilde{z})$:

$$\partial_x \xi(\tilde{z}) = -\partial_{\tilde{z}} \xi \left(\frac{1}{H} \partial_x R + \frac{(z-R)\partial_x H}{H^2} \right). \quad (6.7)$$

Substitution of Equation (6.7) into Equation (6.6) and integration with respect to z yields the vertical velocity w ,

$$w(x, z) = -\frac{b(x)}{\Xi} \int_0^{\tilde{z}} \xi(\tilde{z}) d\tilde{z} + \frac{B(x)}{H(x)\Xi} (\tilde{z}\partial_x H + \partial_x R) \xi(\tilde{z}). \quad (6.8)$$

The calculation of particle paths is simplified if calculations are performed on a regular grid in the transformed vertical coordinate domain \tilde{z} . The vertical motion of an ice particle is then described by the material time derivative $d_t \tilde{z}$ which is related to $w = d_t z$ by

$$\frac{d\tilde{z}}{dt} = \frac{d\tilde{z}}{dz} \frac{dz}{dt} + \frac{d\tilde{z}}{dx} \frac{dx}{dt}, \quad (6.9)$$

and reduces to

$$\frac{d\tilde{z}}{dt} = \frac{w(x, z)}{H(x)}. \quad (6.10)$$

Equations 6.4 and 6.10 describe a continuous flow field for ice particles given ice thickness $H(x)$, bedrock geometry $R(x)$, shape function $\xi(z)$, and accumulation pattern $b(x)$. Ice thickness and bed geometry are given by the RES measurements. $R(x)$ is smoothed so that $H(x)$ is smooth and slowly varying. The shape function

$\xi(x)$ is described by an 8th order Chebyshev polynomial fit to the typical flank shape function predicted by a steady-state, 2-d, finite element model (FEM) of flow at Siple Dome (*Chapter 2; Nereson et al., 1996*). The FEM shape function was chosen because it includes a correction for typical temperature distribution in the ice. Other shape functions, such as the common description for laminar ice flow, could also be used. Since the shape function does not vary with position in the model, its depth-variation does not affect the predicted shape of isochrone layers, only their predicted age.

The accumulation pattern $b(x)$ is chosen to allow the maximum degrees of freedom where we expect the accumulation pattern to vary the most while maintaining calculation efficiency. Since the divide is the main topographic feature in the region, rapid variation in pattern of accumulation may be expected to occur there with relatively smooth variation elsewhere. We choose an arctangent function centered at the divide,

$$\frac{b(x)}{b(0)} = 1 + \alpha_{s,n} \arctan(x/\lambda_{s,n}). \quad (6.11)$$

where $b(0)$ is the accumulation rate at the divide. In the limit of small λ , this function approaches a step function at the divide. At large λ , this function approaches a constant gradient. Different values for λ and amplitude α for the south (s) and north (n) sides of the divide accommodate a wider range of accumulation patterns. The parameters, α_s , α_n , λ_s , and λ_n , are varied in order to find the combination that produces the best match to the observed layer shapes.

6.6 Residual Calculation

For each model calculation, a set of isochrone shapes is predicted for a given amplitude ($\alpha_{s,n}$) and transition length ($\lambda_{s,n}$) of the accumulation pattern. Since the age versus depth relationship is unknown, the goal is to match the shapes of all observed internal layers, and not any particular isochrone. Therefore, we are free to decide which

modeled layer to compare to a given observed layer. Following *Nereson et al.* (1998b) (*Chapter 4*) the shapes of layers with the same average height are compared. Each side of the divide is considered separately so that a layer denoted by the index j is identified by an average height \bar{z}_j^n for the north side of the divide a different average height \bar{z}_j^s for the south side. Points along the horizontal coordinate are denoted by i . The shape of a layer on a given side of the divide is quantified by measuring the elevation S_{ij} at each position i along layer j so that

$$S_{ij}^{s,n} = S(x_i, \bar{z}_j^{s,n}) = z(x_i, \bar{z}_j^{s,n}) - \bar{z}_j^{s,n}. \quad (6.12)$$

The superscript denotes values for the south (s , $x_i < 3$ km) and north (n , $x_i > 3$ km) sides of the divide, respectively. No attempt is made to match the observed layers in the divide zone $x_i = \pm 3$ km. The anomalous flow in this zone associated with ice divides is not accounted for in the model.

Modeled isochrone shapes S_{ij}^m are compared to the observed isochrone shapes S_{ij}^d using a mismatch parameter J which is also calculated separately for each side of the divide for each model calculation:

$$J = \frac{1}{L} \sum_{j=1}^L \omega_j \left(\frac{1}{N_j - p} \sum_{i=1}^{N_j} \frac{(S_{ij}^m - S_{ij}^d)^2}{\epsilon_j^2} \right) \quad (6.13)$$

The term ϵ_j is the expected combined error from the model and the data for a particular layer j . A depth-dependent weighting function ω_j for layer j is chosen to account for the fact that the layers are not uniformly distributed over depth. The number N_j is the total number of points i along a layer j , $p = 1$ is one less than the number of free parameters in the model, and $L = 14$ is the total number of layers. In this application, each layer is sampled every 1000 m, and N_j depends on the length of the RES profile (30 to 50 km).

The error term ϵ_j represents errors in layer shape arising from errors in estimating z and \bar{z} at each point along the modeled and observed layers. We do not account for

contributions to the total error from model simplifications. These errors are difficult to quantify and are addressed instead using sensitivity tests developed in a later section. Errors in the observed layer shapes arise from digitizing and defining a given layer and depend primarily on signal frequency, sampling density, and the reflection strength of the layer (*Chapter 4*). All the data used for this analysis were collected at the same frequency (2MHz) and spatial density (100 m). As the reflection strength of the layer decreases, it is more difficult to identify from RES data. Layers identified using the automatic picking routine are rougher as the reflection strength decreases. An error is therefore associated with picking a layer and is assumed proportional to the “roughness” of the layer, defined as the standard deviation of the difference between the smoothed and raw internal layer shape. This standard deviation for Siple Dome data varies between 1 and 5 meters, increasing with layer depth. We conservatively estimate the combined error ϵ_j at 6 to 10 meters, depending on layer depth.

The weighting function ω_j is applied to correct for the fact that the measured internal layer shapes have different lengths and are unevenly spaced with depth. With no imposed weighting, areas where layers are closely spaced would be weighted more heavily than where layers are sparse. Similarly, short layers which sample only part of the horizontal domain would receive relatively more weight per sample than layers which cover the whole horizontal domain. Therefore, a weighting scheme is applied to correct the effects of varying layer length and vertical spacing. Conceptually, it is simple to separate these two factors so that the total weight for a given layer ω_j is a sum of a weight to correct for its vertical spacing ω_j^v and a weight to correct for its length ω_j^ℓ :

$$\omega_j = \omega_j^v + \omega_j^\ell. \quad (6.14)$$

We define ω_j^v to be proportional to the distance between a given layer j and its

adjacent layers with a scale factor F^v so that

$$\omega_j^v = (\bar{z}_{j+1} - \bar{z}_{j-1})F^v. \quad (6.15)$$

More weight is given where the vertical layer density is sparse. Similarly, we define ω_j^ℓ to be proportional to the number of samples N_j in a layer so that longer internal layers are given more weight than shorter layers:

$$\omega_j^\ell = N_j F^\ell. \quad (6.16)$$

The scale factors F^v and F^ℓ are normalizing factors chosen so that

$$\sum_j \omega_j = \sum_j \omega_j^v + \omega_j^\ell = L. \quad (6.17)$$

With this weighting scheme, each depth interval receives equal weight. Since depth and time are not linearly related, this does not give equal weight to all *time* represented by the internal layers. Younger ages are weighted more heavily according to the depth-age relationship. Since the weight function ω_j is scaled by F^v and F^ℓ , modeled layers which match the observed layers to within the weighted error will produce $J < 1$.

6.7 Results

6.7.1 The Predicted Steady-State Accumulation Pattern

Figure 6.4 shows the range of steady-state accumulation patterns which fit the observed layers to within given error intervals. The black range corresponds to values of λ_s , λ_n , α_s , and α_n which produce a match to within the estimated errors in the data ($J < 1$). The medium and light ranges correspond to $J < 2$ and $J < 3$, respectively. A smooth and well-constrained south-north accumulation gradient is predicted. Relative to the divide, the minimization predicts 40% lower accumulation

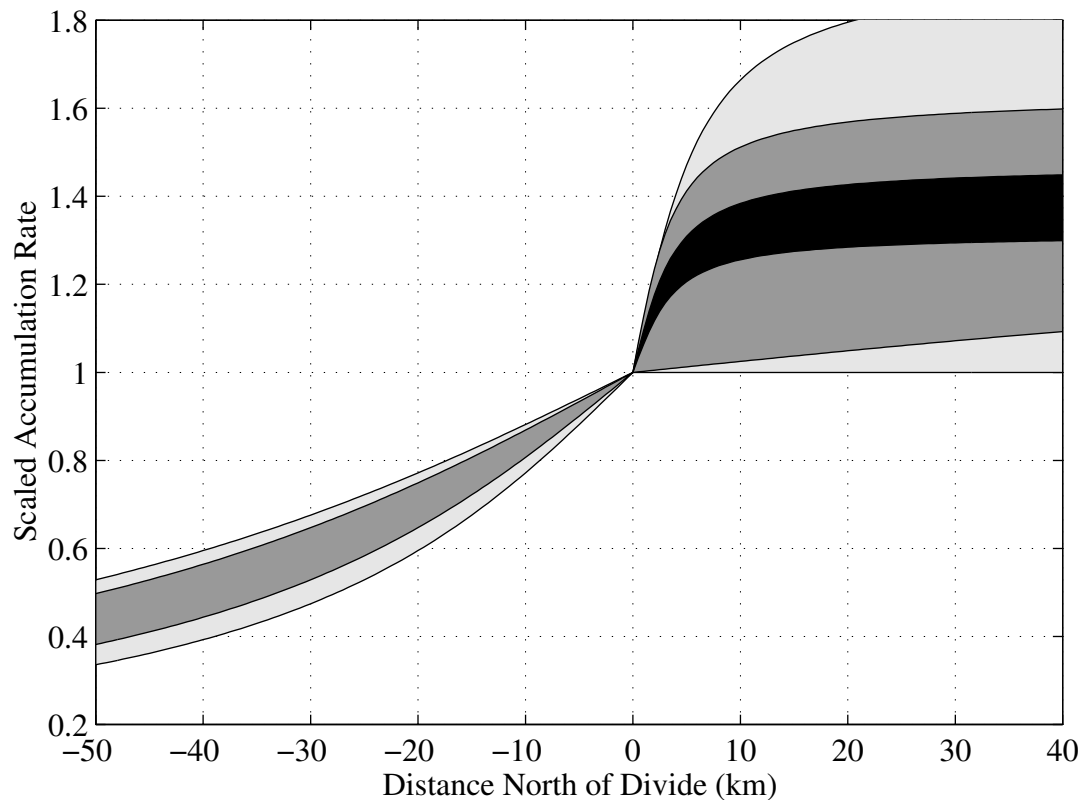


Figure 6.4: Steady-state accumulation pattern which produces the best fit to the observed layer shapes. The black range produces layers which match the data to within the expected errors ($J < 1$). The dark and light gray ranges corresponds to $J < 2$ and $J < 3$, respectively. The accumulation pattern is scaled to the accumulation rate at the divide.

rates at 30 km south of the divide and about 30 – 40% higher accumulation rates at 30 km north of the divide.

Figure 6.5 shows the predicted layer shapes given a spatially constant accumulation pattern (upper panel) and given the spatial pattern shown in Figure 6.4 (lower panel). The improved match to the observed layer shapes from using the derived spatial pattern is apparent. The remaining mismatch at $x = 30 - 40$ km is probably due to 3-d flow effects which are not accounted for in the model.

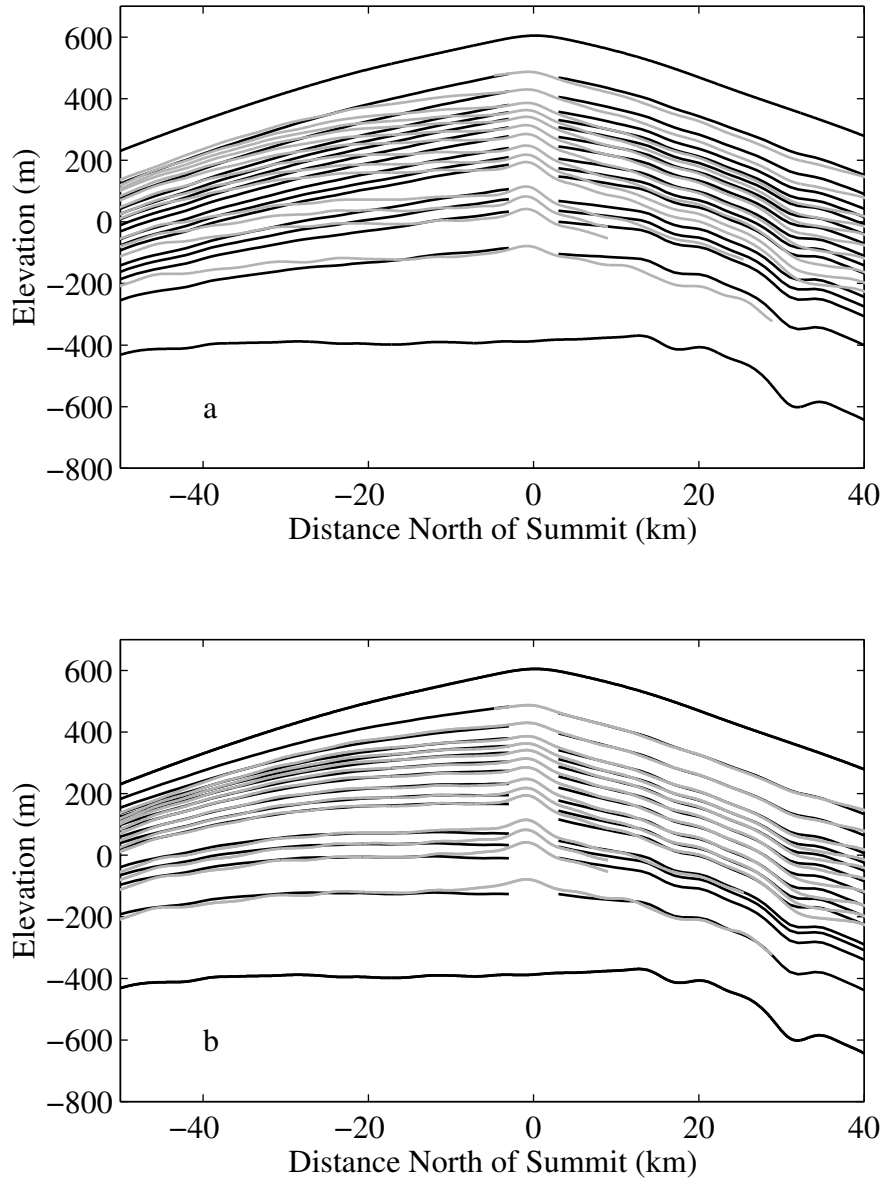


Figure 6.5: (a) RES-detected layer shapes (gray) compared to layer shapes calculated assuming a constant accumulation pattern (black). For the purposes of display, modeled layers shown match the measured layers near the divide. In the residual calculation, modeled and measured layers with the same average depth are compared. (b) RES-detected layer shapes (gray) and layer shapes (black) calculated assuming the steady state accumulation pattern which produces the minimum weighted mismatch J . Modeled and measured layers have the same average depth. The modeled layers shown correspond to the parameters $\lambda_s = 30$ km, $\lambda_n = 5$ km, $\alpha_s = 0.6$ and $\alpha_n = 0.2$. Modeled layer shapes within 3 km of the divide are ignored because the anomalous flow regime associated with ice divides is not accounted for in the ice flow model.

6.7.2 Comparison with other Measurements

The inferred accumulation gradient is consistent with accumulation estimates from chemical analysis of 2-meter snow pits at ± 30 km (from *K. Kreutz, pers. comm.*), but inconsistent with measurements of the pole-to-surface distance over a 1- or 2-year period (Fig. 6.6) and with the accumulation pattern deduced from the physical and electrical stratigraphy of three 100-meter cores taken from ± 30 km and at the divide (*K. Taylor, pers. comm.*). Preliminary analysis of the shallow cores suggests a smaller gradient with 20% less accumulation at 30 km south of the divide and no gradient north of the divide. However, these methods sample different time-averaged windows at Siple Dome. Pole-to-surface distances measure accumulation over 1- or 2-year periods; snow pits span less than 10 years; shallow cores generally span time-scales of 10^1 to 10^2 years; RES layers are detected approximately every 10^3 years in the shallow ice and every 10^4 years in deep ice. Accumulation estimates from analysis of RES-detected internal layers represent averages over at least 10^3 years and do not overlap with measurements from the most recent 100 years on snow pits or shallow cores. Since these RES measurements cannot be used to detect decade to century scale accumulation patterns, it may not be relevant to compare accumulation estimates derived from low-frequency RES measurements to estimates obtained from shallow cores and snow pits.

If Siple Dome is near steady state, then the spatial accumulation pattern should agree with the spatial pattern of the horizontal flux divergence determined from GPS measurements of survey poles (*Chapter 3*). This comparison can be used to determine whether the inferred steady-state accumulation pattern is consistent with the steady-state assumption. Figure 6.6 shows that the inferred accumulation pattern and the calculated flux divergence pattern generally agree north of the divide between 0 and 20 km where the flow begins to turn off the pole line. The patterns strongly

disagree south of the divide. This disagreement suggests that Siple Dome is presently not in steady state and may be significantly thickening along its south flank (see also *Chapter 3*). Analysis presented in *Chapter 7* suggests that this non-steady situation has probably existed for the past 500 years or less and is consistent with the finding that the summit area is presently near steady state (*Chapter 3*). Since the shallowest internal layer used to infer the accumulation rate pattern is about 1000 years old, it is likely that the pattern of accumulation inferred from this analysis reflects the long-term pattern and is not significantly affected by the recent non-steady situation.

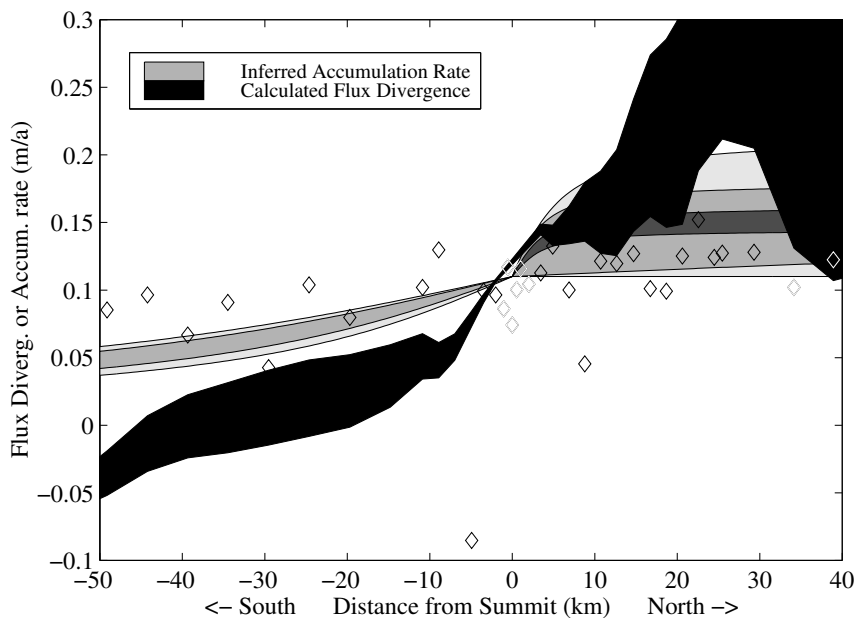


Figure 6.6: Accumulation pattern inferred from the RES layer pattern is denoted by the gray shaded area assuming the accumulation rate at the summit is 0.11 m a^{-1} in ice equivalent units (Mayewski *et al.*, 1995). Dark and light areas correspond to $J < 1$, $J < 2$, and $J < 3$, respectively. The flux divergence calculated from GPS measurements of horizontal velocity is shown by the black region (*Chapter 3*). Diamonds denote accumulation rate estimates in ice equivalent units from pole-to-surface measurements in 1994, 1996 and 1997.

6.7.3 Temporal Changes in the Spatial Accumulation Pattern

Although a steady-state spatial accumulation pattern matches the observed layers to within the measurement errors, it is possible that the spatial pattern has changed with time and the effects of these changes on the internal layer pattern are indistinguishable from the steady-state case. Could a non-steady-state spatial pattern of accumulation also match the observations?

The depth-distribution of the residuals is examined to test this possibility. If a detectable change in the accumulation pattern has occurred, then an accumulation pattern which produces a good match to shallow (young) layers would not produce a good match to (deeper) layers. The residuals along each layer are averaged and the amplitude values α_s and α_n are varied while the transition length values (λ_s and λ_n) are held fixed at 40 km and 5 km, respectively. The horizontally averaged residuals are plotted in gray versus the average depth of the layer and versus a range of normalized amplitude values (Fig. 6.7). The north and south sides of the divide are treated separately.

In Figure 6.7, the panel corresponding to the south side of the divide shows that layers at all depths have minimum residuals for a single amplitude value. This suggests that there has been no change in the amplitude value (and therefore accumulation pattern) over the time represented by the measurements. The panel corresponding to the north side of the divide shows a very broad minimum around an amplitude value of 0.2, possibly suggesting little to no change in the accumulation pattern over time. However, there appears to be a trend to the minimum with shallow layers fitting best to a low value of α_n and deeper layers fitting best to a slightly higher value of α_n . This change with depth shows that the data allow for the possibility that the accumulation gradient north of the divide has decreased over time. Using hypothetical time-scales for Siple Dome to date the internal layers (*Chapter 2; Nereson*

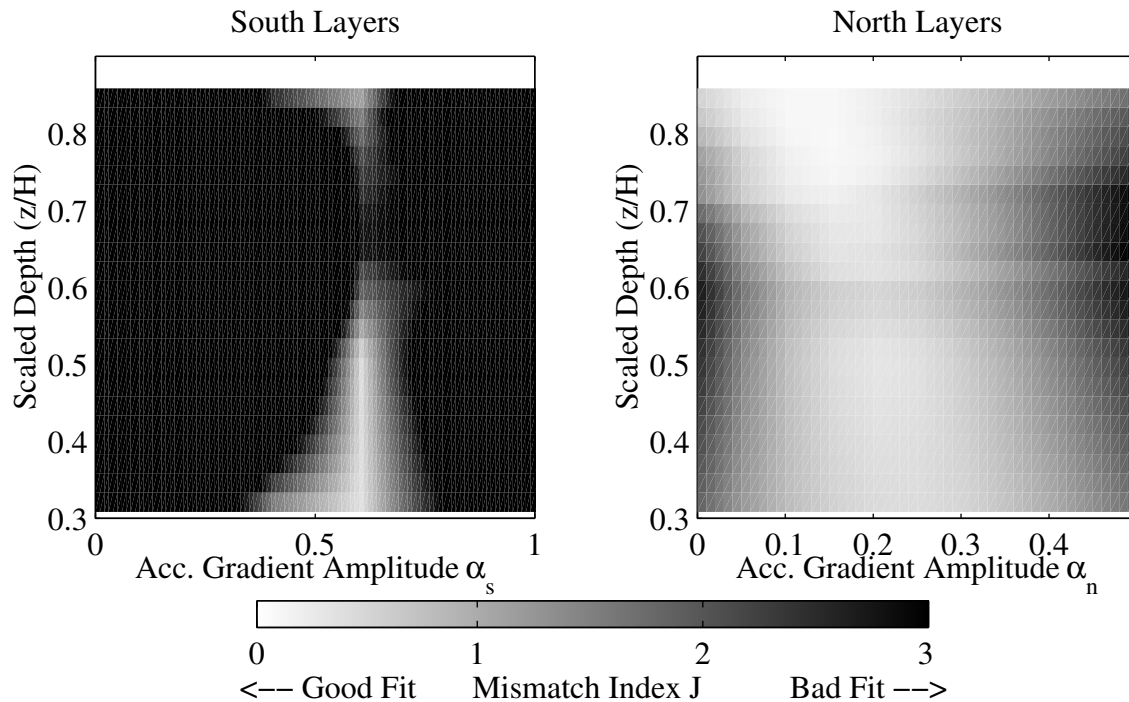


Figure 6.7: Depth distribution of residuals for layers south and north of the divide, respectively. South of the divide, minimum residuals are found at one amplitude value α_s at all depths, suggesting no change over time south of the divide. North of the divide, residuals for shallow (young) layers are minimized at low values for α_n while residuals for deep (old) layers are minimized at slightly larger values.

et al., 1996), the range of time-dependent accumulation patterns shown in Figure 6.8 is implied by the residual pattern pattern shown in Figure 6.7. This accumulation scenario suggests that 5-10 ka BP, accumulation rates were 15-30% higher relative to the divide than in more recent times. The accumulation gradient north of the divide has possibly decreased over the past 10^4 years. Because the range of time-dependent accumulation patterns shown in Figure 6.8 is within the 95% confidence limits of the range of inferred steady state patterns, (Fig. 6.4), we cannot distinguish between the time-dependent and steady-state scenarios.

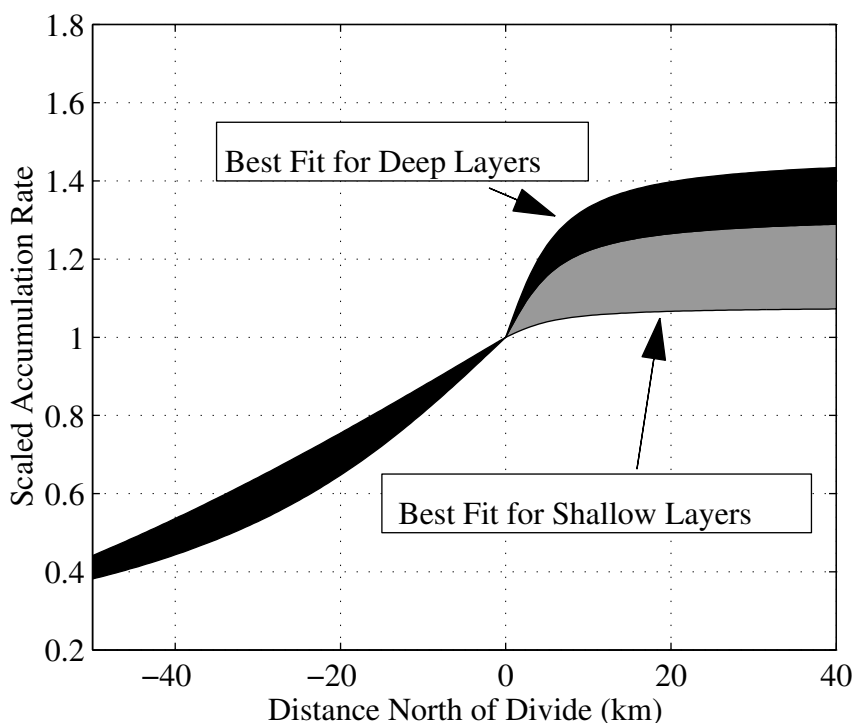


Figure 6.8: Potential time-change in accumulation pattern allowed by the data. Shallow layers correspond to layers younger than about 5 – 7 ka. Deep layers are older than 5 – 7 ka.

Because data for deep layer shapes north of the divide are sparse, the time-dependent scenario shown in Figure 6.8 should be viewed with caution. North of the divide, layers are not detectable over the full region (Fig. 6.3). The residuals at depth are therefore dominated by one deep layer which extends to 25 km from the divide. Because the data are sparse for layers older than 5-10 ka, it is difficult to draw firm conclusions for changes in the spatial pattern prior to that time.

Nevertheless, this analysis is relevant to the hypothesis that a change in the accumulation pattern is responsible for the divide migration inferred at Siple Dome (*Chapter 5; Nereson et al., 1998a*). Analysis presented in Chapter 5 (*Nereson et al.,*

1998a) shows that an *increase* in the gradient is required to move the divide toward Ice Stream D. The possible change in the spatial pattern shown in Figure (6.8) is a *decrease* in the south-north accumulation gradient over time; this change is in the opposite sense. We therefore suspect that temporal changes in the accumulation pattern are not responsible for Siple Dome divide motion. Rather, the divide motion is likely caused by changing conditions at the boundaries of Siple Dome at the margins of Ice Streams C and/or D.

To make this a firm conclusion, the ability of RES-detected internal layer shapes to record changes in the accumulation pattern over time needs to be quantified. What kinds of accumulation pattern changes would produce a detectable change in the internal layer pattern? Is this signal distinguishable from other factors which might affect the layer shapes such as changes in ice thickness? The shape of an internal layer depends on (1) the amount and distribution of deposited snow since the layer was formed at the ice surface and (2) the amount and distribution of strain the layer has experienced since its formation. The first depends on the accumulation pattern since the time of layer deposition, and the second depends on both the accumulation history and the thickness history of the ice sheet.

6.8 Sensitivity to Temporal Changes in Accumulation Distribution

Recovery of information about temporal changes in the spatial pattern of accumulation is limited by how well and how many internal layers are measured and how well the strain history is known. Measurements from the University of Washington RES system can detect internal horizons every 50-100 meters in an ice column corresponding one layer every 0.5 – 20 ka (for Siple Dome) with a measurement uncertainty

of about 10 meters.² Any detectable changes in the accumulation distribution must persist over a time interval sampled by the internal layer pattern and must produce a change in distance to adjacent internal layers which is greater than the measurement uncertainty. The strain history is especially difficult to estimate for older (deeper) layers. The total strain depends on the history of the velocity field, which in turn depends on history of accumulation – the quantity we are trying to find. In general, older layers have a more complicated strain history.

A simple analytic argument can be used to quantify these factors and make a first-order estimate of the limits of using RES to interpret accumulation changes. Consider a perfectly plastic ice sheet. Any change in the accumulation pattern will be accommodated by a change in the velocity field with no change in the ice thickness. (In a real ice sheet, the ice thickness is relatively insensitive to accumulation changes (*Paterson, 1994*), so this perfectly plastic extreme is a reasonable starting point.) Suppose we sample the internal stratigraphy at two places on the ice sheet: Site A and Site B, separated by some distance x . Both A and B are sufficiently close together that the ice thickness H is essentially equal at both sites. Under a constant accumulation pattern, isochrones will appear at the same depth at both sites. If a non-constant spatial pattern exists, a given isochrone will be found at different depths. If we make the additional assumption that the ice moves only vertically, then we can predict the difference in depth to a particular isochrone between the two sites Δz . A change in the spatial pattern over time will produce a deviation from the predicted steady-state depth-difference. Figure 6.9 shows this situation schematically.

Both sites have the same ice thickness H , and constant vertical strain rate $\partial_z w$. Site A has a constant accumulation rate $b_A(t) = b_0$ and Site B has a variable accumulation rate $b_B(t)$. At Site A,

²The uncertainty is about 1/10 of the dominant wavelength of broad-band transmitted signal with a center frequency of 2 MHz (wavelength in ice = 82 m).

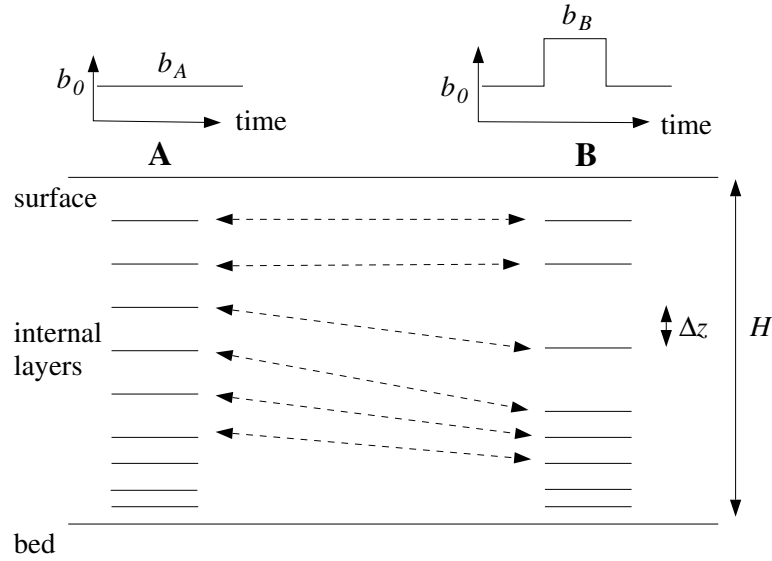


Figure 6.9: Schematic of the analysis used to determine the sensitivity of internal layer shapes to a change in the distribution of accumulation.

$$d_t z = b_0 \frac{z}{H}. \quad (6.18)$$

Solving for $z(t)$ gives the Nye time-scale:

$$z_A(t) = H \exp\left(\frac{b_0 t}{H}\right). \quad (6.19)$$

where time proceeds forward so that $t = 0$ is the present, and t is negative. Site B has a time-dependent accumulation rate, simulating changes in the accumulation pattern between points A and B. The time-scale for site B is

$$z_B(t) = H \exp\left(\frac{1}{H} \int_t^0 b_B(t) dt\right). \quad (6.20)$$

This simplified scenario is not fully realistic. In reality, ice deposited between sites A and B would have some intermediate thickness associated with an interme-

diate accumulation rate. The ice particles along the deposited layer between sites A and B would travel horizontally as well as vertically over time, to be found eventually beneath, say, site B. Therefore, the layer thickness pattern beneath Site B does not reflect deposition at Site B, but some average between sites A and B. Despite this limitation, this exercise can still shed some quantitative light on the first-order sensitivity of layer shapes to accumulation change.

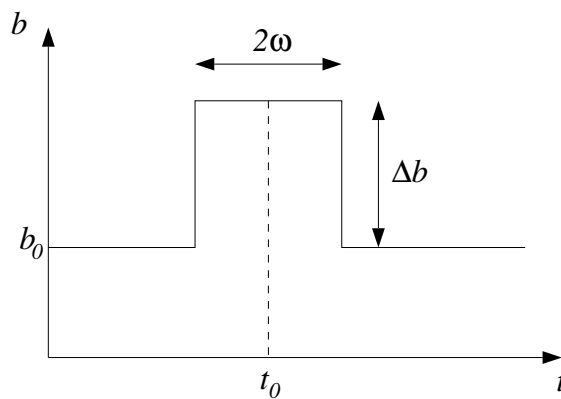


Figure 6.10: Hypothetical accumulation history at Site B.

We are interested in the depth to a particular isochrone at each site, and the size of the depth-difference ($\Delta z = z_A - z_B$) between the sites is for a given accumulation history at Site B. For example, we can detect the difference between a spatially constant accumulation pattern and one that deviates from a constant pattern if the changed pattern causes isochrones at Site B to be deeper or shallower than at site A by an amount detectable using RES techniques (≈ 10 m for 2MHz). Assume $b_B(t)$ is a step-change in time relative to b_0 with center t_0 , duration or width 2ω , and magnitude Δb (Fig. 6.10). The difference in depth Δz to a given isochrone between the two sites can be calculated from equations (6.19) and (6.20).

For layers deposited prior to the step change (deep layers): $t < t_0 - \omega$,

$$\Delta z = H \exp\left(\frac{b_0 t}{H}\right) \left(\exp\left(1 - \frac{-2\omega \Delta b}{H}\right) \right). \quad (6.21)$$

For layers deposited during the accumulation change: $t_0 - \omega < t < t_0 + \omega$,

$$\Delta z = H \exp\left(\frac{b_0 t}{H}\right) \left(1 - \exp\frac{\Delta b}{H}(t - t_0 - \omega) \right). \quad (6.22)$$

For layers deposited since the accumulation change,

$$\Delta z = 0. \quad (6.23)$$

Equations (6.21) and (6.22) have four important time-scales: (1) the fundamental H/b time-scale, (2) a time-scale related to the duration of the accumulation change ω , (3) when the change occurs t_0 , and (4) the amplitude of the change scaled to the ice thickness $H/(\Delta b)$. The interplay of these time-scales is shown in Figure 6.11. The contour lines are the maximum $\Delta z/H$ values for a given age (t_0), duration (w), and magnitude (Δb) of an anomalous accumulation pattern. All values are scaled to the fundamental time-scale $\tau = H/b$. Largest Δz values are obtained for recent, long-duration, and high-magnitude variations in the accumulation pattern. There appears to be a critical duration value w below which Δz values vary significantly with the mean age of the accumulation anomaly and above which Δz values vary slowly with the anomaly age.

When $\Delta b = 1/(2\omega)$ and $2\omega \rightarrow 0$, these equations describe the unit impulse response of the layers to an accumulation change (Nye, 1965). They can therefore be combined to solve for any combination of step-changes in the accumulation pattern. Figure 6.12A shows the response to the same step-change in accumulation pattern which occurs at two different times. Recent changes produce a larger Δz signal. The effects of ancient accumulation changes decay with time and are eventually unde-

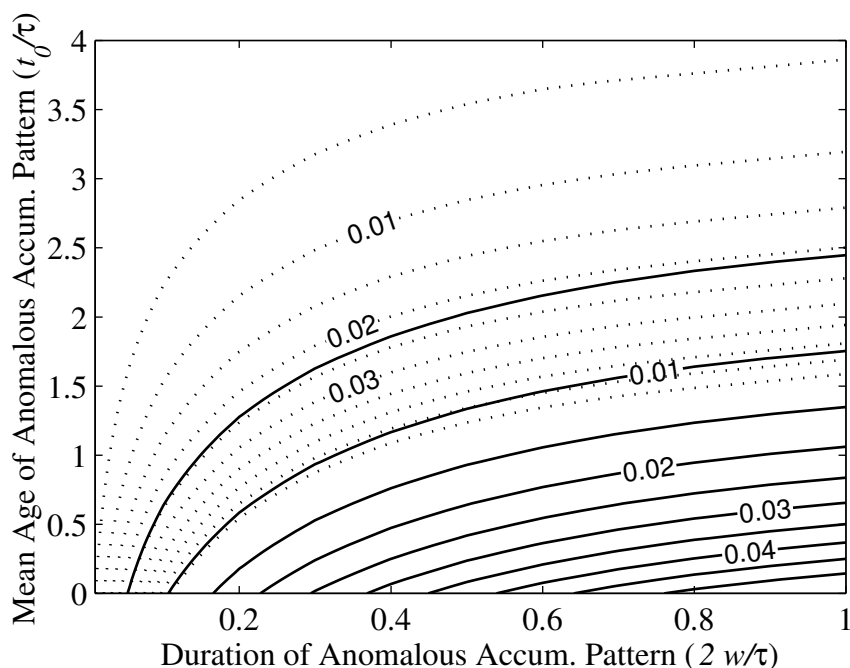


Figure 6.11: Contours of maximum $\Delta z/H$ values in the ice column versus the duration w and mean age t_0 of an anomalous accumulation pattern at Site B for $\Delta b/b_0 = 0.1$ (solid) and $\Delta b/b_0 = 0.5$ (dotted). All values are scaled to the fundamental time-scale $\tau = H/b_0$. The Δz signal increases as w and Δb increase and as t_0 decreases.

tectable. For example, curve 2 (dashed) in Figure 6.12A would not be detected with an error in Δz as large as 10 m.

Figure 6.12B shows how various accumulation scenarios can produce a similar signal in the internal layer pattern. Long, low-amplitude changes such as a small step change of long duration (curve 2) could produce a similar signal to several high amplitude, frequent changes (curve 3). For comparison, the depth difference arising from an accumulation pattern where Site B has higher accumulation rates for all time is shown (curve 1). Because layers must conform to the surface and the bed, the maximum Δz is reached at mid-depth. The longer the duration of the accumulation change, the lower the amplitude required to produce a signal in the layers.

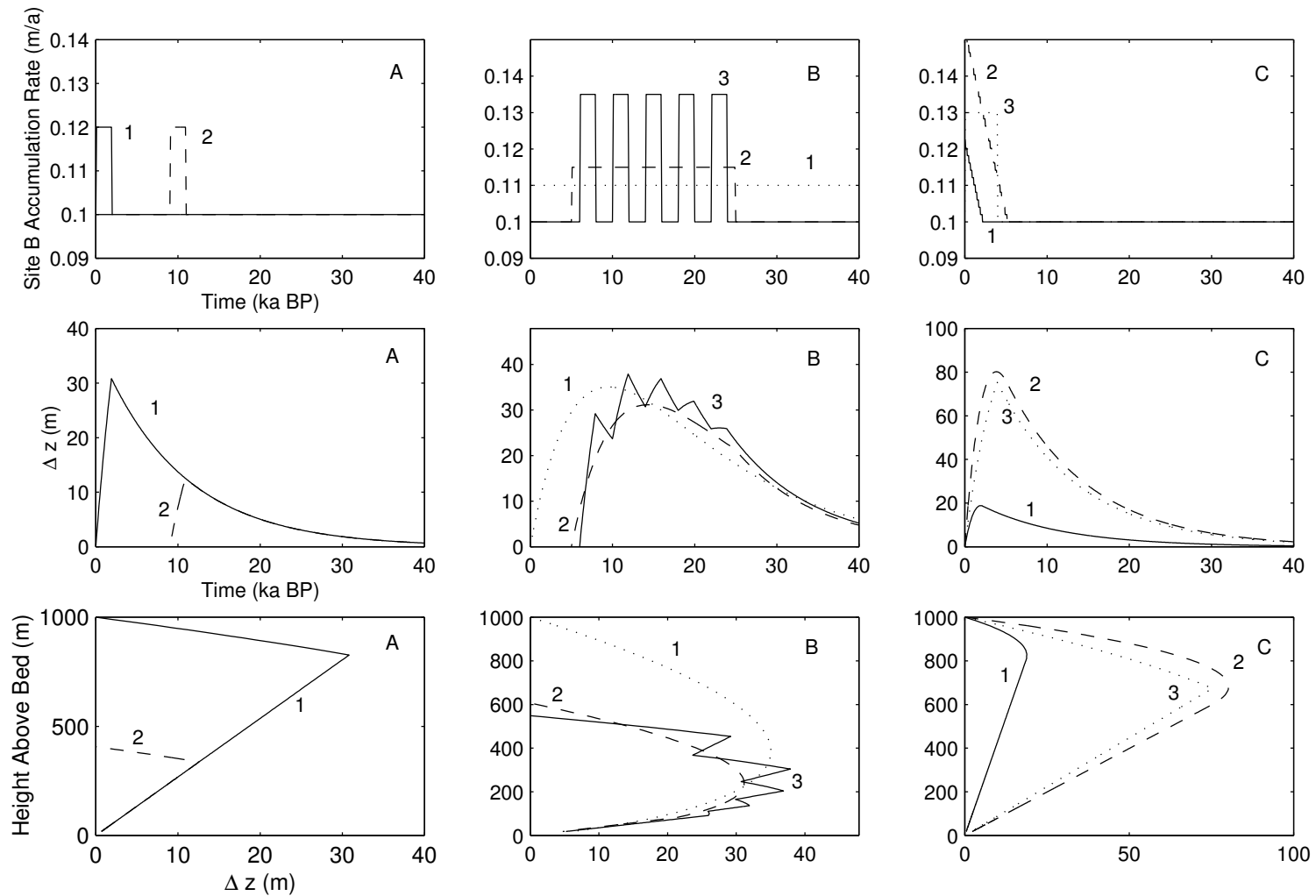


Figure 6.12: Top row shows the accumulation history at Site B. Site A is held constant at 0.10 m a^{-1} . Middle row shows the difference in depth to a given isochrone plotted versus time for each accumulation history. Bottom row shows the difference in depth to a given isochrone plotted versus depth.

Figure 6.12C shows the response of the layers to a steady increase ($0.1 \times 10^{-6} \text{ m a}^{-2}$) in the accumulation rate at Site B. The curves 1 and 2 correspond to different ages of the onset (2000 and 5000 years), but both increase at a rate ($0.5 \times 10^{-9} \text{ a}^{-2}$) toward the low end of the expected range required to move the Siple Dome divide (*Chapter 5; Nereson et al., 1998a*), assuming that Sites A and B are 20 km apart. The figure shows that if the accumulation rate gradient has been steadily increasing for the past 2000-5000 years, a detectable signal should be observed in the internal layer pattern ($\Delta z > 10 \text{ m}$). If the change has occurred more recently than 1500 years ago, the signal would be below our detection limit. Also plotted is the predicted response to a step-change occurring 3000 years before present (curve 3). The predicted response of the layers to this step-change is not distinguishable from a gradual change.

Some general conclusions can be drawn from this simple exercise. Recovery of information about past accumulation patterns from RES-detected internal layer shapes is limited by the sparseness of data, the measurement error, and the way this information is recorded in the internal layer pattern. Even if an infinite number of internal layers could be measured, the recovery of past changes is still limited because the cumulative strain of a given layer depends on the accumulation history since its deposition. It is possible for different accumulation histories to produce the same cumulative strain.

1. Infrequent changes of long duration ($> 5-10 \text{ ka}$) are detectable if the amplitude is greater than about 10% of the scale accumulation rate b_0 for recent times ($< 5 \text{ ka BP}$); the detectable amplitude must be greater for changes older than 10^4 a ($> H/b$).
2. Frequent changes of short duration ($\approx 2 \text{ ka}$) are detectable if the amplitude is at least 30-50% of the scale accumulation rate b_0 . Because of the compressed

time-scale at depth, frequent changes are only detectable in the upper portion of the ice sheet.

Moreover, it is difficult to distinguish between a gradual change in the accumulation pattern, and a step change, even for the shallowest layers.

6.9 Sensitivity to Changes in Ice Thickness

All analysis to this point has assumed constant ice thickness over time. However, Siple Dome is located in a very dynamic area of the West Antarctic Ice Sheet and it is likely that its thickness and configuration have been quite different in the past. One hypothesis is that during the LGM, the whole Siple coast was once much thicker and has subsequently thinned via retreat of the grounding line and/or initiation of ice stream activity. Initiation of streaming flow at the edges of what is now Siple Dome would cause a wave of rapid thinning to propagate inward from the ice stream margins to the present divide, analogous to the predicted thinning wave associated with a potential drop in sea-level for East Antarctica described by *Alley and Whillans* (1984). The effect of such thinning on the internal layer pattern and associated implications for the inferred accumulation pattern is not immediately clear.

I use a coupled surface-evolution and particle-tracking model (e.g., Waddington, 1981) to determine the effect of rapid thinning of Siple Dome on the internal layer pattern. The surface-evolution model uses a finite-difference scheme to solve the continuity equation:

$$\partial_t h = -\partial_x q + b(x, t); \quad (6.24)$$

In this application, we consider a flat-bed ice sheet deforming as an isothermal, parallel-sided slab so that the variation of horizontal velocity with depth is

$$u(x, z, t) = \frac{2A}{n+1}(\rho g)^n (\partial_x h(t))^n h(t)^{n+1} (1 - (1 - \tilde{z}^4)), \quad (6.25)$$

where $\tilde{z} = z/h(x, t)$, the flow parameter $A = 0.5 \times 10^{-17} \text{ Pa}^3 \text{ a}^{-1}$, Glen's flow law exponent $n = 3$, ice density $\rho = 917 \text{ kg m}^{-3}$, and gravity $g = 9.8 \text{ m s}^{-2}$. Ice flux q can be written in terms of the ice thickness profile h as:

$$q = \bar{u}h = \frac{2A}{n+2}(\rho g)^n (\partial_x h)^n h^{n+2}. \quad (6.26)$$

Equation (6.24) is solved explicitly with a prescribed accumulation history $b(x, t)$ on a finite difference grid with spacing of 2 km (about twice the ice thickness) and a time-step of 1 year. The initial profile is a symmetric 2-d ice divide, 1500 meters thick at its center, corresponding to a "Vialov" profile (*Vialov*, 1958) with spatially constant accumulation rate $b(x) = 0.10 \text{ m a}^{-1}$, and truncated at 50 km from the divide. The flux is calculated at the midpoint of each grid node as recommended by *Waddington* (1981). The ice thickness at the boundaries of the domain is prescribed. Changing ice stream activity is simulated by rapidly decreasing or increasing the ice thickness at the boundaries points at a prescribed rate.

A separate particle tracking model takes as input the geometry $h(x)$ and depth-averaged horizontal velocity field $\bar{u}(x)$ from the surface evolution model at 100-year intervals and interpolated to a 20-year time-step using Chebyshev polynomials. The vertical velocity field is determined from incompressibility,

$$\partial_x u = -\partial_z w. \quad (6.27)$$

The total velocity field is thus given by

$$u(x, z, t) = u_s(x, t)(1 - (1 - \tilde{z})^4) \quad (6.28)$$

$$w(x, z, t) = -\frac{\partial u_s(x, t)}{\partial x} H(x, t) \left(\tilde{z} + \frac{1}{5} \left((1 - \tilde{z})^5 - 1 \right) \right) \quad (6.29)$$

$$-u_s(x, t) \frac{\partial H(x, t)}{\partial x} \left(\tilde{z}(1 - \tilde{z})^4 + \frac{1}{5}(1 - \tilde{z})^5 - \frac{1}{5} \right). \quad (6.30)$$

where $u_s(x, t) = (5/4)\bar{u}(x, t)$. Ice particles originating at the surface are tracked in this time-dependent velocity field for 10-15 ka using a time step of 20 years. The age field is then contoured to reveal the shape of the internal layer pattern.

Figure 6.13 shows the internal layer shapes 3000 years after the initiation of a rapid 500-meter thinning of the ice stream. This thinning affects the shapes of internal layers such that the thinning scenario predicts generally flatter internal layers than the steady-state case. The relative flatness occurs because prior to thinning, the ice sheet itself was flatter and the internal layers at depth contain some “memory” of this former flow regime. At 40 km from the divide, the depth-difference is up to 15 meters. If such thinning occurred at Siple Dome, the inferred accumulation rate on the flanks of the dome would be too low relative to the divide. Since rapid synchronous thinning driven at the edges of the dome has only a modest effect on the layer shapes, the effects of gradual thinning would be minimal. The main effect of the thinning is to alter the age and annual layer thickness distribution (Fig 6.13c). Measurements of annual layer thicknesses and of ^{10}Be (a proxy for accumulation rate) (e.g., *Steig, 1997; Steig et al., 1998*) from the deep ice core would help determine whether thinning has occurred.

Figure (6.14) shows that rapid asymmetric ice thickness changes would significantly affect the internal layer pattern. Layers on the thinning side of the divide would appear shallower than in the steady state case (a result of the initial thicker and flatter ice sheet there), and we would under-predict accumulation rates there. Layers observed on the south flank of the Siple Dome appear to exhibit this feature since they are significantly shallower than layers on the north flank. Is this feature a signal of asynchronous thinning rather than the spatial variation of accumulation? The presence of a convex-up bump feature in the near-divide layer pattern (*Chapter 4; Nereson et al., 1998b*) and the near-steady state mass balance found at the

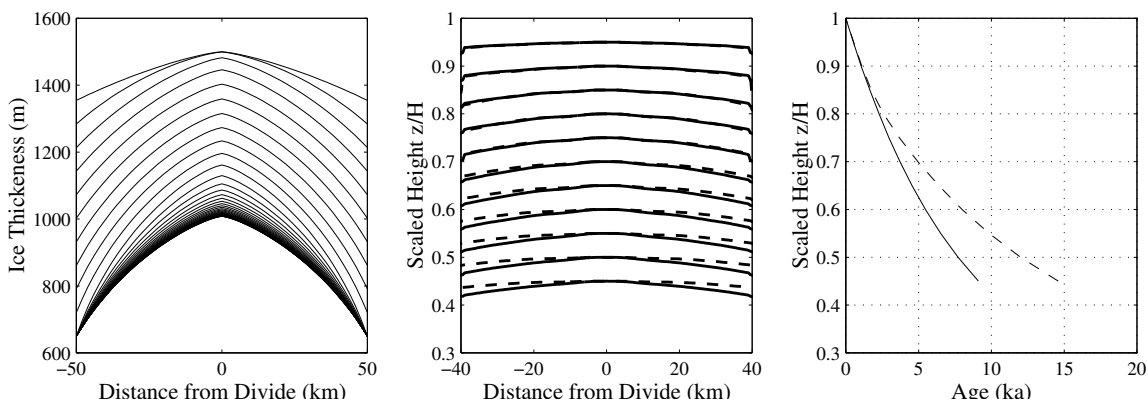


Figure 6.13: The effect of symmetric ice sheet thickness change on internal layer shapes for a 500-meter thinning which begins 3000 years before present. (a) Surface profiles at 100-year intervals. Thinning at the boundaries is complete after 1000 years with full adjustment of the surface after 4000 years. (b) Selected internal layer shapes for the steady state case (solid) and for the thinning scenario (dashed). (c) Age versus depth relationship at the summit for the steady-state case (solid), and for the thinning scenario (dashed).

Siple Dome summit (*Chapter 3*) suggest that major asynchronous thinning of Siple Dome in the past several thousand years is not likely. We therefore conclude that the spatial accumulation pattern and not asynchronous thinning is the cause of the shape of the shallow layers south of the divide.

6.10 Conclusions

A steady state ice flow model and minimization scheme are used to predict the pattern of accumulation over Siple Dome from the observed pattern of internal layering. Relative to the divide, the model predicts up to 60% less accumulation on the south flank of Siple Dome and about 40% more accumulation on the north flank. The pattern is consistent with the hypothesis that storms approaching Siple Dome from the north to deposit most of their moisture on the wind-ward side of the dome as a result of

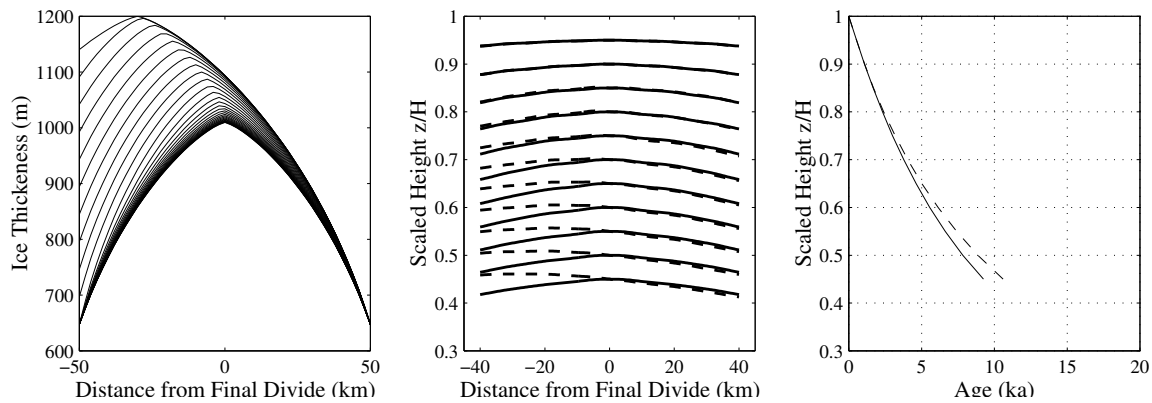


Figure 6.14: The effect of asymmetric ice sheet thickness change on internal layer shapes for thinning which begins 3000 years before present. (a) Surface profiles at 100-year intervals. Thinning at the boundaries is complete after 1000 years with full adjustment of the surface after 4000 years. (b) Selected internal layer shapes for the steady state case (solid) and for the thinning scenario (dashed). (c) Age versus depth relationship at $x = 0$ for the steady-state case (solid), and for the thinning scenario (dashed).

orographically induced uplift (e.g., *Bromwich, 1988*). Because the predicted pattern produces a match to the observed internal layer shapes at all depths to within errors, it is possible that the accumulation pattern has not changed in the past 10^4 years. However, the data do allow for a 15-30% decrease in the accumulation gradient north of the divide sometime between 5 – 15 ka BP.

Certain changes in the accumulation pattern over the past 10^4 years should produce a detectable signal in the internal layer pattern. Because RES layers sample the time domain infrequently (every 10^3 to 10^4 years) and because the internal layer shapes lose memory of accumulation changes, a low frequency, low amplitude change can be indistinguishable from a series of high-frequency, high-amplitude changes.

Synchronous thinning of the ice sheet would leave a minimal signal in the layer shapes, making them shallower toward the dome margins than predicted under steady

state. If such thinning has occurred then our analysis would under-predict the true accumulation rates far from the divide. Significant asynchronous thinning ($O(H/2)$) would significantly affect layer shapes. However, even small asymmetric changes would be accompanied by significant shifts in the divide position (*Chapter 5*; *Nereson et al.*, 1998a; *Hindmarsh*, 1996a). Since it appears that there have been no dramatic shifts in the divide position over the past several thousand years (*Chapter 4*; *Nereson et al.*, 1998b), and since it appears that the dome is not presently dramatically thinning or thickening (*Chapter 3*), we are not motivated to suspect this mechanism has significantly affected the layers at Siple Dome for at least the past several thousand years. However, we cannot rule out this possibility for older times without independent evidence.

If a gradual increase in the south-north accumulation gradient at $0.1 - 1.5 \times 10^{-9} \text{ a}^{-2}$ is the cause of the inferred divide migration, this signal should be detectable in the internal layer pattern. The internal layers at Siple Dome show no evidence for an increase in the accumulation gradient of this magnitude over the past 3-5 ka. Such a change would appear in the pattern of residuals shown in Figure 6.7. The spatial pattern of residuals allows only for a *decrease* in the accumulation gradient sometime during the past 5-15 ka. Although we cannot make conclusions about small changes in the accumulation pattern over the past 1500 ka (recent changes are not large enough to be detectable in the 2MHz RES layers), the existing evidence suggests that we can rule out changes in the accumulation pattern as the main cause of Siple Dome divide migration.

The likely candidates causing divide migration are changes occurring at the boundaries of Siple Dome at the margins of Ice Streams C and D. Small changes in elevation at these boundaries could lead to divide migration. Although rapid ($\sim 0.5 \text{ m a}^{-1}$) and sustained ($> 1000 \text{ a}$) asynchronous thinning of Siple Dome has been ruled out in

this analysis, smaller, second-order changes at the boundaries of Siple Dome sufficient to produce divide migration are possible.

Chapter 7

THE EVOLUTION OF ICE DOMES AND RELICT ICE STREAMS

This chapter is a manuscript in preparation for publication in the *Journal of Glaciology*.

7.1 Summary

A 2-D finite-difference continuity flow model is used to simulate the evolution of an inter-ice stream ridge flanked by stagnated ice streams. The model tracks the elevation of small scale features which form at the ice stream margin and shows that these features are initially lifted onto the flanks of the evolving dome before they are carried down-slope by ice flow. The time-scales which govern the evolution of the dome and the lifting of surface features can be estimated from the fundamental characteristics of the dome/stream system based on a perfectly-plastic description of ice flow. The volume adjustment time-scale corresponding to the incorporation of the stagnant Siple Ice Stream adjacent to the NE flank of Siple Dome is about 1000-1500 years. The present geometry and elevation of scar features on both flanks of Siple Dome suggest that the dome is in the early stages of dome/stream evolution and that the relict ice streams have stagnated less than 500 years ago.

7.2 Introduction

Several small ice domes and ridges along the Siple Coast of the West Antarctic Ice Sheet (WAIS) are commonly bounded by linear topographic features with widths on

the order of the ice thickness on their flanks (*Scambos et al.*, 1998). One of these features has been interpreted as a former ice stream margin (*Jacobel et al.*, 1996). New satellite imaging techniques and detailed GPS surveys have enabled detailed mapping of the spatial pattern and elevation of these “scar” features (*Scambos et al.*, 1998). Scar features on Siple Dome, the ridge between Ice Streams C and D, lie 20–100 meters above the level of active or recently active ice streams (Fig. 7.1). If these features are markers left behind by a former flow regime, then their present elevation and shape may hold information about the timing and nature of WAIS evolution.

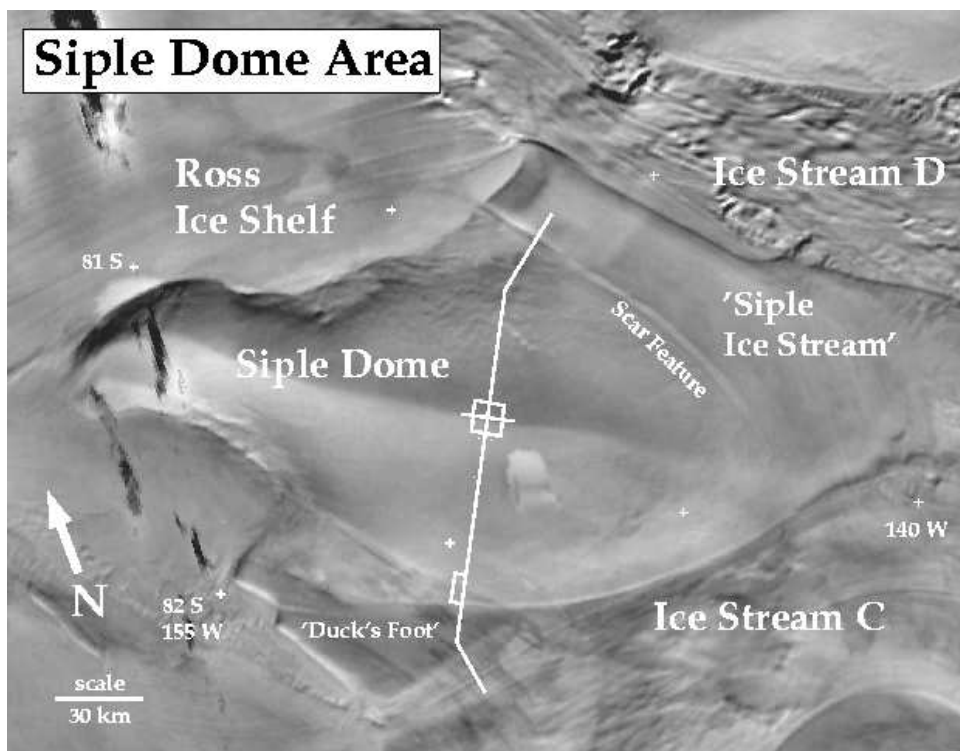


Figure 7.1: AVHRR image of Siple Dome and Ice Streams C and D showing linear topographic “scar” features on the flanks of Siple Dome labeled “scar feature” and “Duck’s Foot”. Courtesy of T. Scambos, National Snow and Ice Data Center, University of Colorado.

One hypothesis about these features is that their elevation relative to the surroundings is indicative of recent thinning of WAIS along the Siple Coast, and these scar features mark the “trimline” of past ice sheet elevation (*G. Hamilton, pers. comm.*; *T. Scambos, pers. comm.*). I propose a second, alternative hypothesis that following the shut-down of an ice stream, adjacent inter-ice stream ridges are allowed to expand into former actively streaming regions. A wave of thickening which travels faster than the ice causes small scale topographic features associated with the former margin of the ice stream to be lifted onto the flank of the ridge.

This chapter develops the second hypothesis. A 2-d continuity model is used to show that expansion of an ice dome into a formerly active ice stream would initially lift small-scale topographic features onto the flanks of dome. As the dome reaches a new steady state, ice flow carries the feature down slope. For a wide range of dome characteristics, even modest dome expansion results in scar uplift for an initial period. A simple analytic calculation relates the timing of this evolution to fundamental characteristics of the ice-sheet/ice-stream geometry.

This chapter does not address the evolution of the scar features themselves. These features generally have topographic wavelengths ranging from 1 to 4 ice thicknesses (*Scambos et al., 1998*). Linearized perturbation theory predicts that undulations in the surface should diffuse rapidly in time. Why these features appear to persist over time remains an open question, but is probably related to their spatial scale (*Gudmundsson et al., 1998*). We assume that the topographic features are sufficiently small that they do not diffuse away quickly, and they are carried along by ice flow as passive markers on the ice surface, much like wave ogives (e.g., *Nye, 1959b*; *Waddington, 1986*).

7.3 *Finite Difference Continuity Model*

A 2-d finite-difference continuity model (hereafter referred to as the “FD model”) is used to track the elevation history of scar features on an evolving ice dome initially flanked by ice streams. The initial surface profile is assumed to be a steady state dome truncated at its flanks by flat sections of ice representing relict ice streams which once flowed perpendicular to the 2-d plane. Prior to stagnation, dome flow into the ice stream is assumed steady-state and two-dimensional. Stream flow is perpendicular to dome flow. All flux from the dome at the ice stream margin is incorporated into the ice stream. At time $t = 0$, stream flow ceases along the relict ice stream and all ice flow in the domain is assumed to be constrained to the 2-d plane (Figure 7.2). We assume symmetry about the divide, so that there is no divide migration during evolution. The new ice stream margin at the edge of the domain is held at its initial elevation by some external constraint such as another active ice stream. For the Siple Dome/Siple Ice Stream/Ice Stream D system for example, we assume that the activity of Ice Stream D is unchanged after stagnation of Siple Ice Stream so that its margin with Siple Ice Stream is held at a fixed elevation. After ice stream shut down, the dome is allowed to expand into the relict ice stream and reach a new steady state configuration according to continuity relationships. As ice accumulates on the relict ice stream and as the dome evolves, a slope develops at the new ice stream margin. All ice flux at this point is incorporated into the still-active ice stream (Ice Stream D for example). The scar feature, initially located at the boundary between the ice dome and the relict ice stream at $t = 0$, is assumed to be a passive marker on the ice surface and is tracked through this evolution process.

In two dimensions, the evolution of the ice thickness $h(x)$ through time t is described by the continuity relation,

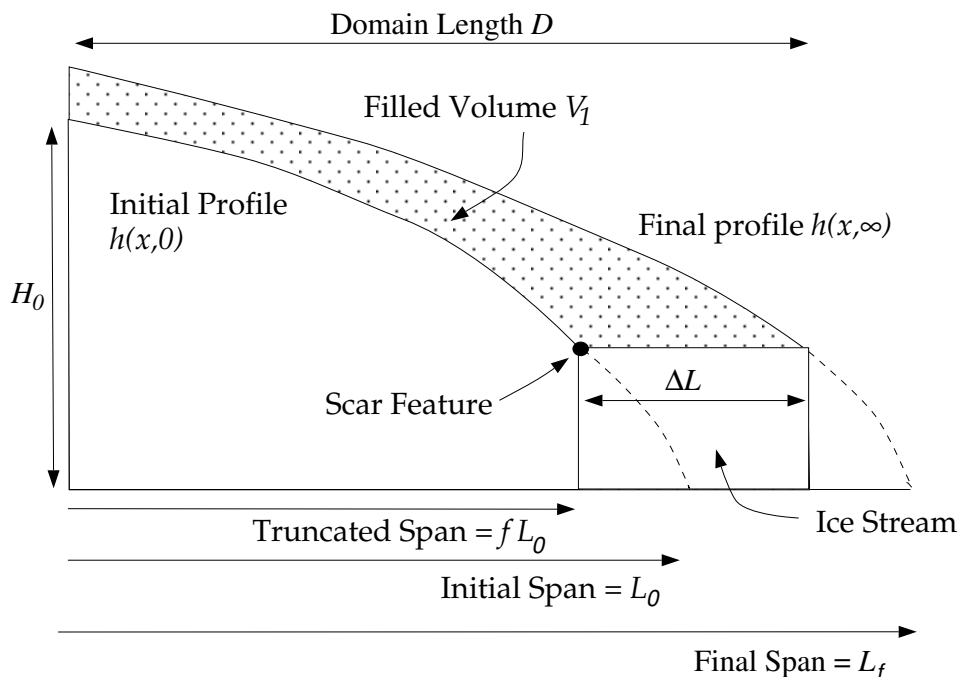


Figure 7.2: Schematic of the initial and final states of simplified ice dome/relict ice stream system. Lined area denotes the portion of the dome which grows during the evolution process. Stippled area denotes the total volume added during evolution.

$$\partial_t h(x, t) = -\nabla_2 q + b(x, t), \quad (7.1)$$

where x is the distance along flow from the divide, y is the transverse horizontal coordinate, and b is the mass balance. The horizontal divergence of ice flux $\nabla_2 q$ is

$$\nabla_2 q = \partial_x q_x + \partial_y q_y, \quad (7.2)$$

where (q_x, q_y) are the horizontal components of ice flux. Assuming that the ice thickness does not vary across the flow line ($\partial_y h = 0$) and that the transverse velocity component is zero ($\bar{v} = 0$), the horizontal flux divergence $\nabla_2 q$ becomes

$$\nabla_2 q = \partial_x(\bar{u}h) + h\partial_y\bar{v}. \quad (7.3)$$

The variation in depth-averaged velocity perpendicular to flow ($\partial_y\bar{v}$) can be expressed in terms of the variation in width between adjacent flow lines W (*Paterson, 1994*)

$$\partial_y\bar{v} = \frac{\bar{u}}{W}\partial_x W. \quad (7.4)$$

The horizontal flux divergence can then be written as

$$\nabla_2 q = \frac{1}{W}\partial_x(W\bar{u}h). \quad (7.5)$$

The depth-averaged velocity along flow \bar{u} is derived from the velocity solution for a parallel-sided slab deforming according to Glen's flow law (*Paterson, 1994*),

$$\bar{u} = -\frac{2\bar{A}}{n+2}(\rho g)^n(\partial_x S)^n h^{n+1}, \quad (7.6)$$

where $S(x)$ is the ice surface profile, \bar{A} is an effective depth-averaged flow parameter, ice density $\rho = 917 \text{ kg m}^{-3}$, gravitational acceleration $g = 9.8 \text{ m s}^{-2}$, and the flow law exponent $n = 3$. The parameter A ranges from $1 \times 10^{-17} \text{ Pa}^{-3} \text{ a}^{-1}$ to $1 \times 10^{-16} \text{ Pa}^{-3} \text{ a}^{-1}$ depending on the accumulation rate and desired initial dome/stream configuration. For the calculations presented in this chapter, we assume a flat bed ($S(x) = h(x)$) and $W = 1$.

The continuity equation (7.1) is solved on a finite-difference grid with horizontal spacing of 2 km. The flux is calculated at the midpoint of each cell and the horizontal spacing is about 2 ice thicknesses. Additional smoothing of the surface slope is not needed to prevent numerical instabilities (*Waddington, 1981; Bindshadler, 1982*). The elevation at the boundaries of the domain is held fixed throughout the calculation. Ice thickness is extrapolated one grid point beyond the domain to determine the

flux derivative at the boundary points. The model is stepped forward at 0.5-year increments using an explicit method. The ice thickness and slope from time step i are used to predict the ice flux at the next time step $i + 1$.

We are also interested in the elevation history of a feature on the ice sheet surface. We assume that the feature remains at the ice surface as snow accumulates. The vertical motion of a point on the ice sheet can be written as

$$d_t z(x, t) = u_s \partial_x h(x, t) + \partial_t h(x, t), \quad (7.7)$$

where u_s is the horizontal velocity at the ice surface. The first term represents the advection of ice thickness, while the second term represents an increase or decrease in surface elevation from dome evolution. The horizontal motion of an ice particle at the surface is

$$d_t x = u_s. \quad (7.8)$$

Equations (7.7) and (7.8) are used to track the position of the scar feature as the dome evolves.

We use this ice flow model to simulate an ice dome/ice stream system with characteristics similar to those found on the Siple Coast in West Antarctica, where ice thickness $H = 600 - 1000$ m, span $L = 20 - 50$ km, and accumulation rate $b = 0.10 - 0.20$ m a⁻¹ ice equivalent. For simplicity, a flat bed and constant accumulation rate are assumed. Figure 7.3 shows the evolution of the ice dome under several scenarios: different dome/stream intersection points, different accumulation rates, different ice stream widths. Figure 7.4 shows the evolution scenarios for a smaller ice dome.

In all cases, scar features are initially lifted onto the flanks of the evolving dome by a wave of thickening which travels faster than the ice (Fig. 7.5). As the ice dome approaches a new steady state, ice flow carries the scar features down-slope

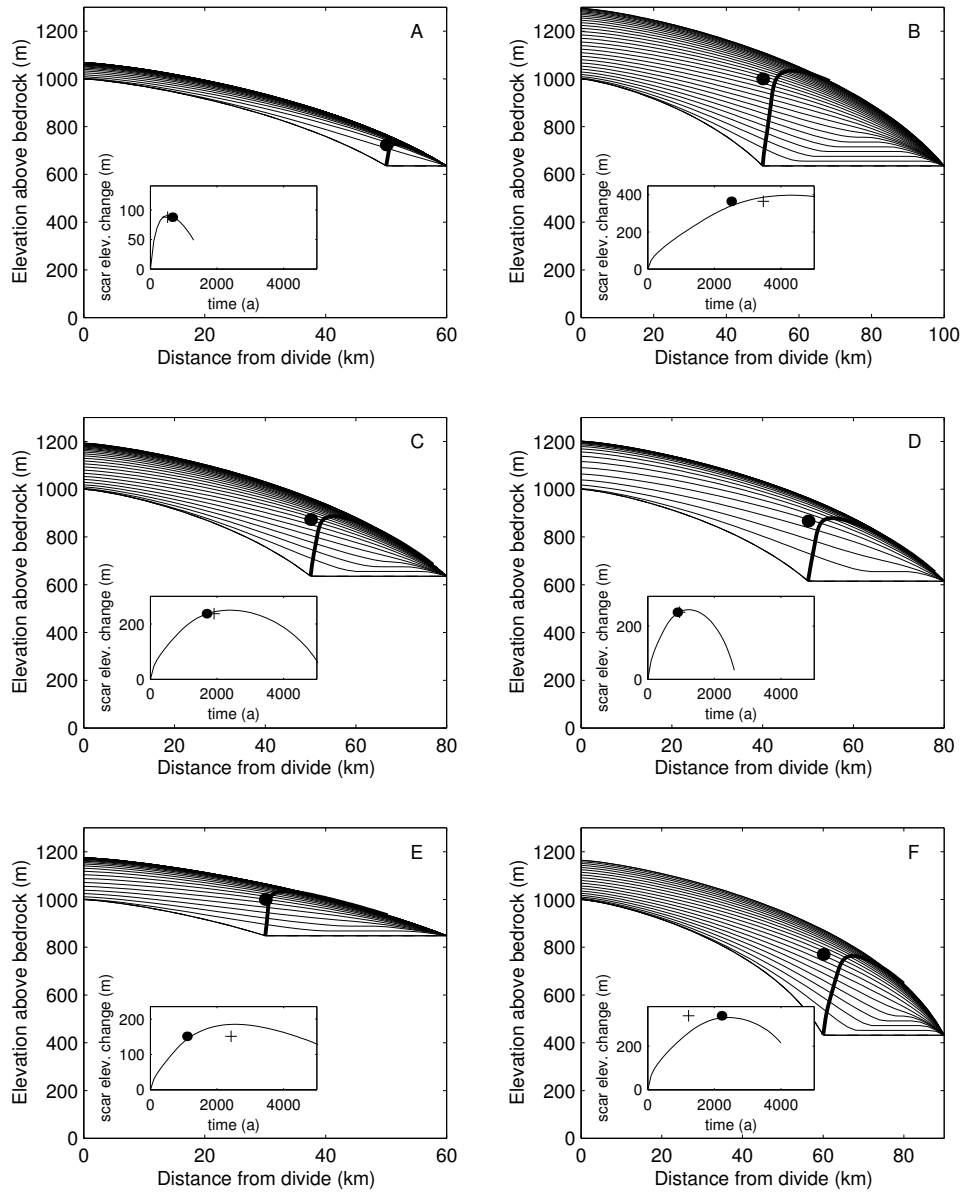


Figure 7.3: Ice surface profiles plotted every 200 years for an evolving ice dome similar in size to Siple Dome. The heavy line in each panel traces the position of a scar feature formed at the margin of a relict ice stream. The black dot shows the position of a scar feature at its maximum elevation predicted from an analytic description of the problem. Inset panels show the scar elevation over time with the predicted time of maximum elevation denoted by + (t_c , eq. 7.26) and \bullet (τ_{fill} , eq. 7.11). For all cases, $b = 0.10 \text{ m a}^{-1}$, except for panel (d) where $b = 0.20 \text{ m a}^{-1}$.

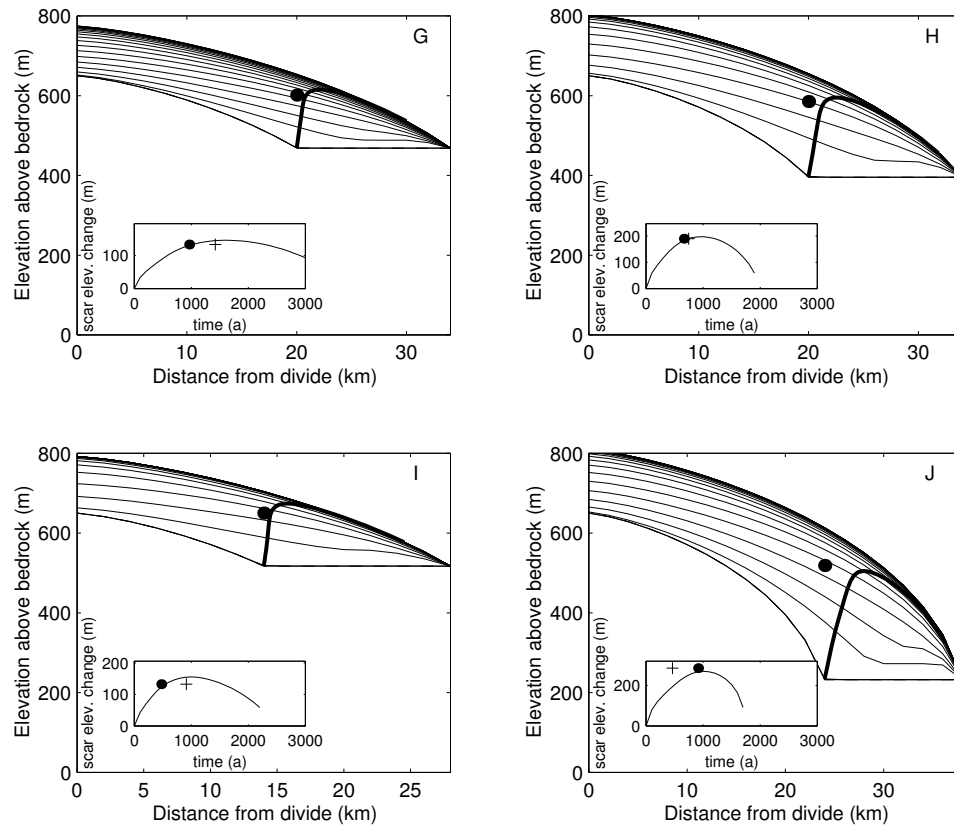


Figure 7.4: Ice surface profiles plotted every 200 years for a small ice dome. The heavy line in each panel traces the position of a scar feature formed at the margin of a relict ice stream. The black dot shows the position of a scar feature at its maximum elevation predicted from a perfectly plastic description of the problem. Inset panels show the scar elevation over time with the predicted time of maximum elevation denoted by + (t_c , eq. 7.26) and • (τ_{fill} , eq. 7.11). For all cases, $b = 0.20 \text{ m a}^{-1}$, except for panel (a) where $b = 0.10 \text{ m a}^{-1}$.

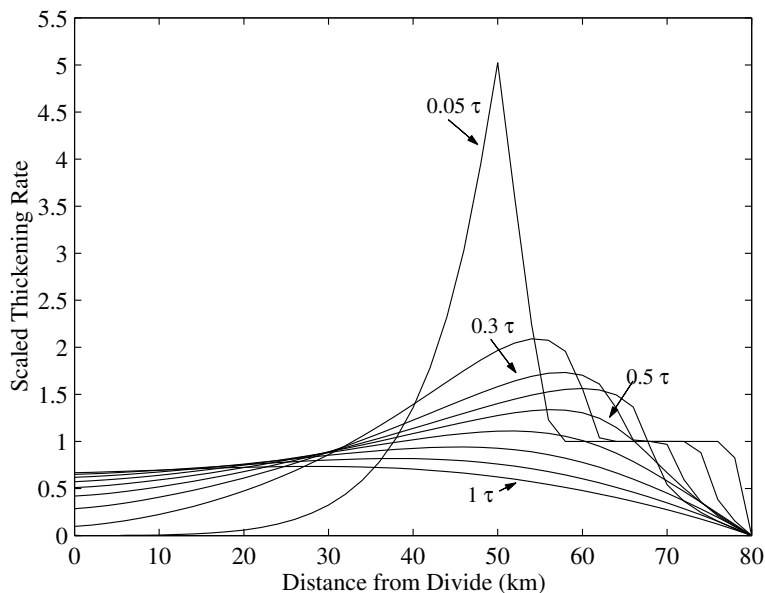


Figure 7.5: Propagation and diffusion of the wave of thickening for case C in Figure 7.3. The thickening rate is scaled to the accumulation rate and the curves are drawn every 200 years and labeled in units of $\tau = \tau_{fill}$. The wave is spread over the domain after about 0.5τ . The wave is almost completely diffused after about 1τ .

and their elevation decreases. The timing of these events is faster for ice sheets with high accumulation rates and narrow relict ice streams (Fig. 7.3a and d). Scars reach high elevations when the relict ice stream is wide (Fig. 7.3b). The timing and maximum elevation seem to be insensitive to where the dome is initially truncated by the stagnated ice stream (Fig. 7.3e and f). The accumulation rate affects only the timing of the elevation process, but not the extreme elevation of the scar feature (Fig. 7.3c and d).

The wave of thickening which propagates over the dome is shown in Figure 7.5 for case C from Figure 7.3. The rate of thickening is scaled to the accumulation rate and the curves, drawn in 200-year increments, are labeled in units of the volume adjustment time-scale $\tau = \tau_{fill}$ which we derive in a later section. For this case

$\tau_{fill} = 1700$ years. The thickening wave is spread over the domain after about 0.5τ . The wave is almost completely diffused after about 1τ .

We have assumed that the margin of the relict ice stream at the edge of the domain is fixed at its initial thickness as if it were a new margin of an active ice stream. Another possibility is that the elevation of this margin is not fixed by another ice stream, but is controlled by evolution of the region outside of the domain. Figure 7.6 shows the growth of a dome/stream system assuming an infinitely wide ice stream so that the edge of the domain is allowed to thicken at the accumulation rate following its stagnation. In this case, the scar feature is raised indefinitely as long as the boundaries are allowed to thicken.

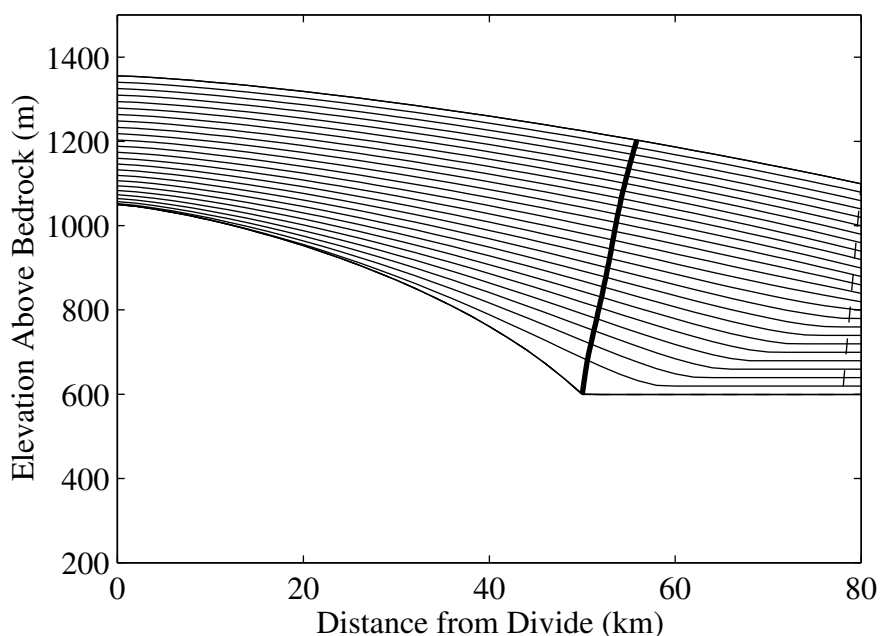


Figure 7.6: Surface profiles of an evolving ice dome drawn every 200 years where the right edge of the relict ice stream is allowed to thicken at the accumulation rate after stagnation. The track of the scar feature is shown by the heavy solid line. The spatially constant accumulation rate is assumed 0.10 m a^{-1} .

7.4 Analytic Evolution Model

Numerical models can be computationally intensive and are generally applicable only to a specific set of initial conditions and assumptions used as input to the model. An analytic description of dome evolution and scar feature elevation is needed to address the general case and for quick estimates of the relevant time and length scales. In this section, the fundamental time-scales which govern the evolution of truncated ice domes and the elevation of scar features are derived from a perfectly-plastic description of ice sheet evolution.

Consider a perfectly plastic ice sheet on a flat bed with thickness $h(x)$ and horizontal coordinate x . Its thickness profile is given by the solution to the force balance equation,

$$\sigma_b = -\rho gh \frac{\partial h}{\partial x}, \quad (7.9)$$

where σ_b is the basal shear stress. Assuming σ_b is everywhere equal to the yield stress σ_0 , the surface profile is given by

$$h(x) = K(L - x)^{1/2} \quad (7.10)$$

where $K = 2\sigma_0/\rho g$ and L is the span (Nye, 1952).

To simulate an inter-ice stream ridge, we truncate the profile at a hypothetical ice stream margin at $x = fL < L$ where $0 < f < 1$, and assume that the interior ice flows as if the ice ridge has a width of length L . L is then its “virtual span” (Fig. 7.2). A scar feature is formed at the ice stream margin $x = fL$. Suppose that this ice stream shuts off at $t = 0$. If flow is confined to 2 dimensions, the dome will expand into the old ice stream and approach a new steady state profile. A perfectly plastic ice sheet responds instantaneously to a change in its mass balance or boundary conditions by changing its thickness and width while maintaining its characteristic parabolic profile. Diffusion of surface perturbations occurs instantaneously. Therefore, evolution of a

plastic ice dome to a new steady profile will proceed through a series of parabolic ice sheet profiles described by the evolution of the 'virtual span' $L(t)$.

The time-scale for evolution of the plastic dome can be described in terms of a "volume filling time", discussed by *Jóhannesson et al.* (1989) for valley glaciers. The volume filling time-scale for the dome/stream case is the time it takes to fill the volume per unit width V_1 , denoted by the stippled region in Figure 7.2, given the spatially constant accumulation rate b over the domain of length D :

$$\tau_{fill} = \frac{V_1}{bD}. \quad (7.11)$$

The main problem with equation 7.11 is that V_1 may be difficult to estimate if the final ice sheet profile is unknown. *Jóhannesson et al.* (1989) assumed that the final ice surface has a similar shape as its initial surface and estimated the volume change by shifting the glacier profile according to its change in length. This approximation is only valid for small changes in glacier span and therefore not generally applicable to the dome/stream case.

For a perfectly plastic ice sheet, V_1 has an exact analytical solution. Integrating equation (7.10) with respect to x for the initial (subscript 0) and final (subscript f) profiles yields the non-truncated volume change:

$$V_{tot} = \frac{2}{3}K \left(L_f^{3/2} - L_0^{3/2} \right) \quad (7.12)$$

The ice stream volume is

$$V_{stream} = (L_f - L_0)K(L_0 - fL_0)^{1/2}. \quad (7.13)$$

The volume of interest V_1 is then

$$V_1 = V_{tot} - V_{stream} \quad (7.14)$$

$$= \frac{2}{3}K(L_f^{3/2} - L_0^{3/2}) - (L_f - L_0)K L_0^{1/2}(1 - f)^{1/2}. \quad (7.15)$$

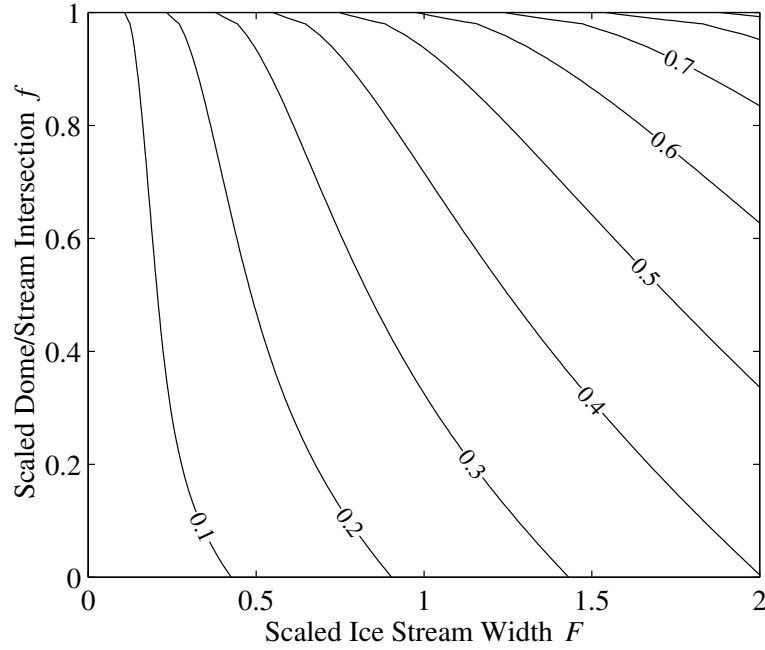


Figure 7.7: Contours of growth time τ_{fill}/τ_0 versus dome/stream intersection position f and scaled ice stream width F

Assuming the ice stream width $\Delta L = FL_0$ is some fraction F of the initial span L_0 , then $D = L_0(F+f)$ and $L_f = L_0(1+F)$. Substituting these expressions, $H_0 = KL_0^{1/2}$, and V_1 into equation (7.11), the total time required for the plastic ice sheet to evolve to its final state is

$$\tau_{fill} = \frac{H_0}{b} \left(\frac{\frac{2}{3}((1+F)^{3/2} - 1) - F(1-f)^{1/2}}{f+F} \right). \quad (7.16)$$

This characteristic adjustment time is related to the fundamental time-scale $\tau_0 = H_0/b$ modified by terms which represent the extent of ice dome growth F and the dome/stream intersection point f . The characteristic time is independent of the initial ice volume and depends only on volume difference between the initial and final ice sheet profiles.

Figure 7.7 shows how the dome/stream adjustment time-scale τ_{fill} , normalized

to the fundamental time-scale $\tau_0 = H_0/b$, varies with the dome/stream intersection factor f and the ice stream width factor F . The adjustment time-scale increases with increasing F and as $f \rightarrow 1$. The dependence of the time-scale on f is expected because ice sheets truncated near their divides (small f) are associated with a smaller total volume change than if truncated near the margin (large f). Dependence of the volume evolution time-scale on f is not as strong in the FD model (e.g., Fig. 7.3e and f, Fig 7.4b, c and d). The weak dependence in the FD model arises because of diffusion and advection effects. For a given ice stream width, ice sheets truncated high on their flanks near the divide are associated with a small volume change V_1 which would tend to decrease the total adjustment time. However, the mean slope here is also small causing slow flow rates and tending to lengthen the adjustment time. Ice sheets truncated low on their flanks have a larger volume change V_1 (contributing to a longer adjustment time), but they also have a higher mean slope and larger flow rates (contribution to shorter adjustment time). The net result is that diffusion and advection in a non-plastic ice sheet tend to diminish the dependence of the adjustment time-scale on f predicted for a plastic ice sheet.

For a doubling of the ice sheet span where $f = 1$ and $F = 1$, $\tau_{fill} \approx 0.6H_0/b$. For small growth where $F \ll 1$ and $f = 1$, τ_{fill} reduces to

$$\tau \approx \frac{H_0}{b} \frac{\Delta L}{L_0}. \quad (7.17)$$

For non-plastic ice sheets, there is a non-zero characteristic adjustment time-scale even in the limit $\Delta L \rightarrow 0$ (e.g., *Chapter 5; Nereson et al.*, 1998a). This is because diffusion processes are slower for non-plastic ice sheets and are instantaneous for plastic ice sheets. Therefore, we expect the plastic approximation to break down when ΔL is small.

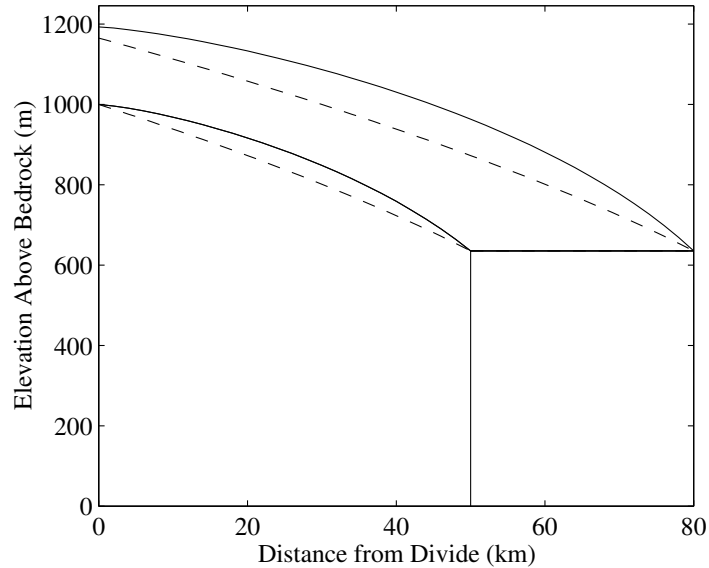


Figure 7.8: A comparison between the initial and final surface profiles from an FD model calculation (solid lines) and from a perfectly plastic approximation (dashed lines). The parameter K in equation 7.10 is chosen so that initial plastic profile matches the FD model profile at the divide and at the ice stream margin. The span of final plastic profile L_f is chosen so the profile matches the final FD profile at the right ice stream margin.

7.5 Numeric vs. Analytic Comparison

The utility of estimating the adjustment time-scales from a perfectly plastic description of ice flow is realized only if the estimated time-scales agree with those predicted from a more realistic description of ice flow. To test the utility of using equation (7.11) to estimate dome/stream adjustment time-scales, I compare this estimate to the evolution time-scales predicted by the FD model which includes a more realistic ice flow description. Figure 7.8 shows the representative plastic ice sheet profiles used to approximate the initial and final profiles from the FD evolution model and to calculate V_1 . The parameter K in equation (7.10) is chosen so that the initial representative

plastic ice sheet matches the FD ice sheet at the divide and at the position of the scar feature. The final plastic profile $h(x, \infty)$ is chosen to match the FD final profile at the margin of the relict ice stream at the edge of the domain. The total volume change V_1 predicted using these plastic profiles is about 20-25% less than the FD volume change (Table 1).

Figure 7.9 compares the plastic volume evolution given by equation (7.11) to the volume evolution predicted by the FD model (curves A and B). Because the volume change is scaled to V_1 from the FD model, growth of the plastic ice dome terminates at a scaled volume which is less than unity after time $t = \tau_{fill}$. Volume growth initially occurs at the same rate for both the FD model and the plastic case (curves A and B). This initial agreement is expected. The boundary at the edge of the relict ice stream does not initially affect interior ice flow in either model. The volume growth rate is initially determined only by the accumulation falling on the dome so that the dome grows at the same rate for both cases. Eventually, a slope develops at the ice stream margin in the FD model, increasing ice flux away from the dome, and slowing dome growth. This does not happen during evolution of the plastic ice sheet.

An asymptotic exponential curve $(1 - \exp(-t/\tau_{fill}))$ is also shown in Figure 7.9. It is clear that for at least two cases (curve C, middle and right columns), the FD volume evolution is approximately exponential with a characteristic time-scale close to τ_{fill} . As expected, the plastic approximation fails to match the FD model at small ΔL . Assuming laminar power-law flow with power exponent $n = 3$, *Nereson et al.* (1998a) predicted the adjustment time-scale for small perturbations at the boundaries of Siple Dome to be about 700 years (*Chapter 5*). This time-scale is consistent with the FD model for small ΔL which assumes the same physics of ice flow (Figure 7.9, left column).

It is somewhat coincidental that τ_{fill} is a good estimate of the exponential growth

time-scale for the FD model. The good agreement is at least partially due to the fact that the volume V_1 is about 25% less in the plastic case (Fig. 7.8). If the two methods produced the same value for V_1 , we would over-predict the characteristic time-scale. We are therefore motivated to ask whether τ_{fill} is an appropriate time-scale for a wide range of dome/stream cases, such as those shown in figures 7.3 and 7.4.

Figure 7.10 shows a comparison among (1) the evolution of V_1 from the FD model (pluses), (2) the curve $1 - \exp(-t/\tau)$ where τ is determined by a least-squares fit to V_1 (solid), (3) and the curve $1 - \exp(-t/\tau)$ where $\tau = \tau_{fill}$ (dashed) for all dome/stream configurations shown in Figures 7.3 and 7.4. Table 1 shows the least-squares fit time-scale and its fractional difference from τ_{fill} . The estimate τ_{fill} consistently predicts the fitted FD adjustment time-scale to within about 10%. These comparisons show that estimation of the adjustment time-scale from equation (7.11) using a plastic approximation of the volume change is reasonable even for a non-plastic description of ice-flow.

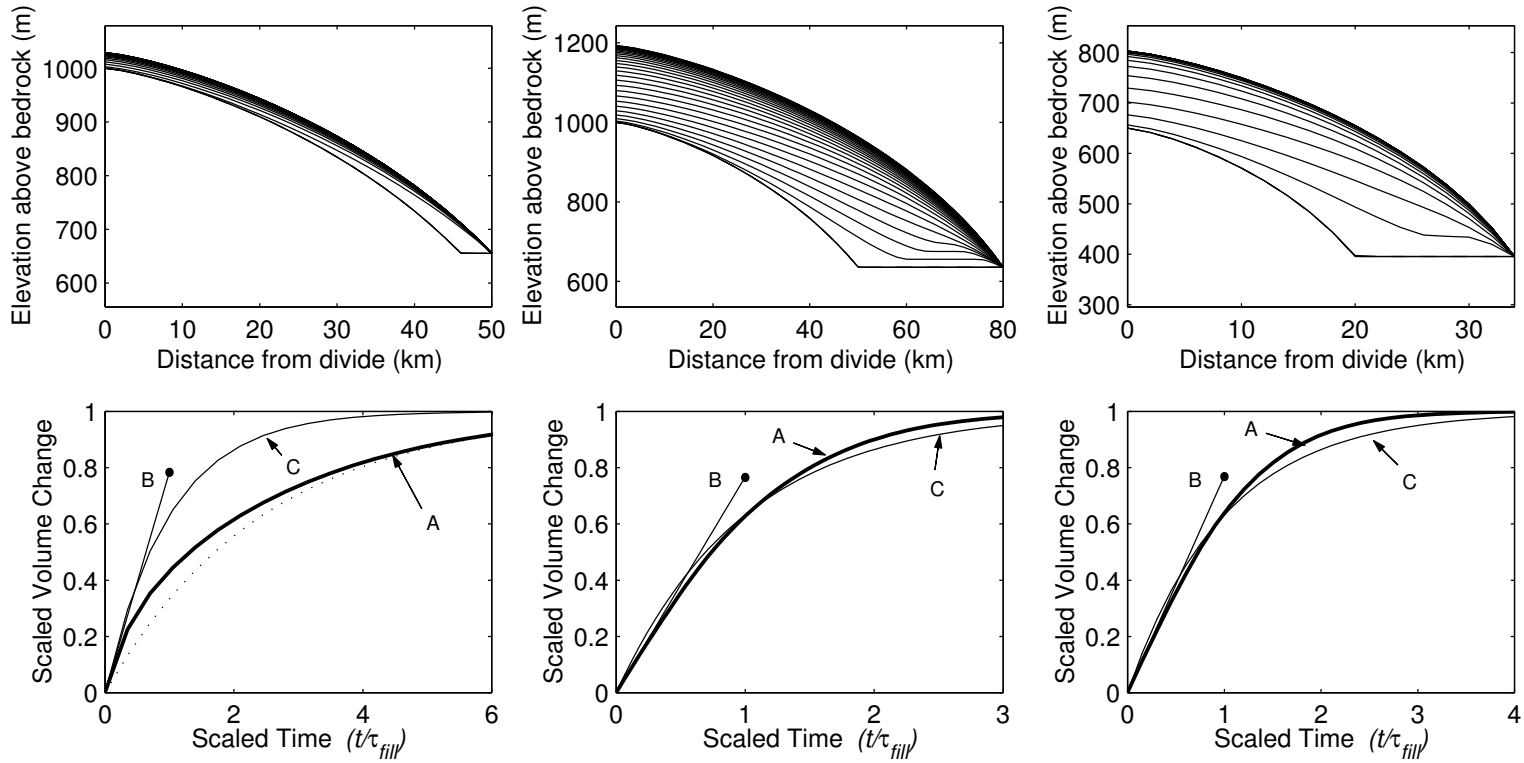


Figure 7.9: Comparison of ice dome evolution predicted by the finite-difference model and by an analytic approximation based on a perfectly-plastic ice sheet. The upper panels show the evolution of surface profiles predicted by the finite difference model in 200-year increments for three cases: (left) $\Delta L = 4$ km, $b = 0.10$ m a $^{-1}$, $H_0 = 1000$ m; (middle) $\Delta L = 30$ km, $b = 0.10$ m a $^{-1}$, $H_0 = 1000$ m; (right) $\Delta L = 15$ km, $b = 0.20$ m a $^{-1}$, $H_0 = 650$ m. Lower panels show (A) the normalized volume change for the finite-difference model (V/V_∞), (B) linear growth of the ice dome t/τ_{fill} from equation (7.11), and (C) the approximation $(1 - \exp(-t/\tau_{fill}))$. The dotted line in the lower left panel shows the volume evolution given a time-scale predicted by linearized perturbation theory ($\tau \approx 700$ a, *Nereson et al.*, 1998a).

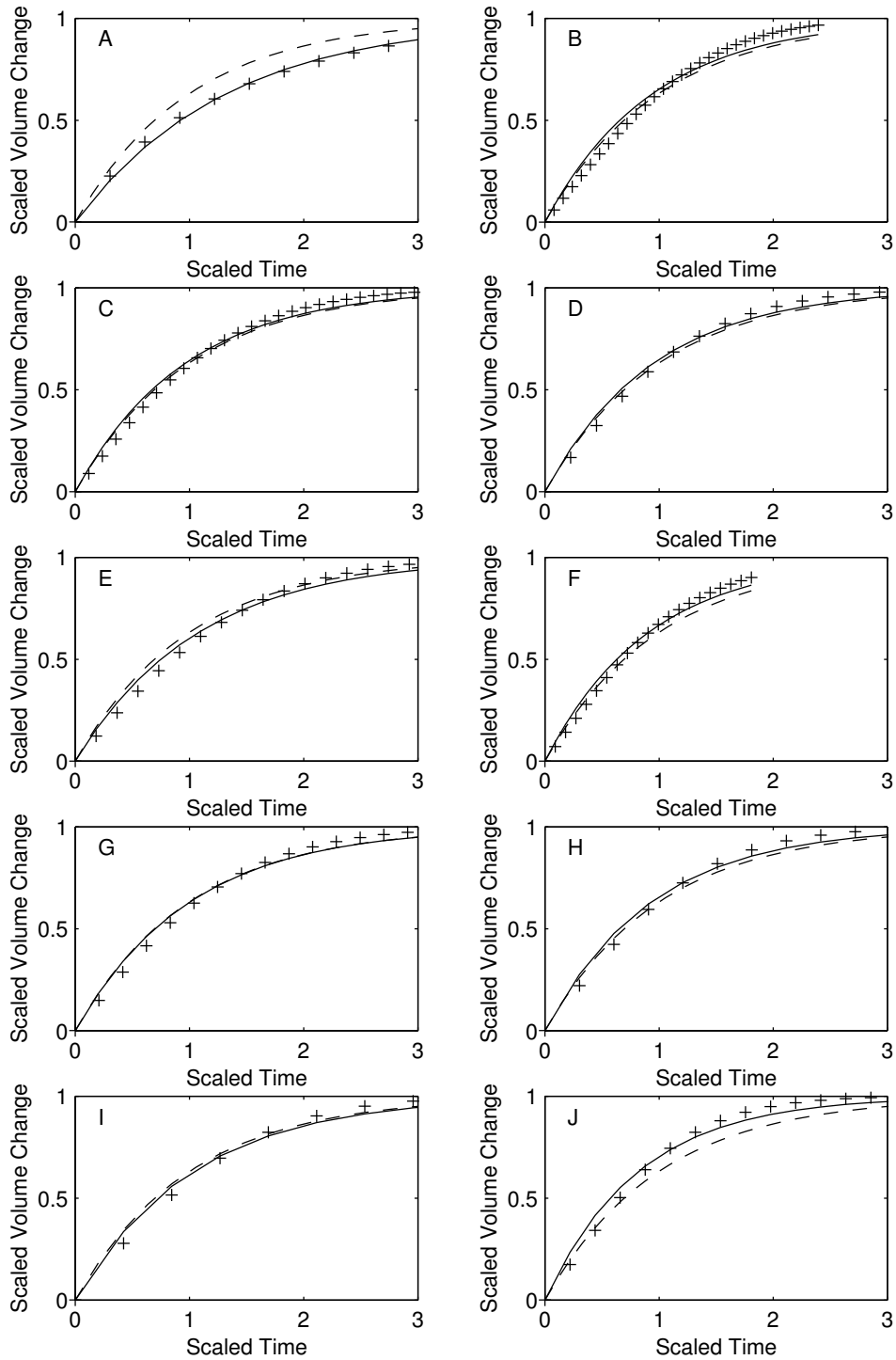


Figure 7.10: Volume evolution $V_1(t)$ scaled to $V_1(\infty)$ according to the FD model for 10 dome/stream evolution cases as summarized in Table 1 and shown in Figures 7.3 and 7.4. Plus markers (+) denote the volume evolution of the FD model. The solid curve is a least squares fit of the equation $1 - \exp(-t/\tau)$ to the FD evolution. The dashed curve corresponds to $1 - \exp(-t/\tau)$ where $\tau = \tau_{fill}$. Time is presented in units of τ_{fill}

Table 7.1: Volume evolution time-scales derived from equation 7.11 using the values listed in the lower table elements for cases A through J shown in Figures 7.3 and 7.4. The numbers in parentheses are the fractional difference in percent from the fitted time-scale τ_{fit} . The last row shows the fractional difference of the total volume change between the FD model and the plastic approximation of V_1 from equation 7.15.

| | Case | | | | | | | | | |
|---------------------------|----------|----------|----------|---------|----------|-----------|-----------|---------|---------|----------|
| | A | B | C | D | E | F | G | H | I | J |
| τ_{fit} (a) | 864 | 2371 | 1631 | 845 | 1181 | 2008 | 966 | 617 | 489 | 745 |
| τ_{fill} (a) | 656 (24) | 2506 (6) | 1684 (3) | 887 (5) | 1095 (7) | 2213 (10) | 963 (< 1) | 662 (7) | 473 (3) | 911 (22) |
| H_0 (m) | 1000 | 1000 | 1000 | 1000 | 1000 | 1000 | 650 | 650 | 650 | 650 |
| ΔH (m) | 58 | 263 | 165 | 171 | 131 | 186 | 101 | 130 | 110 | 148 |
| L_0 (m) | 83,874 | 83,874 | 83,874 | 80,412 | 106,989 | 73,752 | 41,571 | 31,748 | 38,134 | 27,512 |
| ΔL (m) | 10,000 | 50,000 | 30,000 | 30,000 | 30,000 | 30,000 | 15,000 | 15,000 | 15,000 | 15,000 |
| K ($\text{m}^{1/2}$) | 3.45 | 3.45 | 3.45 | 3.53 | 3.06 | 3.68 | 3.19 | 3.65 | 3.33 | 3.92 |
| b (m a^{-1}) | 0.10 | 0.10 | 0.10 | 0.20 | 0.10 | 0.10 | 0.10 | 0.20 | 0.20 | 0.20 |
| f | 0.60 | 0.60 | 0.60 | 0.62 | 0.28 | 0.81 | 0.48 | 0.63 | 0.37 | 0.87 |
| $\Delta V_1/V_1$ (%) | 22 | 24 | 23 | 23 | 29 | 20 | 25 | 23 | 28 | 18 |

7.6 Tracking the Scar Features

Assuming the scar feature remains on the ice surface as snow accumulates, its vertical position through time can be written as

$$d_t z(x, t) = u_s \partial_x h(x, t) + \partial_t h(x, t). \quad (7.18)$$

The first term represents the advected thickness, while the second term represents an increase or decrease in elevation from dome evolution. A given point on the ice surface remains at its original elevation when these two terms are equal. Assuming dome growth so that $\partial_t h > 0$, we define

$$\mathcal{R} = -\frac{\partial_t h}{u_s \partial_x h}. \quad (7.19)$$

When $\mathcal{R} = 1$, the vertical position of the scar feature is static; when $\mathcal{R} < 1$, its elevation decreases; and when $\mathcal{R} > 1$ its elevation increases.

Since the volume evolution has an exponential character and $V \propto L^{3/2}$, the span evolution $L(t)$ can be written as a similar exponential function of time,

$$L(t) = L_f - \Delta L \exp(-t/\tau), \quad (7.20)$$

where

$$\tau = \tau_{fill}. \quad (7.21)$$

The numerator in equation (7.19) is then

$$\frac{\partial h}{\partial t} = \frac{K}{2}(L-x)^{-1/2} \frac{\partial L}{\partial t} \quad (7.22)$$

$$= \frac{K}{2}(L-x)^{-1/2} \frac{\Delta L}{\tau} \exp(-t/\tau) \quad (7.23)$$

Assuming $u(x) = bx/h(x)$, the denominator is

$$u(x) \partial_x h = -b \frac{x}{h(x, t)} \frac{K}{2} (L(t) - x)^{-1/2}, \quad (7.24)$$

and equation (7.19) becomes

$$\mathcal{R} = \frac{\Delta L \tau \exp(-t/\tau) h}{b x}. \quad (7.25)$$

Based on these simple descriptions of the scar evolution, we can predict how long it will take the scar feature to rise to its highest point and what its highest point will be for a given dome/stream evolution scenario. The scar feature will reach its maximum elevation when $\mathcal{R} = 1$ and elevation term $\partial_t h$ (equation 7.23) and the down-slope motion term $u(x)\partial_x h$ (equation 7.24) are equal in magnitude. Solving equation (7.25) for t when $\mathcal{R} = 1$ yields the critical time t_c when scars are predicted to reach their maximum elevation.

$$t_c = -\tau \log \left(\tau \frac{b}{\Delta L} \frac{x}{h(x, t)} \right). \quad (7.26)$$

Equation 7.26 is not strictly correct because we ignored the fact that h and x depend on t . Because the adjustment time-scales are relatively fast, the scar position x does not change much while it is being elevated (Figs. 7.3 and 7.4). Therefore we use $x = fL_0$ in equation 7.26. We further specify $h(x, t)$ to be the final ice thickness at position x , $h(x, t) = h(fL_0, \infty)$. Intermediate values for $h(x, t)$ under-predict the time scar features reach their maximum elevation. The maximum elevation of scar features can be estimated from $h(fL_0, \infty)$.

Figures 7.3 and 7.4 show that t_c accurately predicts the time when the scar reaches its maximum elevation in most cases. The prediction is less accurate when the relict ice stream is thin and scar features occur low on the flanks of the dome. The discrepancy arises because surface velocities are relatively large there and x varies significantly over time. The time-scale τ_{fill} , shown by black dots also produces a good estimate for the maximum elevation time in nearly all cases.

7.7 Application to Siple Dome

Several lines of evidence support the hypothesis that the topographic “scar” features which flank Siple Dome are associated with margins of formerly streaming regions adjacent to Ice Streams C and D. These include (1) disruption of the internal layering at the “scar” features (see Fig. 6.2; *Jacobel et al.*, 1996), (2) evidence for liquid water at the bed beneath the relict ice streams (*Gades*, 1998), and (3) the low surface slopes of the relict ice streams (*Chapter 3*; *Scambos et al.*, 1998). Assuming the Siple Ice Stream and Duck’s Foot are former ice stream areas, these models and time-scales can be used as predictive tools to estimate the timing of their stagnation given the present elevation of their scar features.

For the ridge/stream system represented by Siple Dome and the relict ice streams, $L_0 \approx 60$ km, $\Delta L \approx 30$ km, $b \approx 0.10$ m a⁻¹, and $f \approx 0.6$. The volume adjustment time-scale is about 1500 years and the time when the scar is predicted to reach its maximum elevation is about 2000 years. The scar features are predicted to reach a maximum height of about 250 meters above the initial ice stream margin (Fig. 7.3, panel c).

Measurements of bed topography and the accumulation pattern inferred from RES layer shapes can be input to the FD model to predict the early evolution of Siple Dome assuming the Siple Ice Stream and the Duck’s Foot are former streaming areas which stagnated at similar times. We allow the width between adjacent flow lines to increase away from the divide such that $W/W(0) = (x/L)^2 + 1$, where $L = 50$ km (*Chapter 3*). A surface profile over the dome is assumed where the elevation at the boundaries of the dome (at $\approx \pm 50$ km) are held fixed at their present elevation. An initial model is run for 5000 years until the surface profile is steady state and consistent with the prescribed bed topography and accumulation pattern. Flat surface and bed sections representing the relict ice streams are added to this steady state profile and

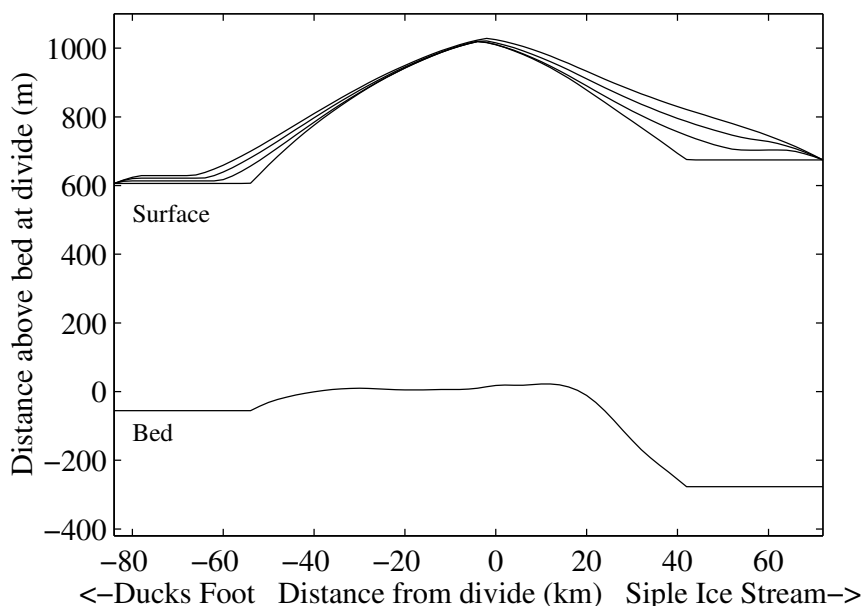


Figure 7.11: Surface profiles from the FD evolution model for Siple dome at 0, 200, 400, and 600 years since synchronous stagnation of the Duck's Foot and Siple Ice Stream.

the model is run again for 1000 years to obtain the predicted Siple Dome evolution profiles. Figure 7.11 shows the initial dome/stream profile and the surface evolution after 200, 400, and 600 years.

Detailed topographic images of Siple Dome show that the Siple Ice Stream is generally flat over most of its area. It appears that the NE part of the dome has expanded slightly into the former ice stream area (*Scambos et al.*, 1998). The present geometry is similar to the profiles shown in Figure 7.11 during the very early stages of evolution. The scar feature associated with the former margin of this flow feature is presently about 50-100 meters above the level of Ice Stream D with higher elevations in the northeastern region where Siple Dome appears to be expanding into the former ice stream area. This elevation pattern can be explained by shut-down of the ice stream

and subsequent incorporation by Siple Dome which began about 100-500 years ago. The age is probably toward the young end of this range since the accumulation rates on the north side of Siple Dome are likely greater than 0.10 m a^{-1} (see *Chapter 6*) and the dome adjustment is therefore faster (Fig 7.11). This age is consistent with the age estimated from analysis of the internal layer pattern detected by radar in the vicinity of the lower part of the Siple Ice Stream (< 400 years, *Gades, 1998*) and from measurements of the depth of buried crevasses in the upper part of the Siple Ice Stream (230-350 years, *N. Lord, pers. comm. to A. Gades; Gades, 1998*).

The northern-most scar features which comprise the Duck's Foot lie about 20-30 meters above the present level of Ice Stream C (Fig. 7.1). These lower elevations are consistent with the hypothesis that streaming activity has ceased at the Duck's Foot more recently than to the north of Siple Dome. However, part of the difference could be due to the difference in accumulation rate over the dome. Higher accumulation rates correspond to fast evolution and associated rates of uplift. Given the accumulation gradient over Siple Dome with lower accumulation rates south of the divide, it is possible that the Duck's Foot near Ice Stream C and Siple Ice Stream on the NE flank of Siple Dome have similar stagnation ages.

Since GPS measurements of survey poles along the south flank of Siple Dome were along a flow line, the thickening rates predicted by the FD model and inferred from GPS measurements can be compared. The calculated horizontal flux divergence along the south flank of Siple Dome suggests that the south flank is thickening rapidly in a zone from about 40km to about 70 km from the divide (*Chapter 3*). Figure 7.12 shows the thickening rates predicted by the FD model for 100, 200, 300, 400, and 500 years since synchronous stagnation of the Duck's Foot and the Siple Ice Stream. The character of the GPS-inferred thickening is similar to the thickening pattern predicted by the FD model 200-500 years after stagnation of the Duck's Foot area

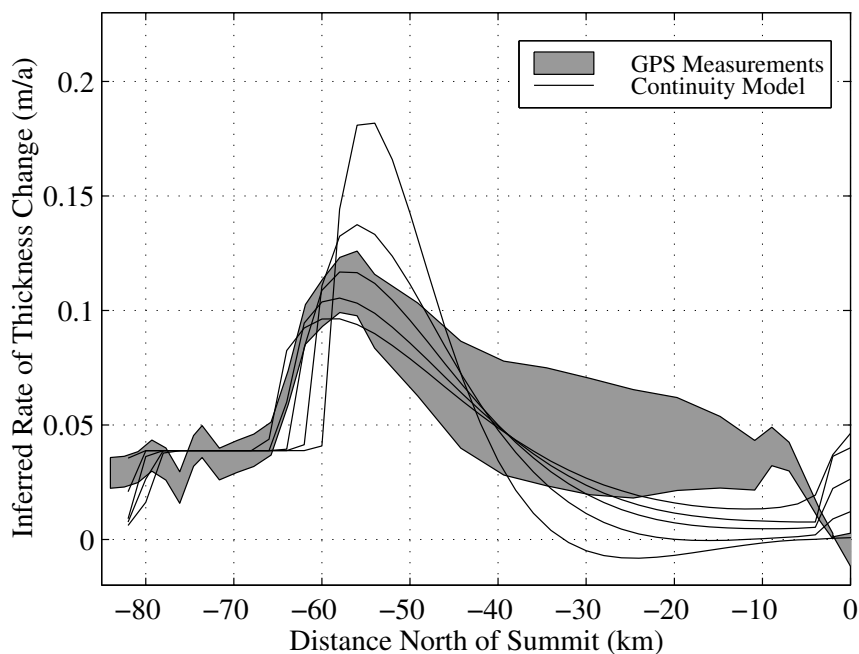


Figure 7.12: Dashed curves show predicted thickening rate pattern from FD continuity model at 100, 200, 300, 400, and 500 years since stagnation of the Duck's Foot area. Shaded area shows the thickening rate inferred from GPS measurements of horizontal velocity and the RES-inferred accumulation pattern.

with the maximum thickening occurring at the former junction of the dome and ice stream.

7.8 Discussion

The expansion of a 2-d ice dome into a stagnated ice stream can be simulated using a numerical model and simple continuity relationships. The time-scales governing volume evolution and scar feature elevation can be derived from the fundamental characteristics of the dome/stream system. This eliminates the need for complicated numerical models to determine order-of-magnitude time-scales for a particular

dome/stagnated ice stream system. Because the time-scales depend only on the difference between the initial and final ice sheet profiles, detailed knowledge of the bedrock topography or ice thickness is not required to estimate the adjustment time-scale.

We assume that the relict ice stream margin at the edge of the domain is held fixed at its initial elevation by the activity of an adjacent actively streaming region outside the domain. The age of the scar features is inferred from their present elevation relative to the actively streaming regions. In reality, actively streaming regions thicken and thin over time, changing the assumed boundary condition and the reference elevation level. However, elevation changes at the boundaries would affect the evolution of the dome only after the wave of thickening reached the boundaries of the domain. Evolution of the dome/relict ice stream is initially the same for both the fixed boundary case (Fig. 7.3) and for the non-fixed boundary case (Fig. 7.6). Since Siple Dome is apparently in the early stages of dome/stream evolution, the assumption that the elevation at the new ice stream boundary is fixed does not affect our interpretation of the age of the relict flow features at the edges of Siple Dome.

The slope discontinuity at the ice dome/ice stream margin interface in the FD model is not physically realistic. We assume that ice flow from the dome proceeds as if the ice stream does not exist and that the ice flux to the ice stream is determined by the ice thickness and slope at the ice stream margin (*Hindmarsh, 1993*). The model includes no longitudinal coupling between the ice dome and relict ice stream. This assumption is valid for modeling the general evolution of the ice sheet, but not valid for modeling the specific behavior at the ice dome/ice stream transition where the scar feature is formed (*Hindmarsh, 1993*). On some small scale ($O(H)$), there is a transition zone between the dome and ice stream at $t = 0$. Accurate modeling of this zone at small t when the surface slope varies abruptly over this region requires consideration of longitudinal stress gradients. In addition, the transition zone must

be initially concave in profile so that the dome/stream boundary is smooth. Exclusion of these effects contributes to errors in the FD prediction of scar elevation at small t .

These errors do not affect our conclusions. The elevation of the scar feature is constrained by the general evolution of the dome. After 10^2 years, the slope discontinuity is smoothed out and longitudinal stress gradients ($\partial_x \sigma_{xx}$) become small again (compared to $\rho g \partial_x h$). The errors affect the particular evolution of the scar feature, but not the general character of thickening. Thus, the order of magnitude estimates for the age of the shut down of the relict ice streams is unchanged.

Three-dimensional effects will affect the transient behavior of the ice sheet. The transient behavior of a 3-d dome is controlled by the local flux into the former ice stream area. Areas of the dome with large slopes and ice thickness will expand more quickly. Therefore, we do not expect scar features to be elevated uniformly. At any given instant in the early evolution process, the scar feature may exist at several elevations along its length. Ultimately, the transient effects diminish and the evolution of the dome is governed by the volume response time-scale.

7.9 Conclusions

Topographic features left by relict ice stream margins can be elevated relative to the former streaming surface by growth of the adjacent ice stream ridge. Interpretation of the elevation of former flow features for the past configuration of ice streams or ice sheet may therefore be complicated. The time-scales governing the evolution can be estimated from fundamental properties of the ice sheet/ice stream system as in equation (7.11).

These time-scales, together with the modern geometry of a dome/stream system can be used to estimate the timing of ice stream stagnation. For Siple Dome, the volume adjustment time-scale relevant to the NE flank relict ice stream is about

1500 years. The present geometry and elevation of Siple Dome and its existing scar features suggest that Siple Dome is in the early stages of evolution where $t < \tau_{fill}$. Based on this analysis, shut down of the Siple Ice Stream probably occurred in the past 500 years. This age is consistent with other estimates based on analysis of the internal stratigraphy across the feature (Gades, 1998). The scar features on the south flank of Siple Dome could be associated with a flow regime which shut down nearly synchronously with the Siple Ice Stream. The thickening rate predicted by a model of Siple Dome evolution for the Duck's Foot area is generally consistent with the rate of thickening inferred from GPS measurements (Chapter 3) for an ice stream stagnation age of 200-500 years.

The recent shut-down age implied for the Siple Ice Stream and Duck's Foot has implications for the explanation for the divide migration toward Ice Stream D which has likely persisted for at least the past 1000 years (Chapter 4; Nereson *et al.*, 1998b). In order to cause the inferred divide migration, changes occurring at boundaries of Siple Dome must also have persisted for at least 1000 years (Chapter 5; Nereson *et al.*, 1998a). The more recent shut-down age predicted by this analysis does not support the hypothesis that the divide migration is caused by thickening of the Siple Ice Stream since its stagnation. The thickening inferred along the south flank of Siple Dome is also a recent event (< 500 years) and would tend to move the divide in the opposite direction than is inferred from the internal layer pattern (Chapter 4; Nereson *et al.*, 1998b). It appears that the recent stagnation of these flow features is not the cause of the divide migration. A remaining possibility is past activity of the now-relict flow features when they were active. In particular, gradual thinning of the south margin of Siple Dome associated with past streaming activity of Ice Stream C and Duck's Foot would move the divide in the observed direction.

Chapter 8

SYNTHESIS

The analysis and conclusions presented in the previous chapters are parts of an interconnected puzzle. When brought together, these pieces describe the history of ice flow at Siple Dome and lead to implications about the past activity of Ice Streams C and D. This chapter synthesizes the information from the previous chapters and presents the main conclusions of this dissertation grouped into four categories: (1) the present geometry and flow of Siple Dome, (2) the utility of using RES data to infer past changes in ice flow, (3) the history of ice flow at Siple Dome over three time periods and (4) the implications for the past activity of Ice Streams C and D.

8.1 The Modern Geometry of Siple Dome

Siple Dome is an inter-ice stream ridge about 100 km wide over a bedrock plateau between Ice Streams C and D. The summit location is 81.6543° S, 148.8081° W, and 622 m high relative to the WGS84 ellipsoid. Ice thickness at the summit is 1009 ± 7 m as measured by RES (*Raymond et al.*, 1995) (1004 ± 5 m from borehole measurements, *H. Englehardt, pers. comm.*, 1998). The accumulation rate is estimated to be $b = 0.11 \text{ m a}^{-1}$ for the past 1000 years and 0.13 m a^{-1} for the past 30 years (*Mayewski et al.*, 1995). Measurements of ice flow near the divide show that flow is nearly 2-dimensional and perpendicular to the ridge within several ice thicknesses of the summit (*Chapter 3*).

Assuming a spatially constant accumulation rate history with 0.10 m a^{-1} ice

equivalent during interglacial periods and about 40% less during glacial periods, I have used a finite element model of Siple Dome to predict an ice age of 10^4 years at about 60% depth (600 m) and 10^5 years at 90% depth (900 m) (*Chapter 2; Nereson et al.*, 1996). The temperature at the bed is predicted to be below the melting point. This is consistent with analysis showing low RES reflectivity of the bed under Siple Dome relative to recently streaming areas which are at the melting point (*Gades*, 1998) and with borehole temperature measurements (*H. Englehardt, pers. comm.*, 1998).

Internal layers detected by RES are continuous over the entire width of the dome and detected to about 70% of the ice depth (to 700 m). The continuity of layers is disrupted where the profile crosses former shear margins on its flanks. The internal layers are warped convex-up in a region spanning about 4 km beneath the present divide. The large-scale internal layer pattern is asymmetric about the divide. A central part of this dissertation involves analysis of the shape of these layers using ice flow models and new inverse techniques to infer the history of ice flow at Siple Dome.

8.2 Using RES Internal Layers to Infer Ice-Flow History

In general, a set of internal layers detected at a given location using RES is discrete. The number of internal layers which can be detected is inversely related to the RES signal wavelength. Also, because of increased RES signal attenuation with depth, layers are most easily detected in the upper part of an ice sheet. At depth, only the layers with the strongest reflection properties can be detected. Each of the detected layers is associated with an age according to the age-depth relationship appropriate for that location.

The flow history which can be inferred from the shape of these layers is therefore limited by their number density and distribution with depth. If the density is uniform

over the ice thickness, then the temporal resolution of the inferred flow history is limited by the slope of the age versus depth relationship. Frequent changes in ice flow are generally best resolved for the recent past ($< H/b$) represented by the upper part of the ice sheet where more layers are generally detected and where the age-depth scale is approximately linear with depth. Below about 50% depth, where ice age is generally older than H/b , only the strongest reflecting internal layers can be detected. The age versus depth slope here also steepens significantly. Therefore, the few internal layers which can be detected are separated by very long periods of time, making changes in past ice flow less resolvable.

The integrated effect of ice flow over time also limits the resolvable history of ice flow from internal layer shapes. Even if an infinite number of internal layers could be detected by RES, ice flow causes the shapes of internal layers to lose information about prior flow regimes over time. The time-scale for this information loss is related to the fundamental H/b time-scale. This effect is illustrated in Chapter 6 for variations in the spatial accumulation pattern at Siple Dome assuming a simplified model of layer deformation. For a given change in the spatial distribution of accumulation, its effect on the internal layer shapes is reduced by a factor of $(1 - 1/e)$ after H/b years. Because of this flow effect, information about the flow regime associated with the age of the deepest internal layers ($\gg H/b$) is lost.

Given these limitations, RES methods were used at Siple Dome to detect variations in ice flow of period 10^3 a over the past 5-10 ka ($< H/b$). The resolvable flow variations are limited to those which cause internal layer shapes to be deformed more than about 10 meters (about 1/10 of the 2Mhz signal wavelength in ice). Prior to about 10 ka ($> H/b$), only very large and long-lived changes in ice flow are potentially detectable and no such changes were detected in Siple Dome data. Therefore, the flow history of Siple Dome inferred from RES measurements is limited to the past 10^4 years.

8.3 The History of Siple Dome

8.3.1 The Distant Past (> 5000 a)

The continuity of the internal layer pattern suggests that Siple Dome has not been over-run by fast-flowing ice streams in the past 10^4 years, the approximate age of the deepest detected internal layer. Further, the presence of the near-divide bump in the internal layer pattern is suggestive of long-term stability of the Siple Dome divide position. Given the present ice thickness and accumulation rate at Siple Dome, a bump formed by non-linear ice dynamics would take at least 5000 years to develop to its present amplitude (*Chapter 4; Nereson et al., 1998b*). However, we cannot eliminate the possibility of thinning of Siple Dome in the past which may have been related to thinning of WAIS and/or the initiation of ice stream activity. Rapid thinning would decrease the amount of time required to form a divide bump by differential downward motion of the ice.

The pattern of internal layers is consistent with an accumulation pattern which has not changed in the past 10^4 years. Relative to the divide, the pattern predicts up to 60% less accumulation to the south and 40% more accumulation to the north (*Chapter 6; Nereson et al., 1997*). The data also allow the possibility for a slight decrease in the south-north gradient on the north flank over the past several thousand years. Sensitivity tests show that large or long-term changes in the accumulation pattern would be detectable in the pattern of internal layers, but layer shapes are not sensitive to small or short-term changes in the spatial accumulation distribution, and that the sensitivity decreases with age of the event. Synchronous thinning of the boundaries on either side of Siple Dome would only minimally affect the inferred accumulation pattern. Asynchronous thinning of the boundaries of Siple Dome would have larger effects, causing inferred accumulation rates on the thinning side of the

dome to be artificially low.

8.3.2 *The Intermediate Past (1000–5000 a)*

Analysis of the shape of the divide bump present in the internal layer pattern shows that the divide has been migrating toward Ice Stream D at 0.05 to 0.50 m a⁻¹ for the past few thousand years. Possible causes of divide migration include a steady increase in the south-north accumulation gradient of $0.10 - 0.5 \times 10^{-9}$ a⁻¹, or a relative thickening of the north side of Siple Dome at a rate of 0.005 – 0.040 m a⁻¹ for the past few thousand years (*Chapter 5; Nereson et al., 1998a*). The spatial pattern of accumulation inferred from the large-scale layer shapes shows no evidence for an increase in the accumulation gradient in the past 5000 years. The only evidence for change is in the opposite sense to that required to move the divide toward Ice Stream D (i.e., a *decrease* in gradient). It is therefore unlikely that changes in the spatial accumulation pattern have caused the observed divide migration.

Thickening of Siple Ice Stream since its stagnation could also cause divide migration, if stagnation occurred more than about 2000 years ago. However, models of dome/ice stream evolution suggest that stagnation of the relict ice streams which flank Siple Dome (Siple Ice Stream and Duck’s Foot) occurred less than 500 years ago (*Chapter 7*). Any adjustment of the shape of Siple Dome associated with this stagnation is just now beginning to affect the divide position. Since the divide has likely been migrating for the past few thousand years, we can rule out recent stagnation of these relict ice streams as the cause of the migration. A remaining possibility is the activity of the relict ice streams prior to stagnation. Thinning of the Ice Stream C-side of Siple dome, or thickening of the Ice Stream-D side would tend to move the divide toward Ice Stream D. It is possible that while Ice Stream C and the Duck’s Foot were actively streaming, the ice stream slowly thinned and caused the southern

boundary of Siple Dome to gradually decrease in elevation until its recent stagnation.

8.3.3 *Present and Recent Past (< 1000 a)*

Measurements of horizontal strain rate and estimates of the accumulation rate suggest that the summit of Siple Dome is near steady state or slightly thinning at its summit at one or two centimeters per year (*Chapter 3*). GPS measurements of surface velocity across Siple Dome suggest that it is thickening significantly along its south flank relative to the divide, with the most pronounced thickening occurring 40–60 km from the summit where the flux divergence is negative (*Chapter 3*). The spatial pattern and magnitude of the thickening is consistent with the hypothesis that the Duck's Foot area is a former region of fast flow which ceased about 300–500 years ago (*Chapter 7*). According to a dome/stream evolution model, the present elevation of the scar feature on the north flank of Siple Dome suggests that this area also stagnated less than 500 years ago. This finding is consistent with analysis of the internal stratigraphy over the relict margin (*Gades, 1998*).

8.3.4 *Complimentary Studies*

Measurements from the deep ice core will help test these hypotheses about the flow history of Siple Dome. Measurements of total gas content in the ice should determine whether Siple Dome has thickened or thinned rapidly in the past. Measurements of annual layer thicknesses will provide accurate dates for the stratigraphic layers and could be used in conjunction with measurements of beryllium isotopes (an accumulation rate proxy) to determine the strain history of the dome. These measurements will better determine the history of accumulation and whether the Siple Dome summit is indeed in steady state. Measurements from 100-m cores taken at 30 km north and south of the divide can be used to test the accumulation pattern inferred from

RES layers in this analysis (*Chapter 6; Nereson et al., 1997*). Measurements of the depth distribution of vertical strain near the summit will better constrain the flow description used in flow models and determine whether the divide bump feature in the internal layers is a non-linear rheology effect or an accumulation distribution effect.

8.4 Implications for Past Activity of Ice Streams C and D

Several lines of evidence support the hypothesis that the topographic “scar” features which flank Siple Dome are associated with margins of formerly streaming regions adjacent to Ice Streams C and D. These include (1) disruption of the internal layering at the “scar” features (*Jacobel et al., 1996*), (2) evidence of liquid water currently at the bed beneath the relict ice streams (*Gades, 1998*), and (3) the low surface slopes of the relict ice streams (*Chapter 3; Scambos et al., 1998*). Given this evidence, it is reasonable to assume the Duck’s Foot and Siple Ice Stream are indeed relict ice stream areas.

Based on a dome/stream evolution model, the modern elevation of topographic “scar” features, and the pattern of modern inferred thickening on the south flank of Siple Dome, stagnation of the Duck’s Foot and the Siple Ice Stream probably occurred within the past 500 years. This recent stagnation age for the Siple Ice Stream is consistent with other independent estimates based on analysis of the internal layer pattern and measurements of the depth to buried crevasses (*N. Lord, pers. comm to A. Gades; Gades, 1998*). Analysis presented in Chapter 7 suggests that stagnation of the Duck’s Foot is also recent and may be nearly synchronous with stagnation of the Siple Ice Stream.

The general stability of the Siple Dome divide position and the near steady-state situation of the summit area suggests that any ice stream activity that occurred prior to this stagnation (> 500 years ago) must have been such that the summit of

Siple Dome was unaffected. This requires that the elevation at both north and south boundaries of Siple Dome either remained fixed or changed synchronously. Given this constraint, allowable changes in ice stream activity include (1) on-and-off switching of the ice streams (including the Duck's Foot and Siple Ice Stream) sufficiently quickly that the Siple Dome divide position and its elevation are not significantly affected, (2) a relatively steady flow of the ice streams with no associated changes in their elevation at the boundaries of Siple Dome, or (3) steady flow of the ice streams involving gradual but mostly synchronous increases or decreases in elevation at the boundaries of Siple Dome.

Evidence for migration of the Siple Dome ice divide toward Ice Stream D for the past several thousand years indicates slight asynchronous activity of the bounding ice streams – eliminating option 2. Since the direction of divide motion has been in one direction over that time, and since there is no evidence for changes in the migration rate, rapid on-and-off switching (option 1) seems less likely than gradual thinning of Ice Stream C at the south boundary of Siple Dome relative to the Siple Ice Stream (option 3). If option 3 is correct and ice stream flow has been slightly asynchronous but steady for several thousand years prior to stagnation of Siple Ice Stream and Duck's Foot (and Ice Stream C), then the recent stagnation events are not part of the natural variability of the ice streams and may represent a major reorganization of the ice stream system.

The evidence for recent reorganization of the ice stream configuration following a relatively stable period for the prior several thousand years and the evidence for long-term stability of Siple Dome supports a quasi-stable hypothesis for the WAIS ice stream system. Inter ice stream ridges, because they commonly occur over bedrock plateaus (*Shabtaie and Bentley, 1987*), may be relatively stable and define general channels for ice streams. Ice streams flowing around the bedrock plateaus can quickly

switch on and off or change their boundaries over short time-scales (10^2 a). The allowed changes in ice stream configuration are partially constrained by the presence of the inter-ice stream ridges and probably controlled by thermal and physical conditions at or near the ice stream bed (e.g., *Alley et al.*, 1987; *Kamb*, 1991; *Anandakrishnan and Alley*, 1997; *Jacobson and Raymond*, 1998).

BIBLIOGRAPHY

- Alley, R. B., Flow-law hypotheses for ice-sheet modeling, *Journal of Glaciology*, 38(129), 245–256, 1992.
- Alley, R. B., et al., Abrupt increase in Greenland snow accumulation at the end of the Younger Dryas event, *Nature*, 362, 527–529, 1993.
- Alley, R. B., et al., Visual-stratigraphic dating of the GISP2 ice core: basis, reproducibility, and application, *Journal of Geophysical Research*, 102(C12), 26,367–26,381, 1997.
- Alley, R. B., and C. R. Bentley, Ice-core analysis on the Siple Coast of West Antarctica, *Annals of Glaciology*, 11, 1–7, 1988.
- Alley, R. B., and I. M. Whillans, Response of East Antarctica ice sheet to sea level rise, *Journal of Geophysical Research*, 89, 6487–6493, 1984.
- Alley, R. B., and I. M. Whillans, Changes in the West Antarctic Ice Sheet, *Science*, 254(5034), 959–963, 1991.
- Alley, R. B., D. D. Blankenship, C. R. Bentley, and S. T. Rooney, Till Beneath Ice Stream B 3. Till Deformation: Evidence and Implications, *Journal of Geophysical Research*, 92(B9), 8921–8929, 1987.
- Anandakrishnan, S., and R. B. Alley, Stagnation of Ice Stream C, West Antarctica by water piracy, *Geophysical Research Letters*, 24(3), 265–268, 1997.

- Anandakrishnan, S., R. B. Alley, and E. D. Waddington, Sensitivity of the ice-divide position in Greenland to climate change, *Geophysical Research Letters*, *21*(6), 441–444, 1994.
- Bentley, C. R., Antarctic Ice Streams: A Review, *Journal of Geophysical Research*, *92*(B9), 8843–8868, 1987.
- Bindschadler, R., A numerical model of temperate glacier flow applied to the quiescent phase of a surge-type glacier, *Journal of Glaciology*, *28*(99), 239–265, 1982.
- Bindschadler, R., and P. Vornberger, Changes in the West Antarctic Ice Sheet since 1963 from declassified satellite photography, *Science*, *279*(5351), 689–692, 1998.
- Bindschadler, R. A., ed., *West Antarctic Ice Sheet Initiative: Science and Implementation Plan*, WAIS Working Group, National Science Foundation, 1995.
- Bolzan, J. F., E. D. Waddington, R. B. Alley, and D. A. Meese, Constraints on Holocene ice-thickness changes in central Greenland from the GISP2 ice-core data, *Annals of Glaciology*, *21*, 33–39, 1995.
- Boyce, W. E., and R. C. DiPrima, *Elementary Differential Equations and Boundary Value Problems*, John Wiley & Sons, New York, NY, 4th edn., 1986.
- Bromwich, D. H., Snowfall in high southern latitudes, *Reviews of Geophysics*, *26*(1), 149–168, 1988.
- Bromwich, D. H., Y. Du, and T. R. Parish, Numerical simulation of winter katabatic winds from West Antarctica crossing Siple Coast and the Ross Ice Shelf, *Mon. Weather Rev.*, *122*, 1417–1435, 1994.

- Carrasco, J. F., D. H. Bromwich, and Z. Liu, Mesoscale cyclone activity over Antarctica during 1991. 1. Marie Byrd Land, *Journal of Geophysical Research*, *102*(D12), 13,923–13,937, 1997.
- Clarke, T. S., and C. R. Bentley, Evidence for a recently abandoned ice stream shear margin, *EOS*, *76*(46), F194, 1995.
- Cuffey, K. M., and G. D. Clow, Temperature, accumulation and ice sheet elevation in central Greenland through the last deglacial transition, *Journal of Geophysical Research*, 1997.
- Cutler, N. A., C. F. Raymond, E. D. Waddington, D. A. Meese, and R. B. Alley, The effect of ice sheet thickness change on the accumulation history inferred from GISP2 layer thicknesses, *Annals of Glaciology*, *21*, 26–32, 1995.
- Dahl-Jensen, D., S. J. Johnsen, C. U. Hammer, H. B. Clausen, and J. Jouzel., Past accumulation rates derived from observed annual layers in the GRIP ice core from Summit, Greenland, in *Ice in the climate system*, edited by W. R. Peltier, vol. 12 of *NATO ASI Series I*, pp. 517–532, Springer-Verlag, 1993.
- Dansgaard, W., and S. J. Johnsen, A flow model and a time scale for the ice core from Camp Century, Greenland, *Journal of Glaciology*, *8*(53), 215–223, 1969.
- Denton, G. H., J. G. Bockheim, S. C. Wilson, and M. Stuiver, Late Wisconsin and early Holocene Glacial history, Inner Ross Embayment, Antarctica, *Quaternary Research*, *31*, 151–182, 1989.
- Dixon, T. H., An introduction to the Global Positioning System and some geological applications, *Reviews of Geophysics*, *29*(2), 249–276, 1991.

- Doake, C. S. M., and E. W. Wolff, Flow law for ice in polar ice sheets, *Nature*, *314*(6008), 255–257, 1985.
- Drewry, D. J., Antarctica: Glaciological and Geophysical Folio, Tech. rep., Scott Polar Research Institute, Cambridge, 1983.
- Engelhardt, H., N. Humphrey, B. Kamb, and M. Fahnestock, Physical conditions at the base of a fast moving Antarctic ice stream, *Science*, *248*, 57–59, 1990.
- Firestone, J., E. Waddington, and J. Cunningham, The potential for basal melting under Summit, Greenland, *Journal of Glaciology*, *36*(123), 163–168, 1990.
- Fisher, A. M., R. W. Jacobel, N. M. Sundell, and A. M. Gades, Bedrock topography and internal stratigraphy of the Siple Dome summit, *EOS, Transactions*, *76*, F194, 1995, Abstract.
- Fisher, D. A., R. M. Koerner, W. S. B. Paterson, W. Dansgaard, N. Gundestrup, and N. Reeh, Effect of wind scouring on climatic records from ice-core oxygen-isotope profiles, *Nature*, *301*(5897), 205–209, 1983.
- Gades, A. M., Basal Structure of Black Rapids Glacier, AK, and Siple Dome, West Antarctica Inferred from Radio Echo-Sounding, Ph.D. thesis, University of Washington, 1998.
- Giovinetto, M. B., and C. Bull, Summary and analysis of surface mass balance compilations for Antarctica, 1960-1985, Report no. 1, Byrd Polar Research Center, The Ohio State University, 1987.
- Gudmundsson, G. H., C. F. Raymond, and R. Bindshadler, The origin and longevity of flow-stripes on Antarctic ice streams, *Annals of Glaciology*, *27*, 1998, in press.

- Hammer, C. U., Acidity of polar ice sheets in relation to absolute dating, past volcanism, and radio-echos, *Journal of Glaciology*, 25(93), 359–372, 1980.
- Harrison, C. H., Radio echo sounding of horizontal layers in ice, *Journal of Glaciology*, 12(66), 383–397, 1973.
- Hindmarsh, R. C. A., Qualitative dynamics of marine ice sheets, in *Ice in the Climate System*, pp. pp. 67–100, Springer-Verlag, 1993, NATO ASI Series I: Global and Environmental Change.
- Hindmarsh, R. C. A., Stochastic perturbation of divide position, *Annals of Glaciology*, 23, 94–104, 1996a.
- Hindmarsh, R. C. A., Stability of ice rises and uncoupled marine ice sheets, *Annals of Glaciology*, 23, 105–115, 1996b.
- Hindmarsh, R. C. A., Normal modes of an ice sheet, *J. Fluid Mech.*, 335, 393–413, 1997a.
- Hindmarsh, R. C. A., Use of ice-sheet normal modes for initialisation and modelling small changes., *Annals of Glaciology*, 25, 1997b.
- Hooke, R., Flow law of a polycrystalline ice in glaciers: comparison to theoretical predictions, laboratory data and field measurements, *Reviews of Geophysics and Space Physics*, 19(4), 664–672, 1981.
- Hughes, T., Is the West Antarctic Ice Sheet disintegrating?, *Journal of Geophysical Research*, 78(33), 7884–7910, 1973.
- Hughes, T., West Antarctic Ice Streams, *Reviews of Geophysics and Space Physics*, 15(1), 1–45, 1977.

- Hulbe, C. L., and I. M. Whillans, Stop-and-go GPS in Antarctica, *Surveying and Land Information Systems*, 53(2), 151–158, 1993.
- Hulbe, C. L., and I. M. Whillans, Evaluation of strain rates on Ice Stream B, Antarctica, obtained using differential GPS, *Annals of Glaciology*, 20, 254–262, 1994.
- Hutter, K., *Theoretical glaciology; material science of ice and the mechanics of glaciers and ice sheets*, D. Reidel Publishing Company/Tokyo, Terra Scientific Publishing Company, 1983.
- Hvidberg, C. S., Steady state thermo-mechanical modelling of ice flow near the centre of large ice sheets with the finite element technique, *Annals of Glaciology*, 23, 116–123, 1996.
- Jacobel, R., T. Scambos, C. Raymond, and A. Gades, Changes in the configuration of Ice Stream flow from the West Antarctic Ice Sheet, *Journal of Geophysical Research*, 101(B3), 5499–5504, 1996.
- Jacobel, R. W., A. J. Fisher, and N. M. Sundell, Internal stratigraphy from ground-based radar studies at Siple Dome summit, *Antarct. J. U. S., 1996 Review*, in press.
- Jacobson, H. P., and C. F. Raymond, Location of ice stream margins, thermal effects, *Journal of Geophysical Research*, 1998, in press.
- Jóhannesson, T., C. Raymond, and E. Waddington, Timescales for adjustment of glaciers to changes in mass balance, *Journal of Glaciology*, 35(121), 355–369, 1989.
- Kamb, B., Rheological nonlinearity and flow instability in the deforming bed mechanism of ice stream motion, *Journal of Geophysical Research*, 96(B10), 16585–16595, 1991.

- Lorius, C., D. Raynaud, and J. R. Petit, Late-glacial maximum – Holocene atmospheric and ice-thickness changes from Antarctic ice-core studies, *Annals of Glaciology*, 5, 88–94, 1984.
- Mayewski, P. A., M. S. Twickler, and S. Whitlow, The Siple Dome ice core - reconnaissance glaciochemistry, *Antarctic Journal of the U.S.*, 30, 85–87, 1995.
- Mellor, M., and R. Testa, Creep of ice under low stress, *Journal of Glaciology*, 8, 147–152, 1969.
- Moore, J. C., E. W. Wolff, H. B. Clausen, and C. U. Hammer, The chemical basis for the electrical stratigraphy of ice, *Journal of Geophysical Research*, 97(B2), 1887–1896, 1992.
- Morse, D., Glacier Geophysics at Taylor Dome, Antarctica, Ph.D. thesis, University of Washington, 1997.
- Nereson, N. A., and C. F. Raymond, Recent Migration of Siple Dome Divide Determined from 1994 Radio-Echo Sounding Measurements, *Antarctic Journal of the U.S.*, 1997, (in press).
- Nereson, N. A., E. D. Waddington, C. F. Raymond, and H. P. Jacobson, Predicted age-depth scales for Siple Dome and inland WAIS ice cores in West Antarctica, *Geophysical Research Letters*, 23(22), 3163–3166, 1996.
- Nereson, N. A., C. F. Raymond, R. W. Jacobel, and E. D. Waddington, The history of the spatial accumulation pattern at siple dome, west antarctica, from radar measurements, *EOS Transactions, 1997 Fall Meeting Supplement*, 78(46), F252, 1997, abstract.

- Nereson, N. A., R. C. A. Hindmarsh, and C. F. Raymond, Sensitivity of the divide position at Siple Dome to boundary forcing, *Annals of Glaciology*, 1998a, in press.
- Nereson, N. A., C. F. Raymond, E. D. Waddington, and R. W. Jacobel, Migration of the Siple Dome ice divide, West Antarctica, *Journal of Glaciology*, 1998b, (in press).
- Nye, J. F., Reply to Mr. Joel E. Fisher's comments, *Journal of Glaciology*, 2(11), 52–53, 1952.
- Nye, J. F., A method of determining the strain-rate tensor at the surface of a glacier, *Journal of Glaciology*, 3(25), 409–418, 1959a.
- Nye, J. F., The deformation of a glacier below an ice fall, *Journal of Glaciology*, 3(25), 387–408, 1959b.
- Nye, J. F., A numerical method of inferring the budget history of a glacier from its advance and retreat, *Journal of Glaciology*, 5(41), 589–607, 1965.
- Paren, J., and G. Robin, Internal reflections in polar ice sheets, *Journal of Glaciology*, 21(85), 251–259, 1975.
- Paterson, W. S. B., *The Physics of Glaciers*, Pergamon Press, Oxford, 3rd edn., 1994.
- Paterson, W. S. B., and E. D. Waddington, Estimated basal temperatures at Crête Greenland, throughout a glacial cycle, *Cold Regions Science and Technology*, 12, 99–102, 1986.
- Raymond, C., N. Nereson, A. Gades, H. Conway, R. Jacobel, and T. Scambos, Geometry and stratigraphy of Siple Dome, Antarctica, *Antarct. J. U.S.*, 1995 Review, 30(5), 91–93, 1995.

- Raymond, C. F., Deformation in the vicinity of ice divides, *Journal of Glaciology*, *29*(103), 357–373, 1983.
- Reeh, N., A flow line model for calculating the surface profile and the velocity, strain rate, and stress field in an ice sheet, *Journal of Glaciology*, *34*(127), 46–54, 1988.
- Retzlaff, R., and C. R. Bentley, Timing of stagnation of Ice Stream C, West Antarctica, from short-pulse radar studies of buried surface crevasses, *Journal of Glaciology*, *39*(133), 553–561, 1993.
- Robin, G., Ice cores and climatic change, *Philos. Trans. R. Soc. London, Ser. B*, *280*(972), 143–148, 1977.
- Scambos, T., and N. Nereson, Satellite image and GPS study of the morphology of Siple Dome, Antarctica, *Antarct. J. U.S., 1995 Review*, *30*(5), 87–89, 1995.
- Scambos, T. A., N. A. Nereson, and M. A. Fahnestock, Detailed topography of Roosevelt Island and Siple Dome, West Antarctica, *Annals of Glaciology*, *27*, 1998, (in press).
- Schøtt, C., E. Waddington, and C. F. Raymond, Predicted time-scales for GISP2 and GRIP boreholes at Summit, Greenland, *Journal of Glaciology*, *38*(128), 162–168, 1992.
- Shabtaie, S., and C. R. Bentley, West Antarctic Ice Streams draining into the Ross Ice Shelf: Configuration and mass balance, *Journal of Geophysical Research*, *92*(B2), 1311–1336, 1987.
- Steig, E. J., How well can we parameterize past accumulation rates in polar ice sheets?, *Annals of Glaciology*, *25*, 418–422, 1997.

- Steig, E. J., D. L. Morse, E. D. Waddington, and P. J. Polissar, Using the sunspot cycle to date ice cores, *Geophysical Research Letters*, *25*, 163–166, 1998.
- Van der Veen, C. J., Dynamics of the West Antarctic Ice Sheet, in *The West Antarctic Ice Sheet: the need to understand its dynamics*, edited by C. J. Van der Veen, and J. Oerlemans, pp. 1–16, D. Reidel Publishing Company, Holland, 1987.
- Vialov, S. S., Regularities of glacial shield movement and the theory of plastic viscous flow, *International Association of Hydrological Sciences*, *47*, 266–275, 1958.
- Waddington, E. D., Accurate modelling of glacier flow, Ph.D. thesis, University of British Columbia, 1981.
- Waddington, E. D., Wave ogives, *Journal of Glaciology*, *32*, 325–334, 1986.
- Waddington, E. D., D. A. Fisher, R. M. Koerner, and W. S. B. Paterson, Flow near an ice divide: analysis problems and data requirements, *Annals of Glaciology*, *8*, 171–174, 1986.
- Waddington, E. D., C. F. Raymond, D. L. Morse, and W. D. Harrison, Flow law for ice at low deviatoric stress, and implications for ice divide and ice core studies, *EOS*, *77*(46), F196, 1996, Fall Meeting Supplement.
- Weertman, B. R., Interpretation of ice sheet stratigraphy: A radar-echo sounding study of the Dyer Plateau, Antarctica, Ph.D. thesis, University of Washington, 1993.
- Weertman, J., Position of ice divides and ice centers on ice sheets, *Journal of Glaciology*, *12*(66), 353–360, 1973.
- Weertman, J., Stability of the junction of an ice sheet and ice shelf, *Journal of Glaciology*, *13*(67), 3–11, 1974.

Whillans, I. M., and C. J. van der Veen, New and improved determinations of velocity of Ice Streams B and C, West Antarctica, *Journal of Glaciology*, 39(133), 483–490, 1993.

Appendix A

THE HORIZONTAL STRAIN TENSOR

A.1 Finding Tensor Components using Least-Squares

The components of the horizontal strain tensor d_{ij} can be found from the change in distance among several survey poles over a measurement period Δt sufficiently long to define the change accurately. A 2-year measurement period was used on Siple Dome. For every measurement k of a change in line length L ,

$$\frac{\Delta L^k}{L^k \Delta t} = d_{ij} n_i^k n_j^k. \quad (\text{A.1})$$

where d_{ij} is the strain rate tensor $i, j = (x, y)$, and n_i^k is the component of the unit vector along L^k parallel to the coordinate direction i .

Let (x_a^k, y_a^k) and (x_b^k, y_b^k) be the k -th set of coordinate pairs a and b observed at times t_1 and t_2 . The distance between these two points at each time is:

$$L^k(t_1) = \sqrt{(x_b^k(t_1) - x_a^k(t_1))^2 + (y_b^k(t_1) - y_a^k(t_1))^2} \quad (\text{A.2})$$

$$L^k(t_2) = \sqrt{(x_b^k(t_2) - x_a^k(t_2))^2 + (y_b^k(t_2) - y_a^k(t_2))^2}, \quad (\text{A.3})$$

and the distance change is

$$\Delta L^k = L^k(t_2) - L^k(t_1). \quad (\text{A.4})$$

The unit vector components for each coordinate pair k can be written as

$$n_x^k = \frac{x_b^k(t_1) - x_a^k(t_1)}{L^k(t_1)} \quad (\text{A.5})$$

$$n_y^k = \frac{y_b^k(t_1) - y_a^k(t_1)}{L^k(t_1)}. \quad (\text{A.6})$$

Using the summation convention, and assuming deformation is constrained to the x and y plane, we can write the product of the component vectors in matrix form as:

$$n_x^k n_y^k = A_{kj}. \quad (\text{A.7})$$

where $j = (1, 2, 3)$ represents the three terms of the summation. Let $B_k = \Delta L^k / L^k$ and $X_j = [X_1, X_2, X_3] = [d_{xx}, d_{xy}, d_{yy}]$. Equation A.1 is then

$$B_k = A_{kj} X_j. \quad (\text{A.8})$$

Our goal is to find the components of the strain rate tensor X_j which satisfy the above equation for each measurement. A least-squares technique is used to find X_j for a set of k measurements. We first define a residual:

$$R_k = A_{kj} X_j - B_k. \quad (\text{A.9})$$

Squaring R gives

$$\begin{aligned} R^2 &= R_k R_k = (A_{kj} X_j - B_k)(A_{k\ell} X_\ell - B_k) \\ &= A_{kj} X_j A_{k\ell} X_\ell - 2A_{kj} X_j B_k + B_k B_k. \end{aligned}$$

To minimize the squared residual, we differentiate with respect to each component of the strain rate X_p and set equal to zero:

$$\frac{\partial R^2}{\partial X_p} = 2A_{kp} A_{k\ell} X_\ell - 2A_{kp} B_k = 0. \quad (\text{A.10})$$

Rearranging yields

$$A_{kp}A_{k\ell}X_{\ell} = A_{kp}B_k. \quad (\text{A.11})$$

Finally, we can solve for the components of the strain rate tensor in matrix form:

$$\mathbf{X} = (\mathbf{A}^T \mathbf{A})^{-1} \mathbf{A}^T \mathbf{B}. \quad (\text{A.12})$$

A.2 Principal Values and Vectors

The principal values P^1 and P^2 and directions \mathbf{n}^1 and \mathbf{n}^2 are found from solutions to the equations

$$\det(d_{ij} - P\delta_{ij}) = 0 \quad (\text{A.13})$$

$$d_{ij}n_j - Pn_i = 0. \quad (\text{A.14})$$

The first equation gives the principal values:

$$[P^1, P^2] = \frac{(d_{xx} + d_{yy}) \mp \sqrt{(d_{xx} + d_{yy})^2 - 4 * (d_{xx}d_{yy} - d_{xy}^2)}}{2}. \quad (\text{A.15})$$

The principal direction for each principal value relative to the original x, y coordinate system is found by rotating the original coordinate system according to the new coordinate system via the matrix of direction cosines β_{ij} :

$$\beta = \begin{vmatrix} \cos(\theta) & \sin(\theta) \\ -\sin(\theta) & \cos(\theta) \end{vmatrix}$$

so that

$$d'_{ij} = d_{ik}\beta_{jl}\beta_{kl}, \quad (\text{A.16})$$

where the primed value indicates the new coordinate system. Solving for θ yields

$$\theta = \frac{1}{2} \arctan \left(\frac{2d_{xy}}{d_{xx} + d_{yy}} \right), \quad (\text{A.17})$$

and since the principal directions must be orthogonal,

$$\mathbf{n}^1 = [\cos(\theta), \sin(\theta)] \tag{A.18}$$

$$\mathbf{n}^2 = [\cos(\theta + \pi/2), \sin(\theta + \pi/2)]. \tag{A.19}$$

Appendix B

VERTICAL MOTION OF THE FIRN

Let (x, y, z) and (u, v, w) represent position coordinates and velocity directions where z is the vertical coordinate. Let e denote strain rate. Conservation of mass requires

$$e_{xx} + e_{yy} + e_{zz} = -\frac{1}{\rho} \frac{D\rho}{Dt}. \quad (\text{B.1})$$

Assuming *Sorge's Law* which states that the variation of density ρ with depth z does not change in time t ($\partial_t \rho = 0$), and assuming no horizontal variation ρ , then

$$e_{xx} + e_{yy} + e_{zz} = -\frac{w}{\rho} \partial_z \rho. \quad (\text{B.2})$$

Rearranging yields

$$e_{zz} = -\frac{w}{\rho} \partial_z \rho - (e_{xx} + e_{yy}). \quad (\text{B.3})$$

The term $(-e_{xx} - e_{yy})$ is equivalent to the vertical strain rate assuming no firn layer in the ice column, e_{zz}^* . Integration of e_{zz}^* over the ice thickness is the vertical motion of a point in the firn in ice-equivalent units w_i . The term e_{zz} , when integrated over the ice thickness, represents the true vertical motion of a point in the firn near the ice surface $w_s = w(h)$. Therefore, integrating equation B.3 over the ice thickness yields

$$w_s = w_i - \int_0^h \frac{w}{\rho} \partial_z \rho dz \quad (\text{B.4})$$

$$= w_i - \int_0^{z_{\text{firn base}}} \frac{w}{\rho} \partial_z \rho dz - \int_{z_{\text{firn base}}}^h \frac{w}{\rho} \partial_z \rho dz. \quad (\text{B.5})$$

$$(\text{B.6})$$

Assuming ice density does not vary below the firn-ice transition we can write

$$w_s = w_i - \int_{z_{\text{firn base}}}^h \frac{w}{\rho} \partial_z \rho dz. \quad (\text{B.7})$$

If ρ is only a function of z , this reduces to

$$w_s = w_i - \int_{\rho_i}^{\rho_s} \frac{w}{\rho} d\rho. \quad (\text{B.8})$$

By substitution we can show that $w(z) = w_i \rho_i / \rho(z)$ is a solution to the above equation with the result

$$w_s = w_i \frac{\rho_i}{\rho_s}, \quad (\text{B.9})$$

where ρ_s is the firn density at the base of the survey pole where w_s is measured.

VITA

Name: Nadine A. Nereson

Date: June 8, 1998

Education

B. A.: Physics and Mathematics, St. Olaf College, 1991

Ph. D.: Geophysics, University of Washington, 1998

Dissertation Title

Ph. D.: The Flow History of Siple Dome and Ice Streams C and D, West Antarctica:
Inferences from Geophysical Measurements and Ice Flow Models

Publications

N. A. Nereson, C. F. Raymond, E. D. Waddington, and R. W. Jacobel. Migration of the Siple Dome Ice Divide, West Antarctica. *Journal of Glaciology*, 1998, in press.

N. A. Nereson, R. C. A. Hindmarsh, and C. F. Raymond. Sensitivity of the Divide Position at Siple Dome, West Antarctica, to Boundary Forcing. *Annals of Glaciology*, 27, 1998, in press.

T. A. Scambos, N. A. Nereson, and M. A. Fahnestock. Detailed Topography of Roosevelt Island and Siple Dome, West Antarctica. *Annals of Glaciology*, 27, 1998, in press.

- N. A. Nereson, E. D. Waddington, C. F. Raymond, and H. P. Jacobson. Predicted age-depth scales for Siple Dome and inland WAIS ice cores in West Antarctica. *Geophysical Research Letters*, 23(22): 3163-3166, 1996.
- N. A. Cutler (now Nereson), C. F. Raymond, E. D. Waddington, D. A. Meese, and R. B. Alley. The effect of ice-sheet thickness change on the accumulation history inferred from GISP2 layer thicknesses. *Annals of Glaciology*, 21:26–32, 1995.

Abstracts and Research Summaries

- N. A. Nereson, C. F. Raymond, R. W. Jacobel, and E. D. Waddington. The History of the Spatial Accumulation Pattern at Siple Dome, West Antarctica, from Radar Measurements. *EOS Transactions, 1997 Fall Meeting Supplement*, 78(46): F252, 1997. abstract.
- N. A. Nereson and C. F. Raymond. The Geometry and Stratigraphy of Siple Dome and Implications for its History. *EOS Transactions, 1995 Fall Meeting Supplement*, 76(46): F194, 1995. abstract.
- N. A. Nereson and C. F. Raymond. Recent migration of Siple Dome divide determined from 1994 radio-echo sounding measurements. *Antarctic Journal of the U. S., 1996 Review Issue*, in press.
- C. Raymond, N. Nereson, A. Gades, H. Conway, R. Jacobel, and T. Scambos. Geometry and stratigraphy of Siple Dome, Antarctica. *Antarctic Journal of the U. S., 1995 Review Issue*, 30(5): 91–93, 1995.
- T. Scambos and N. Nereson. Satellite image and GPS study of the morphology of Siple Dome, Antarctica. *Antarctic Journal of the U. S., 1995 Review Issue*, 30(5): 87–89, 1995.